FUNCTIONAL NEUROIMAGING AND BEHAVIOURAL STUDIES ON GLOBAL FORM PROCESSING IN THE HUMAN VISUAL SYSTEM

Jennifer Blanche Swettenham

Doctor of Philosophy

Aston University

December 2005

Aston University

FUNCTIONAL NEUROIMAGING AND BEHAVIOURAL STUDIES ON GLOBAL FORM PROCESSING IN THE HUMAN VISUAL SYSTEM

Jennifer Blanche Swettenham

Doctor of Philosophy

2005

Magnetoencephalography (MEG), functional magnetic resonance imaging (fMRI) and behavioural experiments were used to investigate the neural processes underlying global form perception in human vision.

Behavioural studies using Glass patterns examined sensitivity for detecting radial, rotational and horizontal structure. Neuroimaging experiments using either Glass patterns or arrays of Gabor patches determined the spatio-temporal neural response to global form. MEG data were analysed using synthetic aperture magnetometry (SAM) to spatially map event-related cortical oscillatory power changes; the temporal sequencing of activity within a discrete cortical area was determined using a Morlet wavelet transform. A case study was conducted to determine the effects of strabismic amblyopia on global form processing; all other observers were normally-sighted.

The main findings from normally-sighted observers were: 1) sensitivity to horizontal structure was less than for radial or rotational structure; 2) the neural response to global structure was a reduction in cortical oscillatory power (10-30 Hz) within a network of extrastriate areas, including V4 and V3a; 3) the extent of reduced cortical power was least for horizontal patterns; 4) V1 was not identified as a region of peak activity with either MEG or fMRI. The main findings with the strabismic amblyope were: 1) sensitivity for detection of radial, rotational, and horizontal structure was reduced when viewed with the amblyopic- relative to the fellow- eye; 2) cortical power changes within V4 to the presentation of rotational Glass patterns were less when viewed with the amblyopic- compared with the fellow- eye.

The main conclusions are: 1) a network of extrastriate cortical areas are involved in the analysis of global form, with the most prominent change in neural activity being a reduction in oscillatory power within the 10-30 Hz band; 2) in strabismic amblyopia, the neuronal assembly associated with form perception in extrastriate cortex may be dysfunctional, the nature of this dysfunction may be a change in the normal temporal pattern of neuronal discharges; 3) MEG, fMRI and behavioural measures support the notion that different neural processes underlie the perception of horizontal as opposed to radial or rotational structure.

Keywords: Magnetoencephalography; Synthetic Aperture Magnetometry; Functional Magnetic Resonance Imaging; Glass patterns; Amblyopia.

To Rohan

Acknowledgements

I am grateful to all of the members of the Neuroscience Research Institute and to my fellow PhD students for helping make my time at Aston so enjoyable. In particular, I would like to thank Sian Worthen, Stefanie Hassel and Alison Fisher for their patience with teaching me how to analyse MEG data. I would also like to thank Gareth Barnes, Arjan Hillebrand and Krish Singh for writing the software I used so much and for always being happy and willing to solve problems and answer questions. For unwavering guidance with the fMRI study I would like to thank Jade Thai, it wouldn't have been achieved without her help. For all his help with writing the thesis, I'd like to thank my supervisor Stephen Anderson.

Thank you to all of my friends, both at Aston and elsewhere, for being great and making life fun. Finally, for always being supportive and understanding, thank you to Ben.

Declaration

I Jennifer Swettenham certify that no part of this thesis, in any form, has been submitted for any other qualification at any University or college. To the best of my knowledge, none of the experiments reported here have been previously carried out by any other investigator. All experimental work was undertaken at Aston University. I was supported by a postgraduate research scholarship from the Neuroscience Research Institute, Aston University. Some of this thesis has been published (Anderson & Swettenham, 2006; Swettenham, Anderson, Holliday,2005).

Contents

Table of Figures

1 The visual system, global form perception and amblyopia

1.1 The functional organisation of the human visual system

1.1.1 Before the cortex

In the primate retina there are two main types of ganglion cells, termed midget and parasol cells. From the retina the ganglion cells project through the optic chiasm, at which point some neurons decussate such that the pathway to the left hemisphere contains information from the right visual field and vice versa. The neurons pass on to four nuclei, the most important for human vision being the lateral geniculate nucleus (LGN). Neurons pass through the LGN, segregated in layers by both the eye of origin and the type of ganglion cell, to the primary visual cortex. There are also very thin layers in the LGN between the magno- (parasol cell) and parvo- (midget cell) layers that have been termed koniocellular.

1.1.2 The cortex

The primary visual cortex, also known as the striate cortex or V1, is the first point at which input from the two eyes converge. It has six layers (I to VI) with several sublayers and is organised into modules with each module containing two "blobs" or "patches" - named because of the dark colour of these regions when the cortex is stained for the mitochondrial enzyme, cytochrome oxidase (CO; Figure 1.1).

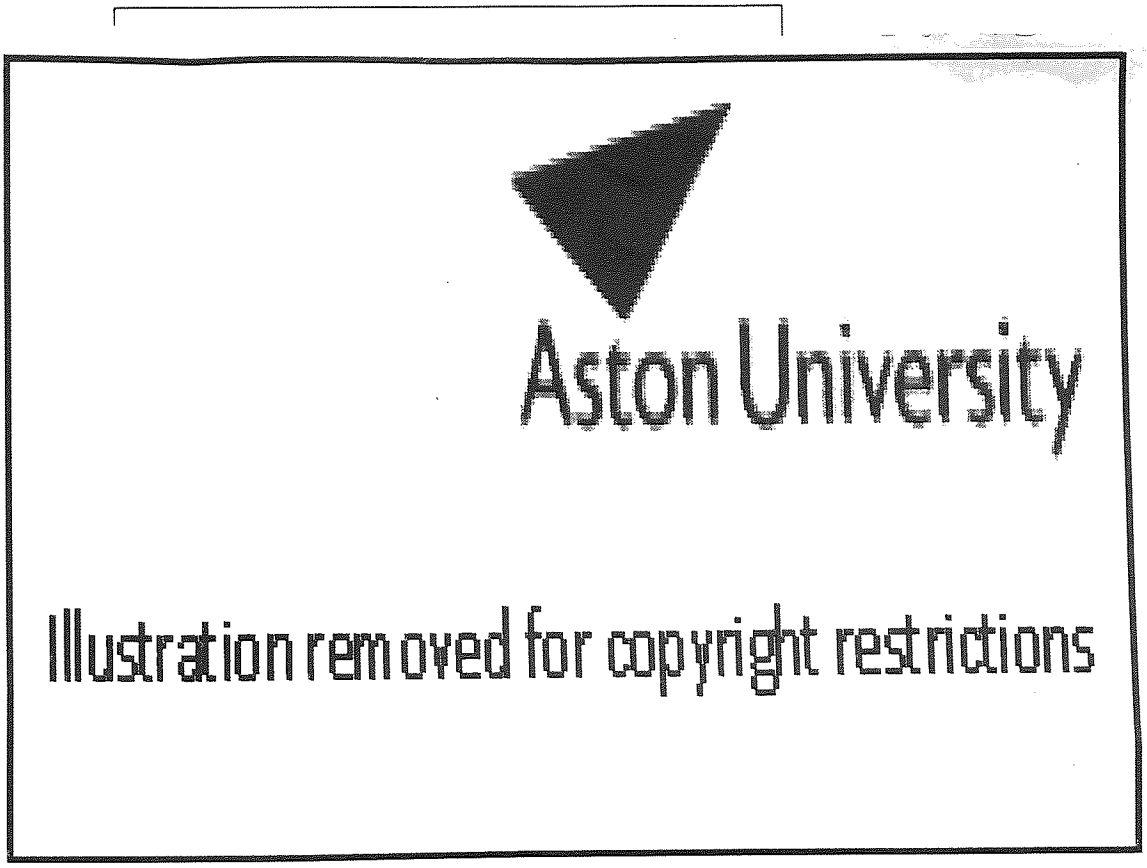

Figure 1.1. A schematic representation of a module in V1. Each module contains two CO blobs or patches, each receiving input from one eye. Taken from Carlson, 1994, p. 163.

The magno-, parvo- and konio-cellular pathways were originally thought to remain segregated from the LGN through V1 and into V2 (Figure 1.2 (a)). However, this model has been replaced with one in which the magno-, parvo- and koniocellular streams become mingled and there are only two major pathways, those from CO patches and those from interpatches (Figure 1.2 (b); reviewed in Sincich & Horton, 2005).

Figure 1.2. a) The tripartite model of the visual system in which the magno-, parvo-, and konio-cellular streams remained separate. It was thought that the magnocellular stream conveyed motion information, the parvocellular stream conveyed form and colour information and the koniocellular stream contributed to colour processing. This is now known to not be true and instead the b) bipartite model is favoured in which the magno-, parvo-, and konio-cellular streams are mixed. Neurons from CO patches project to the thin stripes in V2, neurons from interpatches project to the thick and pale stripes in V2. The pulvinar is the main thalamic input to V2. Taken from Sincich & Horton, 2005.

Retinotopic mapping is the identification of brain areas based on responses to specific stimuli within specific regions of the visual field. Such techniques with functional magnetic resonance imaging (fMRI; Tootell, Hadjikhani, Mendola, Marrett, Dale, 1998) and positron emission tomography (PET; Hasnain, Fox, Woldorff, 1998) have led to the identification of visual areas with a hierarchy starting at V1. It can be seen from Figure

1.3 that, with the exception of V1, these retinotopically mapped regions do not correspond with Brodmann areas. In addition, visual areas vary massively in size and boundary location between individuals, independently of the overall size of the brain (Amunts, Malikovic, Mohlberg, Schormann, Zilles, 2000; Andrews, Halpern, Purves, 1997).

Figure 1.3. Locations of human visual cortical areas superimposed on an image of an individual observer's brain, a) and b) show the right hemisphere from the midline, c) and d) show the right hemisphere with the posterior to the left and the anterior to the right. Using fMRI with tests for motion and retinotopy, the locations of visual areas for this observer are shown in a) and c). The Brodmann areas are shown in b) and d). Taken from Tootell *et al.*, 1998.

Visual information passes from V1 to V2 and then onto other visual areas. Based on lesioning studies in the macaque, Ungerleider and Mishkin (1982) proposed a two stream model of visual processing. The ventral stream (or so called "what" pathway) was proposed to be involved in object discrimination. The dorsal stream (or so called "where" pathway) was proposed to be involved in processing spatial landmarks. In support of the role of ventral areas in object recognition, there is a large area of inferior occipital and temporal cortex called the lateral occipital complex (LOC) that responds to pictures of objects (see section 1.2.2). The LOC is part of a series of ventral areas activated by form including V1 and V4 (Lerner, Hendler, Ben-Bashat, Harel, Malach, 2001). The role of the dorsal stream has since been reconsidered as being involved in the visual guidance of actions (Milner & Goodale, 1997). Dorsal visual areas that are sensitive to moving stimuli such as V3a may underlie the visual monitoring of actions (Tootell *et al.*, 1997).

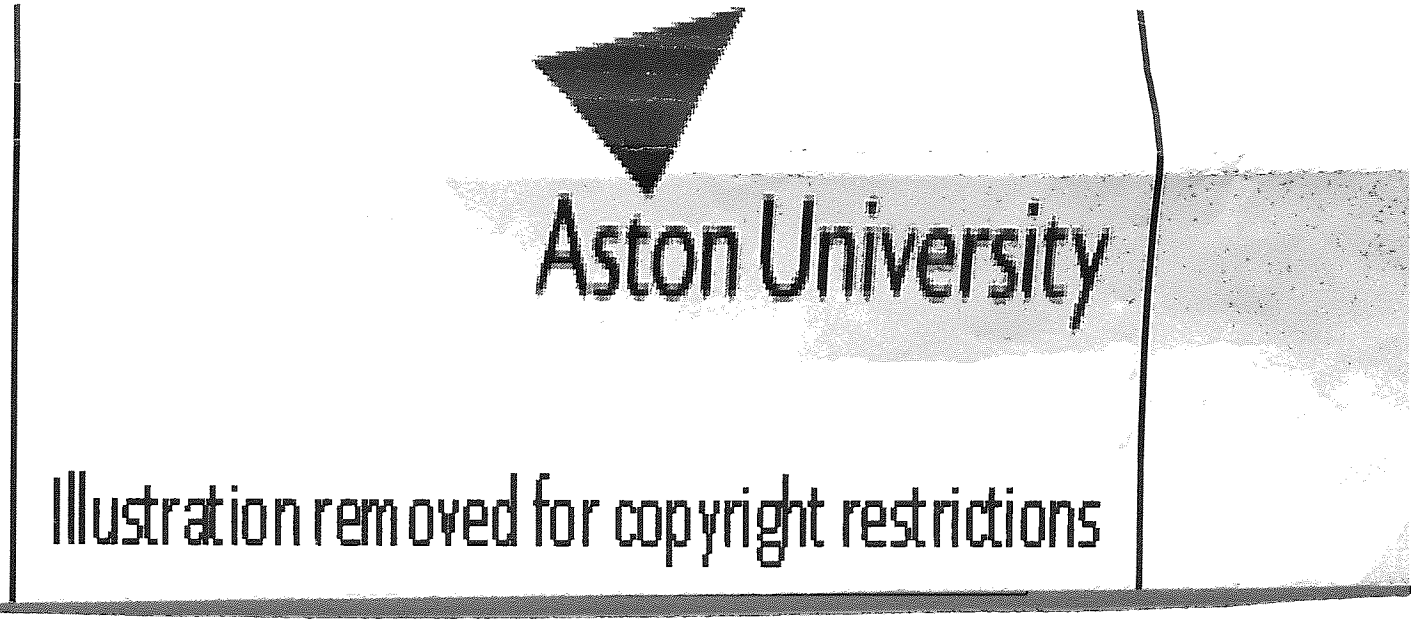

Figure 1.4. A schematic diagram of Ungerleider and Mishkin's (1982) model of two streams of visual processing in primate cerebral cortex. Taken from Milner & Goodale, 1997, p. 22.

1.2 Global form perception

The perception of global form requires the processing of image features across visual space. The generally accepted view of the visual system is that primary visual areas have relatively small receptive fields and therefore process visual features over a localised region of the visual field (Olshausen & Field, 2005), whereas higher visual areas have larger receptive fields with input pooled across visual space (Felleman & Van Essen, 1991; Tootell *et al.*, 1997). Consequently, the receptive field sizes indicate that higher visual areas, rather than V1, may provide the neuronal locus of global form processing. To qualify this, many human neuroimaging studies have used global form stimuli. In addition, behavioural studies have investigated the effect of a range of variables on the sensitivity of the visual system to detection of global form. A brief review of these studies, with particular attention given to experiments that used Glass patterns, is given in the following sections.

1.2.1 Behavioural studies of global form perception

In 1969, with the aid of a can of spray paint and a photocopier, Glass demonstrated a novel visual stimulus that has become widely used in visual form experiments. By superimposing a copy of a field of sprayed dots onto the original field of dots and rotating it, Glass (1969) created a moiré rotational pattern centred on the pivot. Thus, although the initial field of random dots contained no global form, the associations between the two fields created form analogous to the transformation. Advances in stimulus generation techniques have enabled the generation of Glass patterns in which the common rule by which dot pairs are oriented, and the proportion of dot pairs oriented according to this rule, can be modulated. With Glass patterns, different global

structures can be compared whilst maintaining the same dot density and luminance of the pattern.

Several studies have investigated possible differences in processing different Glass pattern types. Using forced-choice paradigms to determine the lowest signal-to-noise ratio necessary for form detection, some studies have reported lower sensitivity for the detection of horizontal Glass patterns in comparison with radial, rotational and hyperbolic patterns (Kelly, Bischof, Wong-Wylie & Spetch, 2001; Wilson & Wilkinson, 1998; Wilson, Wilkinson & Asaad, 1997). Similarly, higher sensitivity for rotational than for horizontal Glass patterns was found with a paradigm to determine the minimum amount of noise that could be detected within the structure (i.e. noise-to-signal ratio; Kurki & Saarinen, 2004). In addition, Seu and Ferrera (2001) found higher sensitivity for detection of both radial (spiral angle 0°) and rotational (spiral angle 90°) Glass patterns than for spiral patterns with angles between 0° and 90°. Lower sensitivity for intermediate spirals ($0° < \text{angle} < 90°$) could not be explained through loss of symmetry, as sensitivity to spiral patterns was greater than for translational patterns which have one axis of symmetry (Seu & Ferrera, 2001). Additionally, an explanation based on differing orientation statistics (Stevens, 1978) could be ruled out as these were constant for all spiral patterns. Ultimately, Seu and Ferrera fitted their data with a model based on Wilson and Wilkinson's (1998) multi-stage nonlinear filter, but with an added spiral detector for the 45 degree angle. These detectors are weighted to maximise the output from the rotational filter and minimise output from the spiral detector, thereby creating the lowest detection thresholds for rotational patterns. Using arrays of Gabor patches arranged on a regular grid, Achtman, Hess and Wang (2003) also found higher sensitivity for the detection of rotational patterns than for radial or spiral patterns. These

findings may relate to the response properties of neurons in V4 where electrophysiological studies in macaque have revealed groups of neurons that respond more strongly to radial, rotational or hyperbolic gratings than to conventional linear gratings (Gallant, Braun, Van Essen, 1993; Gallant, Connor, Rakshit, Lewis, Van Essen, 1996). Similarly, human V4 has shown stronger activation in response to radial and rotational gratings than to linear gratings (Wilkinson *et al.*, 2000). Moreover, the discrimination of radial and rotational Glass patterns was significantly worse in an observer that had a small lesion in this area (Figure 1.5; Gallant, Shoup & Mazer, 2000).

Figure 1.5. Coronal (left), axial (middle), sagittal (right) sections with arrows indicating a small lesion in putative V4 in a human neurological patient. This patient had normal luminance and orientation processing but impaired global form processing. Taken from Gallant *et al.*, 2000.

In contrast, other studies have not found different sensitivities with different pattern types (Dakin & Bex, 2002; Maloney, Mitchison & Barlow, 1987). Dakin and Bex (2002) claimed the reason some studies found an advantage for detection of rotational Glass patterns was that, by presenting rotational patterns in a circular window, they had inadvertently created a smooth stimulus edge that could be used as a cue. Similar

concern was raised by Maloney *et al.* (1987) regarding radial Glass patterns producing a rim of partner dots at the edge of a circular stimulus. Dakin and Bex found that presenting Glass patterns in a square rather than a circular window, or introducing a fringe of noise around the stimulus edge, equalised detection thresholds for rotational and horizontal Glass patterns. Studies of spatial integration had also suggested that whilst global pooling occurred with the processing of radial and rotational Glass patterns, only local information was used in the processing of parallel patterns (Wilson & Wilkinson, 1998; Wilson, Wilkinson & Asaad, 1997). However, a more recent study reported that global pooling occurs for the detection of dot pairs even without global structure in the Glass pattern (Kurki, Laurinen, Peromaa, Saarinen, 2003).

Further studies of Glass pattern perception have shown that the perception of structure is largely unaffected by changes in dot density and separation of the dots within a pair (Kurki *et al.*, 2003; Wilson & Wilkinson, 1998; Wilson *et al.*, 1997). Wilson and colleagues (1997) reported no changes in Glass pattern sensitivity with densities of 3-12 percent and pair separations of 4.5-13.0 arc min. They also demonstrated that form perception was not dependent on the dots within a pair being the nearest to each other - shapes were still visible even when the mean dot spacing was half the pair spacing. Similarly, the detection of global form in arrays of Gabor patches is determined by the orientations of the sinusoidal carriers and is invariant to changes in patch density, number, position, spatial frequency and contrast (Achtman *et al.*, 2003; Wang & Hess, 2005). However for Glass patterns, if the dots within a pair have opposing polarity (i.e. one white and one black dot) then the perception of structure is not perceived (Glass & Switkes, 1976).

The experiments discussed above have explored the processing of global form with stimuli such as Glass patterns and Gabor patches. These stimuli elicit a perception of form but not of an object. Accordingly, they could be considered to involve *intermediate form processing* (Gallant *et al.*, 2000). To recognise an object may involve the integration of many different shapes and a higher level of processing. Grill-Spector and Kanwisher (2005) have recently demonstrated that the detection and categorisation of objects occur concurrently, whereas within-category identification (e.g. distinguishing a pigeon from birds) takes more time (Figure 1.6). Detection of an object could not be achieved without categorisation and vice versa, indicating that these processes may share a common mechanism.

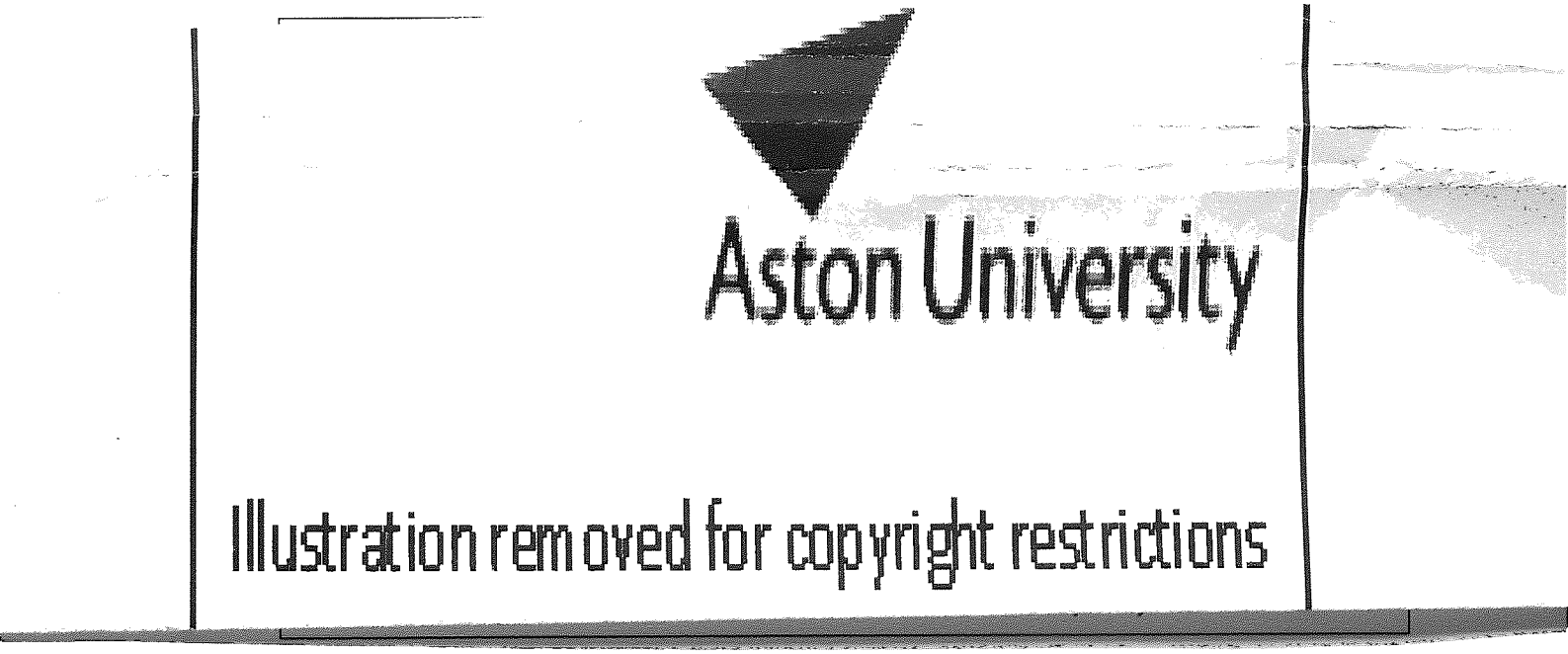

Figure 1.6. Naming performance as a function of display time for object detection, categorisation (e.g. bird) and identification (e.g. pigeon). The data are averaged for 15 observers. Taken from Grill-Spector & Kanwisher, 2005.

1.2.2 Neuroimaging studies of global form perception

It is now well established that there are areas within ventral occipital and temporal cortex more strongly activated by the presentation of pictures of objects than of scrambled objects (Figure 1.7). This area has been termed the LOC and includes a large region of mainly non-retinotopic cortex. The LOC responds to visual shapes irrespective of whether the shape depicts a known or unknown object and with responses that are invariant to size, position and luminance (reviewed in Grill-Spector, Kourtzi, Kanwisher, 2001).

A hierarchical axis of object processing from V1 through to V4/V8 and then into and within the LOC has recently been demonstrated (Lerner *et al.*, 2001). Using fMRI and pictures of cars and faces that had varying levels of intactness (from intact to broken into 256 blocks, see Figure 1.8 (a)), Lerner and colleagues found that responses in anterior regions of cortex decreased as images were increasingly scrambled (Figure 1.7). This is indicative of global representations being processed in the anterior part of the LOC. Activity in the anterior LOC was not reduced by superimposing a grid onto an intact image, indicating that the activity reduction in this area to scrambled images was not due to the lines or edges present in the pictures.

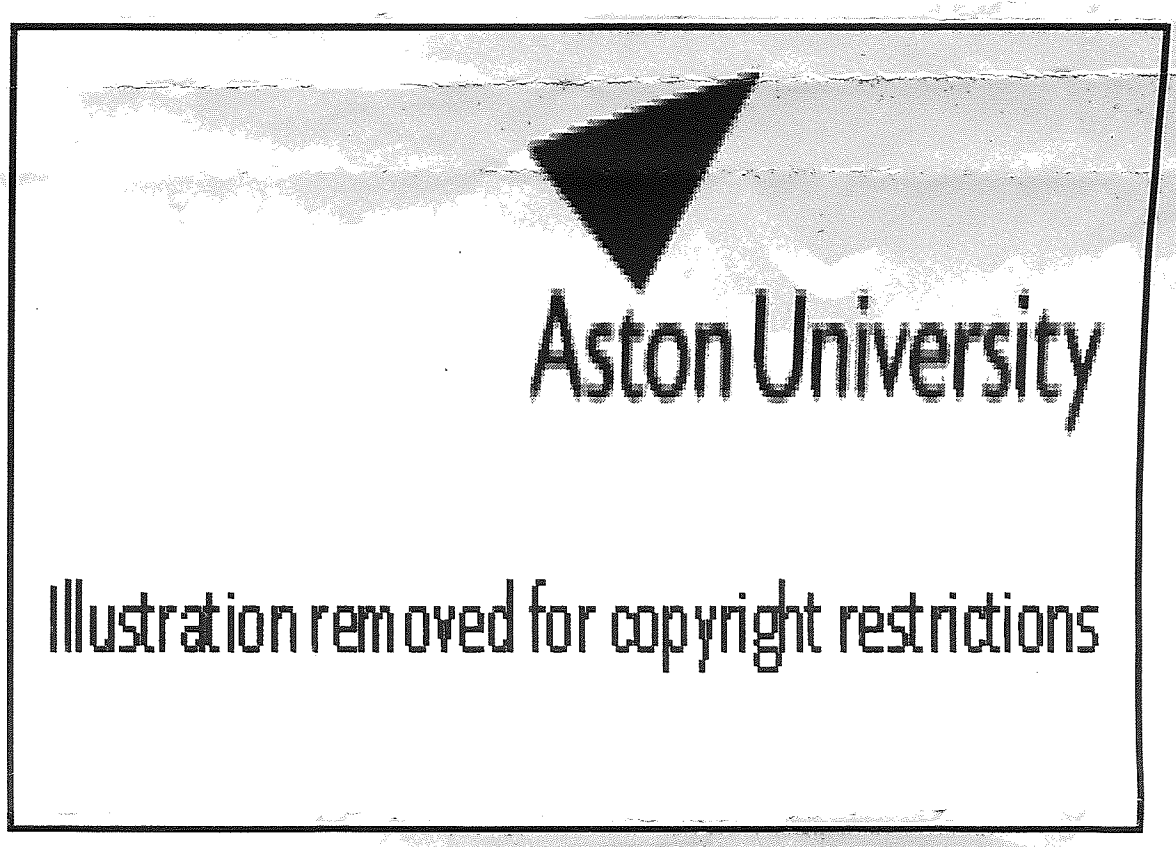

Figure 1.7. Sensitivity to face scrambling along the LOC determined using fMRI. Activations to full (green) and scrambled (orange) faces are shown superimposed on a) the right hemisphere of an inflated brain with the main sulci labelled as STS (superior temporal sulcus), ITS (inferior temporal sulcus) and OTS (occipito-temporal sulcus); b) an axial slice. Adapted from Lerner *et al.*, 2001.

Lerner *et al.* (2001) showed that activity in V1 increased as images became increasingly scrambled. The reduction of activity in the LOC, and the increase of activity in V1, with progressively more scrambled images are illustrated in Figure 1.8 (a). A similar relationship between V1 and the LOC was found in another fMRI study using line stimuli oriented either randomly or to form a two-dimensional or a three-dimensional percept (Murray, Schrater & Kersten, 2004). As the percept of the lines became more "object-like", activity increased in the LOC but decreased in V1. Murray *et al.* suggested that the reduced activity in V1 was the product of *negative* feedback from high-level visual areas (such as the LOC) elicited by form processing or perception.

In contrast, other fMRI studies have found that the presentation of contours defined by Gabor elements increased activity in both V1 and the LOC (Altmann, Bülthoff, Kourtzi, 2003; Kourtzi & Huberle, 2005; Kourtzi, Tolias, Altmann, Augath, Logothetis, 2003). Figure 1.8 (b) shows comparable activations in early visual areas and the LOC in response to two concentric closed contours in the array of Gabor patches (Altmann *et al.*, 2003). In addition, the response in V1 was enhanced when observers had detected the contours (as indicated by button presses) but attenuated when they had not. Altmann *et al.* postulated that this modulation of activity in V1 could be due to *positive* feedback from higher visual areas that was dependent on perception of the global form.

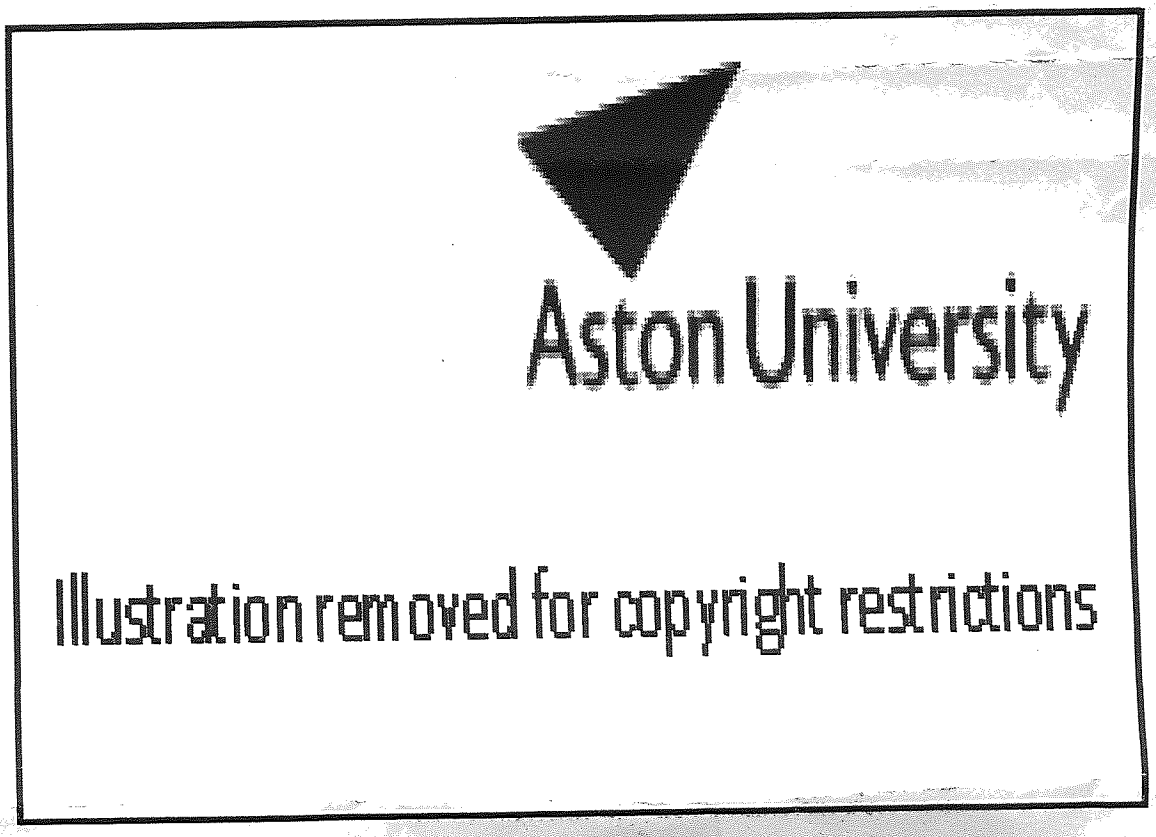

Figure 1.8. FMRI responses to the presence of global form; a) the left and right histograms show the BOLD response in the LOC and V1 respectively. The histograms show (from left to right) that as pictures of faces were increasingly scrambled, activation in LOC decreased but activation in V1 increased. Samples of face stimuli as used in the experiment are shown along the top of the panel. Adapted from Lerner *et al.* 2001; b) the histogram shows (from left to right) that the BOLD response in V1, V2, VP, V4v and the LOC increased following presentation of closed contours (black) relative to presentation of random patterns (stripes). Samples of Gabor element stimuli as used in the experiment are shown on the right side of the panel. Adapted from Altmann *et al.*, 2003.

Global form perception has also been found to have no effect on the BOLD response in V1 (Braddick, O'Brien, Wattam-Bell, Atkinson, Turner, 2000). Following the presentation of concentrically oriented lines (Figure 1.9 (b)), regions of activation were observed in the middle occipital gyrus, the intraparietal sulcus and the ventral occipital surface, but not in V1 (green areas, Figure 1.9 (a)). The activations on the ventral occipital surface were close to V4 as defined by Hasnain *et al.* (1998). This figure also illustrates (red areas) spatially distinct brain regions that were activated using an analogous motion coherence stimulus.

Using fMRI, Wilkinson *et al.* (2000) observed stronger activations in V4 to radial and rotational gratings than to conventional parallel gratings. They also noted that activation to all three pattern types was similar in V1, but in V2 there was a non-significant trend for greater activation to radial and rotational gratings than to conventional parallel gratings. The gratings were qualitatively comparable with Glass patterns with which behavioural studies have indicated global pooling for radial and rotational but not translational patterns (Wilson & Wilkinson, 1998; Wilson *et al.*, 1997).

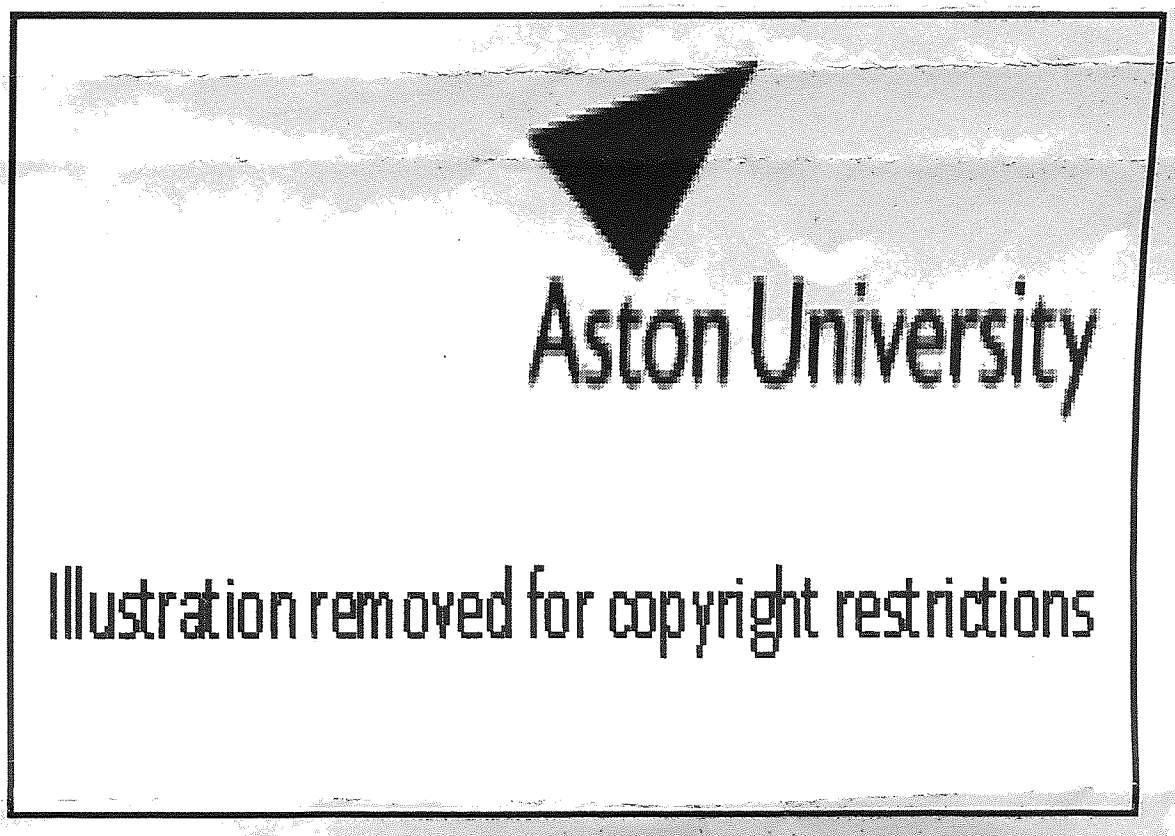

Figure 1.9. Schematic illustration of neural regions activated by form coherence (green) and motion coherence (red). Within individuals, areas activated by form coherence did not overlap with areas activated by motion coherence; b) the global form stimulus consisted of an array of lines, those within the central region were concentrically oriented, the remainder were randomly oriented. Adapted from Braddick *et al.*, 2000.

The studies discussed above present conflicting evidence for the effect of global form on V1, with increased (Altmann *et al.*, 2003; Kourtzi & Huberle, 2005; Kourtzi *et al.*, 2003), decreased (Lerner *et al.*, 2001; Murray *et al.*, 2004), and unchanged (Braddick *et al.*, 2000; Wilkinson *et al.*, 2000) activity reported. The reason for these differences are unclear but may be related to the stimuli and/or tasks employed.

Tasks that required observers to either monitor the stimulus for form or to pay attention to the local features produced enhanced activity in V1 (Altmann *et al.*, 2003; Kourtzi & Huberle, 2005). Kourtzi and Huberle (2005) also reported that tasks requiring attention to global rather than local form elicited greater processing in the LOC. Both Lerner *et al.* (2001) and Murray *et al.* (2004) used passive viewing paradigms and, as stimuli became more "object-like", the observer may have shifted attention from the local features to the global percept, thereby reducing activity in V1. This is plausible as the stimuli used in these studies (pictures of faces and cars, Lerner *et al.*; three-dimensional shapes, Murray *et al.*) are known to strongly activate the LOC (Kanwisher, Chun, McDermott, Ledden, 1996; Malach *et al.*, 1995). However, although Braddick *et al.* (2000) and Wilkinson *et al.* (2000) also used a passive viewing paradigm their stimuli were two-dimensional and may not have been sufficiently "object-like" to induce a shift of attention to the global percept. Consistent with this idea, both studies report ventral occipital activity to global form that was within or close to V4 but was not anterior enough to be the LOC.

By far the most common neuroimaging technique used in studying human visual function is fMRI, reflecting its pre-eminence in the field of functional imaging in general. Although the spatial resolution of images obtained with this technique is excellent, the temporal resolution is generally in the order of seconds. However, a rapid event-related adaptation paradigm has recently been used to investigate the temporal sequence of processing of global form (Kourtzi & Huberle, 2005). This method is based on the theory of neuronal adaptation, which is responses decline in repeatedly stimulated neurons (Carandini, Movshon, Ferster, 1998). With fMRI, neuronal

adaptation would be reflected as a smaller haemodynamic response to two stimuli presented so close in time that the neural processing elicited by each stimulus overlaps, than the haemodynamic response from the same two stimuli presented further apart in time so that the neural processing associated with the first stimulus had finished before the second stimulus was presented (see Boynton & Finney, 2003). Accepting this principle, Kourtzi and Huberle (2005) suggest that form processing in V1 is transient, lasting between 100 and 400 ms after pattern offset, whereas form processing in the LOC is sustained for longer than 400 ms after stimulus offset.

The temporal resolution of activity revealed by electroencephalography (EEG) is excellent but the spatial localisation of current sources is poor because of signal distortion by the brain tissue and skull. Using EEG, a larger N170 component of the event-related potential (ERP) was observed in response to rotational Glass patterns than to random or translational Glass patterns (Figure 1.10; Ohla, Busch, Dahlem, Herrmann, 2005). The earlier P100 peak was unaffected by pattern type. Based on previous studies of the components of the ERP, Ohla *et al.* speculated that this difference for rotational Glass patterns may arise in extrastriate areas (Di Russo, Martinez, Sereno, Pitzalis, Hillyard, 2001). Although ERPs have been widely used as a measure of neural processing, there is evidence that differences in visual perceptual experience are better revealed using analysis techniques that do not require signal averaging (Cosmelli *et al.*, 2004). Such techniques conserve data that is time- but not phase-locked to the onset and are discussed in the next chapter.

Figure 1.10. Grand averaged ERPs at an occipital electrode in response to random (dotted line), translational (grey line) and rotational (black line) Glass patterns (n = 16). The N170 amplitudes were enhanced in response to rotational patterns. No pattern type differences were found with the P100 amplitude. Taken from Ohla *et al.* 2005.

In summary, behavioural studies of global form perception have tended to use stimuli that can be well controlled for local visual cues, such as Glass patterns or arrays of Gabor elements. In contrast, neuroimaging studies have mostly used higher-order stimuli such as pictures of objects and scrambled objects. Using Glass patterns with neuroimaging studies would provide a link between behavioural sensitivities and neural responses in areas such as V4.

1.3 Amblyopia

Amblyopia is a visual disorder that cannot be overcome by refractive correction and has no observable basis in the eye. The visual deficits are the legacy of conditions such as strabismus, anisometropia or light deprivation (i.e. cataracts) during critical periods in

the development of the visual system. These critical periods occur between approximately 6 months and 8 years of age, and disruption of the visual system outside of this range will not lead to amblyopia (reviewed in Daw, 1995). Most often the causative conditions only affect one eye, resulting in an amblyopic and a non-amblyopic (fellow) eye. Clinically, a reduced visual acuity of 6/9 or worse, with a full refractive correction in place, is indicative of amblyopia. However, amblyopes may still perceive sharp edges and do not always report the visual world as blurred (Hess, Pointer, Simmers, Bex, 2003).

Amblyopia is a relatively common visual disorder that affects 2-3 percent of the population (Hillis, Flynn, Hawkins, 1983). With the exception of careers that require excellent binocular vision (e.g. airline pilot), amblyopia does not affect lifetime occupational class (Chua & Mitchell, 2004; Fielder, 2002). The most worrying health risk is losing vision in the fellow eye and being reliant only on the amblyopic eye for vision. However, there is some evidence that in this event the function of the amblyopic eye can improve, indicating some residual plasticity in the visual system (Chua & Mitchell, 2004; reviewed in Moseley & Fielder, 2001).

The site of the amblyopic dysfunction is widely considered to be the cortex (reviewed in Hess, 2001). This makes amblyopia an interesting condition to investigate using psychophysical and neuroimaging paradigms, not only to increase understanding of amblyopia *per se* but also the neural development of the visual system in general. The following sections briefly discuss the low- and high-level effects of amblyopia and the neuroimaging studies that have been performed to investigate this condition.

1.3.1 Contrast sensitivity and visual acuity in amblyopia

Accepting that the amblyopic classification may not accurately reflect the original cause of amblyopia, McKee *et al.* (2003) undertook by far the largest study to date to explore the low-level visual deficits associated with all types of amblyopia. Four hundred and twenty seven observers with abnormal vision were clinically categorised and submitted to a battery of tests determining visual acuity, contrast sensitivity and binocular function. By plotting the acuity and contrast sensitivity performance for each of the visual categories it was found that the strabismic, anisometropic and strabismic anisometropic groups represented distinctly different visual functioning compared with each other and with the normally-sighted group (Figure 1.11). It can also be seen from Figure 1.11 that the acuity and contrast performance of deprivational amblyopes was similar to that of anisometropic amblyopes. This was surprising considering the different causes of the visual loss.

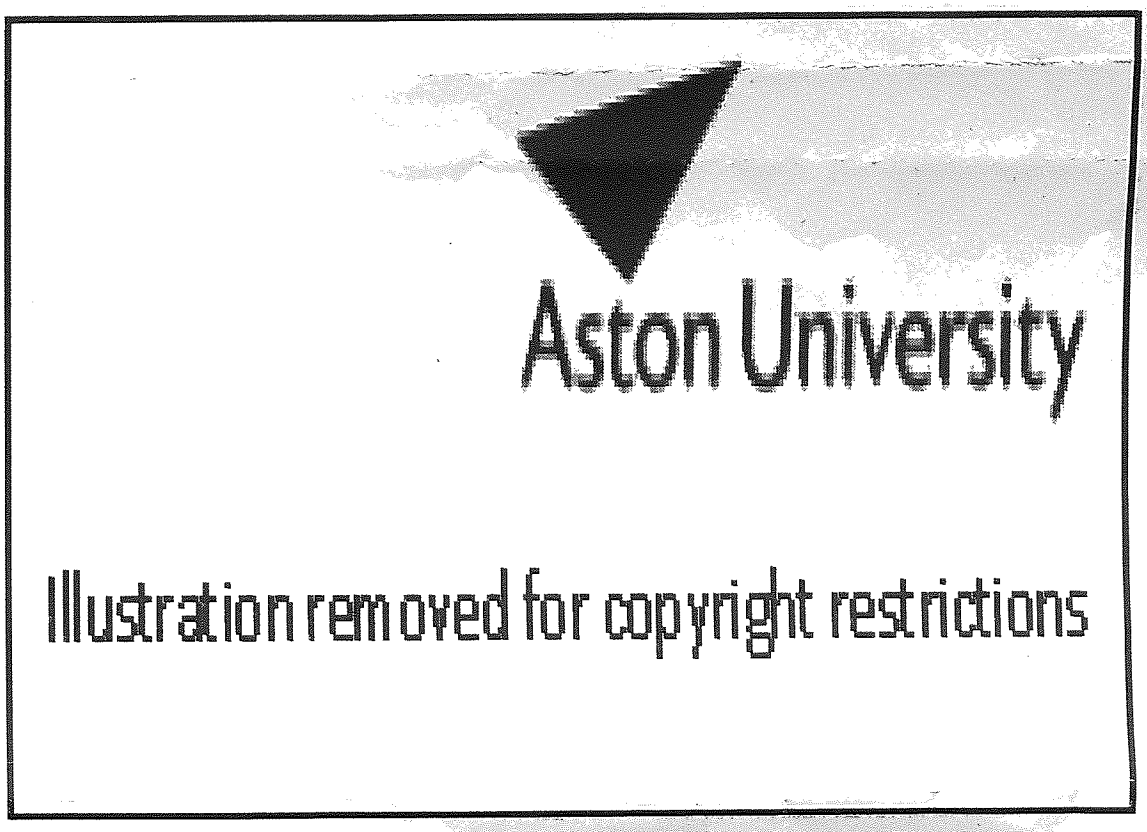

Figure 1.11. Mean locations in contrast sensitivity and acuity space for 11 clinically defined categories of observers. The diagonal bars show 1 SEM along the principal axis of the elliptical distributions. Note the clear separation of normals, strabismics, strabismic anisometropes and anisometropes. Taken from McKee *et al.*, 2003.

Figure 1.11 shows that strabismic amblyopes, who invariably have disrupted binocular vision, have higher contrast sensitivity than normally-sighted observers. In addition, further analysis showed that those anisometropic observers lacking central binocular function had similarly elevated contrast sensitivity. McKee *et al.* suggested that the increased contrast sensitivity associated with loss of binocular function may reflect changes in V1 cortical neurons. More specifically, as a developmental lack of binocular vision results in all neurons being monocularly driven (Hubel & Wiesel, 1968; Hubel, Wiesel, LeVay, 1977; Kiorpes, Kiper, O'Keefe, Cavanaugh, Movshon, 1998), then when a stimulus is monocularly viewed (as in their study) there will be more neuronal activation in a visual system that contains all monocularly driven cells than in a normal

visual system which contains mostly binocularly driven cells. Note that with observers lacking binocular function, the increased contrast sensitivity relative to normally-sighted observers is also observed with fellow-eye viewing (McKee *et al.*, 2003). The findings of McKee *et al.* are broadly consistent with those of earlier studies investigating contrast sensitivity and acuity (Levi & Klein, 1982a; 1982b; 1985; Levi, Klein, Wang, 1994a; 1994b).

1.3.2 Form perception in amblyopia

Beyond the acuity and contrast deficits discussed above, amblyopes make errors in judgements of position, orientation and global form that cannot be simply explained by reduced contrast sensitivity or visual blurring in childhood (Barrett, Pacey, Bradley, Thibos, Morrill, 2003; Levi *et al.*, 1994a; reviewed in Hess, 2002; Popple & Levi, 2005; Wang, Levi, Klein, 1998; Wilson, 1991). One proposed model for this extra visual loss is undersampling. In this model the visual deficits in amblyopia are thought to arise as a consequence of neural undersampling in which case the high spatial frequency components of a visual image would not be veridically represented by the sampling array. This occurs in normal peripheral vision (Anderson & Hess, 1990). Several psychophysical studies have suggested that undersampling is an important contributor to positional uncertainty (Wilson, 1991; Levi & Klein, 1996; Wang *et al.*, 1998; Levi, Klein, Sharma, 1999; Sharma, Levi, Coletta, 1999), while others have concluded that, if it occurs, its effects are dwarfed by neural disarray (Hess, Wang, Demanins, Wilkinson, Wilson, 1999; Demanins, Wang, Hess, 1999). In the latter model, the normally highly topographical arrangement of the visual system, which runs from the retina to the cortex and then to higher cortical layers where it converges with input from other areas of the visual field, is thought to be disrupted. This would then invalidate the lateral

connections in the cortex that allow modulation of input from surrounding cortical columns. However, neural disarray and undersampling are not mutually exclusive (Figure 1.12).

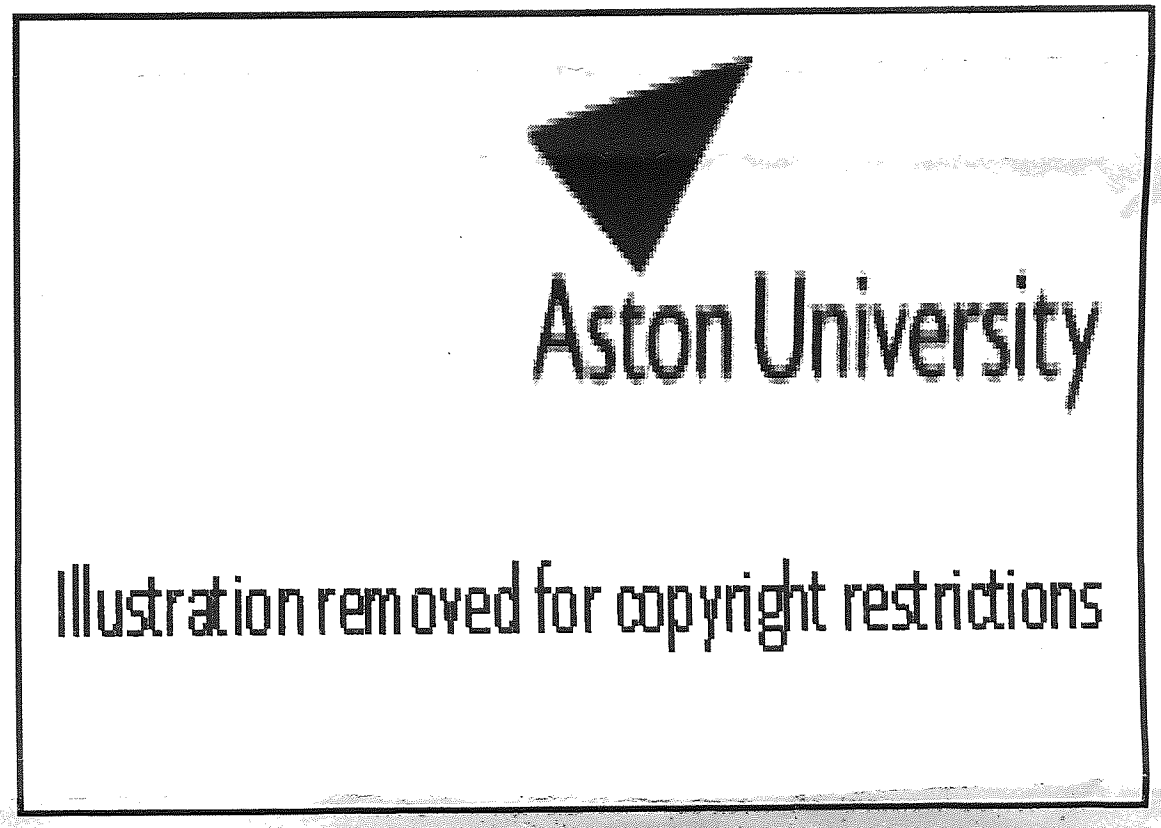

Figure 1.12. Simulation of the effects of spatial undersampling and position irregularity in producing perceptual distortions. The degree of undersampling increases from top to bottom. Position irregularity increases to the right. The panel on the right centre is suggestive of the amblyopic perceptual distortions. Adapted from Wilson, 1991.

Misperceptions have also been attributed to the shrinkage of ocular dominance columns (Barrett *et al.*, 2003; Wilson, 1991). The shrinkage of ocular dominance columns has been observed with animal models of amblyopia (Hubel, Wiesel, LeVay, 1977; Kiorpes

et al., 1998; LeVay, Wiesel, Hubel, 1980), but its occurrence in human amblyopia remains controversial. Human postmortem studies have not found evidence of any such shrinkage (Horton & Hocking, 1996; Horton & Stryker, 1993) but a recent *in vivo* neuroimaging study has (see section 1.3.3.1; Goodyear, Nicolle, Menon, 2002). Barrett *et al.* (2003) postulated that common misperceptions of gratings by amblyopes could arise from shrinkage of ocular dominance columns. They found that when amblyopes sketch how they perceive single gratings with their amblyopic eye, the resulting picture often looks like the summing of two component gratings (Figure 1.13). Whatever the underlying cause of these errors, the sketches illustrate how the effect of amblyopia is far more complicated than that expected by merely reduced acuity.

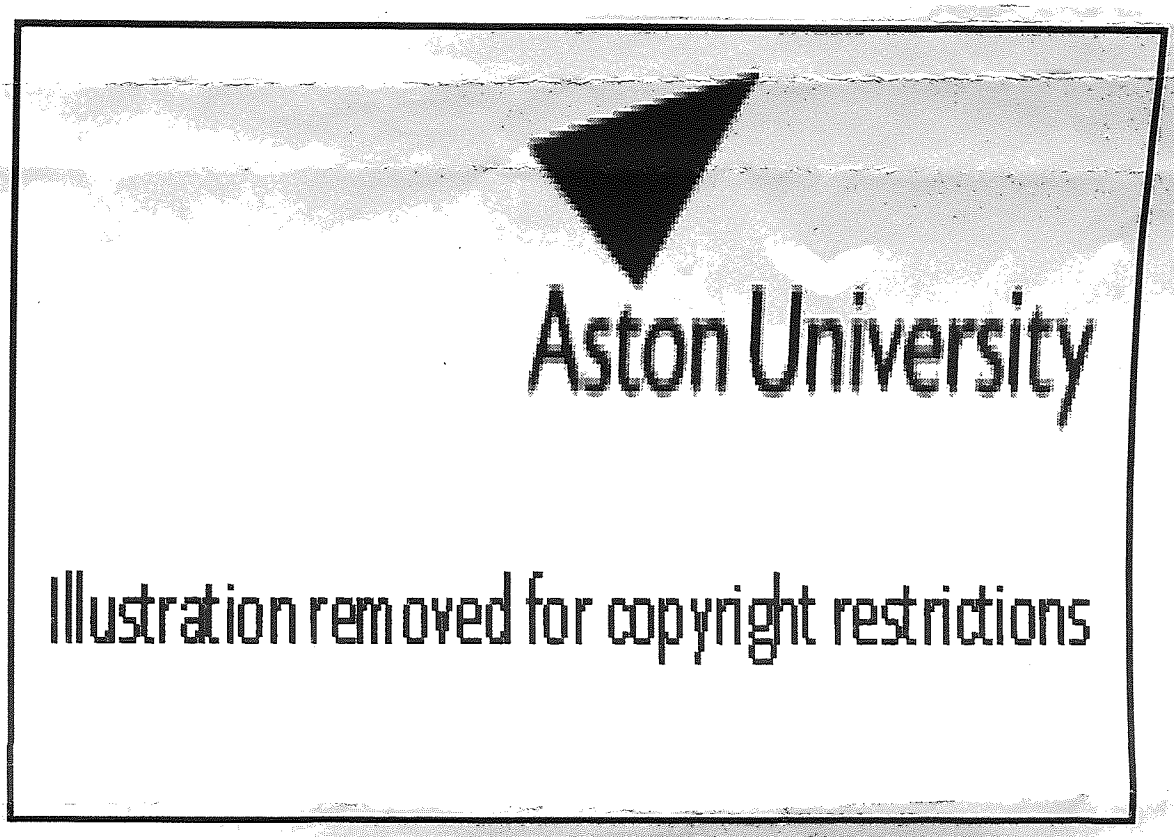

Figure 1.13. Amblyopic viewing of single gratings results in misperceptions similar to those shown in the right hand column (as sketched by amblyopes). Comparable patterns can be generated when two component gratings (two left columns) are summed (third column). The orientation and number of cycles of the grating that was presented to the amblyope is shown next to the sketch. Taken from Barrett *et al.* 2003.

Interestingly, although amblyopes make errors in the judgement of position and orientation of local elements, studies suggest that the integration process to create a global percept is essentially normal (Hess, McIlhagga, Field, 1997; Mansouri *et al.*, 2004; Simmers & Bex, 2004). This conclusion of normal integration is based on the

ability to match performance with the fellow eye by increasing positional and/or orientational jitter. In contrast, based on findings of deficits in symmetry detection, Levi and Saarinen (2004) propose that integration of local information is reduced in amblyopia. Additionally, a "counting" task in which amblyopes consistently underestimated the number of elements in a briefly presented stimulus, led Sharma, Levi and Klein (2000) to conclude that the amblyopic visual system was more limited than the normal visual system in the number of elements it could process. Glass pattern perception has also recently been investigated with amblyopia. In children that have had profound form deprivation due to dense cataracts, the detection of rotational Glass patterns was worse than that of normally-sighted children (Lewis *et al.*, 2002). Similarly, sensitivity to rotational and translational structure was poorer in strabismic amblyopes than in normally-sighted controls (Rislove, Hall, Kiorpes, 2005).

1.3.3 Neuroimaging of amblyopia

A range of neuroimaging techniques and stimuli have been used to explore the neural basis of amblyopia. Following the large body of animal work indicating dysfunction in V1 (Blakemore, 1990; Movshon & Kiorpes, 1990), several studies used paradigms to investigate this area. More recently, because animal work has shown that the physiological deficits in V1 are not sufficient to explain the full range of perceptual deficits in amblyopia (Kiorpes *et al.*, 1998), some imaging studies have used more complex stimuli in an attempt to assess the integrity of higher-order visual areas. Taken together, these studies make it clear that there must be cortical deficits associated with amblyopia both within and beyond area V1.

1.3.3.1 FMRI

Early fMRI studies reported that monocular stimulation of the amblyopic eye yielded reliable activity in area V1 but reduced activity in areas V2, V3 and V5 (Sireteanu *et al.*, 1998). However numerous fMRI studies have since reported that V1 is dysfunctional in amblyopia (Algaze, Roberts, Leguire, Schmalbrock, Rogers, 2002; Barnes, Hess, Dumoulin, Achtman, Pike, 2001; Choi *et al.*, 2001; Goodyear, Nicolle, Humphrey, Menon, 2000; Lee *et al.*, 2001). Perhaps the clearest evidence for this comes from Barnes *et al.* (2001). They examined strabismic adults using large field, high contrast (50 %), temporally modulated (8 Hz) sinusoidal stimuli that were well within the amblyopic passband of each observer. In comparison with responses driven by the fellow eye, those driven by the amblyopic eye were reduced in areas V1 and V2. Barnes *et al.* concluded that both these visual areas are anomalous in amblyopia.

Some studies have employed high-resolution fMRI to characterise ocular dominance columns within human V1 (Goodyear *et al.*, 2002; Liu *et al.*, 2004). Goodyear *et al.* (2002) obtained maps of ocular dominance columns in adults with either early- (< 2 years) or late-onset amblyopia using a 4-T MRI scanner. Their stimulus was a high contrast (66 %), sinusoidal grating, drifting at 2 Hz. For each adult with early-onset amblyopia, pixels of the fMRI map representing the fellow eye significantly outnumbered those representing the amblyopic eye. However, this inter-ocular difference was not observed for adults with late-onset amblyopia, presumably because the onset occurred after the critical period for development of ocular dominance columns (reviewed in Daw, 1995).

Using checkerboard patterns of various sizes and reversal rates, Choi *et al.* (2001) demonstrated that calcarine activity in anisometropes was most reduced for high spatial frequency patterns, while that in strabismics was most reduced for low frequency patterns. A similar study by Lee *et al.* (2001) also reported reduced fMRI responses for high spatial frequency targets in anisometropes but not in strabismics. Both studies illustrate that amblyopia, and the associated cortical deficits, are not a single entity and provide support for the hypothesis that neural undersampling at high frequencies and/or a loss of fine-scale spatial visual processing may form the basis of anisometropic amblyopia (Levi & Klein, 1986; Levi, Waugh, Beard, 1994).

The majority of imaging studies on amblyopia have used simple repetitive patterns as stimuli such as sinewaves or checkerboards. This choice of stimulus reflects the desire of investigators not only to assess function within primary visual areas but also to compare their neuroimaging work with existing behavioural data. To explain the full range of perceptual deficits in amblyopia, however, higher-order cortical function needs to be examined and for this more complex stimuli are required. Lerner *et al.* (2003) attempted this by measuring fMRI responses in amblyopes using images of faces and buildings, stimuli which are thought to activate different neuronal assemblies within higher-order areas (Hasson, Levy, Behrmann, Hendler, Malach, 2002; Levy, Hasson, Avidan, Hendler, Malach, 2001). Data from strabismic and anisometropic amblyopes was combined as no significant differences were found between them. Their studies showed that, with amblyopic-eye viewing, activity within 'face-related' areas of the occipitotemporal cortex was depressed whereas that within 'building-related' areas appeared normal. Amblyopia may therefore be associated with highly specific deficits in the occipitotemporal cortex, though it remains unclear whether the selectivity of the

deficits reflects a disruption of feedforward signals, top-down processes or a combination of the two.

Levodopa, a precursor of the neurotransmitter dopamine, improves visual performance in amblyopes (Gottlob & Strangler-Zuschrott, 1990; Leguire, Rogers, Bremer, Walson, Hadjiconstantinou-Neff, 1992; Leguire, Walson, Rogers, Bremer, McGregor, 1995), but its use remains controversial due to possible side effects (Levi, 1994; Moseley, 2002). The cortical effects of the drug also remain controversial, with some evidence that it increases (Yang *et al.*, 2003) and some that it decreases (Algaze *et al.*, 2005; Rogers, 2003) the neural volume activated by the amblyopic eye.

Finally, fMRI has been used to challenge the generally accepted belief that changes associated with amblyopia occur primarily at the cortical level. Using a 1.5-T scanner, reduced levels of activity were observed within the LGN when checkerboard patterns were viewed with the fellow-eye compared with the amblyopic-eye of an observer with anisometropic amblyopia (Miki, Liu, Goldsmith, Liu, Haselgrove, 2003). Histological analyses suggest that cells within the LGN may be smaller in strabismic amblyopia (Von Noorden & Crawford, 1992).

1.3.3.2 Structural Magnetic Resonance Imaging

Mendola *et al.* (2005) recently completed a detailed study on morphological changes in the cortex of anisometropic and strabismic amblyopes using structural MRI. A large cohort of children and adults were examined, and a battery of psychophysical tests was conducted to assess visual performance in all subjects. Grey matter volume differences between amblyopic and control groups were derived on a voxel-by-voxel basis in the

form of statistical t-maps. The strength of this approach is that no *a priori* assumptions are required about the location or extent of regional brain differences between groups (Ashburner & Friston, 2000; Ashburner & Friston, 2001). Mendola *et al.* (2005) reported significant grey matter reductions in the calcarine cortex, parietal-occipital cortex and the ventral temporal cortex of both anisometropic and strabismic children, noting only small differences between the two types of amblyopia. These morphological changes provide confirmatory evidence that both low- and high-level areas are dysfunctional in strabismic and anisometropic amblyopia. Interestingly, areas of change were much less pronounced in adults: compared with aged-matched controls, grey matter reductions in adult amblyopes were confined to regions of the calcarine cortex (see also Chan *et al.*, 2004). The past ocular history (e.g. therapy, visual experience) of adults may have masked some cortical anomalies.

1.3.3.3 PET

Some of the earliest neuroimaging studies on human amblyopia were completed using PET (Demer, Grafton, Marg, Mazziotta, Nuwer, 1997; Demer, Von Noorden, Volkow, Gould, 1988; Imamura *et al.*, 1997) and single photon emission computerised tomography (SPECT; Kabasakal *et al.*, 1995). These studies all used non-patterned stroboscopic light flashes and/or checkerboard patterns as stimuli and, although they did not agree on the extent of V1 involvement, all provided evidence for occipital cortex dysfunction in human amblyopia. Only a limited number of PET studies on amblyopia have since been completed, principally because its spatial resolution is inferior to fMRI and because it involves invasive procedures (i.e. intravenous injection of radioactive substances).

PET has also been used to examine the cortical metabolic levels of amblyopes in a resting state with their eyes open but without any further visual stimulation (Choi *et al.*, 2002). Compared with normally-sighted observers, Choi *et al.* found a reduction in glucose metabolism within striate and extrastriate cortex as well as areas within the inferior temporal lobe and superior parietal lobe of both anisometropic and strabismic amblyopes.

PET has also been used to assess whether motion processing is selectively depressed in amblyopia. Despite numerous psychophysical studies on this topic (Hess & Anderson, 1993; Simmers, Ledgeway, Hess, McGraw, 2003), no firm conclusions have been reached. A recent PET study reported a reduction in responses within V1 of amblyopes to 6 Hz full-field flicker but not to 25 Hz flicker (Mizoguchi, Suzuki, Kiyosawa, Mochizuki, Ishii, 2005). They concluded from this that the motion pathway might be relatively spared in amblyopia, in general agreement with electrophysiological studies (Kubova, Kuba, Juran, Blakemore, 1996; Shan, Moster, Roemer, Siegfried, 2000). However, PET responses to motion stimuli within the calcarine cortex may vary with clinical subtype, with the motion pathway not being spared in strabismic amblyopia (Demer *et al.*, 1997).

1.3.3.4 MEG

In strabismic amblyopes, the onset of isoluminant red/green gratings produced evoked magnetic responses that were both delayed and reduced in amplitude when viewed by the amblyopic-eye compared with when viewed by the fellow-eye (Anderson, Holliday, Harding, 1999; Figure 1.14). Additionally, by varying the periodicity of the stimulus, the spatial frequency response properties of the activated cortical area in both

amblyopes and normals were derived. The neural site of activity (determined using a dipole model fit to the data) was reported as area V1. They concluded that the poor spatial vision of strabismic amblyopes could, at least in part, be attributed to dysfunction within V1.

The related technique of electroencephalography has also been used to demonstrate reduced evoked potentials in primary visual areas for strabismic individuals (Kubova *et al.*, 1996; Manny & Levi, 1982).

Figure 1.14. The top panels show global magnetic field power plotted as a function of time (ms) from stimulus onset for (a) the fellow and amblyopic eye (indicated by arrow) of strabismic observer JD and (b) the dominant and non-dominant eye (indicated by arrow) of normally-sighted observer RW. The bottom panels show maximum field power plotted against stimulus spatial frequency for (c) the fellow (?) and amblyopic eye (?) of JD and (d) the dominant (?) and non-dominant eye (?) of RW. Adapted from Anderson *et al.*, 1999.

The experiment reported in this thesis (chapter 8) is the only other published work investigating amblyopia with MEG (Anderson & Swettenham, 2006).

1.4 Experimental aims

In this thesis a combination of psychophysical, MEG and fMRI studies were used to understand further the neural processing that underlies human global form perception. Throughout the thesis a perception of global form was generated using either Glass patterns or Gabor patches, each constructed to produce radial, rotational or horizontal form. The principal questions addressed were:

1) Are there differences in sensitivity for detecting different types of global structure? This was investigated by determining both the display time and coherence necessary for detecting radial, rotational and horizontal Glass patterns.

2) What is the spatio-temporal distribution of neural activity associated with the perception of global form? To answer this question, MEG and fMRI studies were performed to investigate the neural response to radial, rotational and horizontal form. Responses were examined for differences between pattern types and the results were compared with psychophysical estimates of sensitivity.

3) Is there any evidence of feedback between primary visual areas and other brain regions in response to form perception? A MEG study was implemented to investigate whether neural activity in V1 and other areas correlated (negatively or positively) with the coherence of the Glass pattern.

4) Can inter-ocular differences for global form perception be observed in an amblyopic observer? In a case study of one strabismic amblyope, MEG and psychophysical experiments were used to assess differences in global form perception using Glass patterns.

2 MEG and fMRI

The purpose of this chapter is two-fold. Firstly, to present a brief description of the theory behind both MEG and fMRI and secondly, to give further information on the methods used throughout this thesis. The first section describes the use of a normalised brain as this is common to both MEG and fMRI group studies.

2.1 The normalised brain

Functional neuroimaging studies are often designed to determine where in the brain activation is occurring. Within a study, the brains of the observers will vary in their overall size, shape and three-dimensional architecture of gyri and sulci. To enable group analyses it is necessary to fit the brains to the same space. With SPM99 (used throughout this thesis; www.fil.ion.ucl.ac.uk/spm/software/spm99/), the individual brains are fitted to a "normalised" or "template" brain called the ICBM 152. This is achieved using automated image-matching algorithms that translate, rotate, scale, shear, and if necessary warp, the brains to best fit the ICBM 152 template (Ashburner & Friston, 1999). However, the surface contours of the brain are not matched and so the locations of gyri and sulci are not known.

The ICBM 152 brain was developed by the Montreal Neurological Institute (MNI) to be more representative of the gross neuroanatomy of the population than the Talairach (TC) and Tournoux brain. It is one of a series of templates created by the MNI and is itself based on a previous template called the MNI 305. The ICBM 152 template was created using magnetic resonance images from 152 observers and has been adopted as the standard template of the International Consortium of Brain Mapping (ICBM). The stereotaxic coordinates are based on the same scaling system as that of Talairach and

Tournoux (1988), but they differ slightly as the ICBM 152 brain is higher, deeper and longer. As such, it is necessary to state whether coordinates are in MNI or TC space. Estimates of the equivalent TC coordinates can be obtained from MNI coordinates using algorithms freely available on the web (e.g. www.mrc-cbu.cam.ac.uk/Imaging/Common/mnispace.shtml).

Talairach and Tournoux (1988) introduced a coordinate system based on the positions of, and distance between, the anterior commissure (AC) and the posterior commissure (PC). The AC and PC are two small subcortical structures superior to the brain stem that can be identified on the midline (Figure 2.1 (a)). The line between the AC and the PC is the AC-PC line and forms the y axis with orthogonal x and z axes (Figure 2.1 (b)). The AC forms the coordinate origin (0, 0, 0). Other brains can be fitted to the TC system by scaling to the distance between the AC with the PC, top, bottom and sides of the brain and between the PC and the back of the brain (Talairach & Tournoux, 1988). In this thesis, this was performed for individual observer analyses (i.e. non-spatially normalised brains) within mri3dX (www.aston.ac.uk/lhs/staff/singhkd/mri3dX/mri3dX.jsp).

Figure 2.1. a) The AC (red crosshairs) and PC (yellow crosshairs) form the basis of the Talairach and Tornoux (1988) proportional grid system. Taken from http://www.sph.sc.edu/comd/rorden/anatomy/na_ac.html. b) The AC-PC line forms the y axis with a perpendicular vertical z axis and horizontal x axis. Taken from Brett, Johnsrude, Owen, 2002.

It should be noted that the Talairach and Tournoux atlas was based on a post-mortem study of one elderly female and only one hemisphere was illustrated. In addition, the linking of coordinates with Brodmann areas was estimated and not based on histological studies. However, an automated labelling system called the Talairach Daemon has since been developed that can rapidly assign accurate neuroanatomical labels to coordinates in TC space (Lancaster *et al.*, 2000). The Talairach Daemon was used throughout this thesis.

2.2 MEG

2.2.1 The physiological basis of the MEG signal

Neurons are electrically active cells and neural communication is reliant on the modulation of neuronal electrical potential. An electrical current has an associated magnetic field and neuronal currents therefore co-occur with neuronal magnetic fields. MEG is the non-invasive measurement of the minute magnetic fields generated by neuronal activity.

Electrical currents are propagated along axons by *action potentials* (Figure 2.2). This process is governed by the opening and closing of voltage-gated channels that allow sodium (Na^+) and potassium (K^+) ions to cross the otherwise hydrophobic neuronal membrane. Action potentials are associated with three ionic currents: 1) an *intracellular* current due to ionic flow in a very small portion of the axon; 2) a *transmembrane* current due to ions crossing the neuronal membrane i.e. radial from the cylindrical axon; and 3) an *extracellular* current due to ionic flow outside the neuron in opposition to the direction of the intracellular current. None of these currents are thought to generate measurable event-related magnetic fields because the action potential is very brief (~ 1 ms) and has periods of both depolarisation and repolarisation (Figure 2.2). During the repolarisation period the pattern of current flow is the reverse of that in the depolarisation period, and as such the currents self-cancel within ~ 1ms and within ~ 2 mm of axonal length (Del Gratta, Pizzella, Tecchio, Romani, 2001).

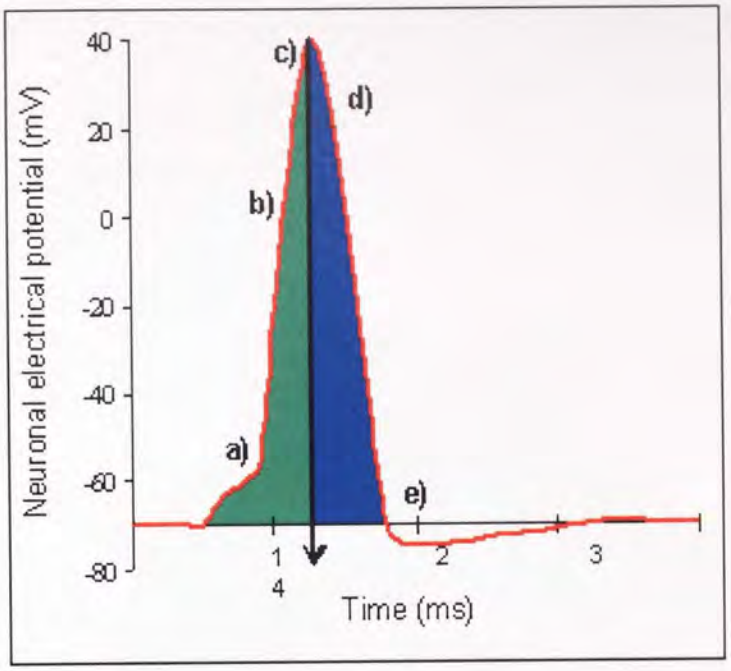

Figure 2.2. Generation of action potentials. Voltage-gated Na^+ channels are closed at the resting potential (~ 70 mV) but open as the neuronal potential becomes less polarised; a) electrical and concentration gradients drive Na^+ influx; b) within 0.5 ms the neuronal potential is positive, Na^+ influx continues due to the chemical gradient; c) voltage-gated Na^+ channels become inactive, Na^+ influx slows; d) voltage-gated K^+ channels open, K^+ efflux repolarises the neuron; e) K^+ efflux causes hyperpolarisation and refractory period. K^+ channels return to closed state. Energy driven pumps restore the Na^+ and K^+ balance. The black arrow indicates the end of the depolarisation period (green) and the start of the repolarisation period (blue) when current directions reverse.

Action potentials pass along axons until the current reaches the synaptic terminals. Synaptic terminals have regions of membrane in close proximity to a recipient (post-synaptic) neuron, the gap between the original (pre-synaptic) and the post-synaptic neuron is the synapse. The electrical potential of the post-synaptic neuron is altered because neurotransmitter released from the pre-synaptic neuron binds with receptors on the post-synaptic neuron's membrane and this triggers the modulation of ion channels (Figure 2.3). If the movement of ions depolarises the post-synaptic neuron then this is an excitatory post-synaptic potential (EPSP); if it hyperpolarises then this is an

inhibitory post-synaptic potential (IPSP). The post-synaptic neuron will receive input from thousands of synapses and the overall electrical potential is the summation of all of these post-synaptic potentials.

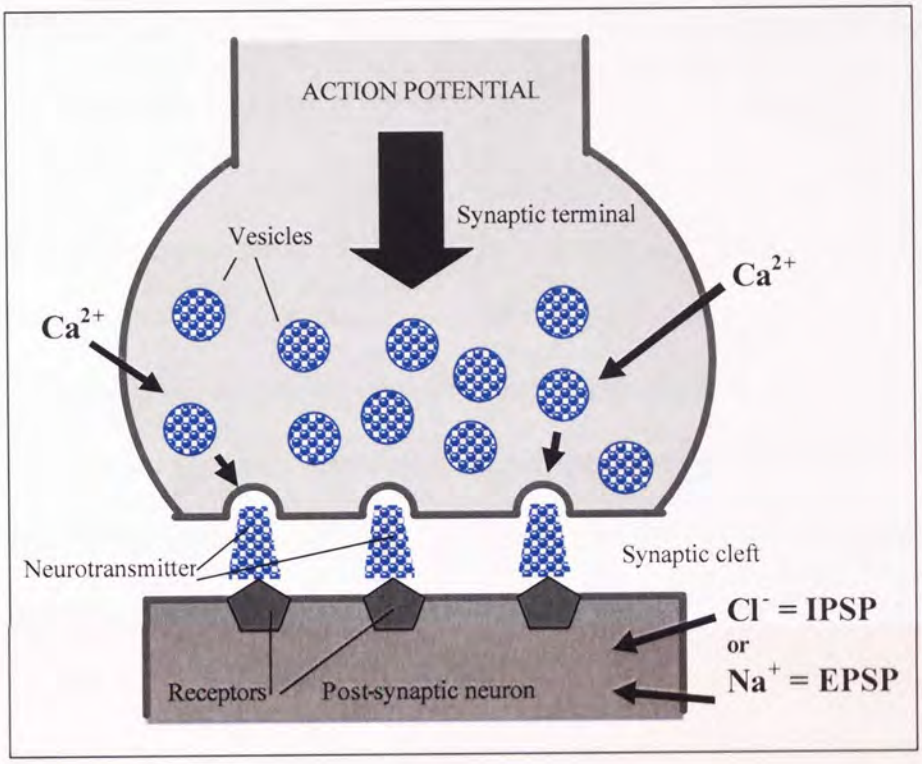

Figure 2.3. At a synaptic terminal the depolarisation from an action potential opens voltage-gated calcium ion (Ca^{2+}) channels. Ca^{2+} influx triggers neurotransmitter release into the synaptic cleft where it binds with receptors on the post-synaptic membrane. These receptors trigger the influx or efflux of ions and produce EPSPs (normally Na^+ influx) or IPSPs (normally chloride (Cl) influx).

Synaptic transmission is slower than the conduction of action potentials because of the chain of events involved in the release and binding of the neurotransmitter. Also in comparison with action potentials the influx of positively charged ions in the pre-synaptic neuron is not quickly countered by an efflux of positive ions. Thus, the

positively charged calcium ions maintain the synaptic terminal in a depolarised state until it is either sequestered by mitochondria or pumped out. This longer repolarisation period provides the timeframe for summation of synaptic currents from several thousands of synapses within a localised region of cortex (Del Gratta *et al.*, 2001). Whether this current will generate a magnetic field that is measurable with MEG depends on the geometry of the neurons.

Within the cortex, pyramidal cells align with each other perpendicular to the cortical layers and are distinctive because of their long apical dendrites. (Figure 2.4 (a)). The apical dendrites and the alignment of many pyramidal cells within a small area of cortex are such that the post-synaptic currents will generate a net magnetic field. The magnetic field recorded with MEG is thought to reflect the activity of approximately 10,000 neurons (VSM MedTech Ltd. literature). In contrast, stellate cells (Figure 2.4 (b)) which are also found in the cortical layers have many radiating dendrites. Therefore, post-synaptic currents from stellate dendrites will be generated in all directions and as such no net magnetic field is produced.

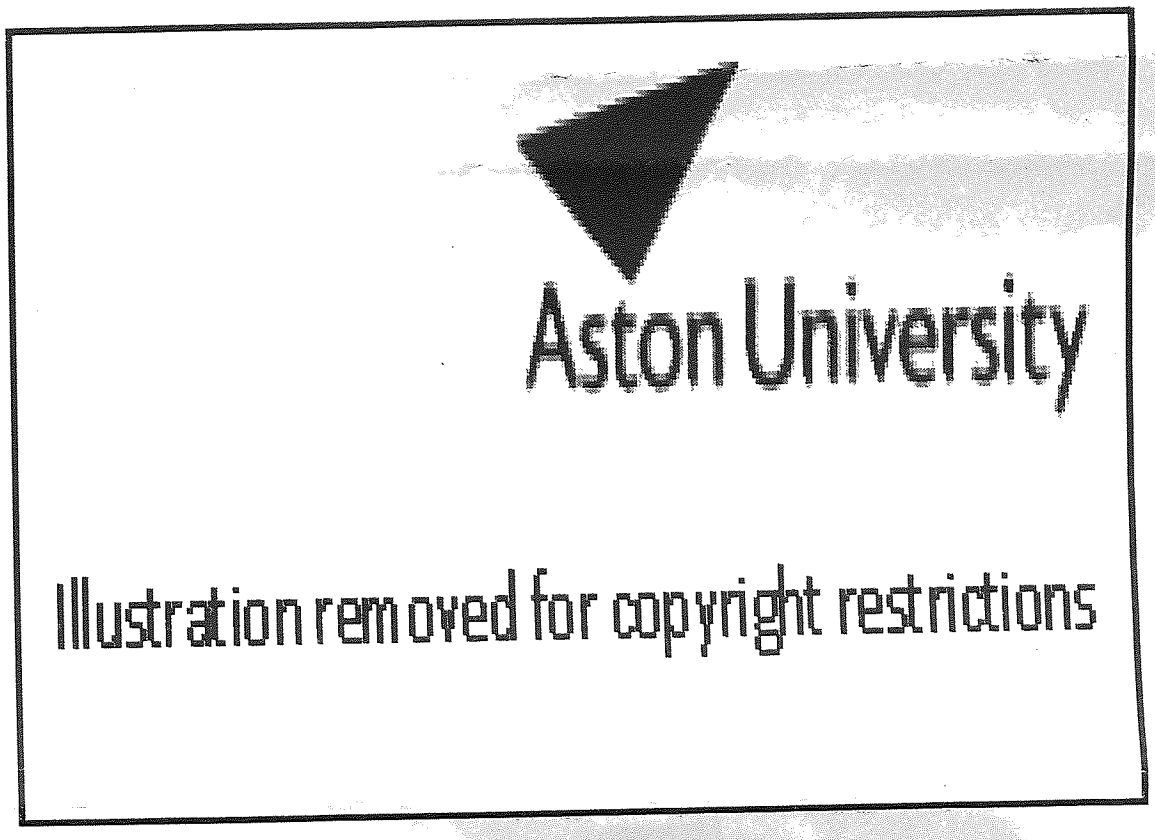

Figure 2.4. a) Pyramidal neurons and b) stellate neurons are both found in the cortex. However, only pyramidal cells produce net magnetic fields. Taken from Cowan & Stricker, 2004.

Although populations of pyramidal neurons will produce a net magnetic field, whether this magnetic field is measurable outside the head is dependent on the orientation of the cortex and the depth of the source.

The surface of the brain is convoluted into sulci and gyri. The post-synaptic current is perpendicular to the layers of the cortex, and associated magnetic fields are perpendicular to the current. Currents generated in sulci flow tangentially in relation to the skull and produce a magnetic field that will leave and re-enter the head (Figure 2.5 (a)). Currents generated at the crests of gyri flow radially in relation to the skull and

produce a magnetic field that does not leave the head (Figure 2.5 (b); Vrba & Robinson, 2001).

Figure 2.5. a) Tangential currents in sulci produce magnetic fields that leave the head, b) radial currents in gyri produce magnetic fields that do not. The direction of the current is indicated by the red arrows, the blue arrows indicate the magnetic fields.

The importance of the orientation of current within the cortex on the measurement of magnetic fields was investigated by Hillebrand and Barnes (2002). They showed that magnetic fields from the crests of gyri were indeed invisible to the MEG system. However, this only accounted for a very small proportion of the cortex. Neural sources that were close to the crests and had marginally tangential currents were highly resolvable because of their closeness to the MEG sensors. The distance between

neuronal sources and the MEG sensors was found to be the most limiting factor for magnetic field detection (Figure 2.6).

Figure 2.6. The detection probability for cortical sources is colour coded with red and blue colours representing high and low detection probabilities respectively. Views show a) the left hemisphere through the midline, note that detection probability decreases with depth; b) the brain surface viewed from the top, note that most of the cortex has high detection probability but there are thin strips of low probability on the crests of gyri and the troughs of sulci. Taken from Hillebrand & Barnes, 2002.

2.2.2 The MEG system

The neuromagnetic field produced by the brain typically has an amplitude of less than 10^{-12} T (Vrba & Robinson, 2001). This is considerably weaker than the magnetic fields created by the Earth's magnetic field or by the muscles of the body (Figure 2.7). All magnetic fields, apart from those produced by neuronal sources, are potential contributors of noise in MEG data. Consequently, to reveal neuronal sources it is necessary to: a) abolish or reduce all other magnetic fields; and b) have detectors that are sensitive in the femtotesla (fT) range.

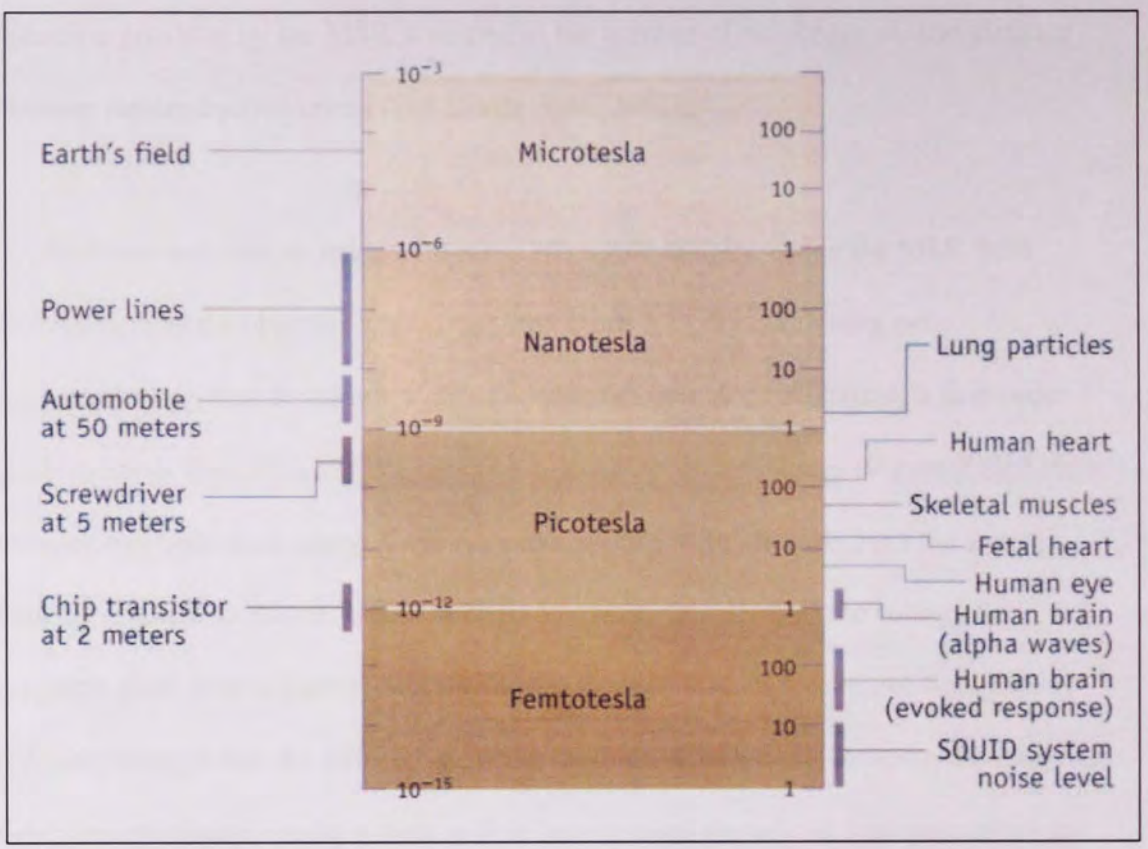

Figure 2.7. Relative magnitudes of magnetic fields, note the amplitudes of neuromagnetic fields at the bottom right of the figure. Taken from VSM MedTech Ltd. with permission.

2.2.2.1 Noise reduction

A simple and effective way of reducing environmental magnetic noise is by fitting the MEG system inside a magnetically shielded room (MSR). The MSR is created using layers of high conductivity material within the walls. Soft magnetic metals such as iron alloys conduct and retain the magnetic flux within the MSR walls, thereby reducing the amount of flux entering the room. Higher frequency noise is attenuated using an aluminium layer in which eddy currents are induced. Eddy currents flow in the direction that opposes the magnetic field that created them and so cancel the noise. The noise

reduction provided by the MSR is related to the number of, thickness of, and distance between the conductive layers (Del Gratta *et al.*, 2001).

Gradiometers are used to reduce the effect of magnetic noise inside the MSR from sources such as the observer's muscles (see Figure 2.7). By combining two superconducting flux transformer pickup coils with opposite orientation, a first-order gradiometer is formed that is not sensitive to noise from far sources (Figure 2.8). This is because magnetic field strength decays exponentially with distance from the source, thus the gradient in magnetic field strength is greater the closer to the source. A magnetic field from a distant source will pass through both coils without significantly reducing strength and the induced opposing currents will cancel. However, the magnetic field strength from a nearby source will be less through the second (compensation) coil than it was through the first (pickup) coil, causing a net current to be induced in the pickup coil. The baseline refers to the distance between the pickup and the compensation coil.

Figure 2.8. a) a single pickup coil acts as a magnetometer and is sensitive to magnetic fields perpendicular to its area from both near and far sources, b) two opposing pickup coils create a first-order gradiometer that is only sensitive to differences in the magnetic field between the two coils. Taken from Vrba & Robinson, 2001.

Higher-order gradiometers can be formed by adding more pickup coils to further increase the sensitivity to near sources (Vrba & Robinson, 2001). However, the MEG system used for all the experiments reported in this thesis had first-order gradiometers combined with a synthetic higher-order gradiometer that monitored environmental noise and subtracted it from the sensor output. The first-order gradiometer coil was 2 cm diameter and the baseline was 5 cm.

2.2.2.2 Signal detection

Gradiometers (superconducting flux transformers) couple the measured magnetic field with highly sensitive magnetic detectors called superconducting quantum interference devices (SQUIDs; Figure 2.9). Changes in voltage across the SQUID circuitry are transmitted to room temperature, amplified and processed by the systems electronics to convert the signals into a linear representation of the magnetic field (Vrba & Robinson, 2001).

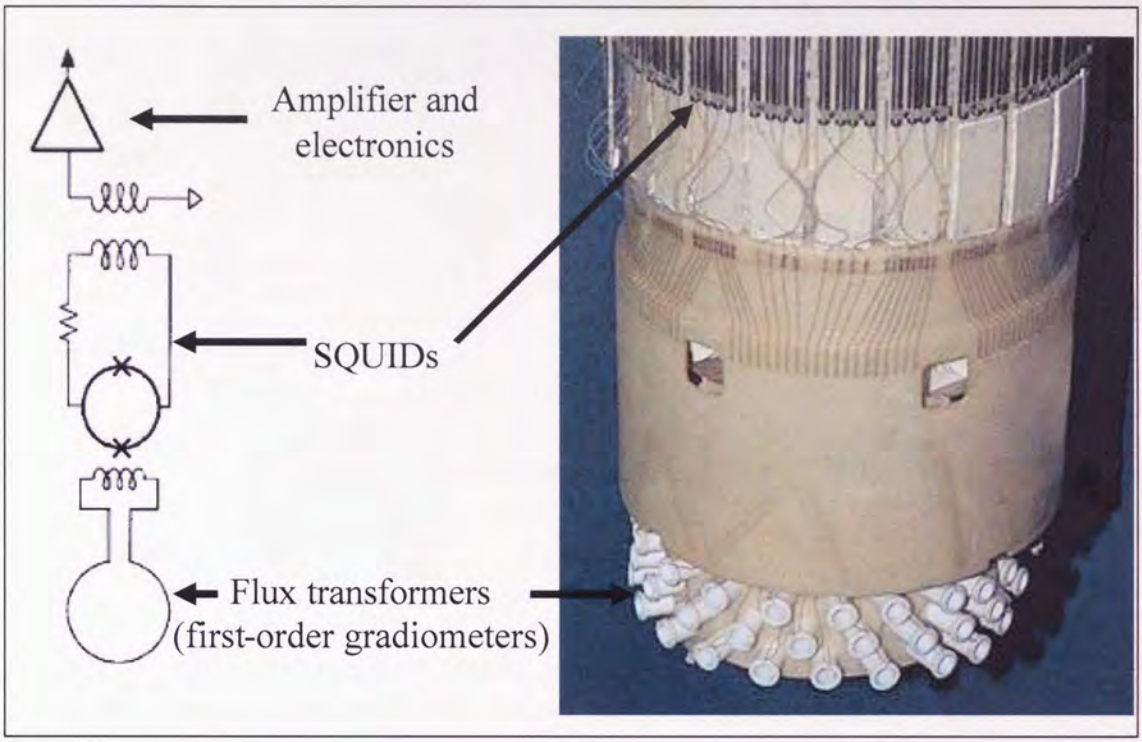

Figure 2.9. The MEG insert. Flux transformers line the inside of the helmet where the observer's head is positioned. Further away from the head the transformers are coupled with the SQUIDs which then send signals for amplification and processing. The insert is immersed in liquid helium inside the dewar. The line diagram on the left is adapted from Vrba & Robinson, 2001; the photograph on the right was taken from VSM MedTech Ltd. with permission.

For superconduction both the flux transformers and the SQUIDs need to be at cryogenic temperatures (4 K or -269 °C). This is achieved through immersion in liquid helium within a well insulated dewar. The dewar has several design features such as a vacuum, layers of superinsulation and heat shields to minimise heat exchange with the environment (Vrba & Robinson, 2001). Periodic refilling with liquid helium is needed to replace liquid that has warmed to the gas state.

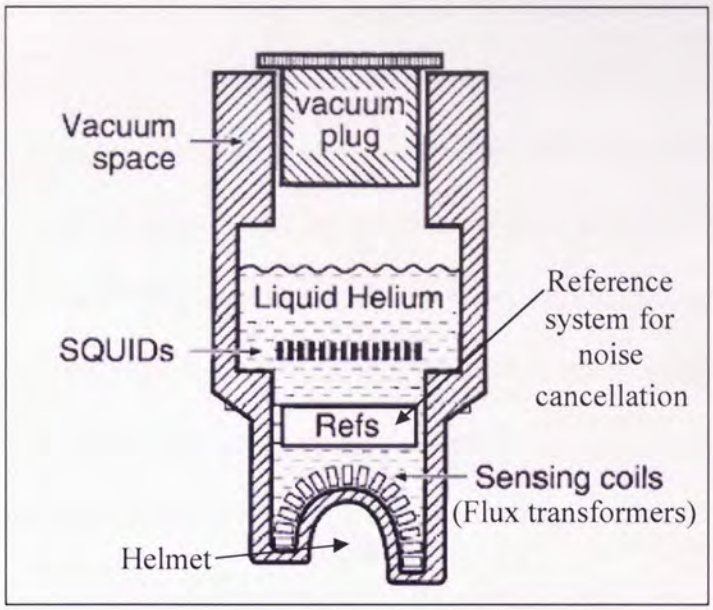

Figure 2.10. Schematic cross section through the dewar. Within the vacuum space there are numerous heat shields and layers of superinsulation. Adapted from Vrba & Robinson, 2001.

2.2.3 MEG data analysis

Mathematical equations to model the neuromagnetic field are described by Hämäläinen, Hari, Ilmoniemi, Knuutila and Lounasmaa (1993). A fundamental problem with analysis of magnetic fields is that any recorded field could be modelled with an infinite number of solutions; this is called the *inverse problem*. The number of independent sources contributing to the neuromagnetic field is also not known and this presents the *forward problem*. To overcome these problems it is necessary to make certain assumptions to constrain the results to a unique answer. However, it must be remembered that the accuracy of the answer is dependent on the accuracy of the assumptions.

The assumptions required for an *equivalent current dipole* (ECD) model are that the head is spherical with uniform conduction and there is only one (or a small number) of discrete neural sources. However, this method only reveals neural responses that are phase- and time-locked to the stimulus and consequently is only suitable for determining evoked responses in primary sensory areas. *Multiple signal classification* (MUSIC) can be used to identify multiple dipoles but requires spatially discrete noise and signal areas. Other models are able to localise distributed neural sources, including the *minimum norm least squares* (MNLS) approach, *low resolution electromagnetic tomography* (LORETA), *focal underdetermined system solver* (FOCUSS) and SAM (*synthetic aperture magnetometry*).

SAM was used throughout this thesis as it has many advantages over other techniques. Firstly, it is sensitive to changes in oscillatory brain rhythms that are not phase-locked to an external event. Such changes in brain rhythms have been associated with a range of cognitive tasks and information processing (Pfurtscheller & Lopes da Silva, 1999) and are eliminated (or greatly reduced) by averaging techniques. This allows the design of experiments with passive and active states that are several seconds long and are comparable with fMRI studies (Singh, Barnes, Hillebrand, Forde, Williams, 2002). Secondly, unlike LORETA it has a relatively high spatial resolution (Barnes, Hillebrand, Fawcett, Singh, 2004). Thirdly, SAM does not require discrete sources (unlike ECDs and MUSIC) and is not confounded by noise sources. Fourthly, it is not biased by near sources (unlike MNLS) because SAM produces spatial filters for all voxels. Fifthly, estimates are not reliant on an initial estimate of activity (unlike FOCUSS). Finally, the responses from groups of observers can be analysed using non-parametric mapping techniques (Singh, Barnes, Hillebrand, 2003).

The only assumption of SAM is that sources between regions are not perfectly synchronised, else this would result in the sources self-cancelling and not being detected. This is a realistic assumption as MEG studies using SAM often have long time windows to explore changes in oscillatory power. It is unlikely that high temporal correlations between areas will be maintained for these periods, and unless the correlation exceeds 30 percent of the time window the sources will be accurately localised (Hadjipapas, Hillebrand, Holliday, Singh, Barnes, 2005).

2.2.3.1 SAM

SAM is a beamforming technique which is increasingly being used to analyse MEG data (reviewed in Hillebrand, Singh, Holliday, Furlong, Barnes, 2005). Reconstruction of neural sources is achieved by first defining a three-dimensional voxel-based space of target locations. For each voxel (typically 5 mm^3), an *optimal spatial filter* is constructed that links activity in that voxel to the MEG system's sensor array. This accounts for the MEG sensors being more sensitive to near than far sources. The filter output is calculated as the weighted sum of the sensor signals, yielding a measure of source power within each voxel as a function of time (Figure 2.11). This output has the same temporal resolution as the original MEG signals and can be thought of as a *virtual electrode* within that voxel. A spectral analysis is completed on the output signal, allowing power changes between matching pre- and post-stimulus time windows to be calculated for any given frequency band.

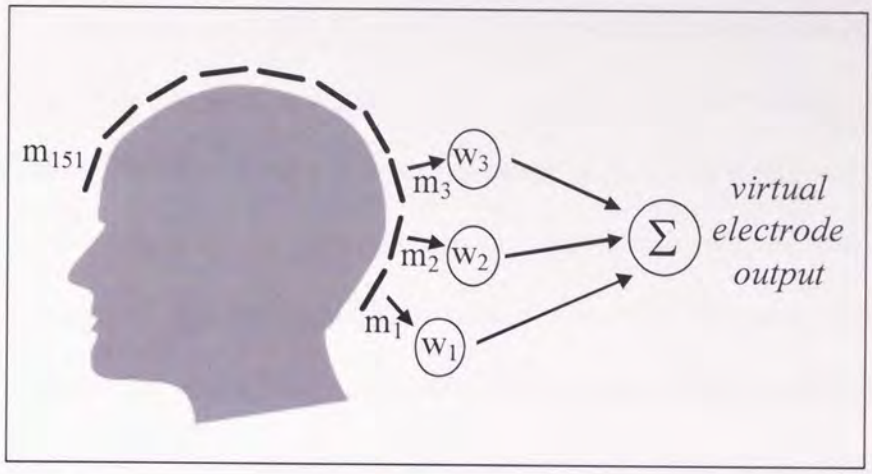

Figure 2.11. Using beamforming techniques the neuronal signal at a location of interest is constructed as the weighted sum of the MEG sensors ($m_1 \ldots m_{151}$), forming a 'virtual electrode'. Ideally, the weights ($w_1 \ldots w_{151}$) are chosen such that only the signal from the location of interest contributes to the beamformer output, while all other signals are suppressed. A different set of weights is computed sequentially for each location in the brain.

For individual observer analysis, the difference between spectral power estimates in the passive and active phases can be assessed for each voxel using a pseudo t statistic (Robinson & Vrba, 1999). This enables a three dimensional 'SAM' image of cortical activity to be generated. *Pseudo t*, are obtained instead of *t* statistics because the variances are spatially smoothed. With SAM, individual observer analysis is valid because the revealed sources have a high signal-to-noise ratio. By superimposing SAM images on a spatially co-registered image of the observer's own anatomical MRI scan, the locations of power changes can be determined relative to minor sulci and gyri that are lost on template brains. However, the SAM images do not show the temporal sequence of power changes within the time window.

The temporal sequencing of events can be explored for virtual electrodes of interest using time-frequency analysis. In this thesis time-frequency plots were calculated using a Morlet wavelet transform. Plots were created from single-trial activation waveforms and from these an average time-frequency plot of induced (and evoked) neural activity was created. The statistical significance of energy changes was assessed using bootstrap analysis (Graimann, Huggins, Levine, Pfurtscheller, 2002). Instead of assuming a normal population distribution, this technique uses the obtained distribution and as such does not make parametric assumptions. Significance for energy increases and decreases were assessed separately as two one-tailed tests ($p < 0.025$).

Group MEG data were analysed using non-parametric permutation analyses (Nichols & Holmes, 2001; Singh, Barnes, Hillebrand, 2003) with the SnPM toolbox (www.fil.ion.ucl.ac.uk/spm/snpm/). Traditional parametric methods are not suitable for group SAM analyses as changes in cortical oscillatory power are variable between observers i.e. the distribution is unlikely to be normal. In addition, pseudo t statistics cannot be used with parametric tests. Following individual observer analyses, data from each observer were spatially normalised with a template brain (see section 2.1). Permutation testing uses the empirical data to generate a probability distribution that the effect of interest can be compared to. Probability distributions of the largest pseudo t values allow identification of voxels with significant power changes (voxel-level test). The significance of a cluster size can similarly be determined from a probability distribution of the size of clusters in which all voxels exceed the user-defined pseudo t value (cluster-level test). This user-defined value is called the primary threshold. Statistical significance of power increases and decreases were assessed separately as two one-tailed tests ($p < 0.025$).

2.3 FMRI

Magnetic resonance imaging relies on the fact that atomic nuclei are weakly magnetic. In a normal environment the orientations of nuclei are random, but if an observer enters a static magnetic field the nuclei align either with the applied field or against it. Nuclei aligned with the field are in a lower energy state than those aligned against it. More nuclei tend to align with the field, rendering the brain weakly magnetic. To alter this energy state, a radio frequency pulse is applied at the precise resonance frequency for a given nucleus (usually hydrogen). This process flips the nuclei such that more are aligned against the main field. When the radio frequency pulse is switched off, the nuclei return to their low energy state. The rate of this return is measured in two dimensions; longitudinal re-growth and transverse relaxation (see Logothetis & Wandell, 2004). Transverse relaxation has an exponential signal decay measured with the time constant, T2*. Measuring T2* is important for fMRI as it is affected by inhomogeneities in the local field which can be altered by the oxygenation level of the blood. High spatial resolution of T2* throughout the brain can be obtained by applying small magnetic field gradients to the static magnetic field (Callaghan, 1991).

The blood oxygenation level dependent (BOLD) signal underlies fMRI. Haemoglobin within the blood either exists in an oxygenated (oxyhaemoglobin) or a deoxygenated state (deoxyhaemoglobin). These two forms have different magnetic properties and so the influence of a given volume of blood on the field inhomogeneities (and T2*) depends on the proportion of each.

The BOLD signal is considered to be an indirect measure of metabolism. All cells require oxygen and glucose for metabolism, and if metabolism increases then more

oxygen and glucose is needed. As discussed in section 2.2.1, neurons are electrically active cells and the electrical potential of neurons requires an unequal distribution of ions between the neuron and the extracellular space. To pump ions against chemical and electrical gradients and to cycle neurotransmitter across membranes requires energy driven pumps. An increase in synaptic transmission rate increases the metabolic demand of the neuron and is generally thought to produce the BOLD signal (Logothetis & Pfeuffer, 2004). Alternatively, it may not be synaptic transmission that directly causes the change in blood flow as there is some evidence that neurotransmitters released from neurons act on the neurovascular system to increase blood flow in active regions (reviewed in Attwell & Iadecola, 2002).

Magnetic resonance imaging has an excellent spatial resolution but it must be remembered that the BOLD signal measures the oxygen level of the blood which is mostly contained within the neurovascular system (Boxerman *et al.*, 1995). This potentially means that the spatial resolution could be blurred by blood flow within veins draining from the active site. In addition, the density of the vascular system is not uniform across brain areas and across cortical layers (Duvernoy, Delon, Vannson, 1981). Duvernoy *et al.* identified four layers parallel to the surface of the cortex that had different densities of vasculature; the vasculature was densest at cortical depths where the neuronal activity was greatest. Even within cortical layers the distribution of capillaries is not homogeneous as it has been shown that there are columns of high vascular density in the CO containing blobs (Figure 1.1; Zheng, LaMantia, Purves, 1991).

An increase in neuronal metabolism increases the neuronal uptake of oxygen and thereby increases the amount of deoxygenated haemoglobin in the blood. This would be expected to reduce the BOLD signal. However, the overall effect of increased neural activity is an increase in oxyhaemoglobin because the associated increase in blood flow oversupplies the required oxygen. Thus, an increase in the BOLD response, with a peak approximately 5 seconds after the event, reflects increased activity. Efficient design of an fMRI experiment and appropriate analysis requires estimates of the event-related response. For a comprehensive review of fMRI, the book "Human Brain Function" is recommended (Frackowiak *et al.*, 1997).

3 Detection of form from noise

3.1 Introduction

It has been proposed that the brain contains specialised "detectors" for radial and rotational shapes (Wilson & Wilkinson, 1998). Such detectors represent mechanisms that would enhance the ability to perceive radial and rotational patterns compared to other patterns (e.g. horizontal). This has previously been investigated by determining the smallest proportion of coherently oriented dot pairs necessary to detect the shape (i.e. the smallest signal-to-noise ratio; see section 1.2.1). However, here we have taken a different approach and have investigated the time necessary to detect different Glass pattern types across a broad range of coherence levels. This provides behavioural measures of visual processing times that can be compared with transient changes in cortical power as measured with MEG.

3.2 Methods

Psychophysical studies were completed to: a) determine the minimum Glass pattern coherence necessary to distinguish it from a zero coherence pattern (the coherence threshold); and b) determine the minimum time a Glass pattern needed to be presented in order to distinguish it from a zero coherence pattern (the temporal threshold).

3.2.1 Observers

Three observers (one male, two female), aged between 25 and 27 years, took part in the initial coherence and temporal thresholds experiments. Observer JS (the author) continued to participate in the additional experiments. All observers had normal or corrected-to-normal vision. All stimuli were viewed monocularly, the eye not being

used was occluded with a dark eye patch. A comparison of thresholds between the right and left eye was made with observer JS. Observers AN and BN each used their dominant eye.

3.2.2 Stimulus generation and presentation

Stimuli were presented on a calibrated Sony GDM F520 monitor and were controlled by a Cambridge Research Systems VSG2/5 card (Cambridge Research Systems, Rochester, Kent, UK). The screen size was 1024 by 768 pixels and the monitor frame rate was 100 Hz (unless otherwise specified). The monitor screen was viewed directly from a distance of 2 m in a dimly lit room.

Glass patterns were generated from 150 pairs of dots positioned within a square (8.2 deg.^{2}) window on a black background (5.0 x 10^{-3} cd m^{-2}). A red fixation circle was provided in the centre of the pattern. The whole stimulus could be seen within five degrees of the fovea. Figure 3.1 shows a representation of a typical Glass pattern.

Each dot within each dot pair was a white square occupying 0.04 deg.^{2} and with a luminance of 70.2 cd m^{-2}. One dot in each pair was randomly positioned within the square window and then the partner dot in each pair was positioned 0.18 deg. from the original dot (centre-to-centre). The orientation of the partner dot relative to the original dot depended on the pattern type and the coherence of the pattern being generated. Dot pairs could form radial, rotational or horizontal patterns. The coherence level was the proportion of dot pairs oriented according to the transformation type. Partner dots that were not oriented to form a pattern type were plotted at a randomly selected orientation.

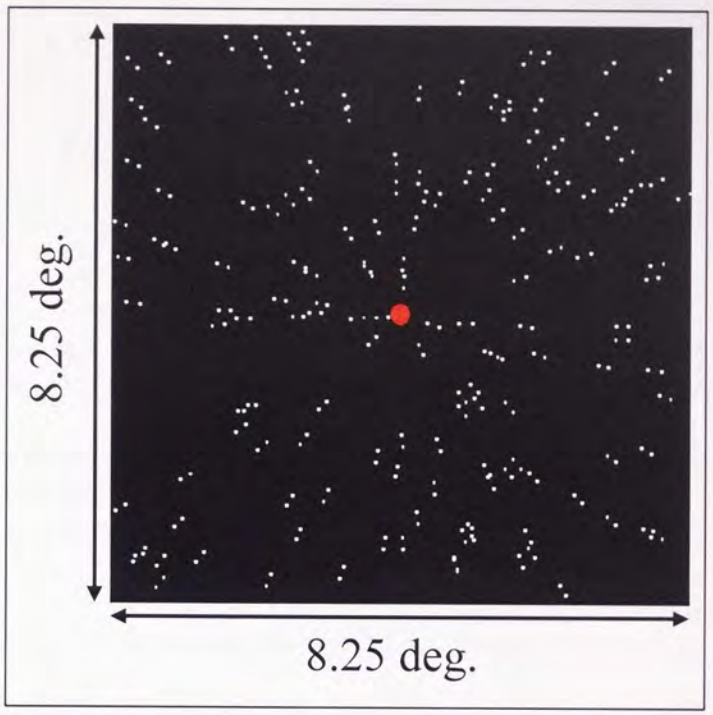

Figure 3.1. Glass patterns composed of 150 white dot pairs (70.2 cd m^{-2}, 0.04 $deg.^2$) on a black background (5 x 10^{-3} cd m^{-2}) with a central red fixation circle (14.5 cd m^{-2}, 0.17 deg. diameter) were generated. Dot pairs were oriented to form radial (shown), rotational or horizontal Glass patterns.

Radial patterns were formed by plotting the partner dot on a virtual line with the centre of the stimulus and the original dot (i.e. on the radial). The partner dot was plotted further away from the centre of the stimulus than the original dot (Figure 3.2 (a)). Rotational patterns were formed by plotting the partner dot on a virtual line orthogonal to the radial and clockwise to the original dot (Figure 3.2 (b)). Horizontal patterns were formed by plotting the partner dot to the right of the original dot (Figure 3.2 (c)). A new screen of dot pairs was calculated and plotted on each monitor frame (10 ms unless otherwise specified).

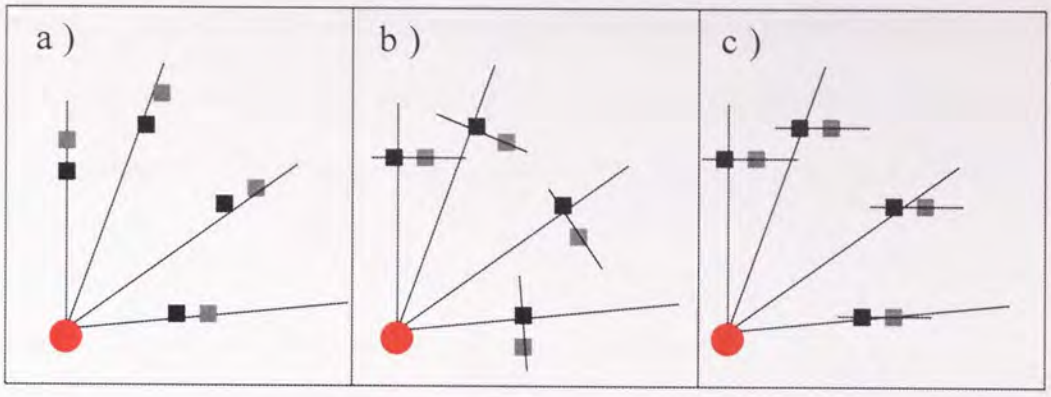

Figure 3.2. Dots within a pair were separated by 0.18 deg. For schematic clarity, the dot that has been randomly positioned is black and the corresponding partner dot is grey. In experiments, all dots were white on a black background. The partner dot was plotted a) on the radial and further from the stimulus centre to form radial patterns; b) orthogonal to the radial and clockwise to the original dot to form rotational patterns; and c) to the right of the original dot to form horizontal patterns.

Coherence and temporal thresholds were determined using the method of constant stimuli in a two-interval forced choice design. Only one Glass pattern type was presented within each run of trials. Observers AN and BN were initially naïve to the stimulus and were shown high coherence examples of each pattern type prior to data collection. The observer was told which pattern type to look for before beginning each run. The observer initiated each run with a button press.

The inter-stimulus interval (ISI) was 1000 ms during which the screen was blank apart from the fixation circle. The fixation circle remained on screen throughout the run. In both experiments, the observer was instructed to indicate, using a button press, the interval that contained the more coherent Glass pattern. Incorrect responses elicited an audible feedback tone. At the end of the run the proportion of correct responses at each coherence or display time was calculated. These data were then fitted using a Weibull

function (Weibull, 1951) with the curve fixed at a detection probability of 0.5 when both intervals contained zero coherence Glass patterns. Thresholds were calculated as the coherence level or display time required for 75 percent correct performance.

3.2.3 Methods for determining coherence thresholds

Each experimental run contained 100 trials with four different coherence levels presented 25 times each in pseudo-random order. The four coherence levels that were chosen were expected to span the detection threshold as predicted by the results of practice trials with observer JS. Each trial consisted of an interval containing a Glass pattern of zero coherence (i.e. noise) and an interval containing a Glass pattern of the selected coherence level. The order of the intervals within each trial was random. Patterns were displayed for 300 ms using a square-wave temporal envelope. Five runs were performed with each pattern type.

3.2.4 Methods for determining temporal thresholds

Temporal thresholds were determined after the coherence threshold experiment had been performed (section 3.2.3), thereby ensuring all observers were well practised at identifying Glass patterns.

Based on the results of practice trials, six display times that were expected to span the detection threshold at each coherence level were chosen. Each run contained these six display times presented in random order. The coherence level of the Glass patterns remained constant within each run. Figure 3.3 illustrates the order of stimuli presentation within trials. Each interval had three sequential stages. The first and last

stage of each interval contained zero coherence Glass patterns (i.e. mask patterns). In each trial the middle stage of one interval contained a Glass pattern of the pre-determined coherence whilst the middle stage of the other interval contained a Glass pattern of zero coherence. The order of the intervals within each trial was random. The display time, and consequently the temporal threshold, refers to the duration of the middle stage only.

Temporal thresholds were determined for all observers with a constant interval time of 900 ms (Figure 3.3 (a)). In an additional experiment the effect of monitor refresh rate was investigated with observer JS. In this additional study the interval duration was again constant at 900 ms and temporal thresholds for coherences between 10 and 40 percent were investigated at monitor refresh rates of 50 and 20 Hz (instead of 100 Hz). Only coherences of 40 percent and less were used because the temporal threshold had to be at least the duration of one frame (i.e. 50 ms at 20 Hz). To maintain the constant interval duration it was necessary for the mask time to decrease as the display time increased. Each mask (pre- and post-target) was of equal duration unless there were an odd number of frames. In this case the remaining frame was added to the last stage. For example, at a monitor refresh rate of 100 Hz, if the display time were 50 ms (i.e. 5 frames) then the preceeding mask would be 420 ms (i.e. 42 frames) and the proceeding mask would be 430 ms (i.e. 43 frames). There was always at least one frame of mask pattern before and after the middle stage.

A final experiment was conducted in order to determine whether the duration of the temporally flanking masks affected temporal thresholds. Temporal thresholds for observer JS were determined as described above, except that each mask was 200 ms

duration (Figure 3.3 (b)). Thus the overall time of each interval, and consequently the total number of dot pairs, did not stay constant.

For observers AN and BN, each run contained 120 trials. For oberver JS, in all temporal threshold experiments, each run contained 240 trials.

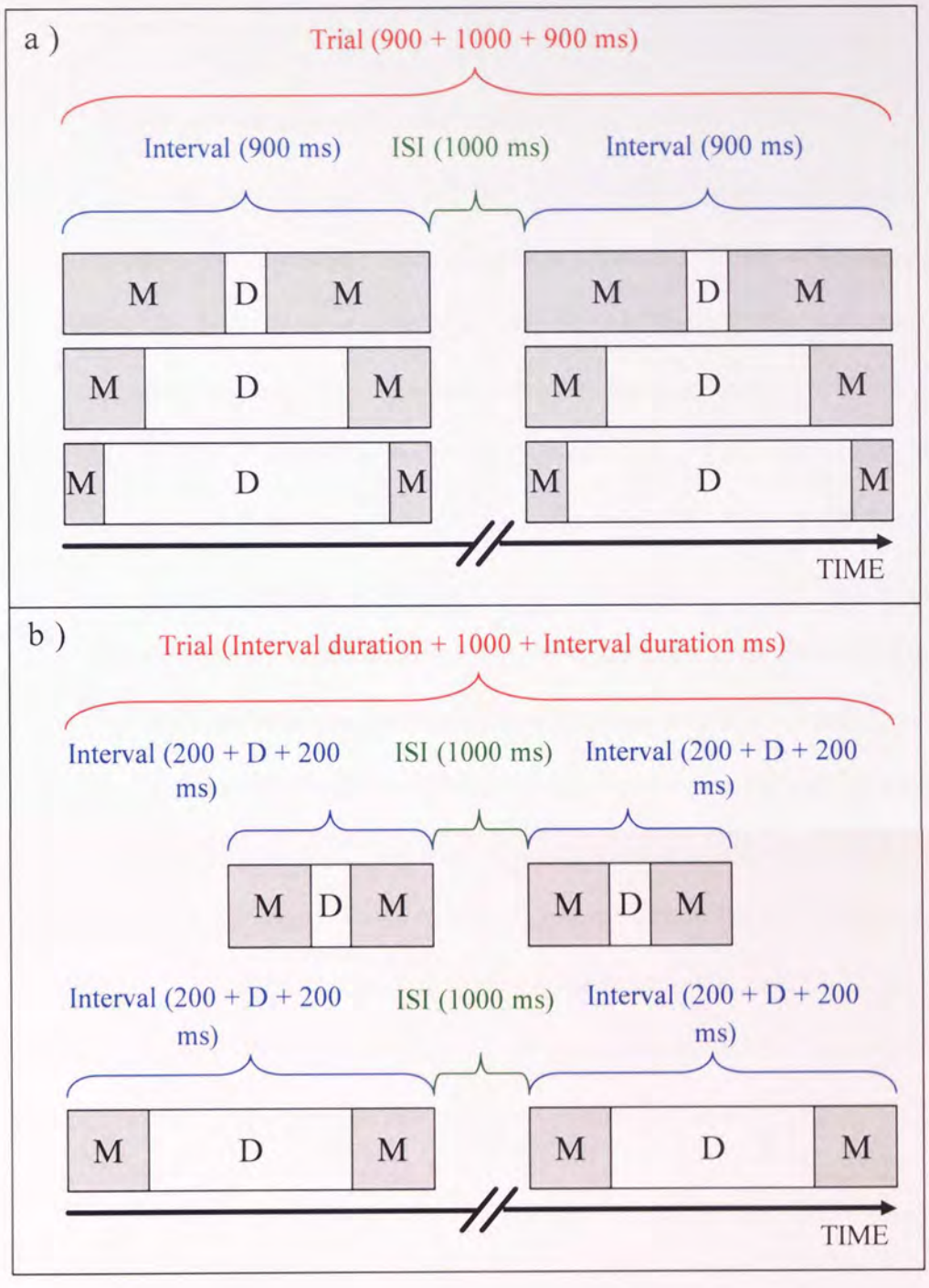

Figure 3.3. Trials consisted of two intervals separated by an ISI of 1000 ms. Each interval had three sections. The first and last sections were masks (M) composed of zero coherence Glass patterns. The middle section (D) of one interval contained Glass patterns of pre-determined coherence, the other interval contained zero coherence Glass patterns. Observers indicated the interval that contained the more coherent Glass patterns. Interval durations were either a) 900 ms, or b) the display time (D) plus two masks of 200 ms.

3.3 Results

3.3.1 Coherence thresholds for Glass patterns

Figure 3.4 shows, for observers AN and BN, the probability of correctly identifying radial, rotational and horizontal Glass patterns as a function of their coherence. The fitted curves show the order in which each data set was obtained. The run order, and thus experience, did not effect coherence thresholds for observers AN and BN with radial (Figure 3.4 (a, b)) or rotational Glass patterns (Figure 3.4 (c, d)) or for observer BN with horizontal Glass patterns (Figure 3.1 (f)). However, observer AN failed to reach threshold performance for the first run with horizontal Glass patterns (Figure 3.4 (e)). For this run the maximum coherence of the target Glass pattern had been thirty percent. At this coherence the performance for detection of radial and rotational patterns by observer AN was near perfect (= 95 %). Performance improved with the second horizontal Glass pattern run for observer AN, where the coherence necessary for detection was 19.4 percent. Observer AN's coherence thresholds for the third, fourth and fifth runs with horizontal patterns were similar at approximately 13-15 percent. The data for observer JS could not be meaningfully plotted in run order as she was already well practised at performing the task before beginning the recorded trials.

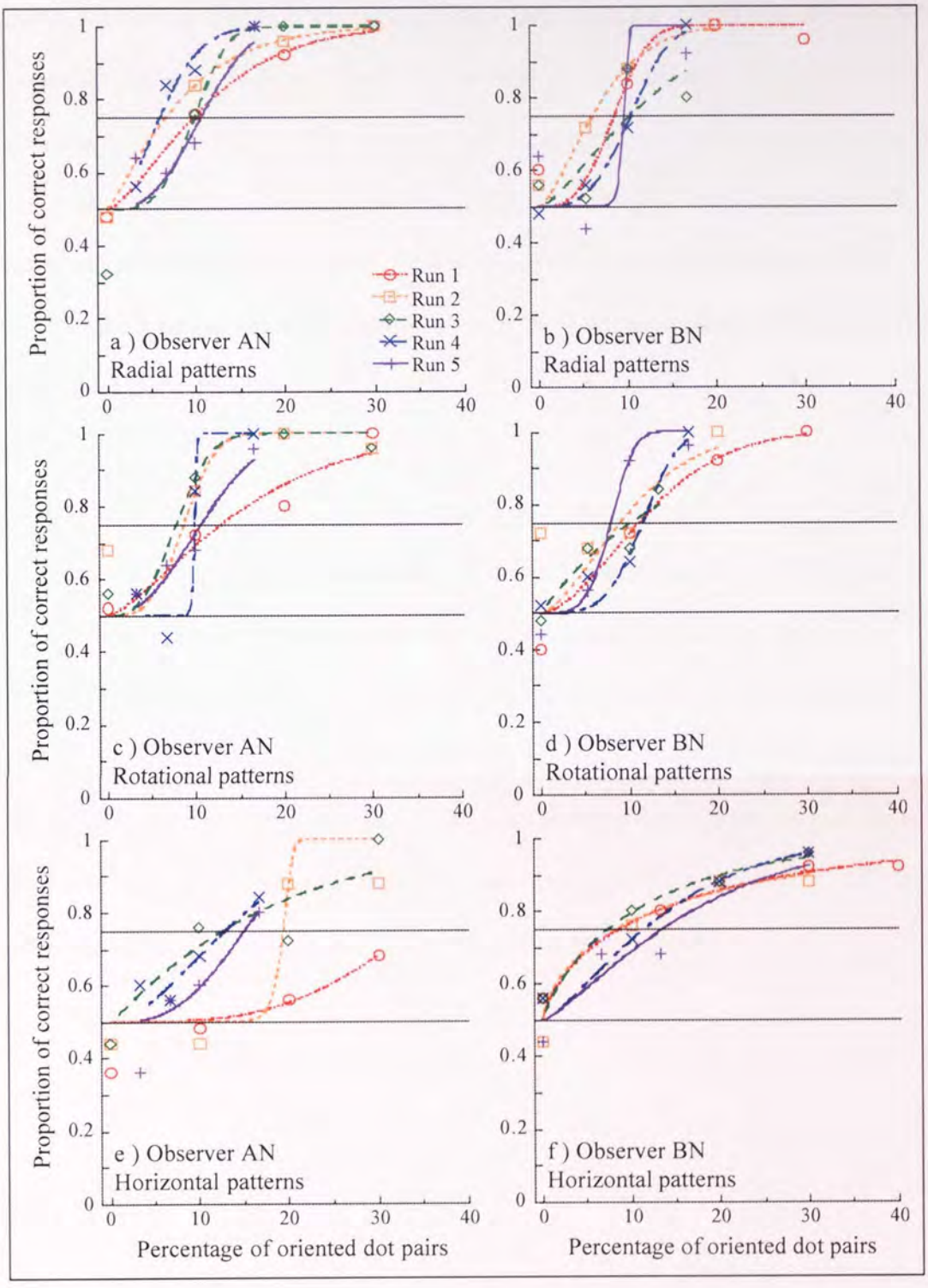

Figure 3.4. The proportion of correct responses for detecting radial (a, b), rotational (c, d) and horizontal (e, f) Glass patterns as a function of coherence for observers AN (a, c and e) and BN (b, d and f). Each Weibull function is fitted to the results for a run with 100 trials. Patterns were presented for 300 ms, the monitor refresh rate was 100 Hz.

Figure 3.5 shows coherence thresholds plotted against the number of runs the observer had completed with that transformation type. Note that a coherence threshold was not obtained for observer AN's first run with horizontal patterns. The coherence thresholds obtained for observer AN with horizontal patterns were higher than his thresholds for radial and rotational Glass patterns. With observer BN, coherence thresholds were similar for all pattern types. For both observers, the number of runs performed did not affect coherence thresholds.

The mean coherence thresholds are shown for each transformation type in Figure 3.6. Observer BN (Figure 3.6 (b)) had similar mean coherence thresholds with all patterns. Observers AN (Figure 3.6 (a)) and JS (Figure 3.6 (c)) had higher mean coherence thresholds for horizontal Glass patterns than for radial or rotational Glass patterns. Observer JS's higher coherence thresholds with horizontal Glass patterns cannot be attributed to inexperience as she was a well practised observer. Additionally, Figure 3.6 (c) shows that for observer JS, the eye that was used in the recording session did not affect the mean coherence thresholds for all transformation types.

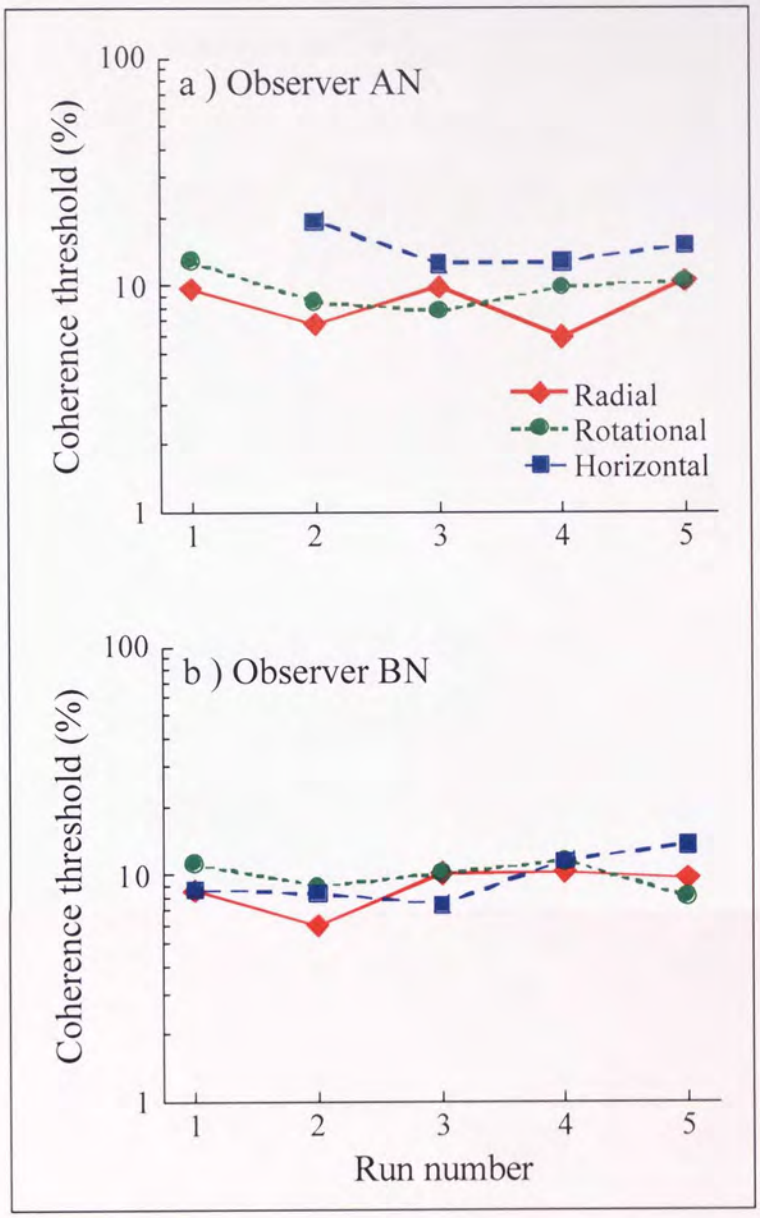

Figure 3.5. The coherence threshold (75 % correct responses) is plotted against the number of times observer a) AN or b) BN had performed a run with that transformation type. Each data point is based on 100 trials, pattern presentation time was 300 ms and the monitor refresh rate was 100 Hz. The coherence threshold was not reached for the first run of horizontal Glass patterns with observer AN.

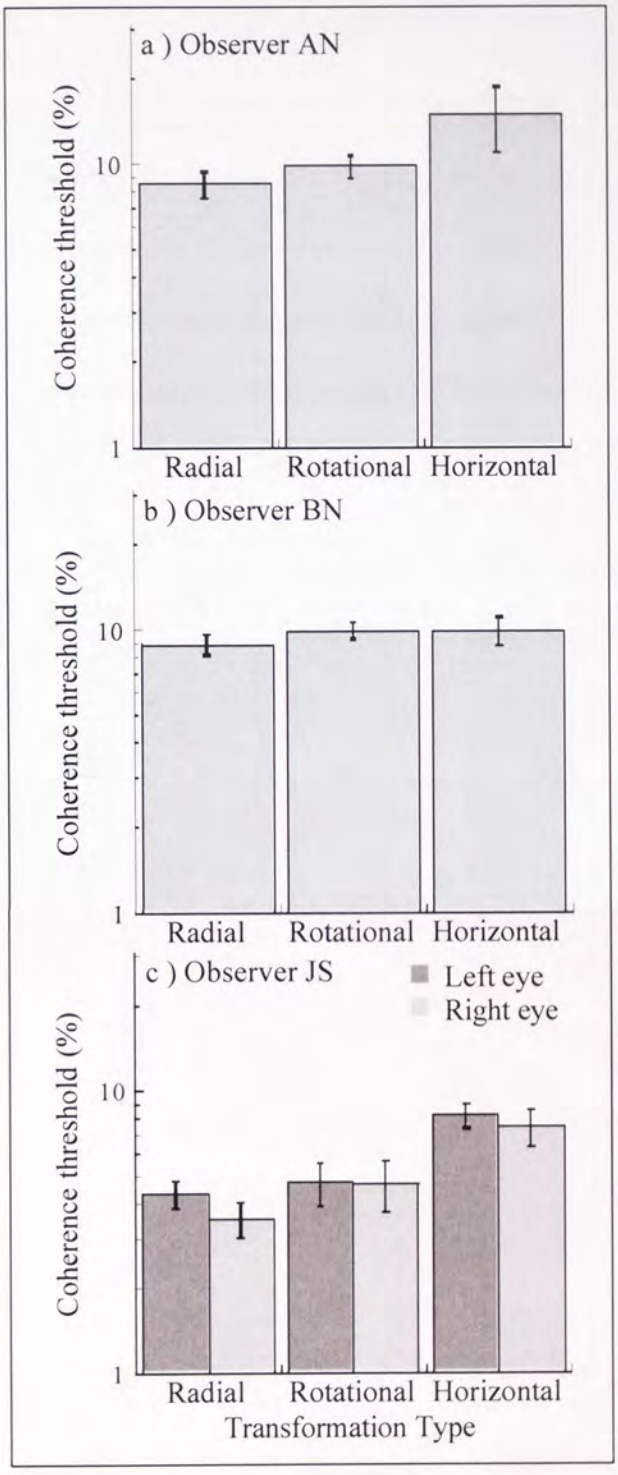

Figure 3.6. The mean coherence threshold based on five runs (except for observer AN with horizontal patterns which is based on four runs) is plotted for each transformation type. Error bars show the S.E.M. Pattern presentation time was 300 ms, monitor refresh rate was 100 Hz. Observers a) AN and b) BN used their dominant eye only. Observer c) JS viewed the stimuli monocularly with both the right and the left eye on different runs.

3.3.2 Temporal thresholds for Glass patterns

Figures 3.7-3.9 show, as a function of display duration, the proportion of correct responses for detection of radial, rotational and horizontal Glass patterns, respectively. The coherence of the target patterns ranged from 5 to 100 percent. For all pattern types, at a given coherence level, the proportion of correct responses increased with increasing display duration. Additionally, all Glass patterns required less display duration to be identified at higher than at lower coherences.

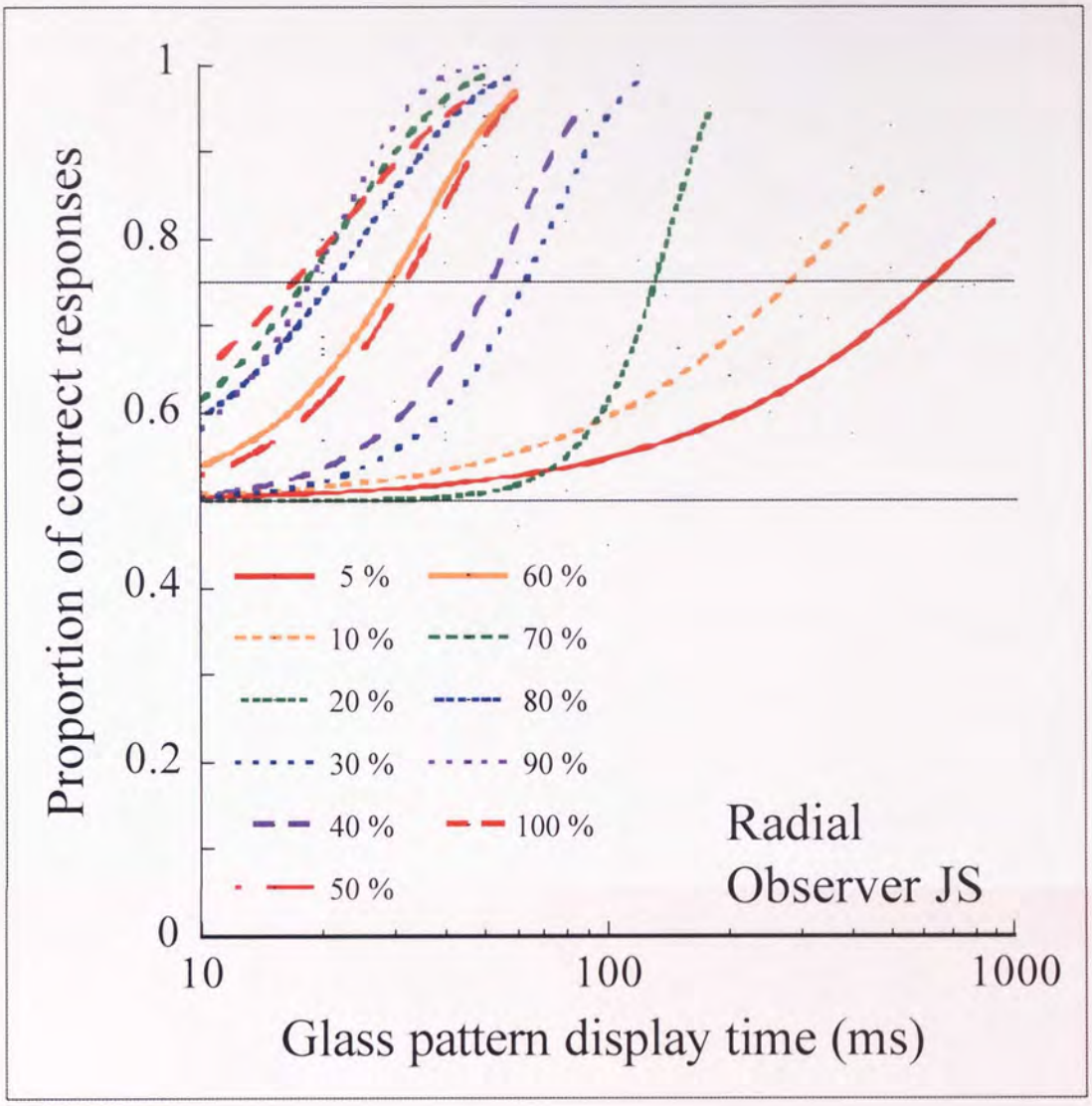

Figure 3.7. The proportion of correct responses to radial Glass patterns are plotted against display duration. Interval duration was 900 ms, monitor refresh rate was 100 Hz. For pictorial clarity the individual data points are not shown. Each Weibull function is fitted to six data points, representing a total of 240 trials, for a given coherence of the radial Glass pattern. Coherences ranged from 5 to 100 percent as indicated in the key. The observer was JS and all stimuli were viewed with her right eye only.

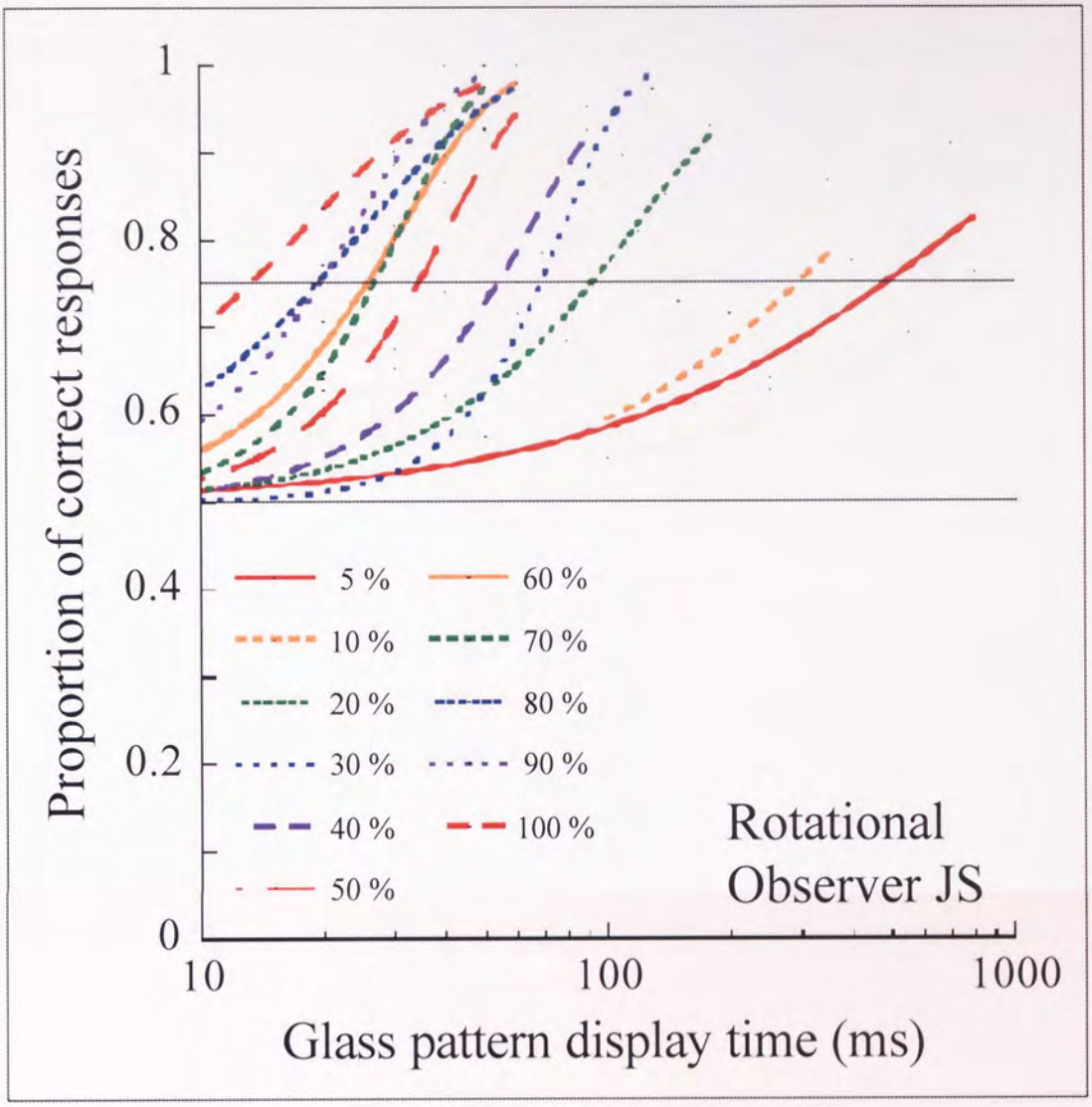

Figure 3.8. As for Figure 3.7 except for rotational Glass patterns.

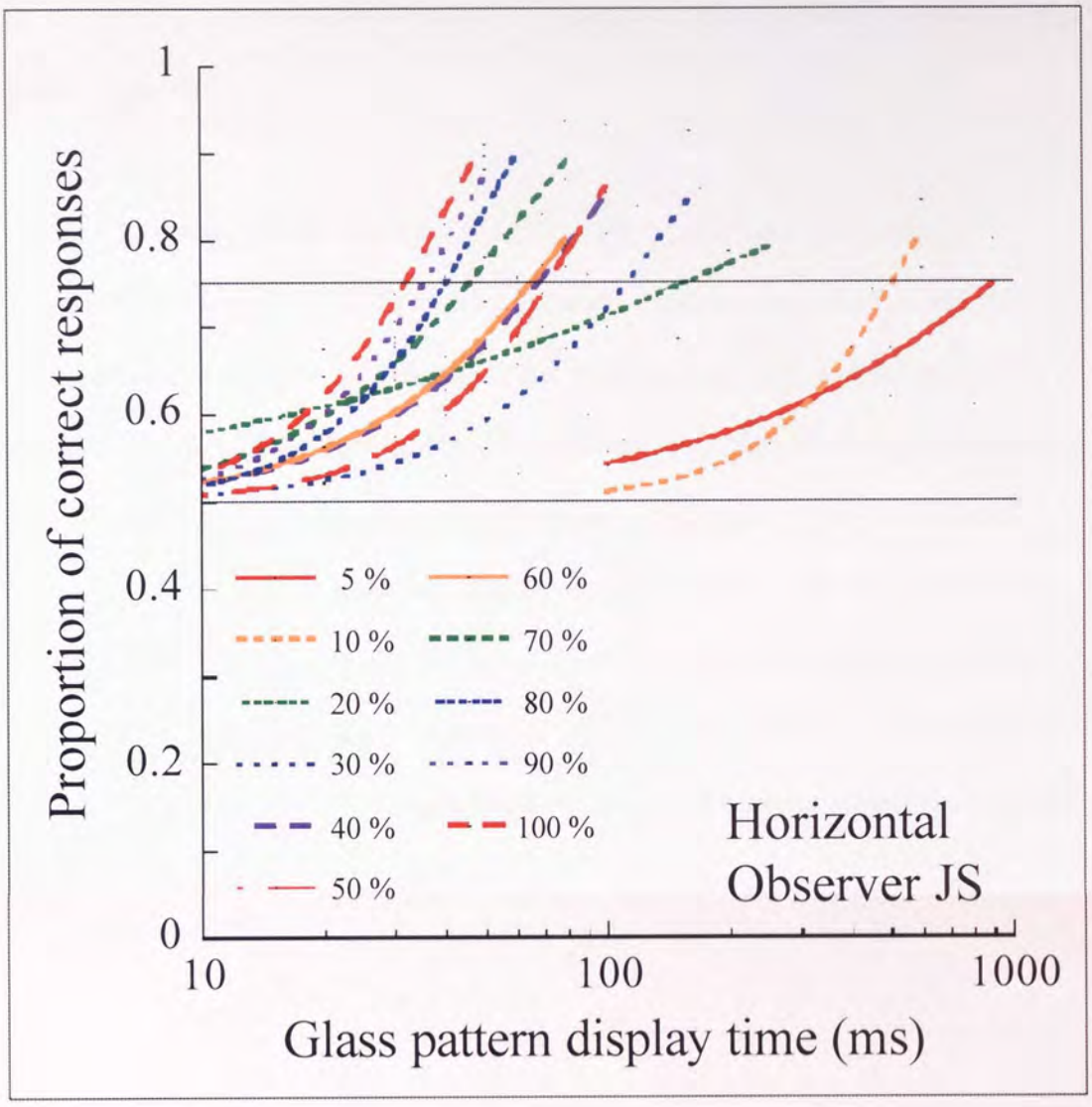

Figure 3.9. As for Figure 3.7 except for horizontal Glass patterns.

Similarly to the previous figures, Figure 3.10 shows the proportion of correct responses as a function of display time for observers AN and BN. The figure shows the results for radial, rotational and horizontal Glass patterns across a range of target coherences. As with observer JS, the results showed that for observers AN and BN the proportion of

correct responses increased with increasing display duration and with increasing Glass pattern coherence.

Figure 3.11 shows (for all observers and all pattern types) the display duration necessary for discrimination of the more coherent Glass pattern from the zero coherence Glass patterns in 75 percent of trials (i.e. the temporal threshold) plotted against the coherence of the target Glass pattern. The data were well fit by power laws (correlation coefficients = 0.98) and the exponents are shown in the figure. Note that for each observer the functions for radial and rotational Glass patterns were near identical. In contrast, the temporal thresholds for detection of horizontal Glass patterns were higher than those for radial and rotational patterns. The only data point that contradicts this is for observer BN at ten percent Glass pattern coherence where her temporal thresholds were similar for all transformation types.

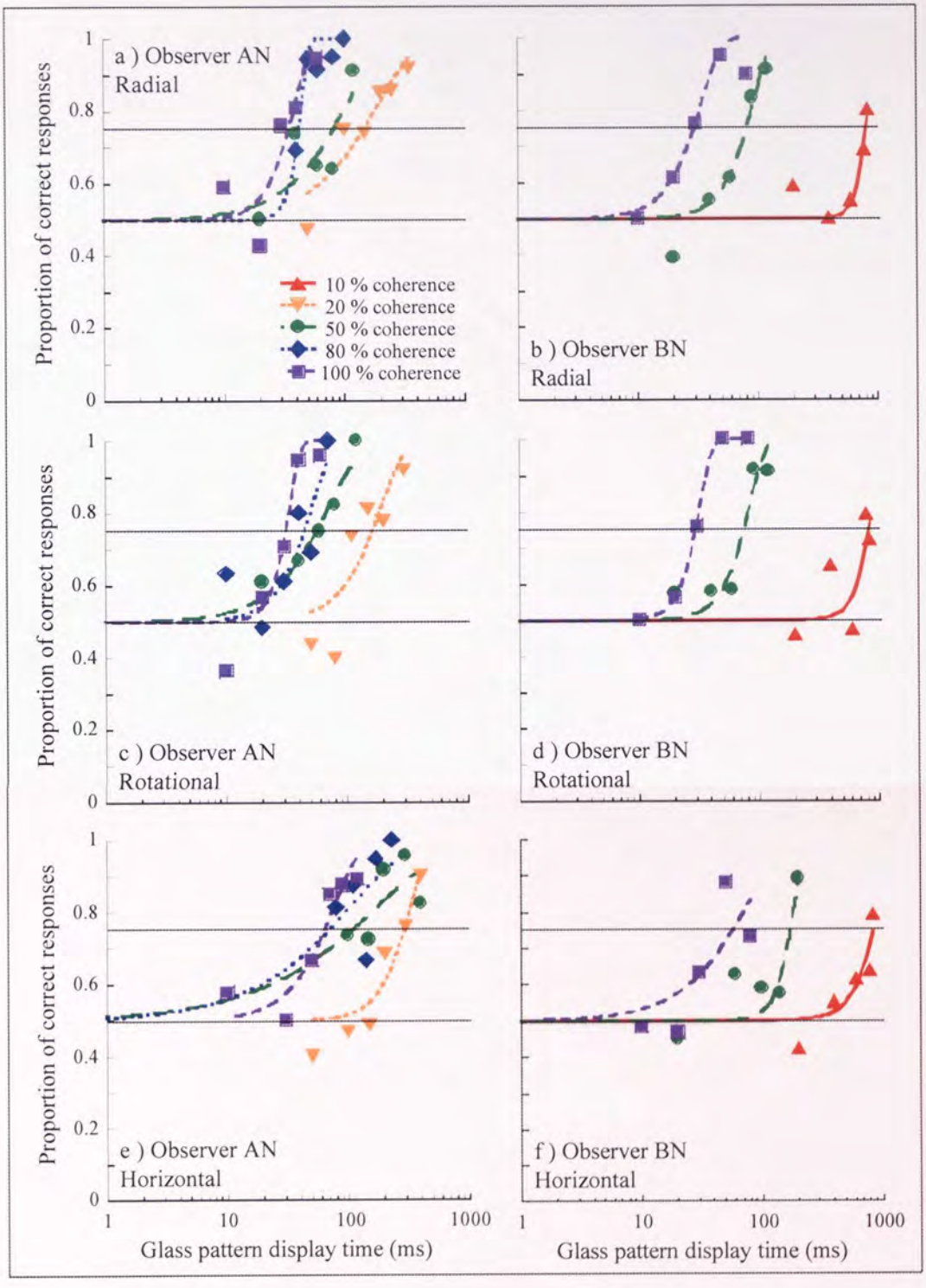

Figure 3.10. The proportion of correct responses to a more coherent radial (a and b), rotational (c and d) or horizontal (e and f) Glass pattern is shown for observers AN (a, c and e) and BN (b, d and f) against display duration. Interval duration was 900 ms, monitor refresh rate was 100 Hz. Each Weibull function represents a total of 120 trials at the coherences indicated in the figure key.

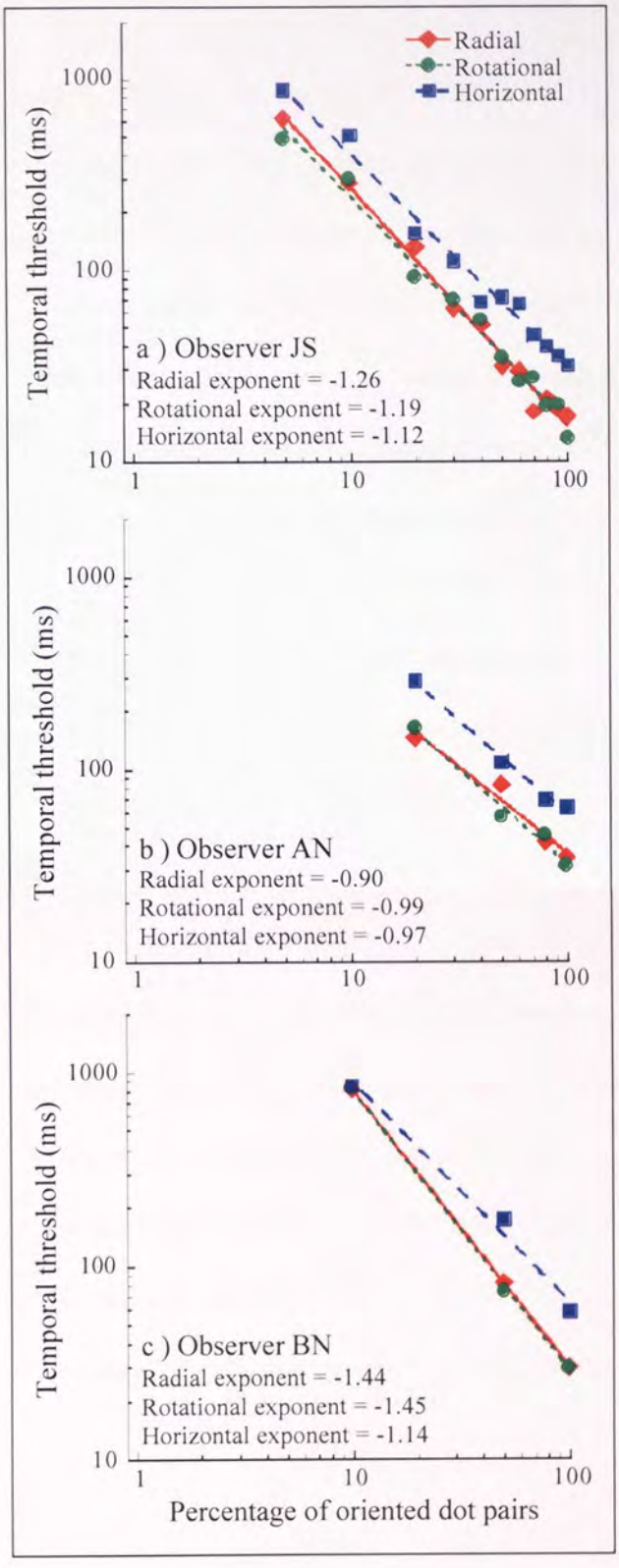

Figure 3.11. Temporal thresholds are plotted against target Glass pattern coherence for observers a) JS; b) AN; and c) BN. Interval duration was 900 ms, monitor refresh rate was 100 Hz. Data points are fitted with a power function (correlation coefficient = 0.98).

Figure 3.12 shows the number of oriented dot pairs needed, by all observers, for detection of radial, rotational and horizontal Glass patterns as a function of the coherence of the target Glass pattern. The number of oriented dot pairs was calculated by multiplying the number of frames that corresponded to the temporal threshold by the number of oriented dot pairs per frame. For observers JS and AN, the number of oriented dot pairs needed for Glass pattern detection was relatively stable across coherences = 20 percent. At coherences less than 20 percent the number of oriented dot pairs at threshold increased. Results with radial and rotational patterns for observer BN were similar, in that the threshold number of dots was elevated at coherences less than 20 percent. However, with horizontal patterns the number of oriented dot pairs at threshold was elevated at 10 and 50 percent relative to 100 percent coherence.

Figure 3.13 shows observer JS's temporal thresholds at 100, 50 and 20 Hz dot refresh rates plotted as a function of a) radial, b) rotational and c) horizontal Glass pattern coherence. Note that temporal thresholds for radial and rotational patterns were not affected by the dot refresh rate within the range tested. However, temporal thresholds for 30 and 40 percent coherent horizontal Glass patterns were higher when the dot refresh rate was 20 Hz than when the rate was 50 or 100 Hz. At lower horizontal coherences, there was no effect of dot refresh rate on temporal thresholds.

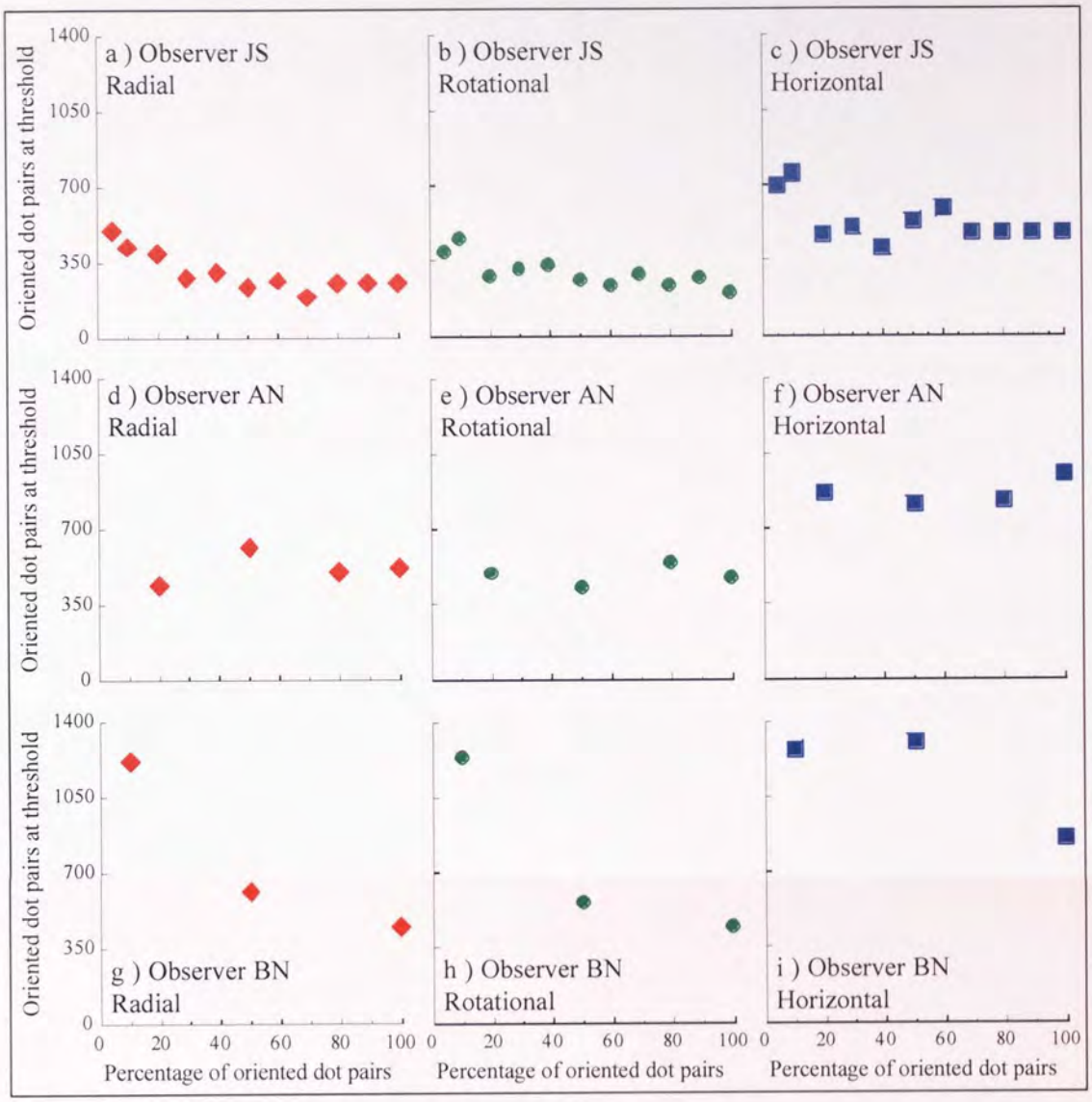

Figure 3.12. The number of oriented dot pairs corresponding to the temporal thresholds for detection of radial, rotational and horizontal Glass patterns, plotted against target Glass pattern coherence for observers JS, AN and BN. Interval duration was 900 ms, monitor refresh rate was 100 Hz.

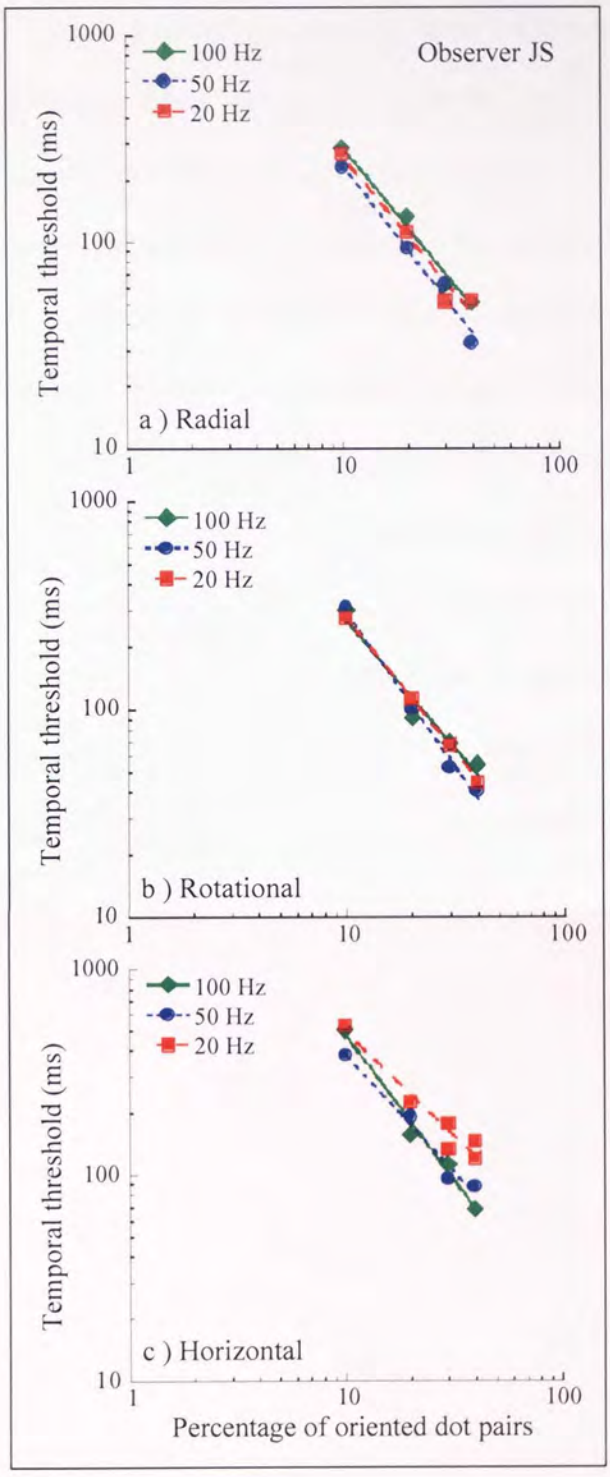

Figure 3.13. Observer JS's temporal thresholds for a) radial, b) rotational and c) horizontal Glass pattern are plotted against target Glass pattern coherence for dot refresh rates of 100, 50 and 20 Hz. Interval duration was 900 ms. Each data point is based on 240 trials. The data for 100 Hz is reproduced from Figure 3.11(a).

Figure 3.14 shows observer JS's temporal thresholds for a) radial, b) rotational and c) horizontal Glass patterns both when the mask time varied to maintain an interval duration of 900 ms and when the mask time was constant at 200 ms. The dashed horizontal line at 500 ms represents the temporal threshold at which the total number of noise dot pairs in an interval was the same for both conditions. At all coherences tested, the mask duration did not affect temporal thresholds for detection of radial or rotational Glass patterns. However, temporal thresholds for detection of horizontal Glass patterns at coherences of 40 percent and above were lower when the mask duration was constant at 200 ms. Conversely, temporal thresholds were higher in the 200 ms mask condition when the coherence was five percent. Thus, for a given coherence, the condition (200 ms mask or 900 ms interval) with the longest mask duration (i.e. more noise) required longer horizontal Glass pattern display duration for detection.

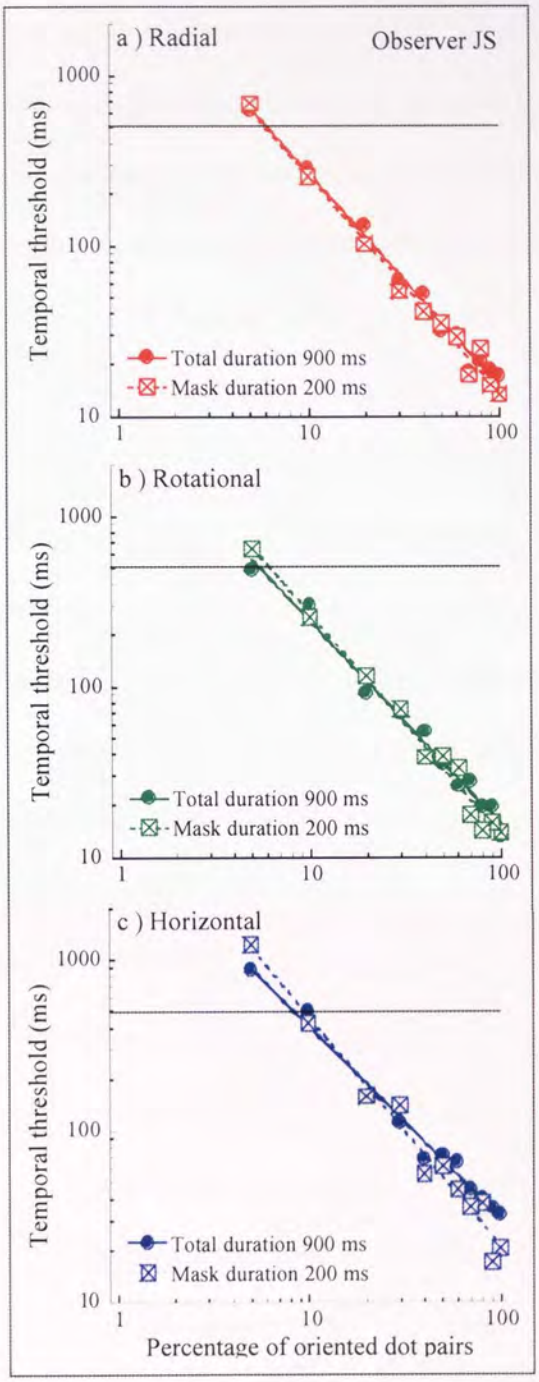

Figure 3.14. Observer JS's temporal thresholds for a) radial, b) rotational and c) horizontal Glass pattern plotted against target Glass pattern coherence. Monitor refresh rate was 100 Hz. Each data point is based on 240 trials. Temporally flanking masks were either 200 ms duration each or were variable to maintain an interval duration of 900 ms (reproduced from Figure 3.11 (a)). The horizontal line at 500 ms indicates the threshold at which the total number of dot pairs is the same in both conditions.

3.4 Discussion

The experiments reported in this chapter provide evidence that the human visual system is more sensitive to the detection of radial and rotational Glass patterns than to horizontal Glass patterns, in agreement with some previous studies (Kelly *et al.*, 2001; Wilson & Wilkinson, 1998; Wilson *et al.*, 1997) but not all (Dakin & Bex, 2002; Maloney *et al.*, 1987).

Relative sensitivities of different pattern types were determined by measuring not only conventional coherence thresholds but also temporal thresholds across a range of coherences. In general, for a given coherence level more display time was needed to detect horizontal patterns than either radial or rotational patterns (Figure 3.11). This effect was observed across a broad range of coherences and suggests a marked temporal advantage for the detection of radial and rotational form, relative to horizontal form.

As coherence of the target Glass pattern decreased, the display time necessary for detection increased (Figure 3.11). However, for each pattern type the number of oriented dot pairs necessary for detection generally remained stable for target coherences between 20 and 100 percent (Figure 3.12). This is indicative of a process with efficient integration of signal, irrespective of differences in coherence and display times. The higher number of oriented dot pairs needed for detection of global form at coherences of 10 percent and less suggests that there may be a different, less-efficient, process in operation. Therefore, two different integrative processes may operate, with a more-efficient process predominating at higher coherences (= 20 percent) and a less-efficient process predominating at lower (< 20 percent) coherences. In the case of observer BN with horizontal patterns, the less-efficient process may dominate at

coherences greater than 20 percent but because only three data points were collected it is not possible to comment further on this. Additionally with observer BN, different integrative processes may underlie the seemingly conflicting results that coherence thresholds were similar for all pattern types (approximately ten percent, see Figure 3.6), as were temporal thresholds at ten percent coherence, but at higher coherences the temporal thresholds for horizontal patterns were higher than those for either radial or rotational patterns. This raises the possibility that previous studies that have focussed only on determining coherence thresholds may have underestimated the detection advantage of radial and rotational patterns (Dakin & Bex, 2002; Kelly *et al.*, 2001; Maloney *et al.*, 1987; Seu & Ferrera, 2001; Wilson & Wilkinson, 1998; Wilson *et al.*, 1997). The only study to date that investigated perception of Glass patterns at supra-coherence threshold supported the finding that sensitivity is higher for rotational than for horizontal patterns (Kurki & Saarinen, 2004).

There are at least two more reasons for suggesting that horizontal patterns are processed differently to radial and rotational patterns. Firstly, the duration of the temporally flanking masks affected temporal thresholds for horizontal but not radial or rotational Glass patterns (Figure 3.14). With horizontal patterns, the temporal threshold was greater in the condition with the longer mask duration, indicative of noise from the mask being integrated into the processing of horizontal patterns. This does not mean that no noise from the mask was integrated into the processing of either radial or rotational patterns but it does suggest that the duration of any mask-integration was less than the shortest mask used here, which generally was 200 ms. This is in contrast to findings with radial and rotational motion coherence where several seconds of flanking noise have been shown to be integrated (Burr & Santoro, 2001). Secondly, at

coherences of 30 and 40 percent with 20 Hz refresh rate the temporal thresholds for horizontal, but not radial or rotational, patterns were increased compared with thresholds at 50 or 100 Hz refresh rate (Figure 3.13). Reducing the dot refresh rate decreases the apparent dot density and also reduces the movement of dot pairs. It seems unlikely that the results were attributable to reduced dot density as this would be expected to affect all coherences. Moreover, studies have reported that detection of Glass patterns is resistant to changes in dot density (Kurki *et al.*, 2003; Wilson & Wilkinson, 1998). However, the increased temporal thresholds for horizontal patterns only occurred at coherences where the temporal thresholds at 50 and 100 Hz refresh rate had been so low that they would only represent one frame of horizontal pattern at 20 Hz refresh rate. Successive frames of coherent dot pairs create a flickering pattern with an illusion of coherent motion (Ross, Badcock & Hayes, 2000). Thus, the increased number of frames necessary for detection of horizontal patterns may reflect a need for movement to aid detection. Temporal thresholds for radial and rotational patterns did not increase which suggests that they can be detected equally well if the Glass pattern is static (just one frame).

The detection of radial patterns was similar to that of rotational patterns. Consequently, these results do not support the notion that any specialised detector for rotational patterns is more efficient than that for radial patterns (see Seu & Ferrera, 2001; and Wilson & Wilkinson, 1998). However, the results suggest fundamental differences in the perception of horizontal patterns compared with either radial or rotational patterns. This could possibly be due to the clearly defined centre of both radial and rotational patterns rendering them more "object like" than horizontal patterns. Additionally, both radial and rotational patterns contain dot pairs oriented in all directions whereas

horizontal patterns only contain dot pairs oriented in one direction. Thus, horizontal patterns may activate less neural units for orientation discrimination than radial or rotational patterns.

MEG will be used in subsequent chapters to examine the temporal processing and spatial distribution of power changes associated with perception of radial, rotational and horizontal form and in particular to explore the neural basis of the behavioural differences between pattern types.

4 MEG: The neural response to global form in centrally-viewed Glass patterns

4.1 Introduction

The psychophysical studies reported in the previous chapter showed that horizontal Glass patterns required a longer presentation time to be distinguished from random Glass patterns than either radial or rotational patterns. This was true across a wide range of coherences. To investigate this further, MEG was used to explore the temporal sequence of neural activity associated with perception of radial, rotational and horizontal Glass patterns. In addition, SAM analysis was used to localise brain areas that showed changes in cortical power in response to coherent form.

Glass patterns are well suited to studies of form perception because the global structure and the extent of pattern coherence can be changed without affecting luminance or dot density. The radial, rotational, horizontal and zero coherence Glass patterns used throughout this thesis all contained dot pairs with the same inter-dot separation and therefore all pattern types were comparable at the local level of processing. However, at the global level (across the whole pattern) the zero coherence patterns did not create a percept of form. Additionally, a new screen of Glass patterns was generated and displayed on each frame (every 10 ms). This created a dynamic pattern and allowed the neural response to the onset of coherence to be dissociated from that merely to a change of screen. Previous neuroimaging studies of global form are reviewed in section 1.2.2.

4.2 Methods

4.2.1 Observers

Eight observers (four males and four females, aged 25-48 years) with no history of neurological dysfunction or injury consented to participate in this experiment. Observer DN was the thesis supervisor. All observers had previously undergone an anatomical MR volume scan and were screened with a questionnaire to ensure they did not have any metallic objects on or within their person. Observers had normal or corrected-to-normal vision. All stimuli were viewed monocularly and the eye not being used was occluded with a dark eye patch. The observer was instructed to maintain fixation and stimuli were viewed passively.

4.2.2 Stimulus generation, presentation and recording

The apparatus used to generate and display the visual patterns was the same as that used in the previous chapter (section 3.2). The monitor was outside the magnetically shielded room and viewed from within at a distance of 2 m via a front-surfaced mirror. The room lighting was dimmed.

Glass patterns were generated by plotting 150 pairs of white dots (70.2 cd m^{-2}, 0.04 $deg.^2$) within a square window (8.25 $deg.^2$) on a black background (5.0 x 10^{-3} cd m^{-2}). Dots within a pair were separated 0.18 deg. (centre-to-centre). A fixation dot was continually provided in the centre of the pattern. For each trial, dot pairs were oriented to form either radial, rotational or horizontal patterns as described in section 3.2.2 and a screen of Glass pattern was generated every 10 ms (every frame). Following stimulus onset, the coherence of the Glass pattern increased linearly from zero to 100 percent

over 100 ms, remained at 100 percent coherence for 300 ms and then decreased linearly to zero over 100 ms. The ISI varied between 3000 ms and 3200 ms, during which time the Glass pattern had zero coherence. A total of 150 trials were presented with 50 trials of each pattern type presented in pseudo-random order.

The neural responses to all trials were recorded using a 151-channel, whole head biomagnetic imaging system (see section 2.2.2) in a single un-averaged run at a sampling rate of 625 Hz. Data collection took approximately nine minutes. The data was DC corrected and lowpass filtered at 80 Hz. Prior to commencing recording the observer was fitted with three electromagnetic head coils. The position of these coils relative to the MEG helmet was localised before and after the run of trials. After recording, the position of these coils relative to the surface of the observer's head was determined using a Polhemus 3D digitiser and this 3D head surface was matched to the observer's MRI-defined head shape using the software Align (www.ece.drexel.edu/ICVC/Align/align11.html).

4.2.3 Data analyses

Recorded data was visually inspected off-line using CTF software (from CTF Systems Inc., Canada) and trials containing excessive spiking were removed.

MEG data was analysed using SAM (see section 2.2.3) to calculate changes in current density within defined time and frequency bands. For each observer, power changes between 1 s pre- and 1 s post-stimulus were calculated in 5-40, 5-15, 10-20, 15-25, 20-30, 25-35, and 30-40 Hz frequency bands. To further investigate power changes over different time windows, cortical current density in the 5-40 Hz frequency band was

calculated for observer DN in 500 ms time windows between zero and 1.5 s post-stimulus onset. Voxels were assigned pseudo t statistics dependant on the magnitude and estimated noise of the power change. Consequently, SAM images are probabilistic maps of power changes.

Individual observer SAM results are shown superimposed on a spatially co-registered image of their own anatomical MR volume scan by use of software called mri3dX (http://imaging.aston.ac.uk/mri3dX/index.shtml). By using the observer's own anatomical scan the locations of minor sulci and gyri, which are lost on group template brains, can be seen. However, to assist the definition of cortical areas the anatomical MR scans of individuals were transformed to Talairach space using the Talairach Manager within mri3dX (see section 2.1). Co-ordinates are reported in the MNI format.

Time-frequency plots were calculated using a Morlet wavelet transform for voxels that had been identified as having maximal pseudo t values with SAM (see section 2.2.3). Only changes that were significant at $p < 0.05$ are displayed on the plot.

Group MEG data were analysed using non-parametric permutation analyses (Nichols & Holmes, 2001; Singh *et al.*, 2003; see section 2.2.3) with the SnPM toolbox (www.fil.ion.ucl.ac.uk/spm/snpm/). SnPM was used to assess statistical significance of group SAM data for voxel- and cluster-level effects ($p < 0.05$) over 1 s time windows and in ten Hz frequency bands between 5 and 40 Hz. With cluster-level analyses the primary threshold for the pseudo t map was always 3.5.

Similarly to the SAM images for individual observers, the group SnPM images were visualised using mri3dX. However, with group analyses the individual anatomical MR volume scans were normalised to the template brain (see section 2.1). Coordinates are in MNI space.

In all SAM and SnPM figures, the left side of the brain appears on the left side of the image.

4.3 Results

4.3.1 Individual data

For each observer, SAM was used to map oscillatory power changes in the cortex to the passive perception of radial, rotational and horizontal Glass patterns. Comparisons of power were between 1 s pre- and 1 s post-stimulus onset and were analysed in several frequency bands between 5 and 40 Hz. Figure 4.1 shows the group mean of the largest power increase and decrease found in each observer, irrespective of spatial location, as a function of the SAM frequency band and the Glass pattern type. There was substantial between-observer variation in the magnitude of the power changes and there were no differences between the pseudo t statistics of the largest power decreases and the largest power increases or between the pseudo t statistics of power changes across frequency bands.

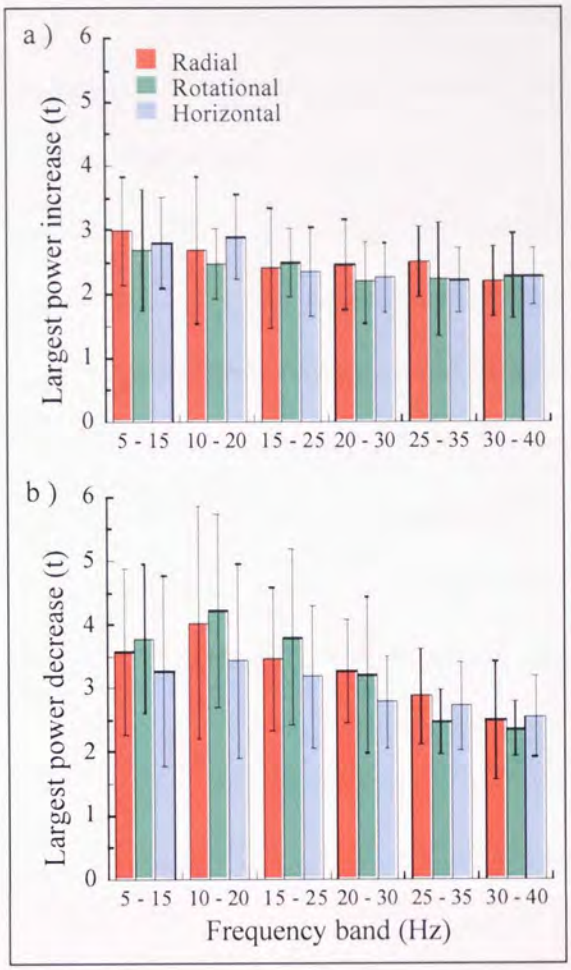

Figure 4.1. The pseudo t statistics of the voxels with the largest a) increase and b) decrease in cortical power (1 s pre- versus 1 s post-stimulus) for each observer were averaged and are shown for each Glass pattern type against the frequency band of the SAM analysis. Error bars show ± one standard deviation.

Despite inter-observer variation in the magnitude of power changes, there were several qualitative features common to observers in response to the onset of coherent form. All observers showed a bilateral decrease in oscillatory power across a broad range of frequencies in extrastriate cortex. Neither V1 nor the cerebellum were identified as centres of areas of power change for any observer (the cerebellum was identified as a region of activation in some group SnPM analyses, see section 4.3.2).

4.3.1.1 SAM images of cortical power changes

Presentation of coherent Glass patterns to observer DN elicited a pattern of responses that was representative of the group. Figure 4.2 shows SAM images for observer DN of statistical estimates (pseudo $t > 2$) of changes in 5-40 Hz frequency band power between the active and passive phases (1 s time window) in response to the presentation of a) radial, b) rotational, and c) horizontal Glass patterns. The images shown contain the voxel of maximal power change (the peak voxel). For all pattern types, this voxel represented a power decrease (indicated by purple-white colours) relative to the passive phase. Peak voxels were in the cuneus of extrastriate cortex and corresponded most closely to V3a (Hasnain, Fox, Woldorff, 1998). The MNI coordinates of these voxels are reported for each pattern in the figure legend.

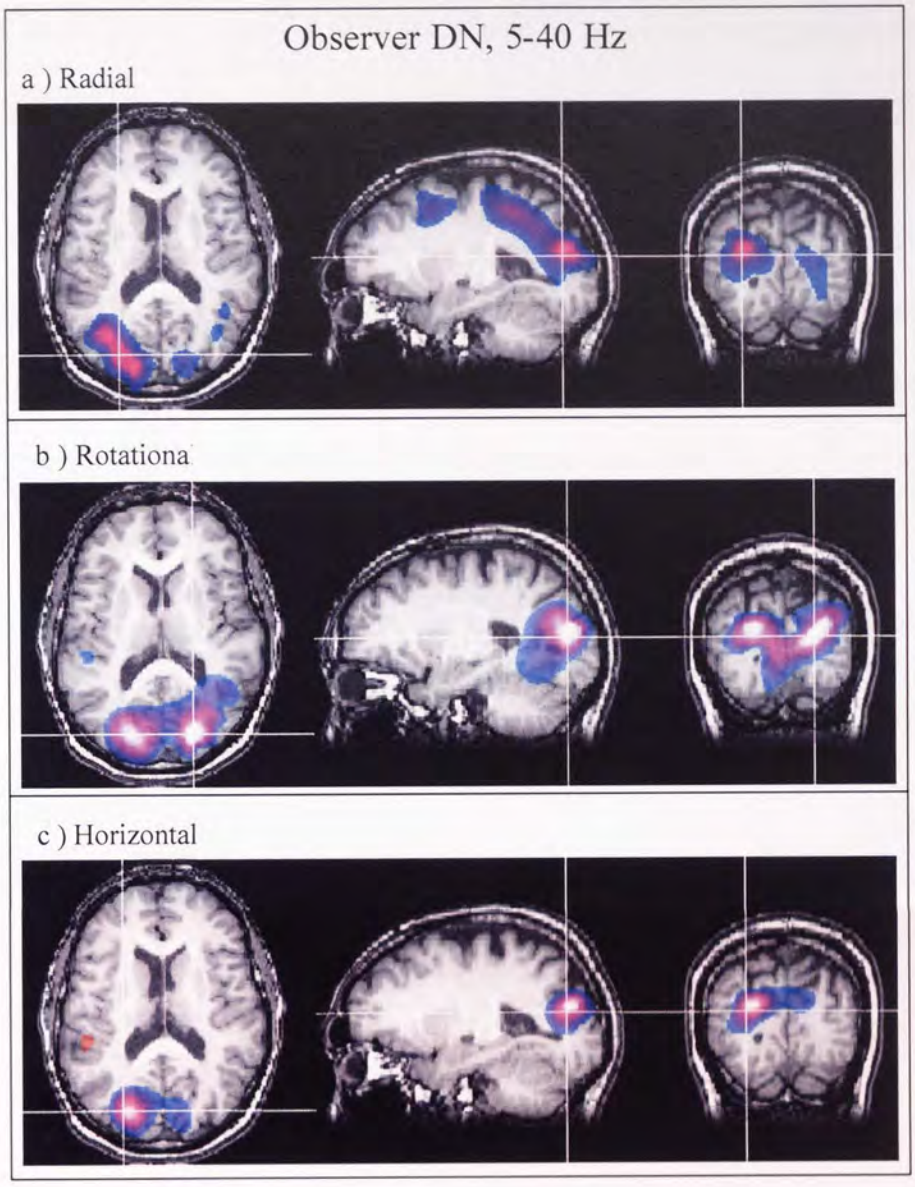

Figure 4.2. SAM images for observer DN showing comparison of cortical power (5-40 Hz) 1 s pre- with 1 s post-presentation of coherent Glass patterns to the right eye. The amplitude of the pseudo t statistic is indicated by the colour overlay on an anatomical MRI of observer DN. Voxels with a pseudo t statistic less than two are not coloured. Decreases in cortical power are shown by a blue-purple-white colour range (white voxels indicate pseudo t = 6); increases are shown by a red-orange-yellow colour range. Brain slices and crosshairs indicate the voxel with the largest pseudo t statistic, this represented a reduction in cortical power in the cuneus of extrastriate cortex for a) radial patterns (MNI: -23, -79, 18; pseudo t = 4.9); b) rotational patterns (MNI: 22, -82, 14; pseudo t = 7.9); c) horizontal patterns (MNI: -23, -79, 18; pseudo t = 6.3).

Figure 4.3 and Figure 4.4 show the results for two more observers. With observer EN (Figure 4.3), all peak voxels were in V3a (Hasnain *et al.*, 1998), being in the middle occipital gyrus following radial patterns and in the cuneus following rotational and horizontal patterns. For observer FN (Figure 4.4) peak voxels were located between V3 and V3a (Hasnain *et al.*, 1998). Radial and rotational Glass patterns produced maximal power reductions in the middle occipital gyrus whilst a voxel in the cuneus was identified following presentation of horizontal patterns.

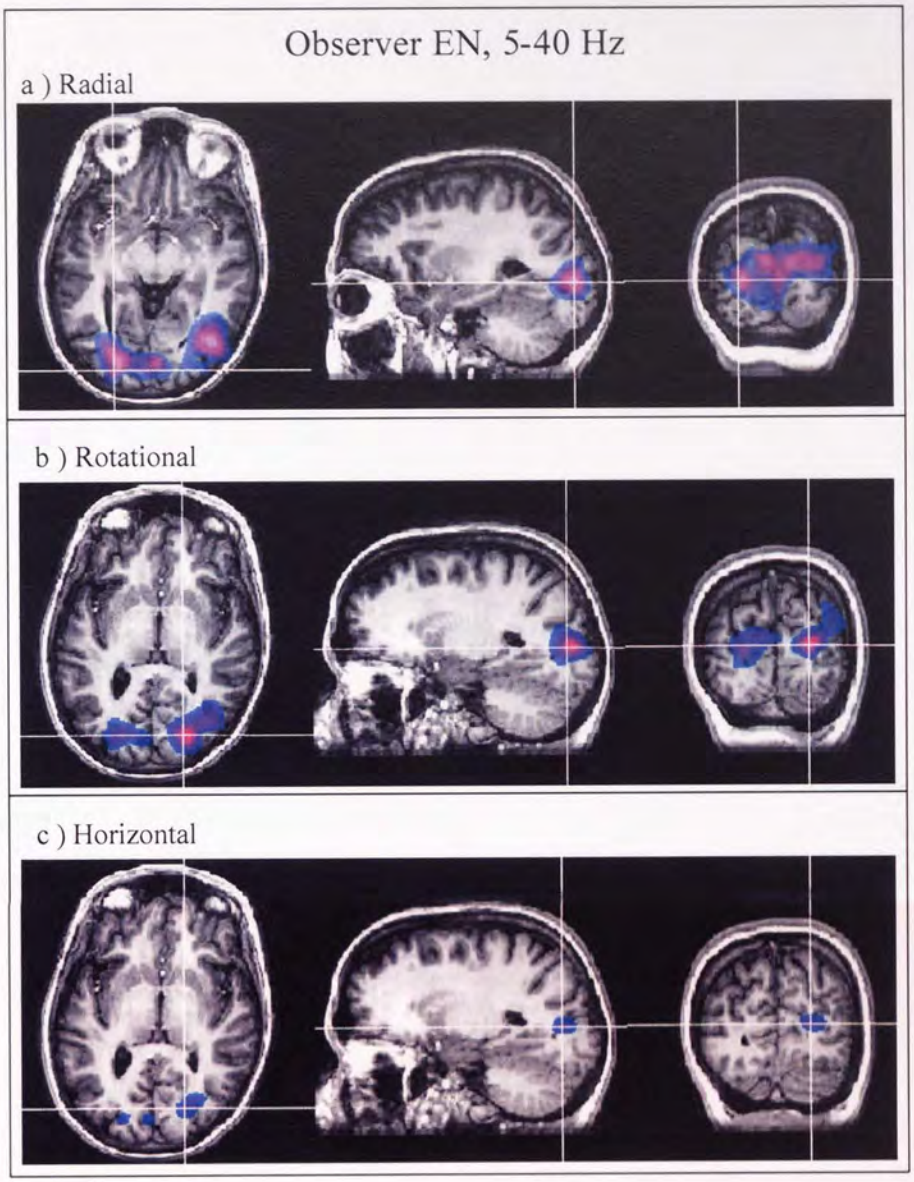

Figure 4.3. SAM images for observer EN showing comparison of cortical power (5-40 Hz) 1 s pre- with 1 s post-presentation of coherent Glass patterns to the right eye. Images are shown on an anatomical MRI of observer EN with the same colour scale as Figure 4.2. Brain slices and crosshairs indicate the voxel with the largest pseudo t statistic, this represented a reduction in extrastriate cortical power in a) the middle occipital gyrus for radial patterns (MNI: -26, -89, 9; pseudo t = 5.2); the cuneus for b) rotational patterns (MNI: 18, -82, 14; pseudo t = 4.5); c) horizontal patterns (MNI: 18, -77, 13; pseudo t = 2.7).

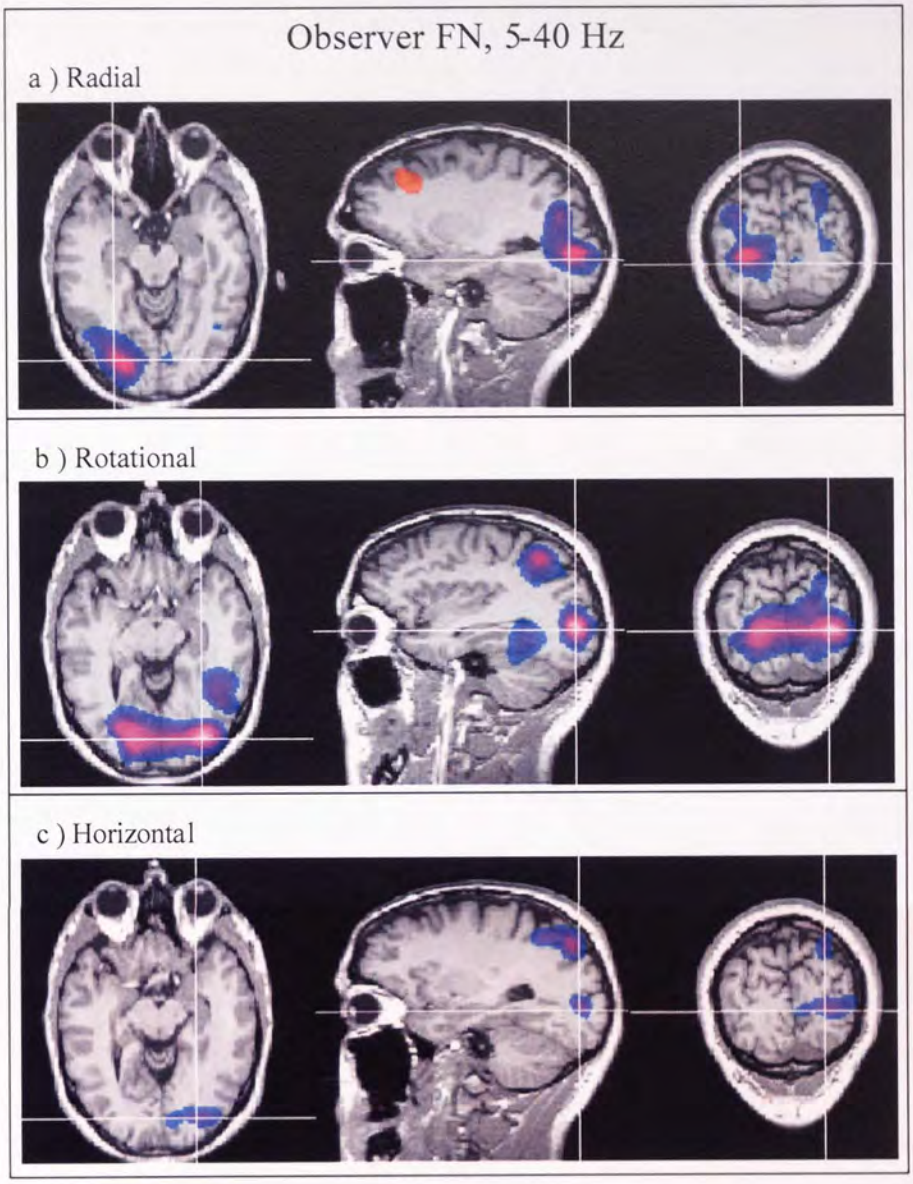

Figure 4.4. SAM images for observer FN showing comparison of cortical power (5-40 Hz) 1 s pre- with 1 s post-presentation of coherent Glass patterns to the right eye. Images are shown on an anatomical MRI of observer FN with the same colour scale as Figure 4.2. Brain slices and crosshairs indicate the voxel with the largest pseudo t statistic, this represented a reduction in extrastriate cortical power in the a) middle occipital gyrus for radial patterns (MNI: -24, -84, 3; pseudo t = 4.3); b) middle occipital gyrus for rotational patterns (MNI: 31, -85, 8; pseudo t = 5.6); c) cuneus for horizontal patterns (MNI: 25, -85, 7; pseudo t = 3.5).

Figure 4.5 shows the neural response (1 s pre- versus 1 s post-presentation, observer DN) to presentation of radial Glass patterns within 10 Hz frequency bands. Similarly, Figure 4.6 shows the neural response to rotational Glass patterns and Figure 4.7 to horizontal Glass patterns. Note that for all pattern types the reductions in power within the extrastriate were most pronounced in the 10-20 Hz and the 15-25 Hz bands.

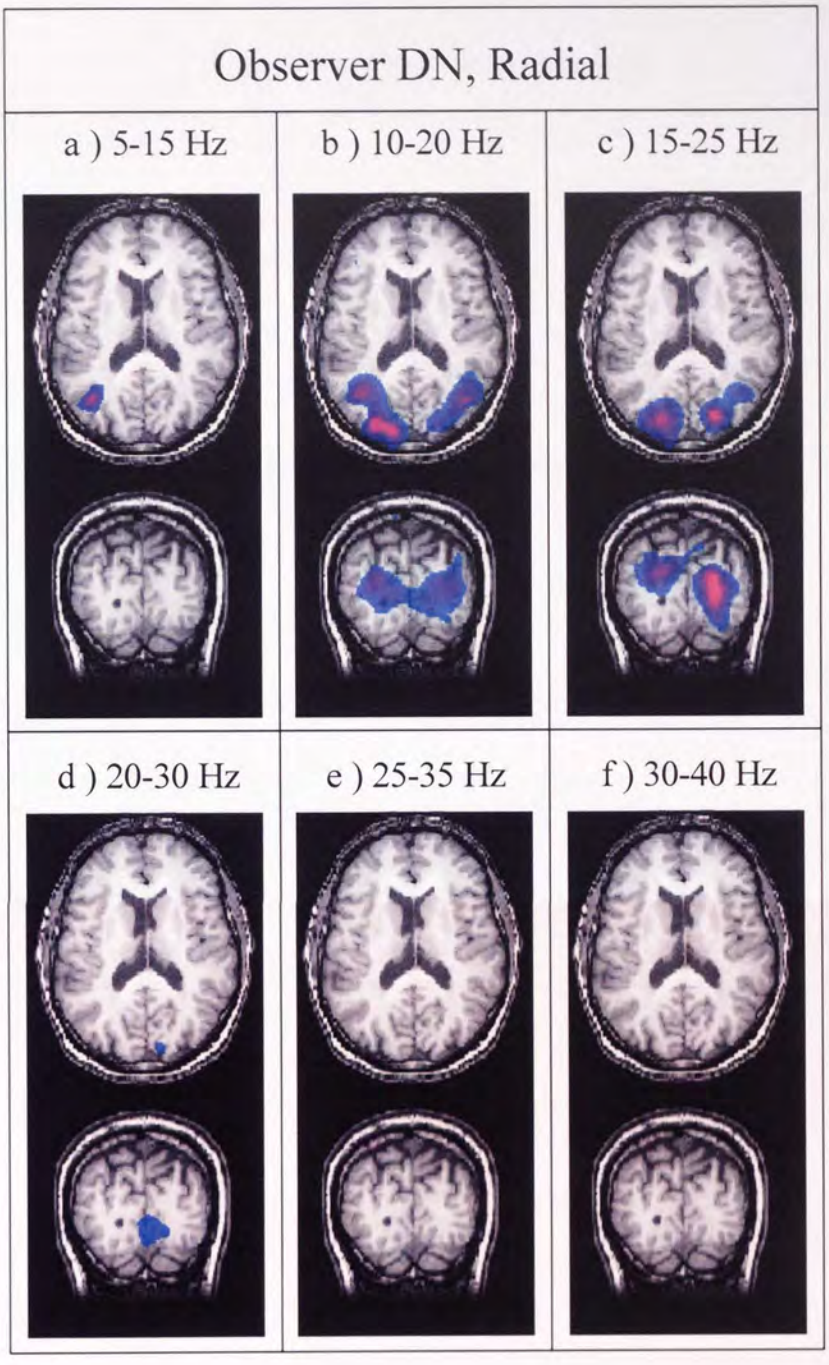

Figure 4.5. SAM images for observer DN showing comparison of cortical a) 5-15; b) 10-20; c) 15-25; d) 20-30; e) 25-35; f) 30-40; Hz power 1 s pre- with 1 s post-presentation of radial Glass patterns to the right eye. Images are shown on an anatomical MRI of observer DN with the same colour scale as Figure 4.2. Coronal and axial slices are shown dissecting the voxel of maximal 5-40 Hz (1 s time window) power change in response to radial patterns (i.e. left cuneus, MNI: -23, -79, 18).

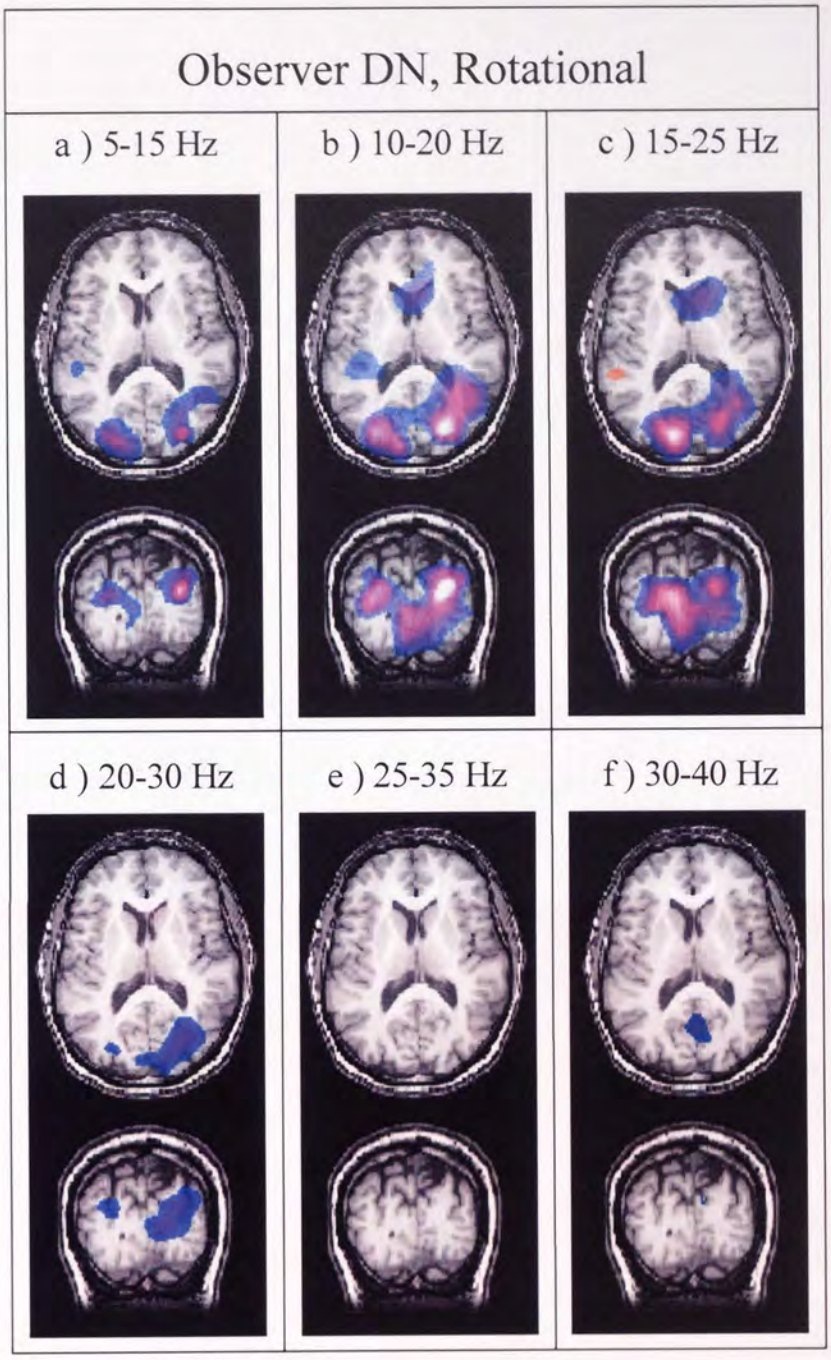

Figure 4.6. SAM images for observer DN showing comparison of cortical a) 5-15; b) 10-20; c) 15-25; d) 20-30; e) 25-35; f) 30-40; Hz power 1 s pre- with 1 s post-presentation of rotational Glass patterns to the right eye. Images are shown on an anatomical MRI of observer DN with the same colour scale as Figure 4.2. Coronal and axial slices are shown dissecting the voxel of maximal 5-40 Hz (1 s time window) power change in response to rotational patterns (i.e. right cuneus, MNI: 22, -82, 14).

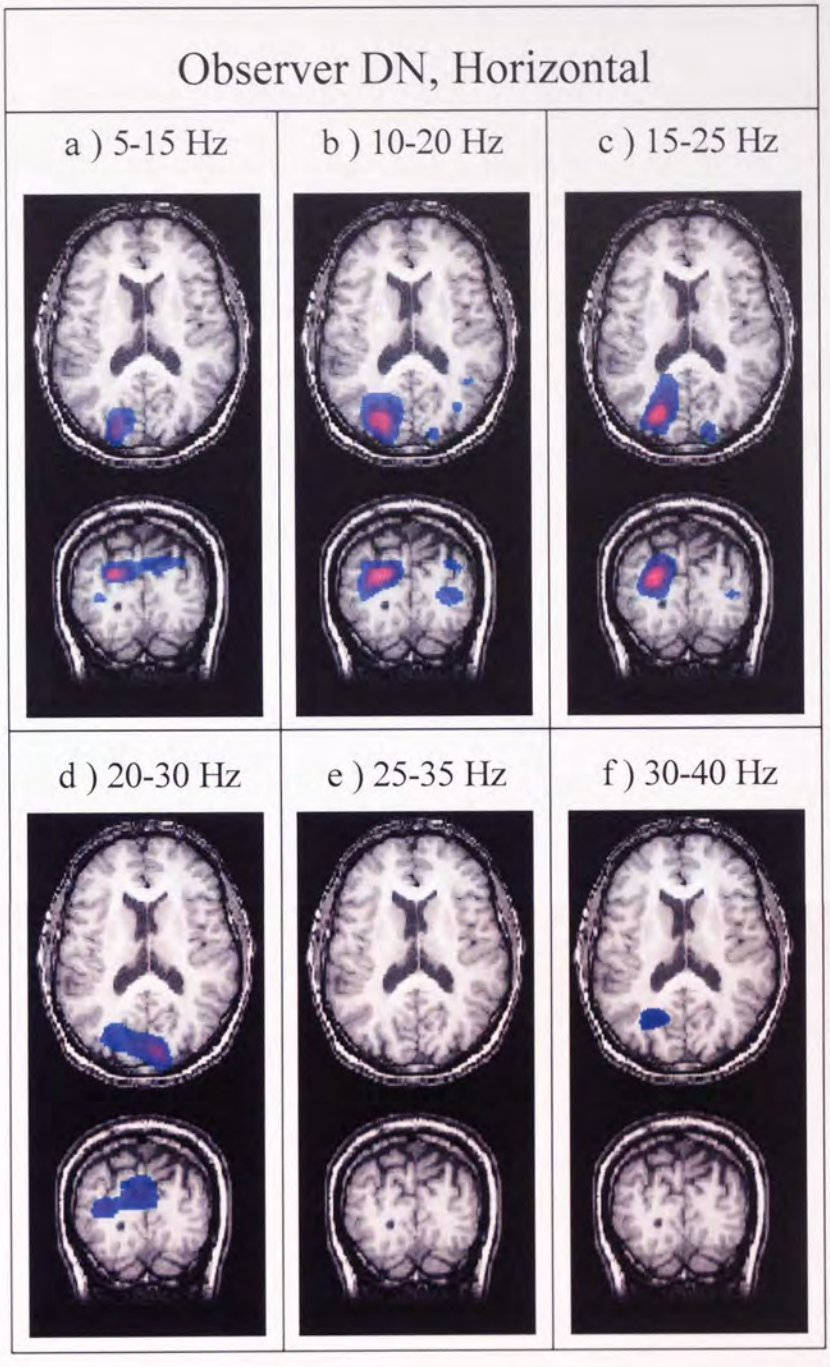

Figure 4.7. SAM images for observer DN showing comparison of cortical a) 5-15; b) 10-20; c) 15-25; d) 20-30; e) 25-35; f) 30-40; Hz power 1 s pre- with 1 s post-presentation of horizontal Glass patterns to the right eye. Images are shown on an anatomical MRI of observer DN with the same colour scale as Figure 4.2. Coronal and axial slices are shown dissecting the voxel of maximal 5-40 Hz (1 s time window) power change in response to horizontal patterns (i.e. left cuneus, MNI: -23, -79, 18).

Figure 4.8 shows, for observer DN, SAM images of changes in 5-40 Hz cortical power in response to presentation of radial Glass patterns, analysed within 500 ms time bands. Results for rotational and horizontal Glass patterns are shown in Figure 4.9 and Figure 4.10 respectively. Following presentation of all pattern types, reductions in 5-40 Hz power within extrastriate cortex were most pronounced in the 0.5-1.0 s time band. There was evidence of power reductions in the 0.0-0.5 s time band in response to radial and rotational Glass patterns but not to horizontal Glass patterns. Additionally, for all pattern types, but especially following presentation of horizontal Glass patterns, there was evidence of an increase in 5-40 Hz power in extrastriate cortex in the 1.0-1.5 s time band.

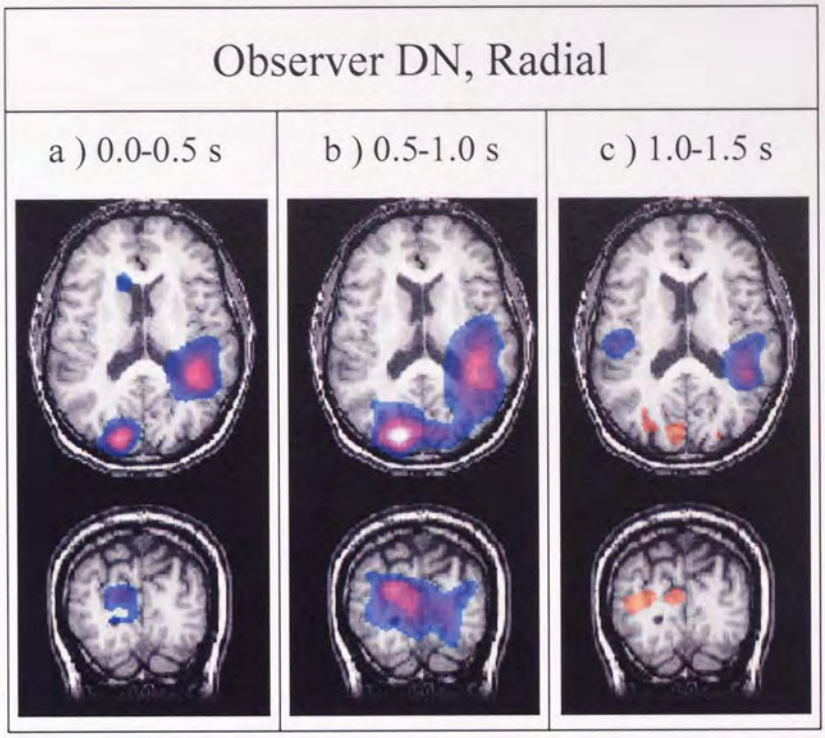

Figure 4.8. SAM images for observer DN showing comparison of cortical 5-40 Hz power 0.5-0.0 s pre-presentation compared with a) 0.0-0.5 s, b) 0.5-1.0 s and c) 1.0-1.5 s post-presentation of radial Glass patterns to the right eye. Images are shown on an anatomical MRI of observer DN with the same colour scale as Figure 4.2. Coronal and axial slices are shown dissecting the voxel of maximal 5-40 Hz (1 s time window) power change in response to radial patterns (i.e. left cuneus, MNI: -23, -79, 18).

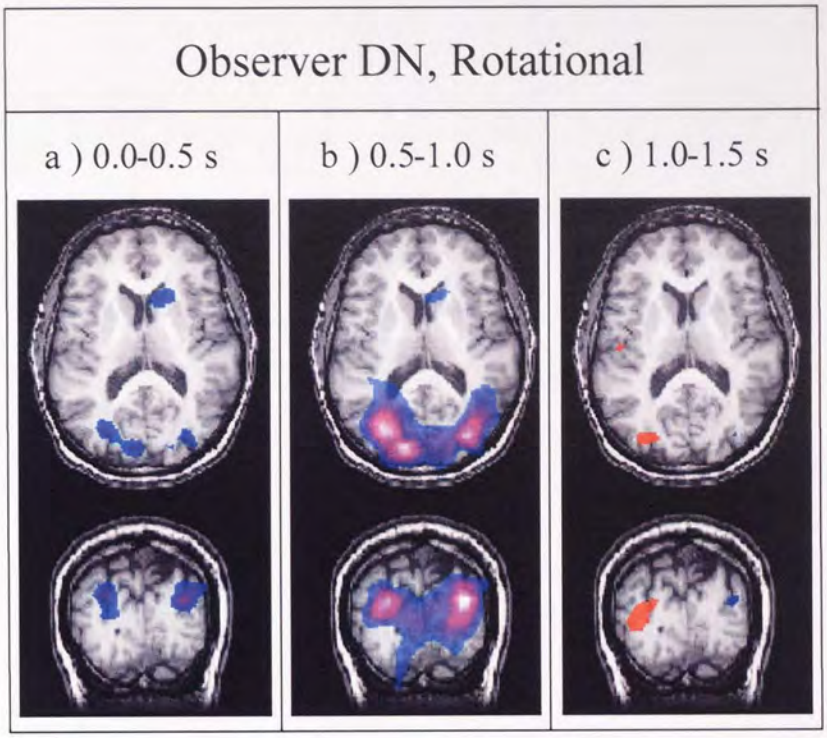

Figure 4.9. SAM images for observer DN showing comparison of cortical 5-40 Hz power 0.5-0.0 s pre-presentation compared with a) 0.0-0.5 s, b) 0.5-1.0 s and c) 1.0-1.5 s post-presentation of rotational Glass patterns to the right eye. Images are shown on an anatomical MRI of observer DN with the same colour scale as Figure 4.2. Coronal and axial slices are shown dissecting the voxel of maximal 5-40 Hz (1 s time window) power change in response to rotational patterns (i.e. right cuneus, MNI: 22, -82, 14).

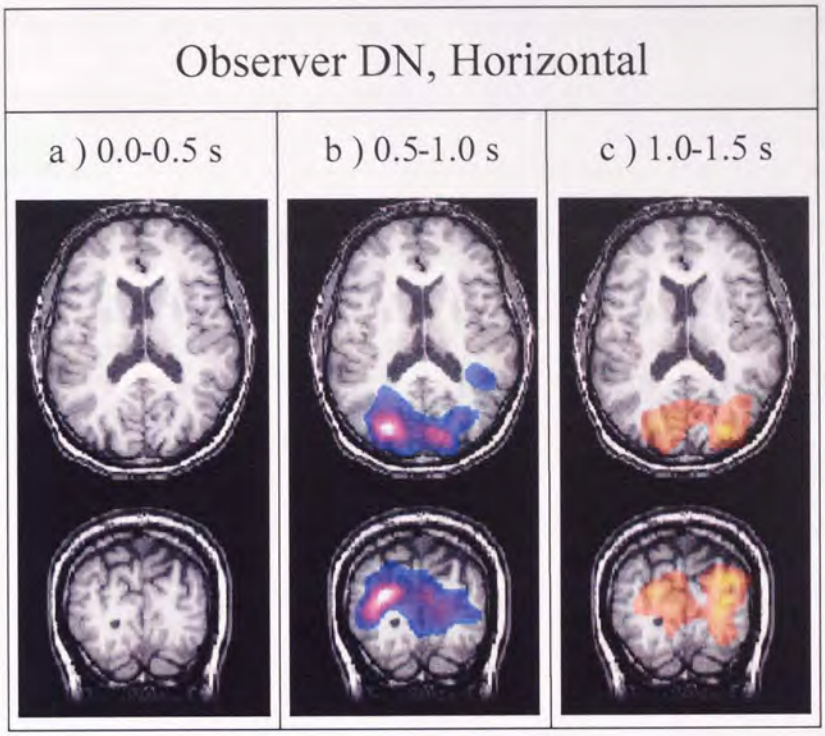

Figure 4.10. SAM images for observer DN showing comparison of cortical 5-40 Hz power 0.5-0.0 s pre-presentation compared with a) 0.0-0.5 s, b) 0.5-1.0 s and c) 1.0-1.5 s post-presentation of horizontal Glass patterns to the right eye. Images are shown on an anatomical MRI of observer DN with the same colour scale as Figure 4.2. Coronal and axial slices are shown dissecting the voxel of maximal 5-40 Hz (1 s time window) power change in response to horizontal patterns (i.e. left cuneus, MNI: -23, -79, 18).

4.3.1.2 Time-frequency plots

Figure 4.11 shows time-frequency plots for observer DN, calculated for voxels of maximal 5-40 Hz (1 s time window) power change in response to a) radial, b) rotational and c) horizontal Glass patterns. These voxels were all in the cuneus of extrastriate cortex, as delineated by the crosshairs in Figure 4.2. The most prominent power change for each pattern type was a reduction in oscillatory power within the beta frequency band (12 - 30 Hz). For radial and rotational Glass patterns this power reduction began approximately 350 ms post-stimulus onset. For horizontal Glass patterns the reduction

began after approximately 500 ms. With all pattern types the reduced oscillatory power was observed until approximately 800 ms after stimulus onset. The reduction in beta frequency activity was followed by an increase in oscillatory power within the beta frequency band between 1000 and 1500 ms post-stimulus onset.

Time-frequency plots for observer EN are shown in Figure 4.12. The voxels analysed showed maximal 5-40 Hz (1 s time window) power changes and were in extrastriate cortex as illustrated in Figure 4.3. Again, the principal power change for each pattern type was a reduction in oscillatory power. With a) radial and b) rotational patterns the associated power decreases occurred over the whole 5-40 Hz frequency range and between approximately 500 ms and 1300 ms post-stimulus onset. Note that power reductions were more pronounced following presentation of radial and rotational patterns than following horizontal patterns. With c) horizontal patterns the power reduction was confined to approximately 500-1000 ms post-stimulus onset and an approximately 20-40 Hz frequency band. No late onset increase in beta activity was observed following radial, rotational or horizontal Glass patterns, this is in contrast to the results for observer DN (see Figure 4.11).

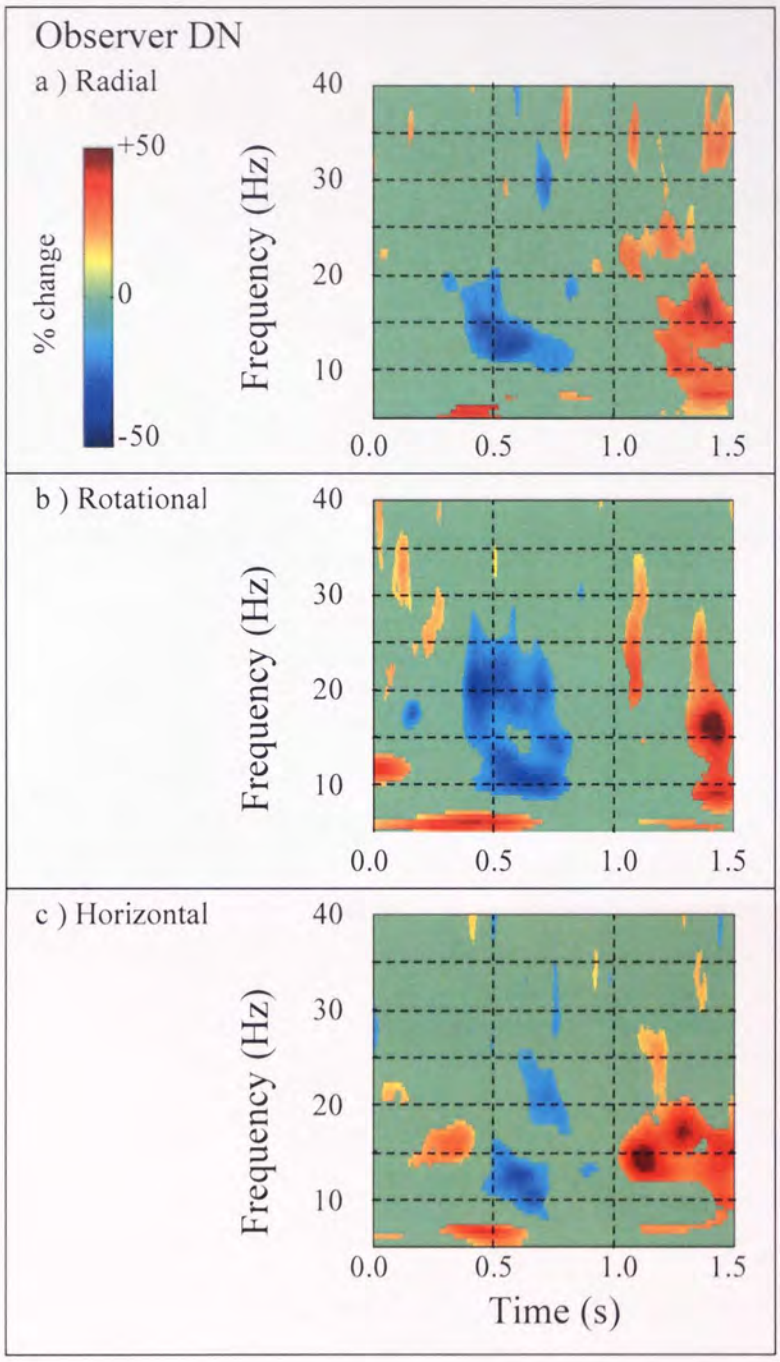

Figure 4.11. Time-frequency wavelet plots representing frequencies from 5-40 Hz over the time scale zero (stimulus onset) to 1.5 s. Plots were computed for peak voxels as determined from SAM analyses of 5-40 Hz, 1 s time window, data for each Glass pattern type with observer DN, right eye viewing (all in extrastriate cortex, see Figure 4.2). Compared with pre-stimulus activity, significant power reductions and increases are shown as blue and red colours respectively, non-significant ($p > 0.05$) changes in power were set to zero (green). See "% power change" key.

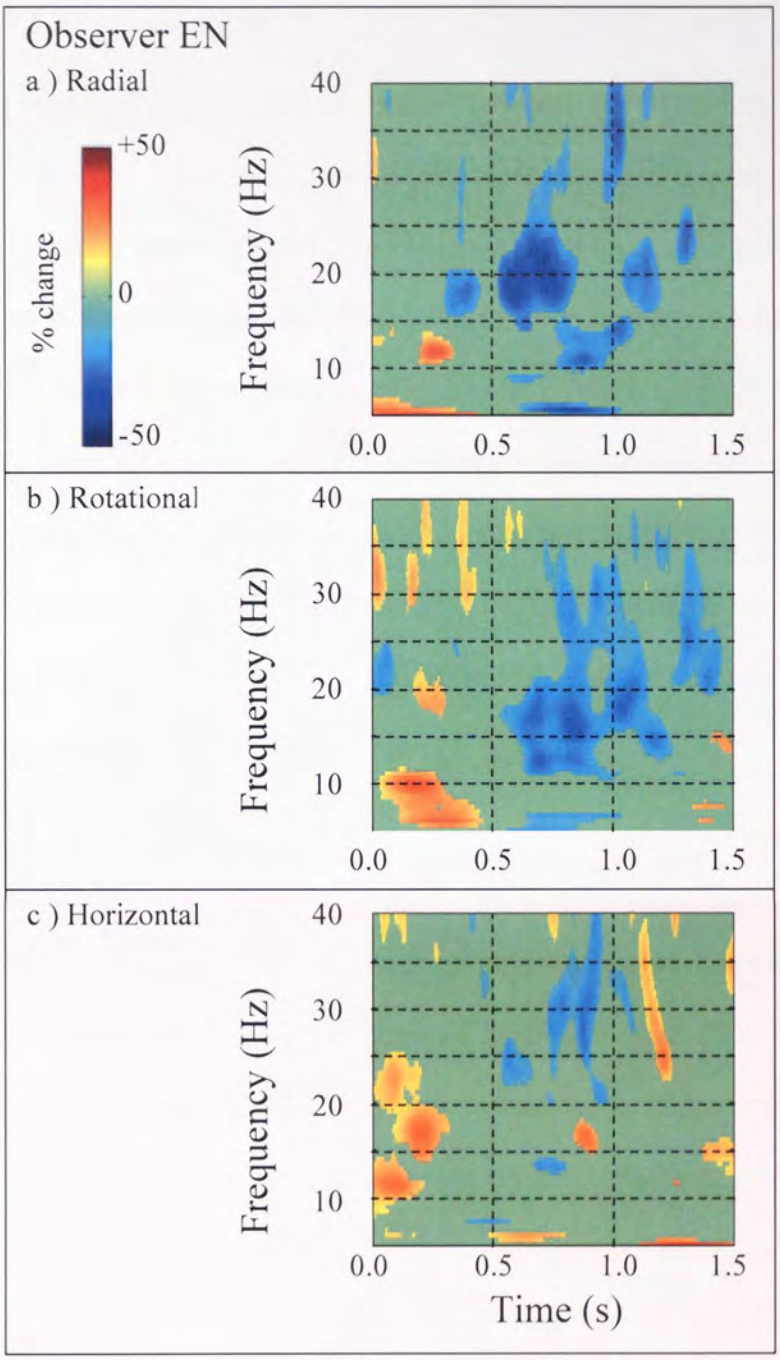

Figure 4.12. Time-frequency wavelet plots computed as in Figure 4.11 but for peak voxels for observer EN with right eye viewing (all in extrastriate cortex, see Figure 4.3).

4.3.2 Group data

Using SnPM, probability maps for voxel-level ($p < 0.05$) and cluster-level (primary threshold 3.5, $p < 0.05$) group effects were computed for cortical power within several frequency bands between 5 and 40 Hz. The group data, displayed in Figures 4.15-4.25, provide evidence that the perception of form resulted primarily in reductions in cortical power. Only the presentation of horizontal Glass patterns elicited an increase in cortical power (5-15 Hz, Figure 4.17), as revealed using cluster-level analysis. The locations of significant group effects, as determined using the Talairach Daemon database (Lancaster *et al.*, 2000), were mostly in extrastriate cortex. However, group effects were also found in the cerebellum and frontal lobe. MNI coordinates for all group effects are reported in the caption of the relevant figure.

Figure 4.13 shows the total cortical volume activated at the cluster-level for left and right eye viewing of each Glass pattern type. The overall volume of activated cortex was similar following presentation of coherent form to either the left or right eye. Note also that rotational Glass patterns activated a larger neural volume than both radial and horizontal patterns, and that viewing horizontal Glass patterns activated a larger neural volume than radial patterns. Inspection of the group data (Figures 4.15-4.25) shows that the hemisphere in which activity was present was not dependent on which eye was used for viewing.

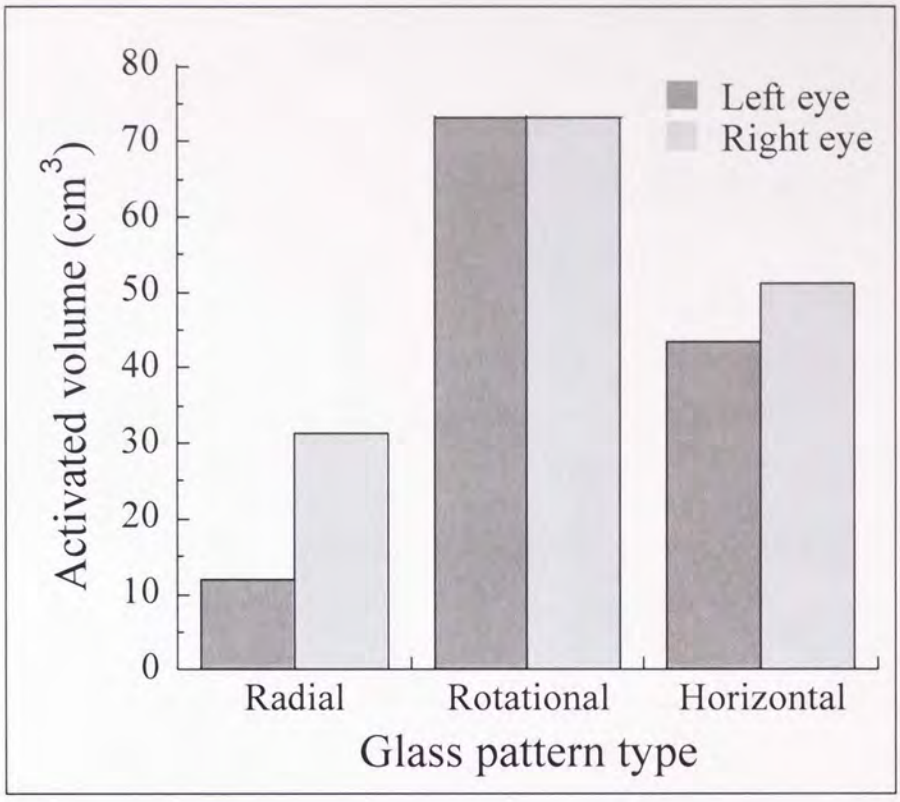

Figure 4.13. Neural volumes activated for the group (n = 8) at the cluster-level (primary threshold 3.5, $p < 0.05$) have been summed for all 10 Hz frequency bands analysed (5-15, 10-20, 15-25, 20-30, 25-35, and 30-40 Hz) when cortical power 1 s pre- was compared with power 1 s post-stimulus. Cumulated volumes are shown for radial, rotational and horizontal Glass patterns and for each viewing eye.

Figure 4.14 shows the neural volumes activated at the cluster-level within each frequency band and for each Glass pattern type. Each bar represents the summed volumes of the left and right eye viewing conditions. The largest volumes of cluster-level activation occurred between 10 and 25 Hz. Figure 4.14 also shows that viewing radial Glass patterns only produced significant activation clusters in the frequency bands 10-20 and 25-35 Hz. A more detailed examination of activation within each frequency band is presented below.

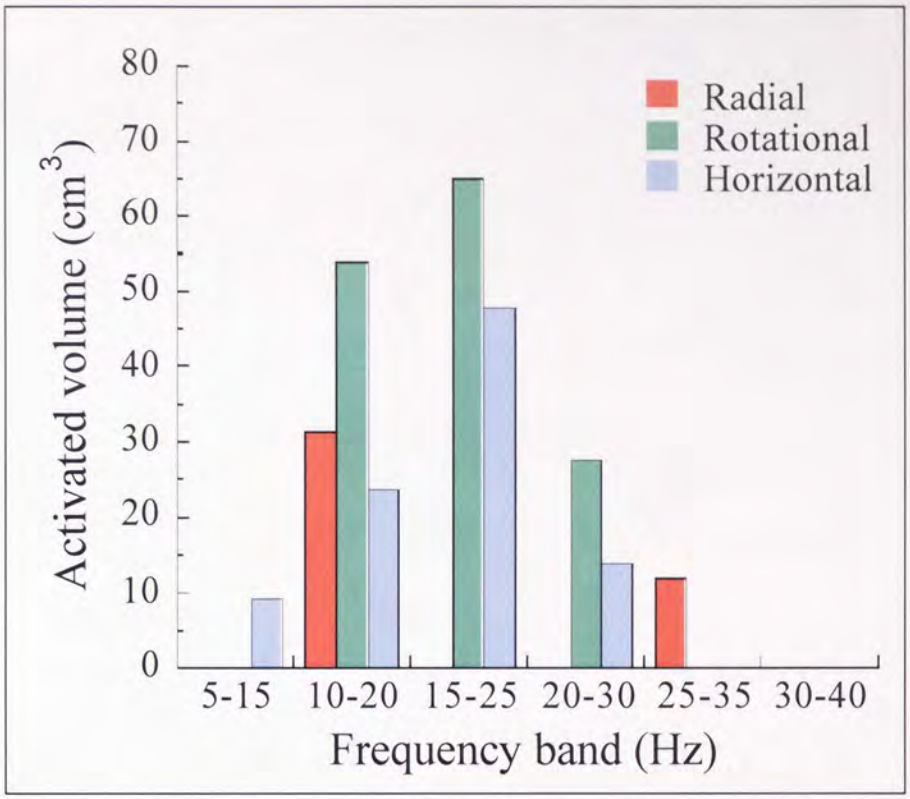

Figure 4.14. Neural volumes activated for the group (n = 8) at the cluster-level (primary threshold 3.5, $p < 0.05$) when cortical power 1 s pre- was compared with power 1 s post-stimulus have been summed across the eye-viewing condition. Cumulated volumes are shown for radial, rotational and horizontal Glass patterns at each 10 Hz frequency band analysed (5-15, 10-20, 15-25, 20-30, 25-35, and 30-40 Hz).

4.3.2.1 5-40 Hz frequency band

Figure 4.15 (a) shows the SnPM voxel-level results for passive viewing of radial Glass patterns revealed by a pre-post stimulus comparison over 1 s in the 5-40 Hz frequency band. Voxels with significantly reduced power ($p < 0.05$) were found within the posterior lobe of the cerebellum. Figure 4.15 (b) shows the same comparison at the cluster-level. In addition to the cerebellar activity (Figure 4.15 (b.2)), a significantly large (primary threshold 3.5, $p < 0.05$) region of reduced power was revealed that spanned areas of extrastriate cortex (Figure 4.15 (b.1)).

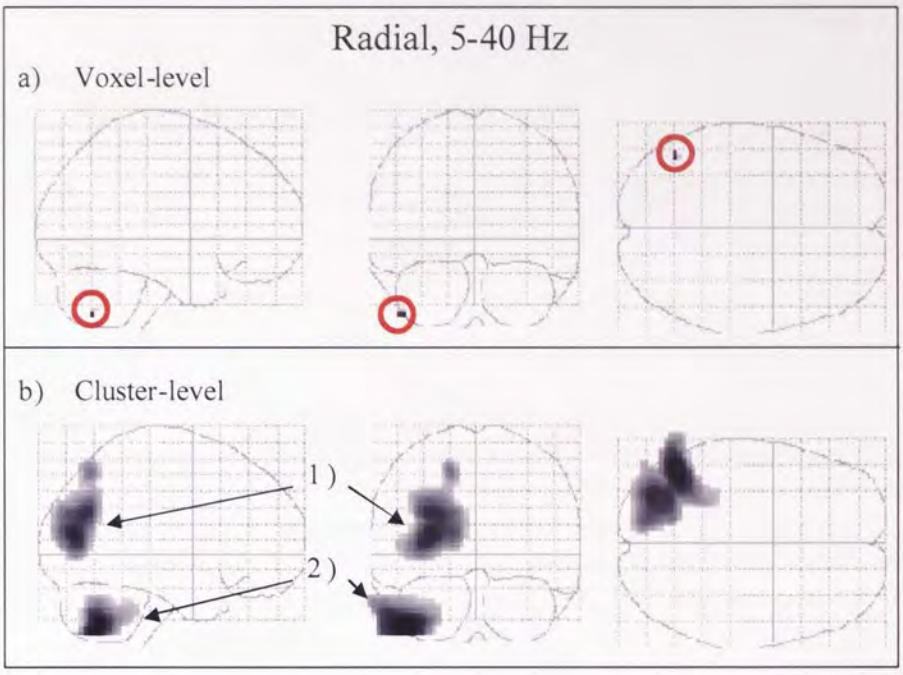

Figure 4.15. Group SnPM (n = 8) results for comparison of 5-40 Hz cortical power 1 s pre- with 1 s post-presentation of radial Glass patterns to the right eye. Activated regions are shown darkened on an outline of the template brain and indicate reductions in power. a) Voxel-level analysis revealed a volume (0.11 cm^3) within the left inferior semi lunar lobule (MNI: -45, -63, -48) that had significantly ($p < 0.05$) reduced power. This region is circled in red for clarity. b) Cluster-level (primary threshold 3.5) analysis 1) revealed a significantly large (33.97 cm^3, $p < 0.05$) region in the left hemisphere that spanned areas of the middle temporal gyrus (MNI: -30, -78, 15) and the precuneus (MNI: -15, -66, 51) and 2) identified a cluster of voxels (21.03 cm^3, n.s.) that contained some voxels significant at the voxel-level (left inferior semi lunar lobule, MNI: -45, -63, -48).

Figure 4.16 shows cluster-level results for rotational Glass patterns. This analysis revealed a left hemispheric region of reduced power that included areas of extrastriate cortex and the cerebellum. There were no areas significant at the voxel-level in response to the presentation of rotational patterns.

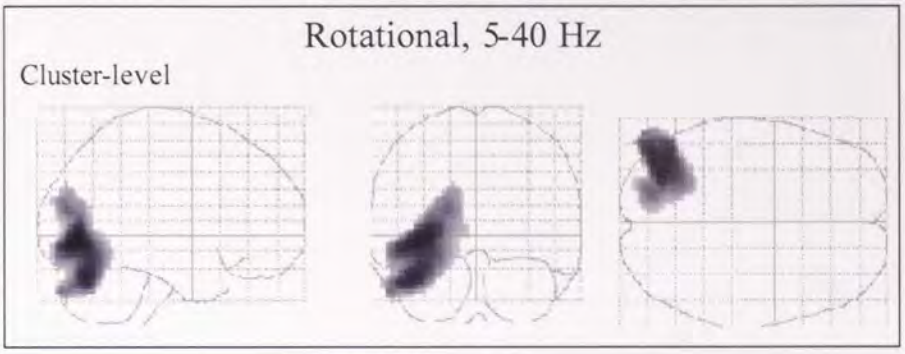

Figure 4.16. Group SnPM (n = 8) results for cluster-level (primary threshold 3.5) comparison of 5-40 Hz cortical power 1 s pre- with 1 s post-presentation of rotational Glass patterns to the right eye. Activated regions are shown darkened on an outline of the template brain. A significantly large (44.63 cm^3, $p < 0.05$) region of reduced power was identified in the left hemisphere that spanned areas of the middle occipital gyrus (MNI: -36, -75, -3), the declive (MNI: -42, -69, -27) and the cuneus (MNI: -18, -81, 18).

Passive viewing of horizontal Glass patterns did not elicit a significant neural response (1 s pre-post stimulus comparison, 5-40 Hz frequency band) at either the voxel- or the cluster-level.

4.3.2.2 5-15 Hz frequency band

SnPM comparison of 1 s pre- with 1 s post-stimulus neural activity within the 5-15 Hz frequency band failed to identify any significant power changes in response to radial or rotational Glass patterns at either the voxel- or the cluster-level, or to horizontal Glass patterns at the voxel-level. However, as shown in Figure 4.17, a significantly large (primary threshold 3.5, $p < 0.05$) cluster was found in the right inferior frontal gyrus following presentation of horizontal Glass patterns. This cluster was the only significant region of activation found with analyses of the group data that represented an increase in cortical power compared with the pre-stimulus power.

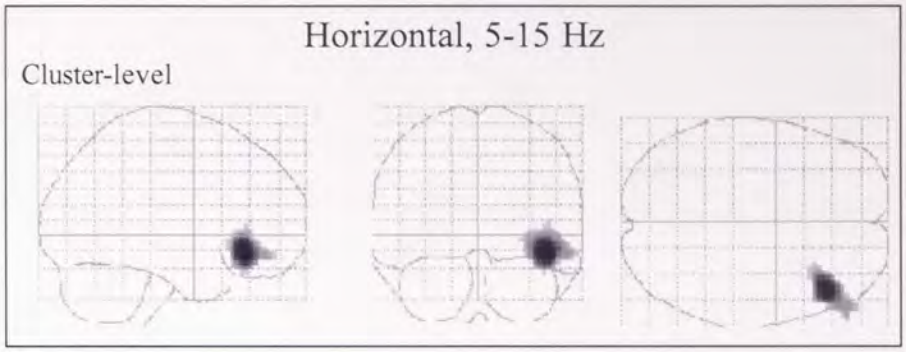

Figure 4.17. Group SnPM (n = 8) results for cluster-level (primary threshold 3.5) comparison of 5-15 Hz cortical power 1 s pre- with 1 s post-presentation of horizontal Glass patterns to the right eye. Activated regions are shown darkened on an outline of the template brain. A significantly large (9.29 cm^3, $p < 0.05$) region of increased power was identified in the right frontal lobe that included BA 47 (MNI: -36, -75, -3) and the inferior frontal gyrus (MNI: 54, 45, -12).

4.3.2.3 10-20 Hz frequency band

Figure 4.18 shows a left hemispheric region of reduced 10-20 Hz power identified by SnPM cluster-level analysis for viewing of radial Glass patterns. This cluster included areas of extrastriate cortex and the cerebellum. The same comparison at the voxel-level did not identify any significant power changes. Following presentation of rotational Glass patterns, there were significant 10-20 Hz power reductions in extrastriate cortex at the voxel-level (Figure 4.19 (a)) and the cluster-level (Figure 4.19 (b-c)). Horizontal patterns elicited significant voxel- and cluster-level power reductions in the cerebellum (Figure 4.20 (a-b)) and extrastriate cortex (Figure 4.20 (c-d)).

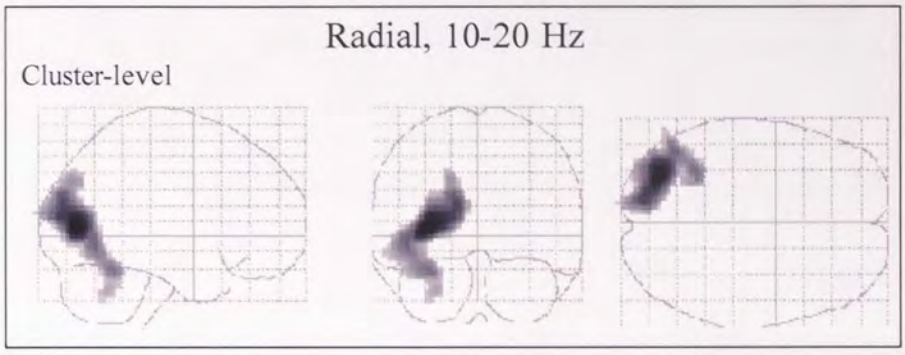

Figure 4.18. Group SnPM (n = 8) results for cluster-level (primary threshold 3.5) comparison of 10-20 Hz cortical power 1 s pre- with 1 s post-presentation of radial Glass patterns to the right eye. Activated regions are shown darkened on an outline of the template brain. A significantly large (31.29 cm^3, $p < 0.05$) region of reduced power was identified in the left hemisphere that spanned areas of the middle occipital gyrus (MNI: -30, -75, 9), the inferior temporal gyrus (MNI: -45, -63, -6) and the culmen (MNI: -33, -51, -21).

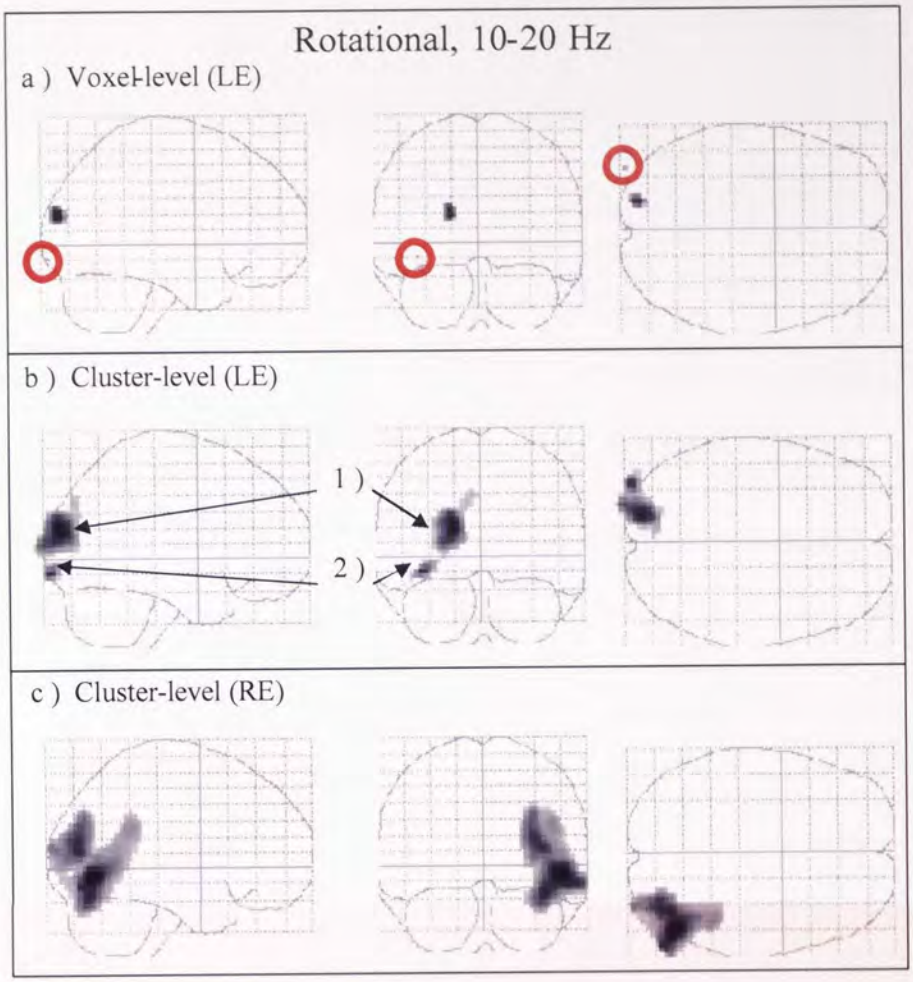

Figure 4.19. Group SnPM (n = 8) results for comparison of 10-20 Hz cortical power 1 s pre- with 1 s post-presentation of rotational Glass patterns. Activated regions are shown darkened on an outline of the template brain. a) Voxel-level analysis (for left eye viewing) revealed a volume within BA 18 of the cuneus (0.86 cm^3; MNI: -18, -87, 18) and a smaller volume within BA 18 of the inferior occipital gyrus (0.03 cm^3; MNI: -39, -96, -9; circled in red) that both had significantly ($p < 0.05$) reduced power. Cluster-level analysis (primary threshold 3.5) identified reduced power b) for left eye viewing in 1) a significantly large (10.80 cm^3, $p < 0.05$) region that spanned BA 18 of the cuneus (MNI: -18, -87, 18), BA 19 of the middle occipital gyrus (MNI: -24, -87, 18) and BA 19 of the cuneus (MNI: -9, -81, 36); and 2) a cluster (1.46 cm^3, n.s.) that contained some voxels significant at the voxel-level (BA 18, inferior occipital gyrus, MNI: -39, -96, -9); c) for right eye viewing in a significantly large (41.69 cm^3, $p < 0.05$) right hemispheric region that spanned the inferior temporal gyrus (MNI: 48, -69, -6) and the middle occipital gyrus (MNI: 39, -72, -15; 33, -81, 15).

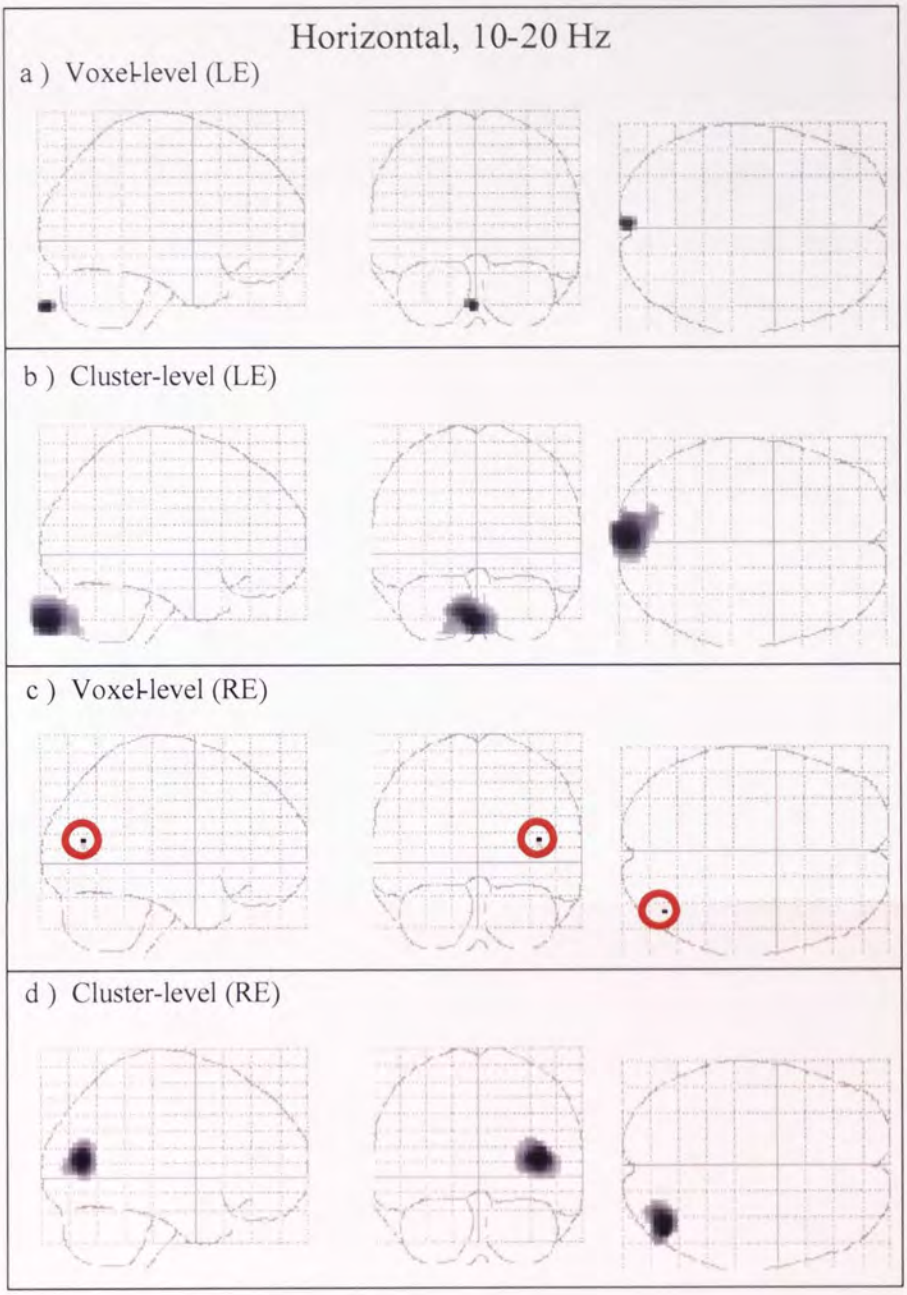

Figure 4.20. Group SnPM (n = 8) results for comparison of 10-20 Hz cortical power 1 s pre- with 1 s post-presentation of horizontal Glass patterns. Activated regions are shown darkened on an outline of the template brain. Regions of significantly reduced power were found for left eye viewing with a) voxel-level analysis (0.73 cm^3; close to the pyramis, MNI: -3, -93, -42) and b) cluster-level analysis (primary threshold 3.5; 14.99 cm^3, $p < 0.05$; close to the pyramis, MNI: -3, -93, -42). Right eye viewing elicited significantly reduced power with c) voxel-level analysis (0.05 cm^3; middle temporal gyrus, MNI: 39, -72, 15; circled in red) and d) cluster-level analysis (primary threshold 3.5; 8.67 cm^3, n.s.; middle temporal gyrus, MNI: 39, -72, 15).

4.3.2.4 15-25 Hz frequency band

SnPM analyses found no significant changes in 15-25 Hz cortical power following viewing of radial Glass patterns. However, significant regions of reduced power in BA 18 and BA 19 of extrastriate cortex were revealed at the voxel- and cluster-level in response to rotational (Figure 4.21) and horizontal (Figure 4.22) patterns.

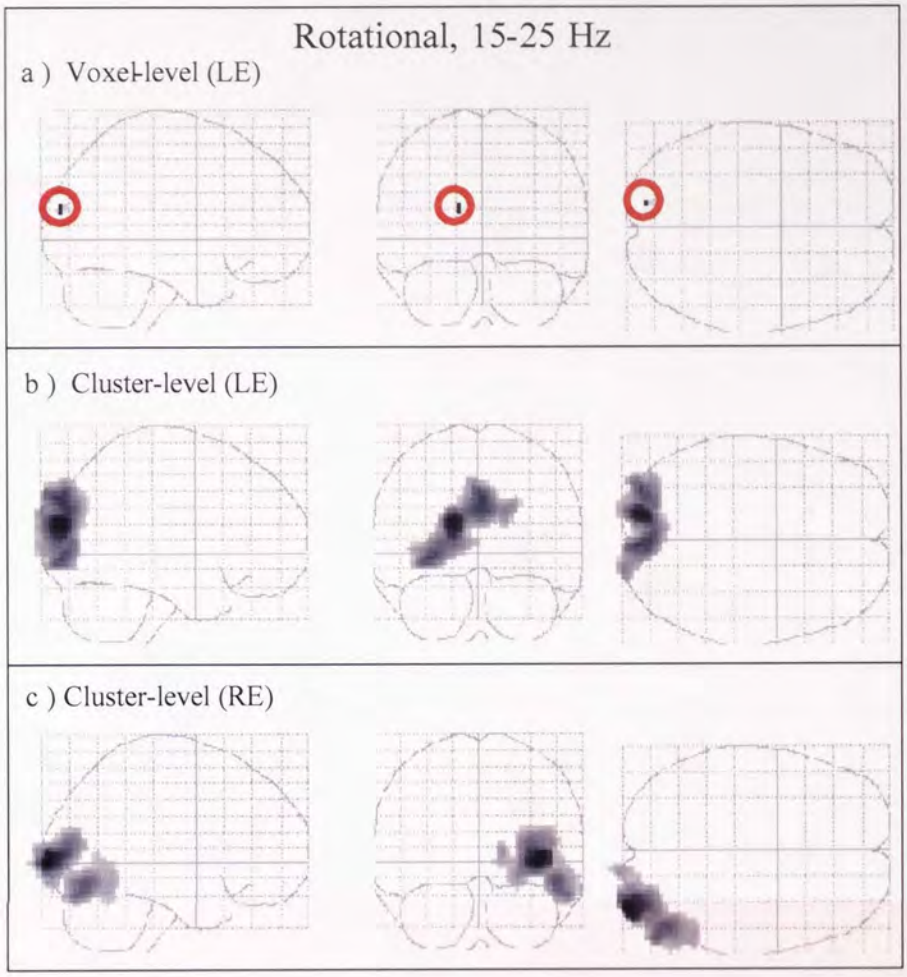

Figure 4.21. Group SnPM (n = 8) results for comparison of 15-25 Hz cortical power 1 s pre- with 1 s post-presentation of rotational Glass patterns. Activated regions are shown darkened on an outline of the template brain. Regions of reduced power were found for left eye viewing with a) voxel-level analysis within BA 18 of the cuneus ($p < 0.05$; 0.08 cm^3; MNI: -15, -87, 21; circled in red) and with b) cluster-level analysis (primary threshold 3.5) spanning BA 18 (MNI: -15, -87, 21) and BA 19 (MNI: 3, -87, 36) of the cuneus (33.43 cm^3, $p < 0.05$). c) Right eye viewing elicited reduced power with cluster-level analysis (primary threshold 3.5, 31.54 cm^3, $p < 0.05$) in areas close to the middle occipital gyrus (MNI: 39, -96, 3) and the fusiform gyrus (MNI: 57, -78, -21) and in BA 19 of the middle occipital gyrus (MNI: 51, -69, -12).

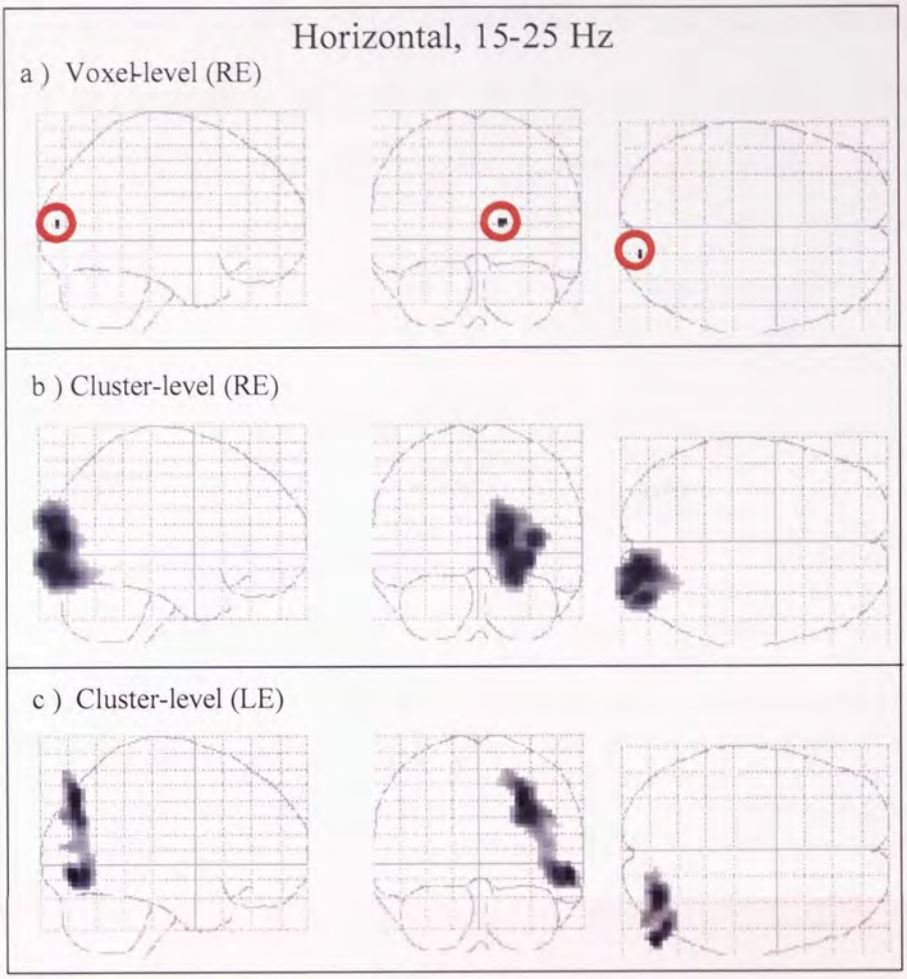

Figure 4.22. Group SnPM (n = 8) results for comparison of 15-25 Hz cortical power 1 s pre- with 1 s post-presentation of horizontal Glass patterns. Activated regions are shown darkened on an out line of the template brain. Regions of reduced power were found for right eye viewing with a) voxel-level analysis within BA 18 of the cuneus ($p < 0.05$; 0.11 cm^3; MNI: 15, -87, 12; circled in red) and with b) cluster-level analysis (primary threshold 3.5) spanning BA 18 (MNI: 15, -87, 12) and BA 19 (MNI: 18, -93, 21) of the cuneus and the lingual gyrus (MNI: 21, -87, -9; 33.16 cm^3, $p < 0.05$). c) Left eye viewing elicited reduced power with cluster-level analysis (primary threshold 3.5, 14.50 cm^3, $p < 0.05$) in areas of the precuneus (MNI: 33, -75, 33) including BA 19 (MNI: 27, -78, 42) and close to the inferior occipital gyrus (MNI: 57, -78, -6).

4.3.2.5 20-30 Hz frequency band

There were no regions of significant 20-30 Hz power change in response to radial, rotational or horizontal Glass patterns at the voxel-level. Cluster-level analyses also

failed to reveal any areas of activity in response to radial patterns, however, areas of reduced power were found in extrastriate cortex and the cerebellum following rotational (Figure 4.23) and horizontal (Figure 4.24) patterns respectively.

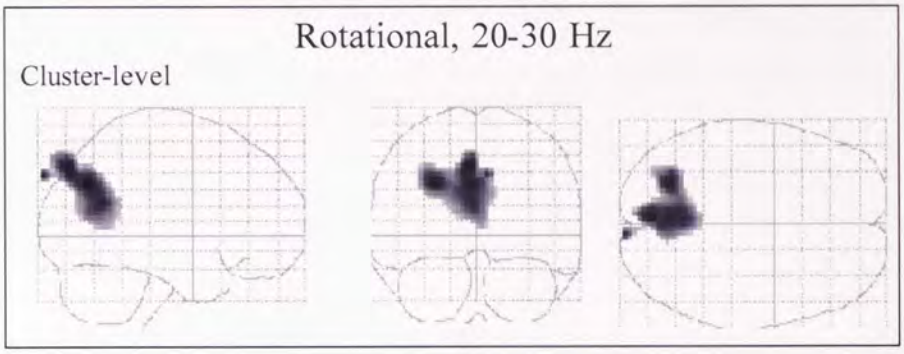

Figure 4.23. Group SnPM (n = 8) results for cluster-level (primary threshold 3.5) comparison of 20-30 Hz cortical power 1 s pre- with 1 s post-presentation of rotational Glass patterns to the left eye. Activated regions are shown darkened on an outline of the template brain. A significantly large (27.59 cm^3, $p < 0.05$) region of reduced power was identified that spanned areas of the precuneus (MNI: -27, -69, 33; -3, -69, 33), including BA 7 (MNI: -6, -81, 45).

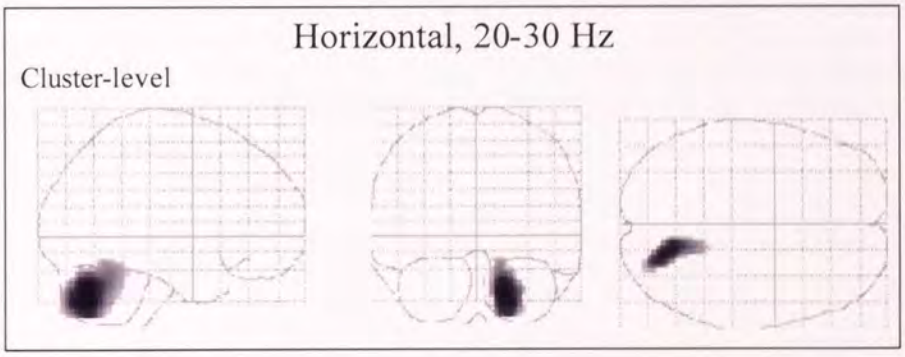

Figure 4.24. Group SnPM (n = 8) results for cluster-level (primary threshold 3.5) comparison of 20-30 Hz cortical power 1 s pre- with 1 s post-presentation of horizontal Glass patterns to the left eye. Activated regions are shown darkened on an outline of the template brain. A significantly large (13.99 cm^3, $p < 0.05$) right hemispheric region of reduced power was identified in the pyramis of the cerebellum (MNI: 15, -66, -36).

4.3.2.6 25-35 Hz frequency band

Only presentation of radial patterns elicited significant 25-35 Hz power changes at the voxel- (Figure 4.25 (a)) or cluster-level (Figure 4.25 (b)). This region of reduced power was in the medial frontal gyrus of the left hemispheric frontal lobe.

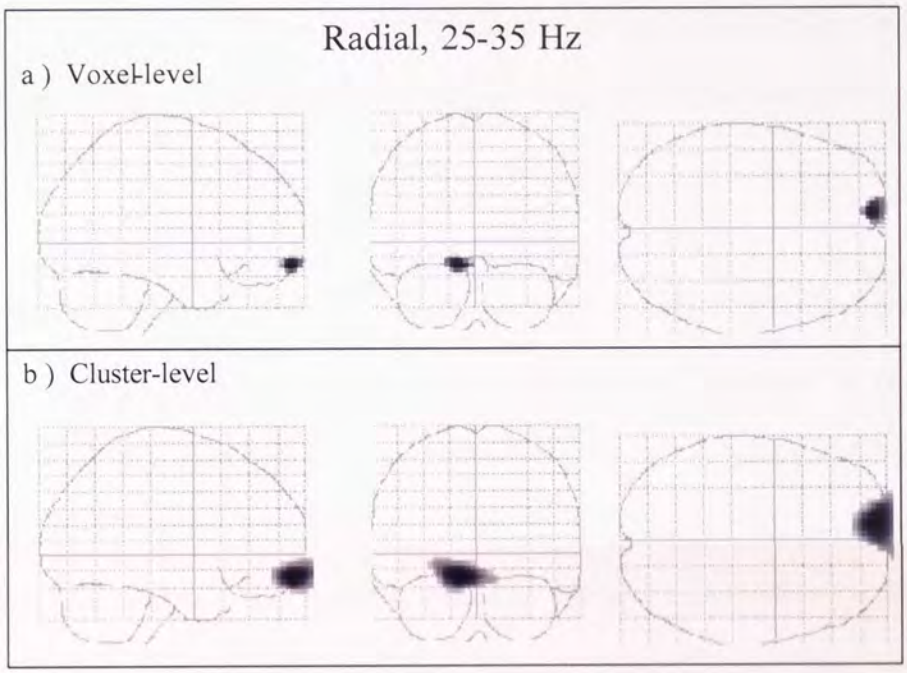

Figure 4.25. Group SnPM (n = 8) results for comparison of 25-35 Hz cortical power 1 s pre- with 1 s post-presentation of radial Glass patterns. Activated regions are shown darkened on an outline of the template brain. A region of reduced power that was centred on BA 11 of the medial frontal gyrus (MNI: -12, 63, -15) was identified for left eye viewing with a) voxel-level analysis ($p < 0.05$; 1.67 cm^3) and b) cluster-level analysis (primary threshold 3.5; 11.99 cm^3, $p < 0.05$).

4.3.2.7 30-40 Hz frequency band

No changes in 30-40 Hz cortical power were found with SnPM analyses at the voxel- or cluster-level in response to radial, rotational or horizontal Glass patterns.

4.4 Discussion

The most prominent change in neural activity following the presentation of coherent form was a bilateral reduction in oscillatory power within regions of extrastriate cortex. Power changes within the 5-40 Hz frequency band were evident in the middle occipital gyrus, cuneus, inferior temporal and occipital gyri and fusiform and lingual gyri. The spatial locations of these oscillatory changes are similar to those previously identified using fMRI as being involved in the processing of coherent form or motion (Braddick *et al.*, 2000).

Regions of reduced oscillatory power revealed by analyses of individual data were primarily located in regions that have previously been labelled as V3 and V3a (Hasnain *et al.*, 1998). Area V3a in human (but not macaque) is thought to be relatively selective for motion stimuli (Braddick *et al.*, 2001; Tootell *et al.*, 1997), and indeed Braddick *et al.* (2000) found that V3a was activated by coherent motion but not coherent form. However, Braddick *et al.* used static arrays of oriented lines as stimuli, whereas the Glass patterns used in the experiments reported here were dynamic (i.e. replotted every 10 ms). Such patterns are known to generate a powerful sensation of motion (Ross *et al.*, 2000), and consequently the V3a activity observed in this study may be an artefact elicited by this sensation. This is explored further in chapter 7 in which static stimuli are used.

Observed reductions in oscillatory power were mainly within the beta frequency band (Figures 4.5-4.7). This is comparable with reduced oscillatory power in the 5-25 Hz range observed using MEG when viewing biological motion inferred from 13 dots, a task that required global form processing (Singh *et al.*, 2003). These regions of reduced

oscillatory power were in the same location as regions of increased haemodynamic response as measured with fMRI (Singh *et al.*, 2002). An increased haemodynamic response is widely considered to correlate with increased neuronal activity and this led Singh *et al.* (2002) to suggest that reduced oscillatory power also indicates increased activity. In support of this, Pfurtscheller (2001) suggests that reduced power within brain rhythms of less than 30 Hz represents increased independence of neuronal assemblies and allows for maximal information processing. Following the reduction in beta frequency band power, an increase in beta band power was observed for observer DN in response to all pattern types. Power rebounds and increased oscillatory power may indicate a resetting of the neural system and a period of deactivation with little information processing (Pfurtscheller, 2001; Pfurtscheller, Neuper, Brunner, Lopes da Silva, 2005).

The magnitude of the oscillatory power reductions was less following horizontal than either radial or rotational Glass patterns (seen in SAM images and time-frequency plots). Additionally, time-frequency plots for observers DN and EN showed that the reduced power associated with horizontal Glass patterns occurred for less total duration than that associated with radial or rotational patterns. Accepting that a reduction in oscillatory power is indicative of neuronal activity, these results provide evidence that less information processing occurred following the presentation of horizontal patterns than either radial or rotational patterns.

There were several differences between individual and group results. These included: a) regions of activation in the cerebellum and frontal lobe were only evident in group analyses; b) group results showed mostly lateralised regions of activation whereas

individual data showed mostly bilateral power decreases; c) less volume of cortex found to be activated by radial than by rotational or horizontal patterns with group analyses, though similar volumes with each pattern type were found at the individual level. The underlying causes of these differences may be attributed not only to genuine inter-observer variability but also to 'spatial smoothness'. For each individual, the beamformer spatial resolution is heterogeneous across the brain, with regions with low neural current having low spatial resolution and vice versa (Barnes, Hillebrand, Fawcett, Singh, 2004). Consequently, areas such as the cerebellum and frontal lobe which have small pseudo t values will be spatially smoother and therefore more spatially consistent across observers following normalisation (section 2.1) than areas that have high pseudo t values. In contrast, peak areas of activation have higher spatial resolution and so are less likely to be spatially consistent across observers. This variability may result in the areas not being identified with SnPM and may explain the predominance of lateralised areas of activation in the group data (Singh *et al.*, 2003). This explanation may also serve for the smaller neural volume activated by radial Glass patterns (Figure 4.13). These patterns produced high pseudo t values and this may have resulted in spatial inconsistency across the group and a reduction in the volume as determined with SnPM.

The LOC is a region in the fusiform gyrus that includes lateral areas of the occipital lobe and posterior areas of the temporal lobe (Grill-Spector *et al.*, 2001). It has been functionally defined as responding more strongly to pictures of objects than to pictures of scrambled objects. Based on this, it was expected to be activated more by Glass patterns with global form than by Glass patterns without global form. Whilst reduced oscillatory power in this area was observed (e.g. Figure 4.21), it was not the main locus of activation. This may be because Glass patterns are textures that have global form but

do not create a defined object (Grill-Spector, Kushnir, Edelman, Itzchak, Malach, 1998).

In agreement with Braddick *et al.* (2000), V1 was not identified as a peak region of activation in response to coherent form. This is consistent with V1 processing local but not global structure. Alternatively, it is possible that the absence of observed activity in V1 is due to self-cancelling magnetic fields due to the cruciform structure of this area. This possibility is explored in the next chapter.

5 MEG: The neural response to global form in Glass patterns viewed off-centre

5.1 Introduction

In the previous chapter it was reported that passive viewing of global form produced decreases in cortical oscillatory power (5-40 Hz) in extrastriate but not striate cortex. While this is in agreement with the findings of Braddick *et al.* (2000) who used fMRI to study global form produced with concentrically oriented lines, it appears inconsistent with fMRI studies that have shown responses in V1 to global form defined by Gabor patches (Altmann *et al.*, 2003; Kourtzi & Huberle, 2005; Kourtzi *et al.*, 2003). Possible reasons for an absence of activity in V1 following the presentation of coherent Glass patterns include:

1) V1 does not process global form.

V1 has generally been considered the first stage in a hierarchical system of brain areas that process increasingly complex elements of visual scenes. Although recent reports question whether current models of V1 visual processing are over-simplistic (reviewed in Olshausen & Field, 2005; and Bair, 2005), it is still accepted that V1 neurons are excited by low level image features and have smaller receptive fields than other visual areas. The fMRI experiment by Braddick *et al.* (2000) compared activity to concentrically oriented lines with activity to randomly oriented lines, as such the baseline and stimulus period both contained the same local cues. They did not find activity in V1 and reasoned that V1 does not process global form though it may be processing the local cues.

2) V1 does not produce observable magnetic fields to centrally viewed stimuli.

V1 occupies a relatively large area of visual cortex lying along the calcarine sulcus and divided by the inter-hemispheric fissure. This results in a structure with four quadrants of cortex. Figure 5.1 shows high-resolution structural magnetic resonance images of V1 that illustrate its three dimensional structure. The magnetic signal recorded with MEG is thought to originate mainly from post-synaptic potentials on pyramidal cells (see section 2.2.1). Pyramidal neurons run perpendicular to the cortex and consequently each quadrant of V1 has pyramidal cells aligned in opposition to those of the opposite quadrant. Activation of geometrically opposed pyramidal cells results in electrical currents flowing in opposite directions (shown by black arrows, Figure 5.1 (d)) and the generation of self-cancelling magnetic fields. To limit cancellation effects, stimuli can be confined to one of the visual field quadrants. This approach has been used successfully to localise V1 with MEG with V1 as retinotopically mapped with fMRI to an accuracy of 3-5 mm (Moradi *et al.*, 2003).

In the previous chapter, Glass patterns were viewed centrally and this may have resulted in self-cancelling magnetic fields within V1. To determine whether the lack of V1 activity reported in chapter 4 reflected a true non-involvement of V1 in global form processing, two different experimental approaches were used. Firstly, the experiment was repeated with Glass patterns presented in a single, lower quadrant of the visual field. Stimuli were presented to the lower visual field because this region produces stronger neuromagnetic recordings than the upper visual field (Portin, Vanni, Virsu, Hari, 1999). This experiment is reported in this chapter. Secondly, an fMRI experiment was performed as this technique is not affected by cancelling of neuronal magnetic fields. This experiment is reported in chapter 9.

Figure 5.1. High resolution images showing a) the calcarine sulcus (red arrows) on a sagittal slice through the inter-hemispheric fissure; b) V1 on a slice perpendicular to the calcarine sulcus; c) V1 at greater magnification. The white arrows point to the stria of Gennari which produces the striated appearance of primary visual cortex; d) the same image as for c, annotated to show the four quadrants of V1 that receive input from 1) the lower-right, 2) the lower-left, 3) the upper-right and 4) the upper-left visual field. The black arrows indicate the direction of net electrical current generated within each quadrant. (Images are taken from Bridge *et al.*, 2005).

5.2 Methods

Methods were as described in section 4.2 except that stimuli were rotational Glass patterns composed of 38 dot pairs covering an area of 4.12 deg^2. The dot density was the same as that for the previous chapter. Glass patterns were presented in the lower-left visual field. The fixation dot was present throughout the recording session and was

positioned 0.5 deg. from the horizontal and vertical meridians. Two male observers (DN and FN, aged 47 and 48 years respectively) took part in this experiment. Stimuli were viewed monocularly with their right eyes. Data was compared with data collected for each observer in chapter 4 where Glass patterns were viewed centrally.

5.3 Results

Figure 5.2 shows SAM images for observer DN of statistical estimates of changes in power in the 10-20 Hz frequency band between the active and passive phases (1 s time window) in response to the presentation of coherent Glass patterns. The summed response to radial, rotational and horizontal pattern types is shown because the neural responses to each pattern type were located in the same regions. The 10-20 Hz frequency band gave the largest pseudo t statistics for observer DN. Figure 5.2 (a-d) shows the four main regions of power change in response to Glass patterns presented to the lower-left visual field. Figure 5.2 (e-h) shows the comparable peaks when Glass patterns were viewed centrally (data from the experiment in chapter 4). Only power reductions were evident (indicated by purple-white colours) and the pseudo t statistics for the peak voxel within each region were similar between viewing conditions. Figure 5.2 (a, b, e, f) shows peak voxels of activation in the cuneus of extrastriate cortex that are superior to V3a (Hasnain *et al.*, 1998). Figure 5.2 (c, d, g, h) shows peak voxels in the temporal lobe with the cross-hairs in Figure 5.2 (d, h) close to V5 (Hasnain *et al.*, 1998).

Figure 5.3 shows the results for observer FN for the 15-25 Hz frequency band. This frequency range gave the largest pseudo t statistics for observer FN. Again, the largest power changes were reductions and the pseudo t statistics for the peak voxel within each

region were similar between viewing conditions. Figure 5.3 (a, d, e) shows peaks in the temporal and occipital lobes that are close to V5 (Hasnain *et al.*, 1998). Figure 5.3 (b, c, f, g) shows peaks in the parietal lobe that are superior to retinotopically mapped visual areas (Hasnain *et al.*, 1998). The peak shown in Figure 5.3 (h) is in the cuneus between areas previously identified as V3a and V4 (Hasnain *et al.*, 1998). Similarly to observer DN, no power changes were evident in V1.

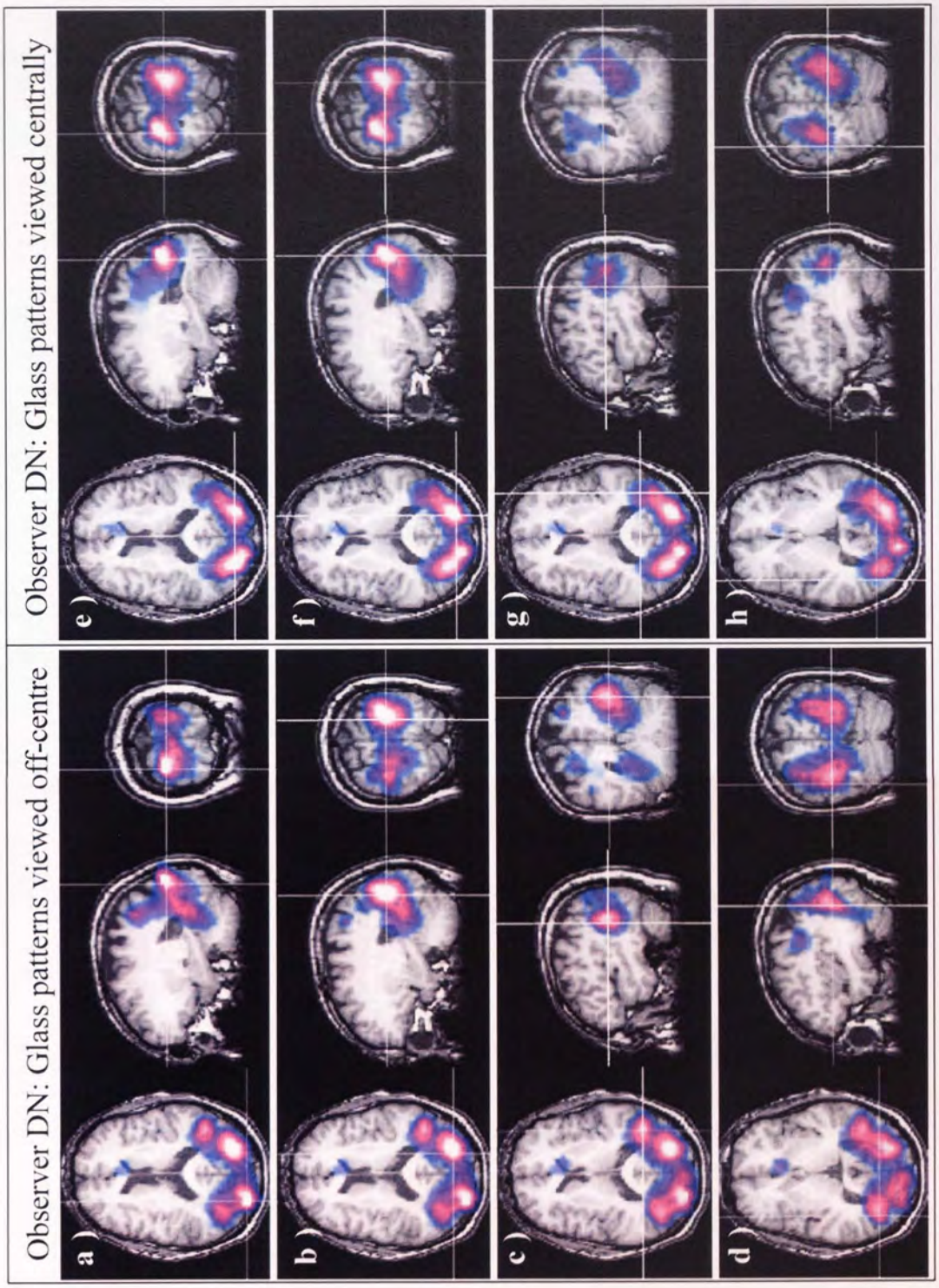

Figure 5.2. Legend on next page

Figure 5.2. SAM images of pseudo t-statistic estimates for observer DN for comparison of cortical power in the 10-20 Hz frequency band 1 s pre- with 1 s post-presentation of radial, rotational and horizontal Glass patterns. At each voxel, the magnitude of the pseudo t statistic is indicated by the colour overlay on an anatomical MRI image of observer DN. Voxels with a pseudo t statistic less than two are not coloured. Decreases in cortical power are shown by a blue-purple-white colour range (white voxels indicate pseudo t = 6). Following viewing of global form in the lower-left visual field, peak voxels of reduced power were identified in the a) left cuneus (MNI: -23, -90, 20; pseudo t = 8.6); b) right cuneus (MNI: 22, -79, 19; pseudo t = 8.2); c) right temporal lobe (MNI: 43, -53, 13; pseudo t = 5.8); and d) left temporal lobe (MNI: -38, -68, 8; pseudo t = 5.3). Viewing global form centrally produced similar power reductions in the e) left cuneus (MNI: -24, -80, 19; pseudo t = 8.4); f) right cuneus (MNI: 22, -82, 15; pseudo t = 7.9); g) right temporal lobe (MNI: 43, -53, 13; pseudo t = 3.1); and h) left temporal lobe (MNI: -38, -68, 8; pseudo t = 3.3).

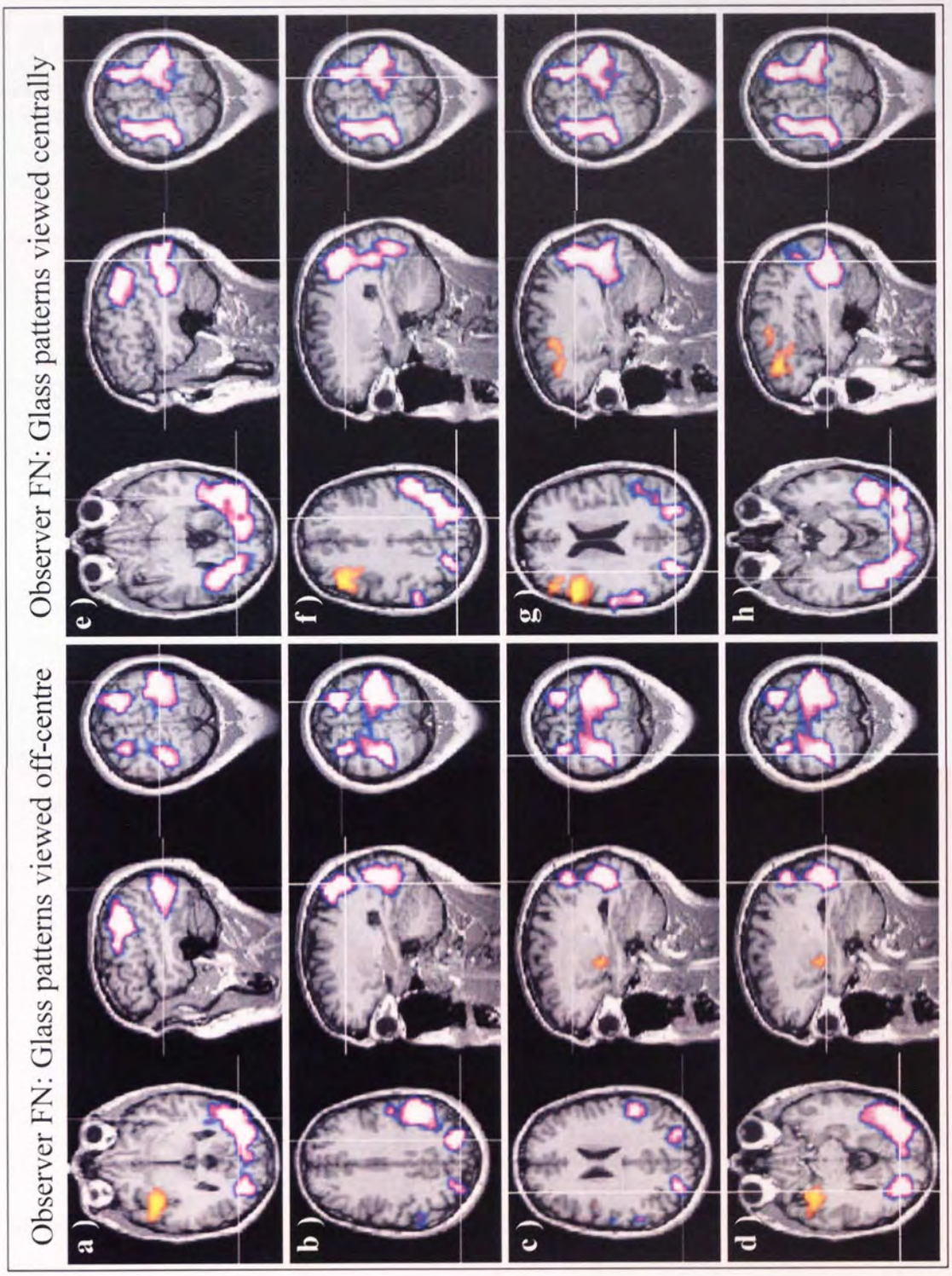

Figure 5.3. Legend on next page.

Figure 5.3. SAM images of pseudo t-statistic estimates for observer FN for comparison of cortical power in the 15-25 Hz frequency band 1 s pre- with 1 s post-presentation of radial, rotational and horizontal Glass patterns. At each voxel, the magnitude of the pseudo t statistic is indicated by the colour overlay on an anatomical MRI image of observer FN. Voxels with a pseudo t statistic less than two are not coloured. Decreases in cortical power are shown by a blue-purple-white colour range (white voxels indicate pseudo t = 2.5); increases are shown by a red-orange-yellow colour range. Following viewing of global form in the lower-left visual field, peak voxels of reduced power were identified in the a) right temporal lobe (MNI: 40, -75, 9; pseudo t = 4.4); b) right superior parietal lobule (MNI: 22, -68, 44; pseudo t = 4.4); c) left precuneus (MNI: -28, -71, 34; pseudo t = 3.4); and d) left middle occipital gyrus (MNI: -35, -74, 3; pseudo t = 3.2). Viewing global form centrally produced similar power reductions in the e) right middle temporal gyrus (MNI: 43, -74, 12; pseudo t = 6.8); f) right superior parietal lobule (MNI: 23, -70, 46; pseudo t = 5.6); g) left precuneus (MNI: -27, -74, 40; pseudo t = 3.5); and h) left cuneus (MNI: -27, -80, 8; pseudo t = 3.6).

Data for this experiment was collected approximately 10 months after the experiment for chapter 4 was conducted. The similar results for each experiment suggest that the neural response to global form is reproducible.

5.4 Discussion

The spatial distribution and magnitude of neural activity to the presentation of Glass patterns was similar when both centrally- and eccentrically-viewed. Importantly, activity within V1 was not evident when eccentrically-viewed. Therefore, it seems unlikely that the absence of V1 activity noted in chapter 4 when Glass patterns were centrally-viewed reflected self-cancelling magnetic fields.

This lack of V1 activity to the presentation of global form is consistent with a previous fMRI study of the neural response to concentrically- versus randomly-oriented lines (Braddick *et al.*, 2000). This study used fMRI and consequently the results would not have been affected by self-cancelling magnetic fields. Similarly to the study presented

here, the baseline period contained the same local features as the stimulus period, though only the stimulus period contained global form. Consequently, Braddick *et al.* concluded that V1 was not processing global form and this is also what the results of the experiment reported here indicate.

6 MEG: The neural response to rotational Glass patterns of different coherence levels

6.1 Introduction

Established theories of visual processing present the visual areas of the brain in a hierarchical structure. Lower visual areas such as V1 process basic features (e.g. orientation) over a small region of the visual field. Output from lower areas is then passed to higher areas for processing of more complex features over larger areas of the visual field. This direction of information flow is termed feedforward, and the initial forward sweep of electrical activity is thought to be mainly responsible for unconscious vision (reviewed in Lamme & Roelfsema, 2000). Conversely, many neurons feedback from higher to lower visual areas and this process is thought to modulate neuronal receptive fields and to be essential for visual awareness (reviewed in Lamme & Roelfsema, 2000).

Feedback can either increase or decrease activity in lower areas and thereby modulate further transmission from lower to higher areas. Studies in macaque have shown that feedback processes may be rapid (Girard, Hupé, Bullier, 2001) and spatially accurate (Angelucci, Levitt, Walton, Hupé, Bullier, Lund, 2002). In response to increasingly "object-like" stimuli (e.g. 3-dimensional versus 2-dimensional shapes), human neuroimaging studies using fMRI have shown proportionally reduced activity in V1 correlated with increased activity in the LOC (Lerner, Hendler, Ben-Bashat, Harel, Malach, 2001; Murray, Schrater, Kersten, 2004). This is indicative of negative feedback from the LOC to V1.

The high temporal resolution of MEG makes it is a potentially useful tool for investigating feedback between V1 and the LOC. In addition, as Glass patterns have the same local features when oriented to create global structure or noise, they are comparable to the scrambled versus non-scrambled face stimuli of Lerner *et al.* (2001) and the various stimuli (e.g. random-motion dots versus structure-from-motion dots) used by Murray *et al.* (2004). Glass patterns with zero, threshold and 100 percent rotational coherence were used to present varying degrees of form and thereby modulate the extent of feedback. In the previous chapter, where responses to coherent Glass patterns were compared with those to zero coherence Glass patterns, no activity was evident within area V1. In this chapter, neural activity following the presentation of Glass patterns was compared with that to a blank screen. Local cues between the active and passive phase were therefore different.

6.2 Methods

Methods were as described in section 4.2 except that stimuli were rotational Glass patterns composed of 38 dot pairs covering an area of 4.12 deg^2. Glass patterns were presented in the lower-left visual field. The fixation dot was present throughout the recording session and was positioned 0.5 deg. from the horizontal and vertical meridians. The coherence of the rotational Glass pattern was either zero, three decibels above the coherence detection threshold, or 100 percent. The coherence threshold for detecting rotational Glass patterns was determined as described in section 3.2 except the Glass pattern dimensions and fixation position were as used for the MEG recording in this section. One male observer (DN, aged 47 years) took part in this experiment, stimuli were viewed monocularly using his right eye.

Glass patterns were presented using a square temporal envelope of 300 ms duration, separated by an ISI of random duration between 3000 ms and 3200 ms, during which time the screen was blank. The MEG recording session contained 120 stimulus presentations, with each coherence level presented 40 times in pseudo-random order. The Glass pattern was its predetermined coherence throughout the display period i.e. it was not ramped. Data was analysed using SAM for power changes between 1 s pre- and 1 s post-stimulus for several 10 Hz frequency bands (range 5-50 Hz).

6.3 Results

Figure 6.1 shows, for observer DN, the proportion of correct responses for distinguishing rotational Glass patterns from zero coherence Glass patterns as a function of the coherence of the rotational pattern. To correctly detect a rotational Glass pattern in 75 percent of trials, observer DN needed 21.1 percent (i.e. eight of the total of 38) of dot pairs to be coherently oriented. This value was increased by three decibels and used as the "threshold" coherence level in the MEG experiment.

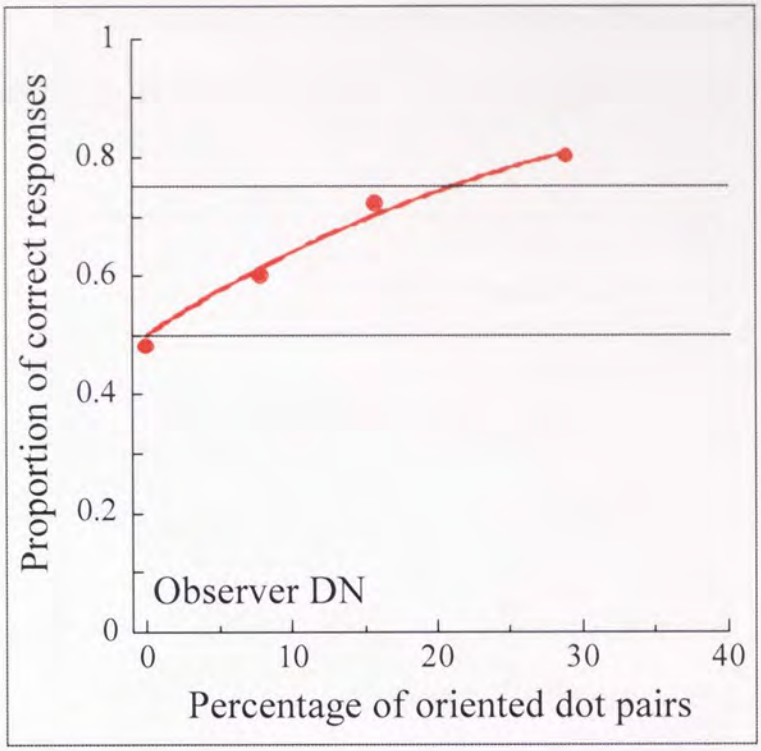

Figure 6.1. The proportion of correct responses for detecting rotational Glass patterns as a function of coherence for observer DN. The Weibull function is based on 100 trials. Patterns were presented for 300 ms, contained 38 dot pairs and were viewed in the lower left visual field. The monitor refresh rate was 100 Hz.

Figure 6.2 shows the pseudo t value of the largest a) increase and b) decrease in cortical power within each 10 Hz frequency band. Small power increases ($3.5 < \text{pseudo } t < 4.5$) were evident with 100 percent coherent patterns at frequencies in the 5-15, 10-20 and 35-45 Hz range. For Glass patterns with either zero or threshold coherence levels, no power increases (pseudo $t > 3.5$) were found for any of the frequency bands assessed. In contrast, there were decreases in cortical power (pseudo $t > 3.5$) associated with several of the frequency bands analysed following presentation of zero (10-20 to 25-35 Hz), threshold (5-15 to 30-40 Hz) and 100 percent (5-15 to 35-45 Hz) coherence patterns. For all three coherence levels employed the largest power decrease occurred in the 20-

30 Hz frequency band. Note that the pseudo t values for power decreases associated with threshold and 100 percent coherence levels were near identical at all frequencies.

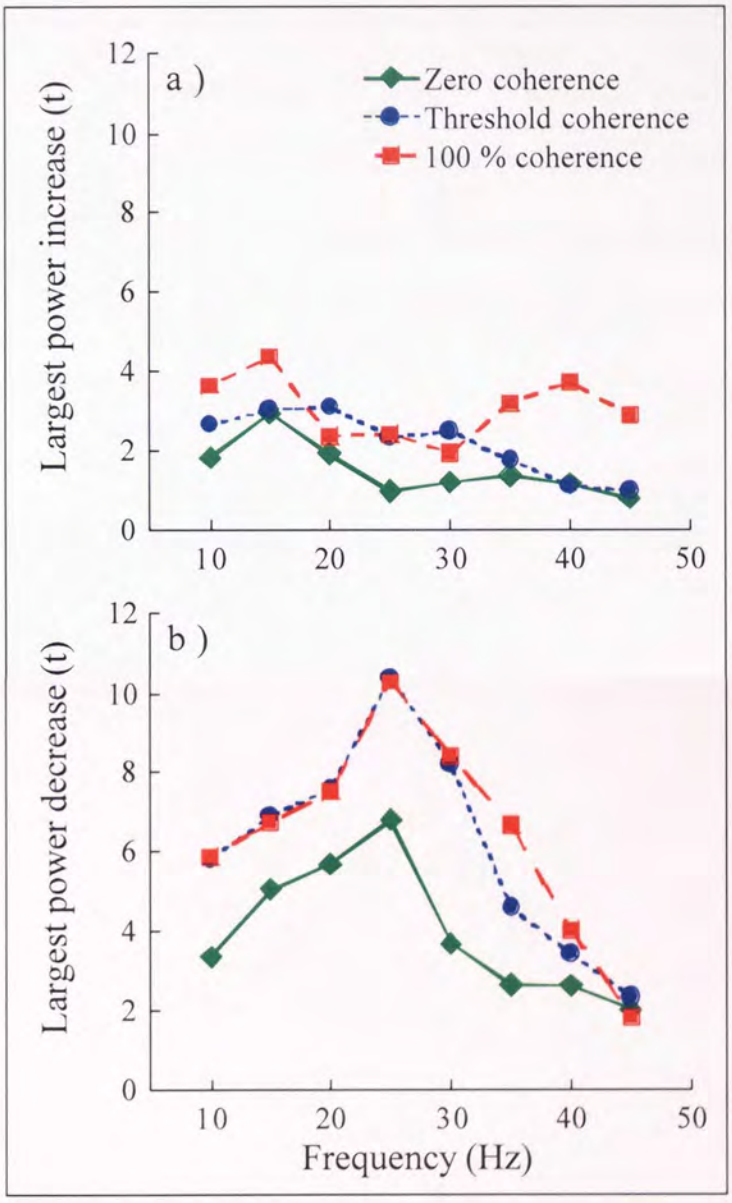

Figure 6.2. The largest a) increase and b) decrease in cortical power, 1 s pre- versus 1 s post-stimulus onset, is plotted against the mid-point of the frequency band analysed (i.e. 20-30 Hz SAM analysis is plotted as 25 Hz on the x-axis).

Figures 6.3-6.5 show that passive viewing of Glass patterns, both with and without rotational form, elicited bilateral reductions in cortical power (5-50 Hz) in extrastriate cortex and ventral areas of occipital cortex. Extrastriate activity was centred on the cuneus and middle occipital gyrus, close to V3a and V3 (Hasnain *et al.*, 1998). Activity in ventral occipital areas was close to V4 and V5 (Hasnain *et al.*, 1998). The location of the voxel with maximal power change within each region of activation was very similar for all Glass pattern coherences. However, threshold and 100 percent coherence Glass patterns produced more pronounced reductions in power than zero coherence Glass patterns.

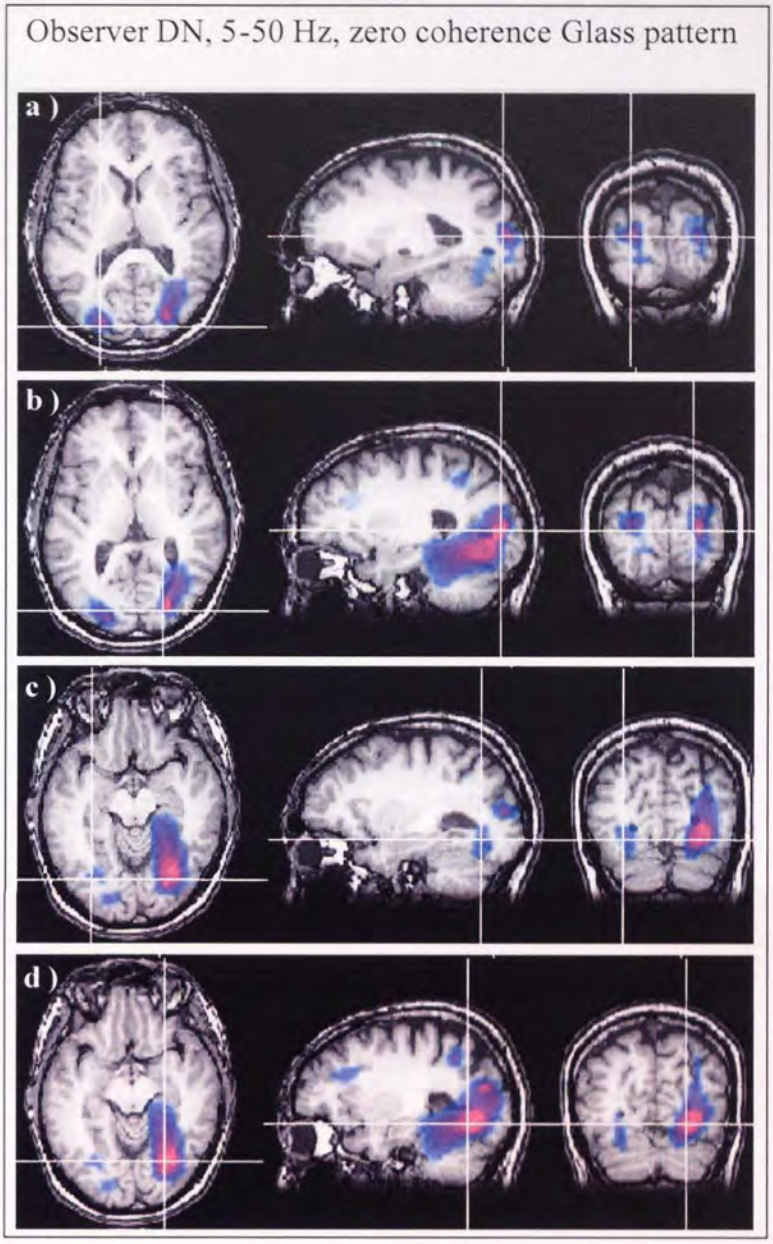

Figure 6.3. SAM images of statistical estimates of power changes in the 5-50 Hz frequency band, 1 s pre- versus 1 s post-presentation of zero coherence Glass patterns to observer DN. The magnitude of the pseudo t statistic is indicated by the colour overlay on an anatomical MRI of observer DN. Voxels with a pseudo t statistic less than two are not coloured. Decreases in cortical power are shown by a blue-purple-white colour range (white voxels indicate pseudo t = 6). Cross hairs indicate the voxel with the largest pseudo t statistic in that region, this represented a reduction in cortical power in the a) middle occipital gyrus (MNI: -21, -88, 13; pseudo t = 4.2); b) cuneus (MNI: 23, -85, 9; pseudo t = 4.9); c) left occipital lobe close to V4 (MNI: -28, -73, -6; pseudo t = 2.6); d) right occipital lobe close to V5 (28, -69, -5; pseudo t = 4.8).

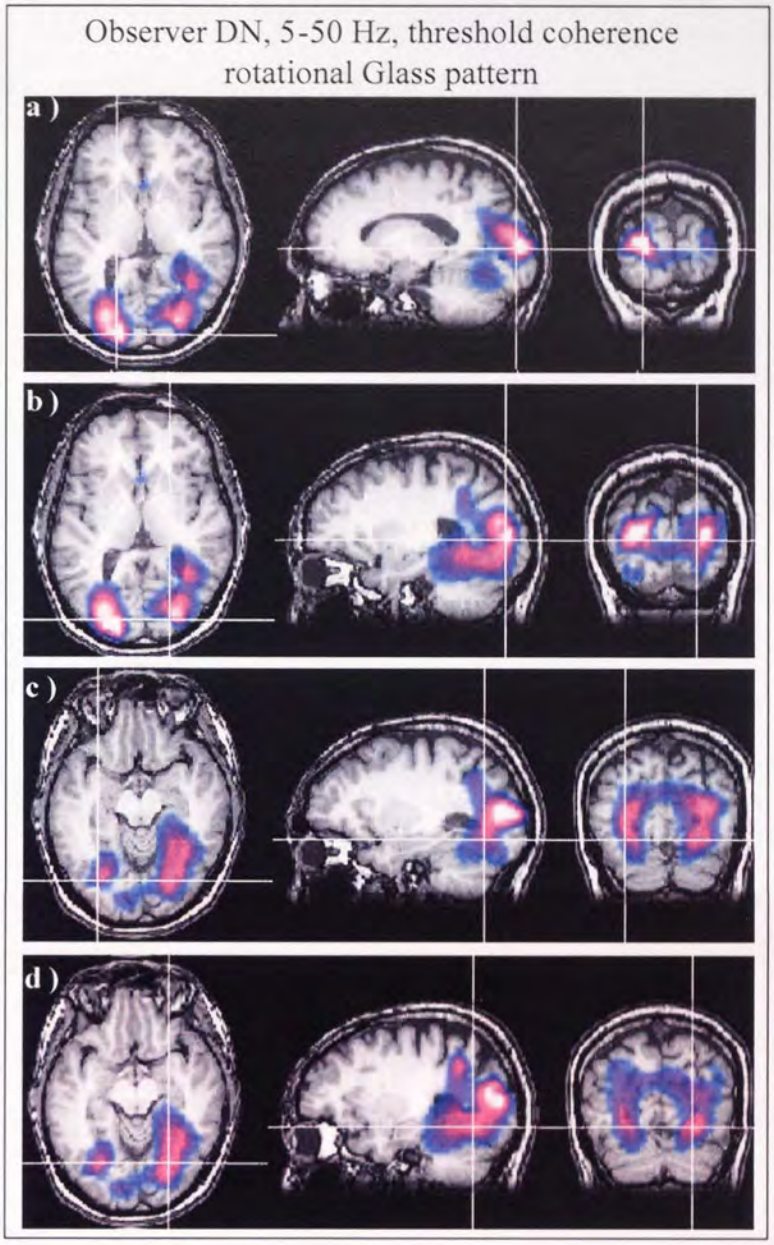

Figure 6.4. SAM images of statistical estimates of power changes in the 5-50 Hz frequency band, 1 s pre- versus 1 s post-presentation of threshold coherence rotational Glass patterns to observer DN. The colour overlay is as in Figure 6.3. Cross hairs indicate the voxel with the largest pseudo t statistic in that region, this represented a reduction in cortical power in the a) cuneus (MNI: -16, -93, 8; pseudo t = 9.7); b) cuneus (MNI: 23, -85, 9; pseudo t = 6.7); c) left occipital lobe close to V4 (MNI: -28, -73, -6; pseudo t = 4.0); d) right occipital lobe close to V5 (28, -69, -5; pseudo t = 4.6).

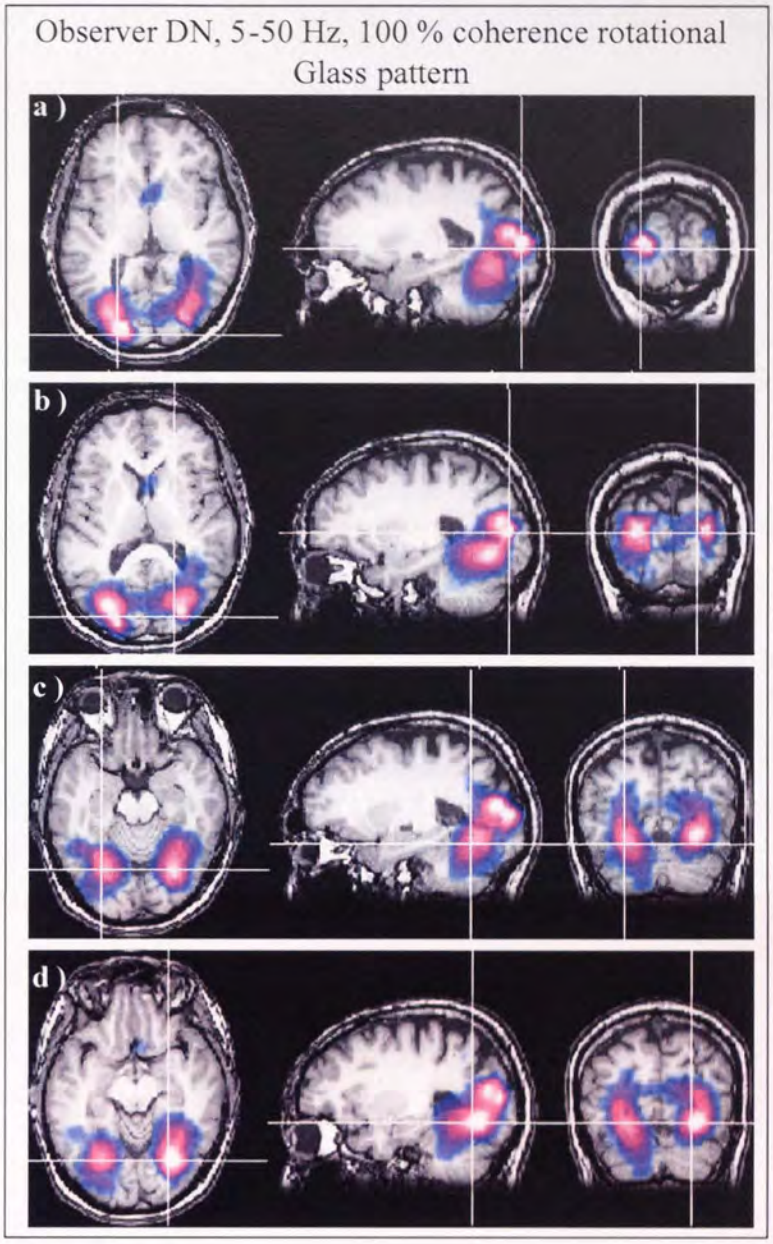

Figure 6.5. SAM images of statistical estimates of power changes in the 5-50 Hz frequency band, 1 s pre- versus 1 s post-presentation of 100 % coherence rotational Glass patterns to observer DN. The colour overlay is as in Figure 6.3. Cross hairs indicate the voxel with the largest pseudo t statistic in that region, this represented a reduction in cortical power in the a) cuneus (MNI: -21.4, -93.6, 7.9; pseudo t = 9.2); b) middle occipital gyrus (MNI: 23, -86, 13; pseudo t = 7.1); c) lingual gyrus (MNI: -24, -67, -11; pseudo t = 5.3); d) right occipital lobe close to V5 (28, -69, -5; pseudo t = 6.7).

Figure 6.6 shows time-frequency plots of energy changes for voxels that showed the largest power changes with SAM analyses (5-50 Hz, 1 s time window) in left extrastriate cortex and right ventral occipital cortex. The plots represent changes between 5 and 40 Hz and between zero and 1.5 s after onset of Glass patterns at each coherence level. Immediately after Glass pattern onset, there was an increase in energy predominantly in the theta frequency band (4-8 Hz) that lasted approximately the duration of the stimulus presentation (i.e. 300 ms). For all plots, there was a marked reduction in oscillatory power within the alpha (8-12 Hz) and beta frequency band (12–30 Hz) that began approximately 100-200 ms post-stimulus onset and continued for approximately 500 ms. This was followed by an increase in oscillatory power in the alpha and beta frequency band that began approximately 800-1000 ms post-stimulus onset and continued for the remainder of the plot. In the left extrastriate cortex this energy increase was larger and approximately 200 ms earlier following presentation of zero coherence Glass patterns than either threshold or 100 percent coherence Glass patterns.

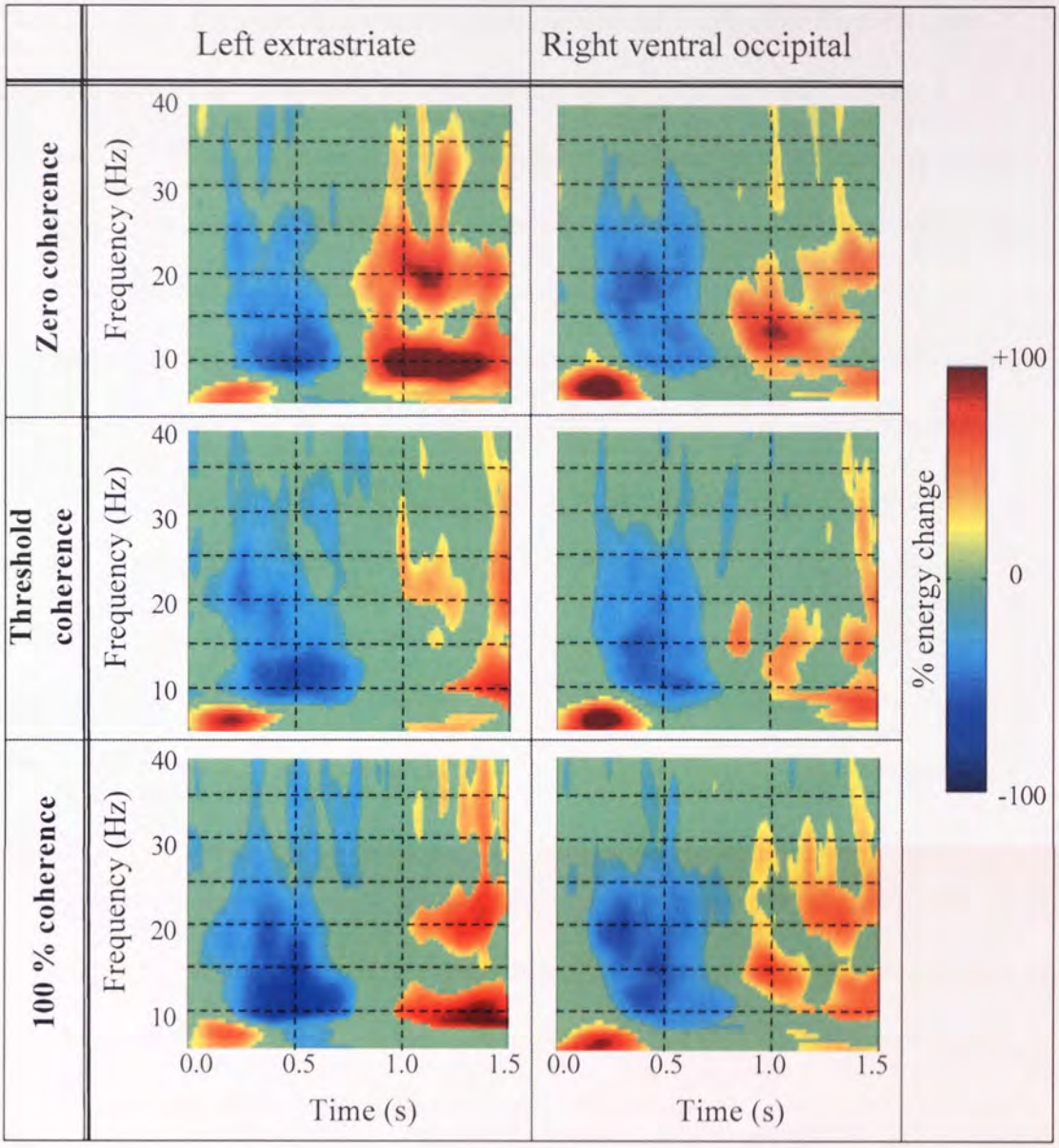

Figure 6.6. Time-frequency wavelet plots representing frequencies from 5-40 Hz over the time scale zero (stimulus onset) to 1.5 s. Plots were computed for peak voxels in the left extrastriate (left panels) and right ventral occipital (right panels) cortex as determined from SAM analyses of 5-50 Hz, 1 s time window, data for each coherence level with observer DN. These voxels are delineated by the cross-hairs in a) and d) respectively of Figures 6.3-6.5. Plots of energy changes following zero, threshold and 100 percent coherence rotational Glass patterns are shown in the top, middle and bottom rows respectively. Compared with pre-stimulus activity, significant energy reductions and increases are shown as blue and red colours respectively, non-significant ($p > 0.05$) changes in energy are green (see "% energy change" key).

The increase in energy in the theta frequency band immediately after stimulus onset (Figure 6.6) was not observed in time-frequency analyses performed in chapter 4 (Figure 4.11). This energy increase may have been an evoked response elicited by the rapid onset of the Glass pattern relative to the blank screen of the ISI. To examine this possibility, further analysis was performed to demarcate evoked neural activity. In addition to time-frequency plots of the type presented previously, in which both induced and evoked activities are revealed, a time-frequency plot was also created from the averaged activation waveforms from all trials. Averaging the waveforms nulls any non-phase locked (induced) activity and these plots show evoked activity as amplitude change per time-frequency bin relative to baseline. Figure 6.7 shows the a) evoked and b) evoked-plus-induced energy changes for a voxel in right extrastriate cortex following onset of threshold coherence rotational Glass patterns. With both plots, increases and decreases in energy are represented by red and blue colours respectively. The plots show that the immediate increase in theta band energy is conserved following trial averaging but the later alpha and beta band energy changes are not. This indicates that the changes in theta oscillatory power evident immediately after stimulus onset were evoked (time- and phase-locked) whereas the other power changes were induced (time- but not phase-locked).

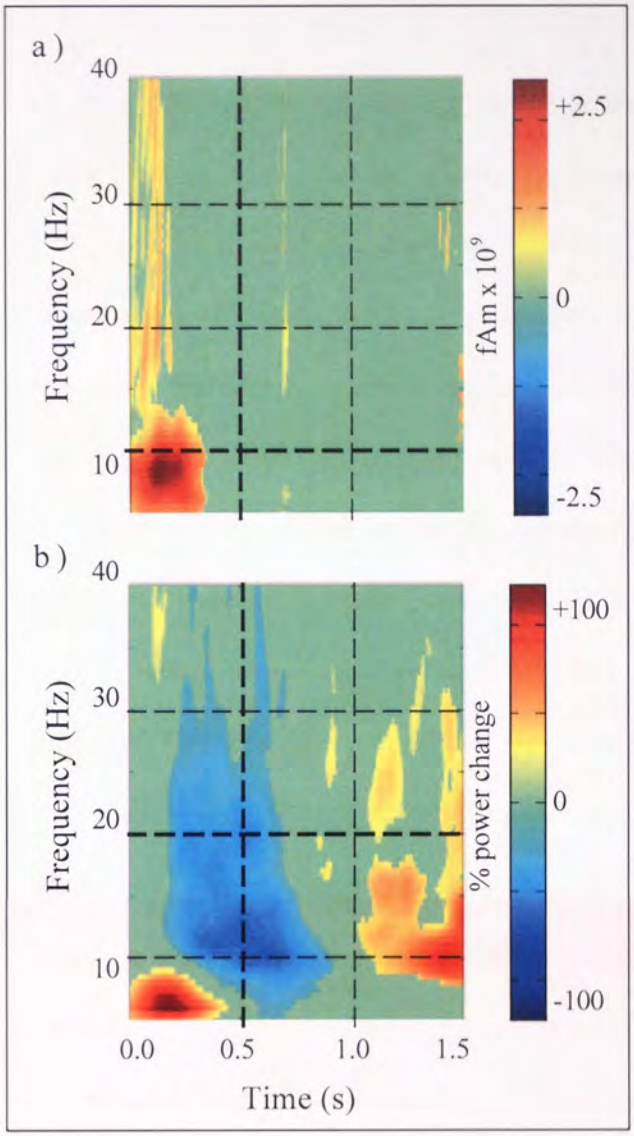

Figure 6.7. Time-frequency wavelet plots of a) evoked; b) evoked-plus-induced; energy changes for frequencies between 5 and 40 Hz over the time scale zero (stimulus onset) to 1.5 s. Plots were computed for the peak voxel in right extrastriate cortex as determined from SAM analyses of 5-50 Hz, 1 s time window, data for threshold coherence Glass patterns with observer DN. This voxel is delineated by the cross-hairs in Figure 6.4 (b). Significant energy reductions and increases are shown as blue and red colours respectively, non-significant ($p > 0.05$) changes in energy are green.

6.3.1 Neural activity within V1

For analysis of the data from this experiment no *a priori* assumptions were made regarding the locations of neural activity. Consequently, time-frequency plots were calculated for voxels that had been identified by SAM analysis as having the largest pseudo t values (Figures 6.3-6.6). None of these identified voxels were in V1, however, it is possible that neural activity in response to Glass patterns did occur in V1. To investigate this a voxel was manually-selected that was slightly superior to the calcarine sulcus and was within V1 as defined by Hasnain *et al.* (1998) and BA 17 as defined by the Talairach Daemon database (Lancaster *et al.*, 2000). Figure 6.8 (a) shows the selected voxel delineated by crosshairs on SAM images of changes in cortical power within the 5-50 Hz frequency band (1 s time window) in response to Glass patterns of zero, threshold and 100 percent coherence. Time-frequency plots calculated for this voxel showed similar energy changes to those previously observed for voxels in extrastriate and LOC (Figure 6.6). Initial increases in theta band power were followed by decreases and then increases in alpha and beta band power. The decreases in beta band frequency power (approximately 200-700 ms post-onset) appeared to become progressively more pronounced with increasing rotational coherence, but this was not assessed statistically. Additionally, increases in beta band energy were larger and approximately 200 ms earlier following presentation of b) zero coherence Glass patterns than either c) threshold or d) 100 percent coherence Glass patterns.

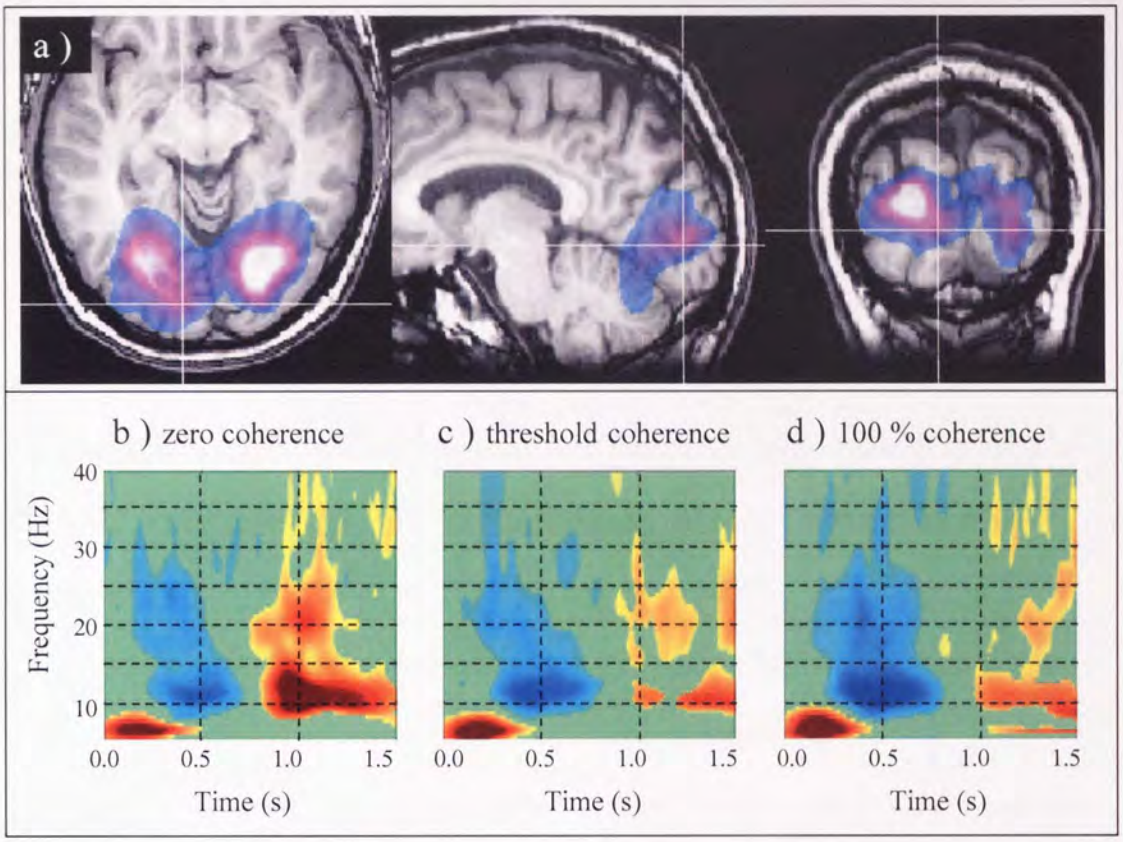

Figure 6.8.a) SAM images for comparison of cortical power (5-50 Hz frequency band) 1 s pre- with 1 s post-onset of Glass patterns (all coherences) to observer DN. The colour overlay is as in Figure 6.3. Time-frequency plots were computed for the voxel in V1 delineated by the crosshairs following b) zero; c) threshold; and d) 100 percent coherence rotational Glass patterns. Significant energy changes are shown as blue and red colours with the same scale as in Figure 6.6.

6.4 Discussion

Although the abrupt presentation of Glass patterns yielded the largest power changes in extrastriate and ventral occipital cortex (Figures 6.3-6.5), it was reported that power changes also occurred in V1 (Figure 6.8). However, the validity of the time-frequency analysis of the voxel in V1 is questionable due to the heterogeneity of beamformer spatial resolution (Barnes *et al.*, 2004). Barnes *et al.* (2004) demonstrated that increasing the amplitude of an electrical source increased the spatial resolution of the

beamformer. Conversely, in regions with low amplitude signal, such as V1 in this experiment, the spatial resolution is low. With low spatial resolution it is possible that power changes from neighbouring sources will be inadvertently incorporated into time-frequency analysis. Thus, it remains an open question as to whether or not the time-frequency analysis of V1 is a true representation of the neural activity within that area.

Previous studies using fMRI have shown less of a haemodynamic response in V1 following presentation of global form than following presentation of similar images without global form (Lerner *et al.*, 2001; Murray *et al.*, 2004). These reductions in activity in V1 were coincident with increases in activity in the LOC and Murray *et al.* (2004) interpreted their results as being the outcome of negative feedback from the LOC to V1. However, here the pseudo t values in V1 were equally small (< 3.0) in response to both zero coherence and rotational Glass patterns and therefore the results presented in this chapter do not support this theory of negative feedback.

For the extrastriate area analysed in response to zero, threshold and 100 percent coherence Glass patterns there was a marked power reduction evident between approximately 200 and 700 ms post-stimulus onset in the alpha and beta frequency bands. This was followed by a power increase in the alpha and beta bands that was earlier and of greater magnitude following zero coherence than either threshold or 100 percent coherence Glass patterns (Figure 6.6). As discussed in section 4.4, it has been suggested that reduced and increased cortical power at frequencies less than 30 Hz reflect increased and decreased neural processing respectively (Pfurtscheller, 2001; Pfurtscheller *et al.*, 2005; Singh *et al.*, 2002). Accepting this, these results are indicative of an early stage of neural processing followed by a period of deactivation that occurs

earlier and to a greater extent following zero coherence than either threshold or 100 percent coherence Glass patterns.

7 MEG: The neural response to global form defined by Gabor patches

7.1 Introduction

The results of chapter 4 showed that passive viewing of global form in Glass patterns elicited pronounced reductions in oscillatory power (5-40 Hz) in regions close to those retinotopically mapped as V3 and V3a (Hasnain *et al.*, 1998). The peaks of these activated regions were often closest to V3a (see Figures 4.2-4.4), an area activated by visual motion (Braddick *et al.*, 2000; Tootell *et al.*, 1997). However, contrary to the results reported in chapter 4, human V3a is not thought to be activated by global form (Braddick *et al.*, 2000). It is possible that the dynamic Glass patterns employed may have elicited a sensation of motion as such patterns have been shown to create an illusion of movement in the direction of the form, i.e. rotational Glass patterns appear to rotate (Ross, 2004; Ross *et al.*, 2000). In this chapter a global form stimulus composed of stationary Gabor patches was used to investigate whether the observed power changes reported previously in V3a reflected a response to global form or motion. FMRI studies that have investigated the perception of closed contours defined by Gabor patches have not found activation in V3a but have shown activation predominantly in the LOC (Altmann *et al.*, 2003; Kourtzi & Huberle, 2005), consistent with the proposed role of the LOC in object recognition (Grill-Spector, Kourtzi, Kanwisher, 2001).

7.2 Methods

Methods were as described in section 4.2 except that the stimuli comprised an array of 36 achromatic Gabor patches with a peak luminance contrast of 90 percent. The grey background was isoluminant with the Gabor patches (50 cdm^{-2}). Each Gabor element had a spatial frequency of three cycles per degree, with a full bandwidth of 1.4 cycles. The sinusoidal carrier was stationary and was always displayed in cosine phase. Gabors

were positioned in a 6 x 6 grid (5.02 deg.^{2}) with a centre-to-centre distance of 0.84 degrees. On each trial, each Gabor patch was spatially jittered up to 0.17 degrees from this base position. The sinusoidal carriers were aligned relative to the centre of the grid to form radial, rotational or random patterns. A total of 120 trials were presented with 40 trials of each pattern type presented in pseudo-random order. The stimulus was presented in the lower-left visual field. The fixation dot was present throughout the recording session and was positioned 0.5 deg. from the horizontal and vertical meridians. Stimuli were displayed for 300 ms with an ISI of 3500 ms during which time the screen was blank. One male observer (DN, aged 47 years) took part in this experiment, stimuli were viewed monocularly using his right eye.

7.3 Results

Figure 7.1 shows, for radially, rotationally and randomly oriented Gabor patches, the pseudo t value of the largest a) increase and b) decrease in cortical power found within each 10 Hz frequency band. Small power increases ($3.5 <$ pseudo $t < 4.5$) were evident following radial form for SAM analyses in the 5-15, 10-20 and 30-40 Hz frequency bands. For rotationally and randomly oriented Gabor patches there were no power increases (pseudo $t > 3.5$) with any of the frequency bands assessed. In contrast, decreases in cortical power (pseudo $t > 3.5$) were evident for frequency bands from 5-15 to 30-40 Hz following radial and random form and from 5-15 to 35-45 Hz following rotational form. The greatest power reductions were in the 10-20 Hz frequency band for radial and rotational form and in the 15-25 Hz band for random form. Except at the higher frequency bands (30-40 Hz and above), the largest reductions in power were recorded for radial patterns.

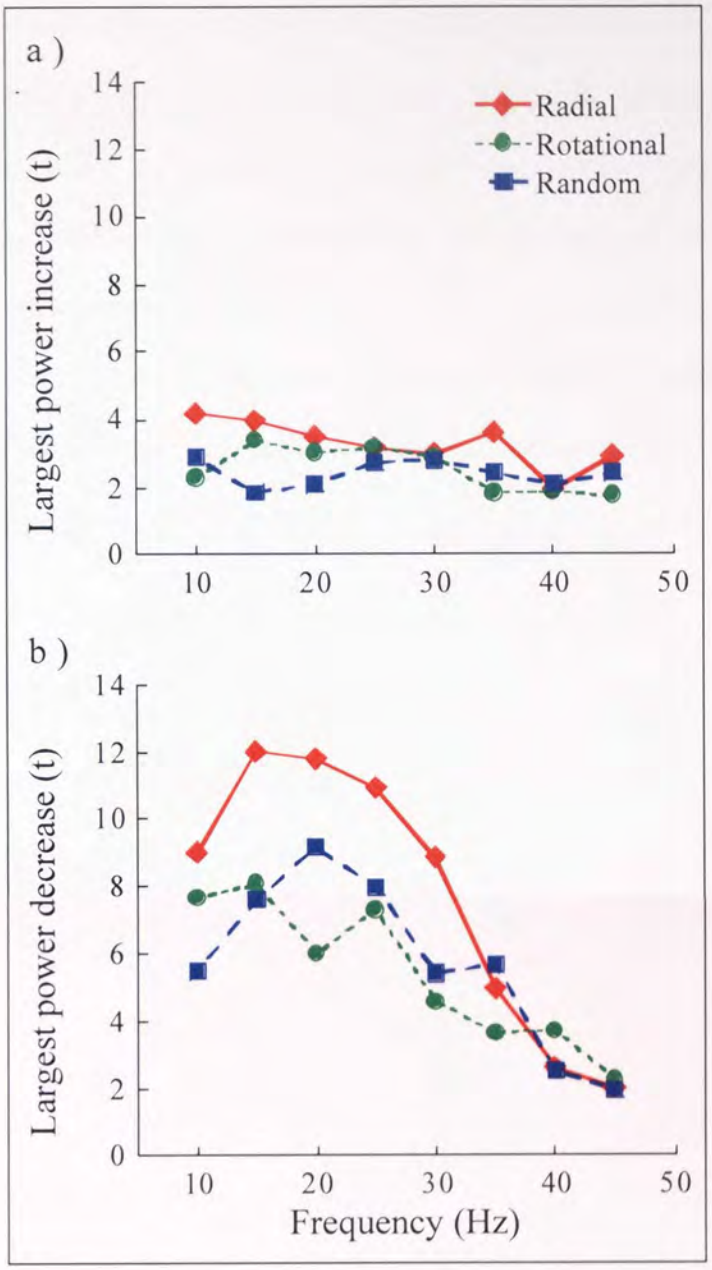

Figure 7.1. The largest a) increase and b) decrease in cortical power, 1 s pre- versus 1 s post-stimulus onset of radial, rotational or random form is plotted against the mid-point of the frequency band analysed (i.e. 15-25 Hz SAM is plotted as 20 Hz on the x-axis).

The largest reductions in oscillatory power (5-50 Hz, 1 s time-window) were in extrastriate cortex and ventral occipital cortex. Figure 7.2 shows, for observer DN, the

spatial location of maximal power reductions in extrastriate cortex for each form type. For all patterns, reductions in power were bilateral, though biased to the left hemisphere, and were centred on the cuneus close to V3a (Hasnain *et al.*, 1998). The magnitude of this power change was least for randomly oriented Gabor elements (see pseudo t values in caption). Figure 7.3 shows bilateral power reductions in the ventral occipital cortex following all pattern types. As in the extrastriate cortex, the power reductions were more extensive for radial and rotational form than for random form (pseudo t values in caption).

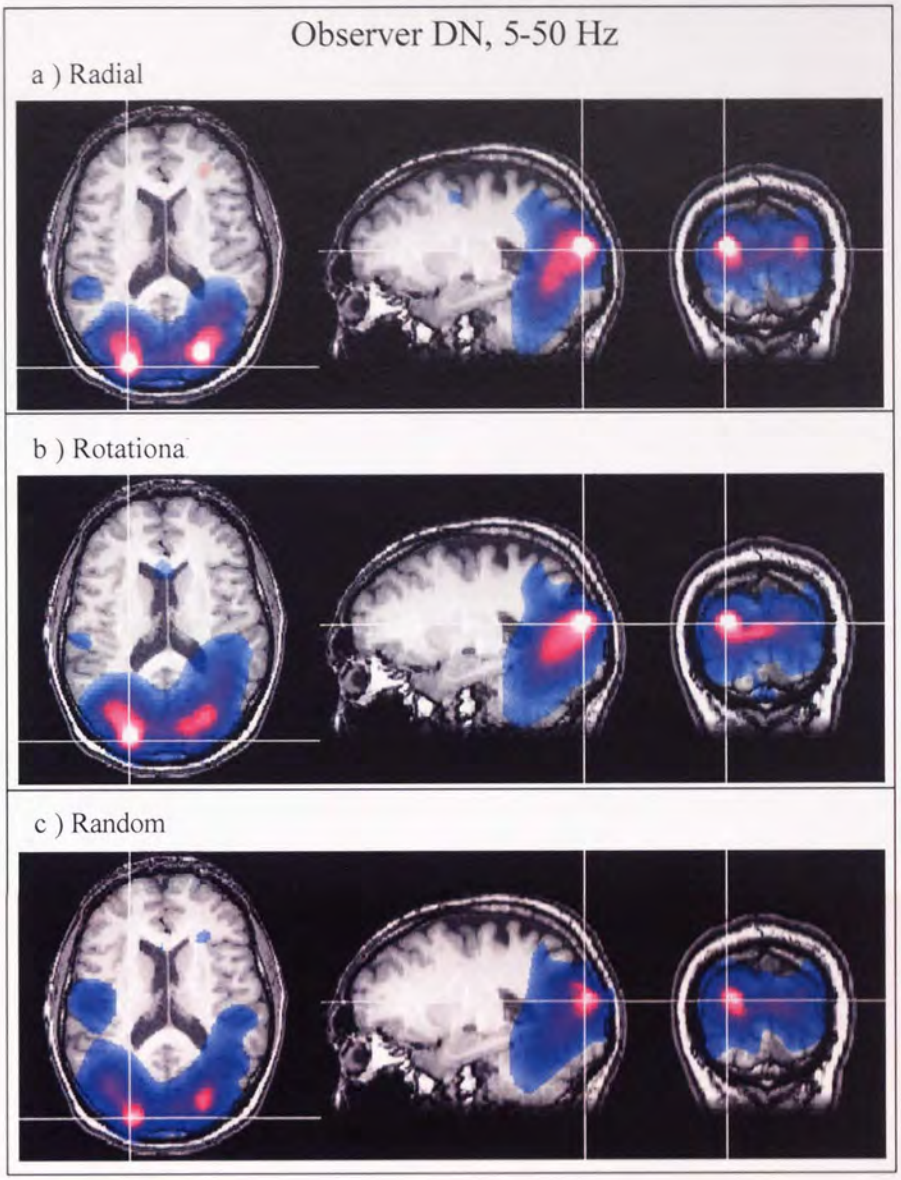

Figure 7.2. SAM images for comparison of cortical power in the 5-50 Hz frequency band, 1 s pre- with 1 s post-presentation of Gabor patterns to observer DN. The magnitude of the pseudo t statistic is indicated by the colour overlay on an anatomical MRI of observer DN. Voxels with a pseudo t statistic less than two are not coloured. Decreases in cortical power are shown by a blue-purple-white colour range (white voxels indicate pseudo t = 12). Cross hairs indicate the voxel with the largest pseudo t statistic in extrastriate cortex. This represented a reduction in cortical power in the left cuneus (MNI: -23, -90, 20) for a) radial global form (pseudo t = 17.9); b) rotational global form (pseudo t = 14.9); and c) randomly oriented Gabor patterns (pseudo t = 11.7).

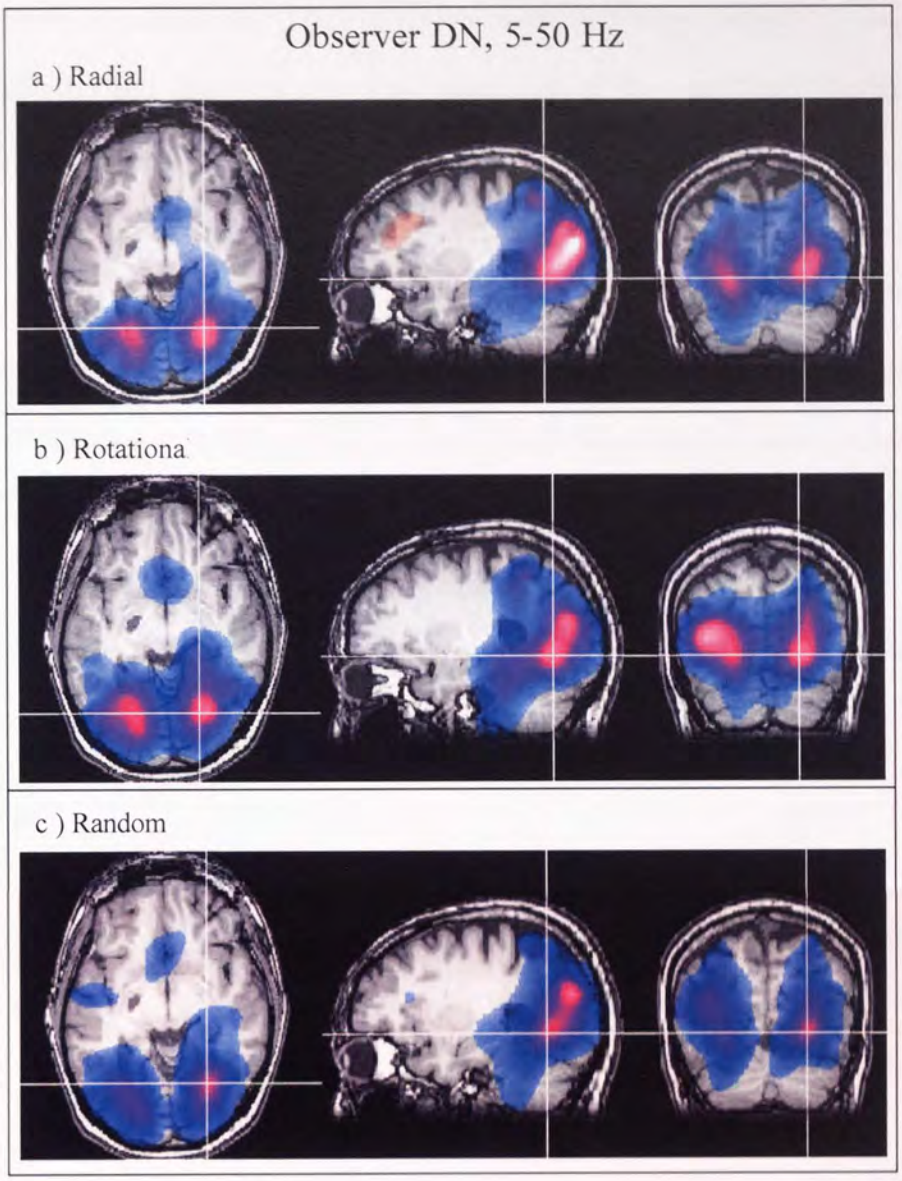

Figure 7.3. SAM images for comparison of cortical power in the 5-50 Hz frequency band, 1 s pre- with 1 s post-presentation of Gabor patterns to observer DN. The colour overlay is as in Figure 7.2. Cross hairs indicate the voxel with the largest pseudo t statistic in ventral occipital cortex. This represented a reduction in cortical power in the a) right middle occipital gyrus (MNI: 28, -65, -0; pseudo t = 9.3) for radial global form; b) right lingual gyrus, BA 19 (MNI: 23, -71, -1; pseudo t = 9.1) for rotational global form; and c) right middle occipital gyrus (MNI: 28, -65, -0; pseudo t = 7.9) for randomly oriented Gabor patterns.

Figure 7.4 shows time-frequency plots of energy changes between 5 and 40 Hz, and between zero and 1.5 s after Gabor pattern onset, for voxels located within extrastriate (left panels) and ventral occipital (right panels) areas. For all plots, immediately after Gabor pattern onset there was an increase in energy in the theta frequency band (4-8 Hz) that lasted approximately the duration of the stimulus presentation (i.e. 300 ms). This was followed by a prominent reduction in oscillatory power within the alpha (8-12 Hz) and beta (12-30 Hz) frequency bands that began approximately 100-200 ms post-stimulus onset and continued for approximately 500 ms. There was evidence of some increases in alpha and beta band power occurring mostly between 1 and 1.5 s after stimulus onset.

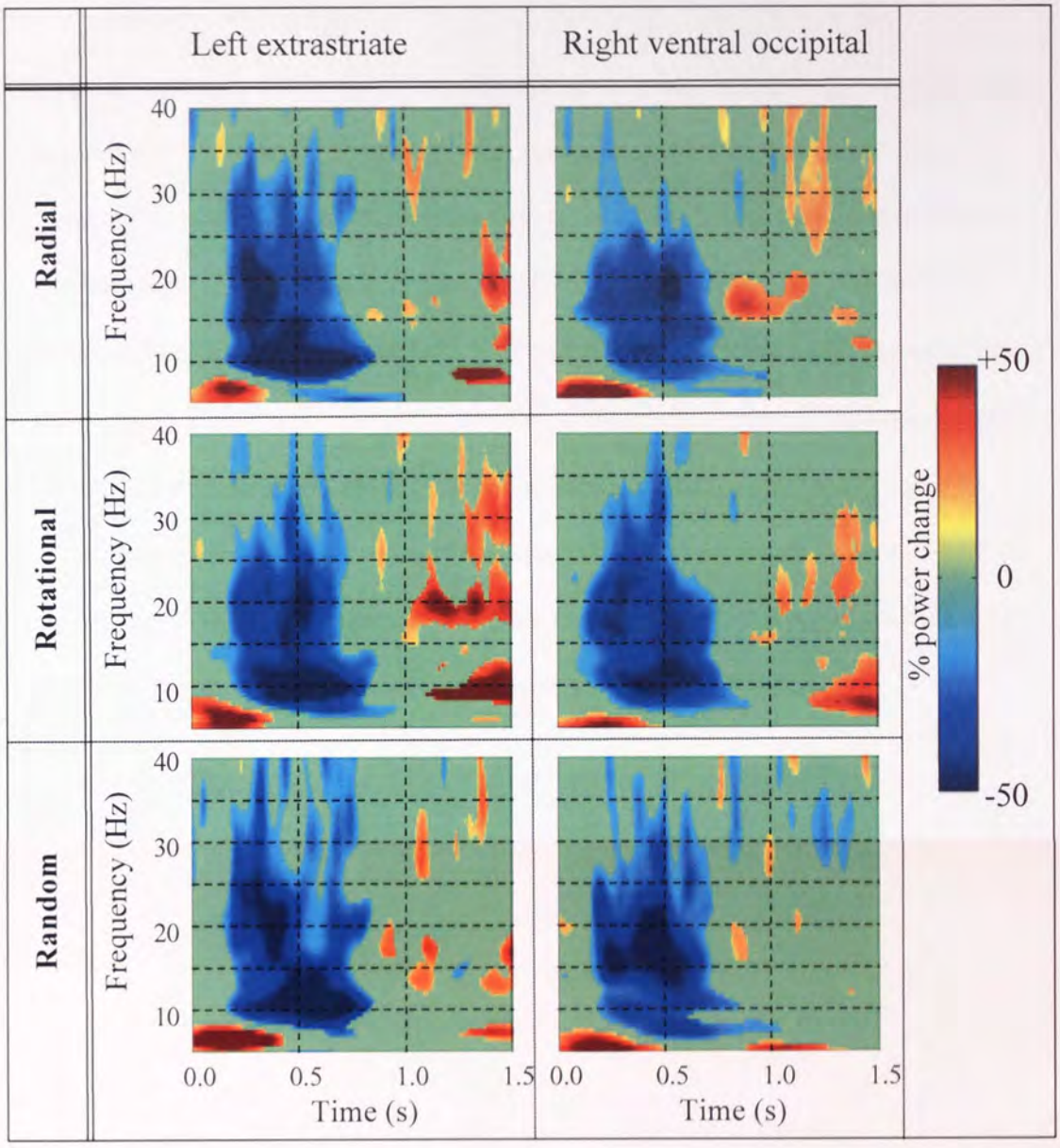

Figure 7.4. Time-frequency wavelet plots representing frequencies from 5-40 Hz over the time scale zero (stimulus onset) to 1.5 s. Plots were computed for peak voxels in the left extrastriate (left panels) and right ventral occipital (right panels) cortex as determined from SAM analyses of 5-50 Hz, 1 s time window, data for each form type with observer DN. These voxels are delineated by the cross-hairs in Figures 7.2-3. Plots of energy changes following presentation of Gabor elements with radial, rotational and random form are shown in the top, middle and bottom rows respectively. Compared with pre-stimulus activity, significant energy reductions and increases are shown as blue and red colours respectively, non-significant ($p > 0.05$) changes in energy are green (see "% energy change" key).

7.4 Discussion

The neural responses to stationary Gabor patches, with their sinusoidal carriers oriented to produce radial, rotational or random form, were similar to those produced by dynamic Glass patterns. In particular, the largest reduction in cortical power occurred in extrastriate cortex, slightly superior to V3a (Hasnain *et al.*, 1998). The area of cortex with reduced cortical power in the 5-50 Hz frequency range covered a large proportion of the occipital lobe and so also included other visual areas. However, the area thought to be V3a (Hasnain *et al.*, 1998) showed reductions in cortical power (5-50 Hz) with high pseudo t values (pseudo $t > 10$) which suggests that this area was activated by form without motion. This is in contrast to a previous fMRI study that reported activation of human V3a by coherent motion but not form (Braddick *et al.*, 2000).

8 Global form processing in strabismic amblyopia: a case study

8.1 Introduction

Strabismic amblyopia has been associated with deficits in global form processing (Hess *et al.*, 1999; Rislove, Hall, Kiorpes, 2005). Rislove *et al.* (2005) found that perception of rotational, and especially parallel, Glass patterns were reduced with strabismic amblyopia. Similarly, the detection of rotational Glass patterns is poorer in children who have been visually deprived through dense congenital cataracts (Lewis *et al.*, 2002), though the neural basis of this deficit may be different to that with strabismic amblyopia. From behavioural studies, it has been suggested that strabismic amblyopes are inaccurate at orientation and position processing but that their integration of local signals to produce global structure is essentially intact (Hess *et al.*, 1997; Mansouri *et al.*, 2004; Simmers & Bex, 2004). In this chapter, MEG was used to examine the neural basis of global form perception, achieved by integration of oriented dot pairs, in a case study of one strabismic amblyope.

As discussed in section 1.3, most neuroimaging studies of amblyopia have used simple repetitive patterns as stimuli, such as sinewaves or checkerboards (Anderson *et al.*, 1999; Barnes *et al.*, 2001; Choi *et al.*, 2001; Lee *et al.*, 2001; but see Lerner *et al.*, 2003) In this chapter, Glass patterns with global form were used as stimuli because they require higher-order processing whilst containing the same local cues as the zero coherence Glass patterns presented in the ISI. Accordingly, results presented in previous chapters have shown that the main response to coherent Glass patterns is reduced oscillatory power in extra-striate and lateral occipital cortex. In response to oriented Glass patterns, SAM and time-frequency analysis were used to assess interocular differences in cortical power changes. This is of specific interest as it has been reported

that neurons driven by the fellow eye of strabismic cats are more highly synchronised than those driven by the amblyopic eye (Roelfsema, Konig, Engel, Sireteanu, Singer, 1994). MEG currently provides the best neuroimaging tool for examining power within brain rhythms with high spatial resolution.

8.2 Methods

One strabismic amblyopic observer AA (female, aged 35 years) with 2° left esotropia, no eccentric fixation and no history of ocular surgery consented to participate in this experiment. AA's refraction and Snellen acuity were: R +0.50/-0.50x10 (6/6); L +2.00/-2.00x170 (6/18+). AA had previously undergone an anatomical MR volume scan and was screened with a questionnaire to ensure she did not have any metallic objects on or within her person. For comparison with a normally-sighted observer, MEG and psychophysical data are presented for observer DN (male, aged 47 years).

Coherence thresholds with radial, rotational and horizontal Glass patterns were obtained, as described in section 3.2, for each eye of both observers. Thresholds were based on two runs with 100 trials in each. The neural response to coherent Glass patterns was determined using MEG and SAM as described in section 4.2.

8.3 Results

Figure 8.1 shows, for both observers, the proportion of correct responses for detecting global structure in radial, rotational and horizontal Glass patterns as a function of the percentage of coherently oriented dot pairs in each pattern. Note that for normally-sighted observer DN, the results for right- and left-eye viewing were similar for each pattern type. The coherence detection thresholds for rotational and radial patterns were

about 6.5 percent, while that for horizontal patterns was 29 percent. The relative disadvantage for detection of horizontal compared with radial and rotational Glass patterns is in general agreement with the results presented in chapter 3. For amblyopic observer AA, there were large interocular differences evident for each pattern type, with performance always being least for the amblyopic eye. With amblyopic-eye viewing, the threshold criterion (75 percent correct performance) was not reached for horizontal patterns, but it was for both rotational and radial patterns when each contained approximately 16 percent coherently oriented dot pairs. Performance increased most rapidly for rotational patterns and was near perfect (= 95%) at coherences of 22 percent with either fellow- or amblyopic-eye viewing. Based on these results we confined SAM analyses to the data for rotational patterns. To avoid response habituation, however, the MEG recordings were completed with all three pattern types presented in pseudo-random order.

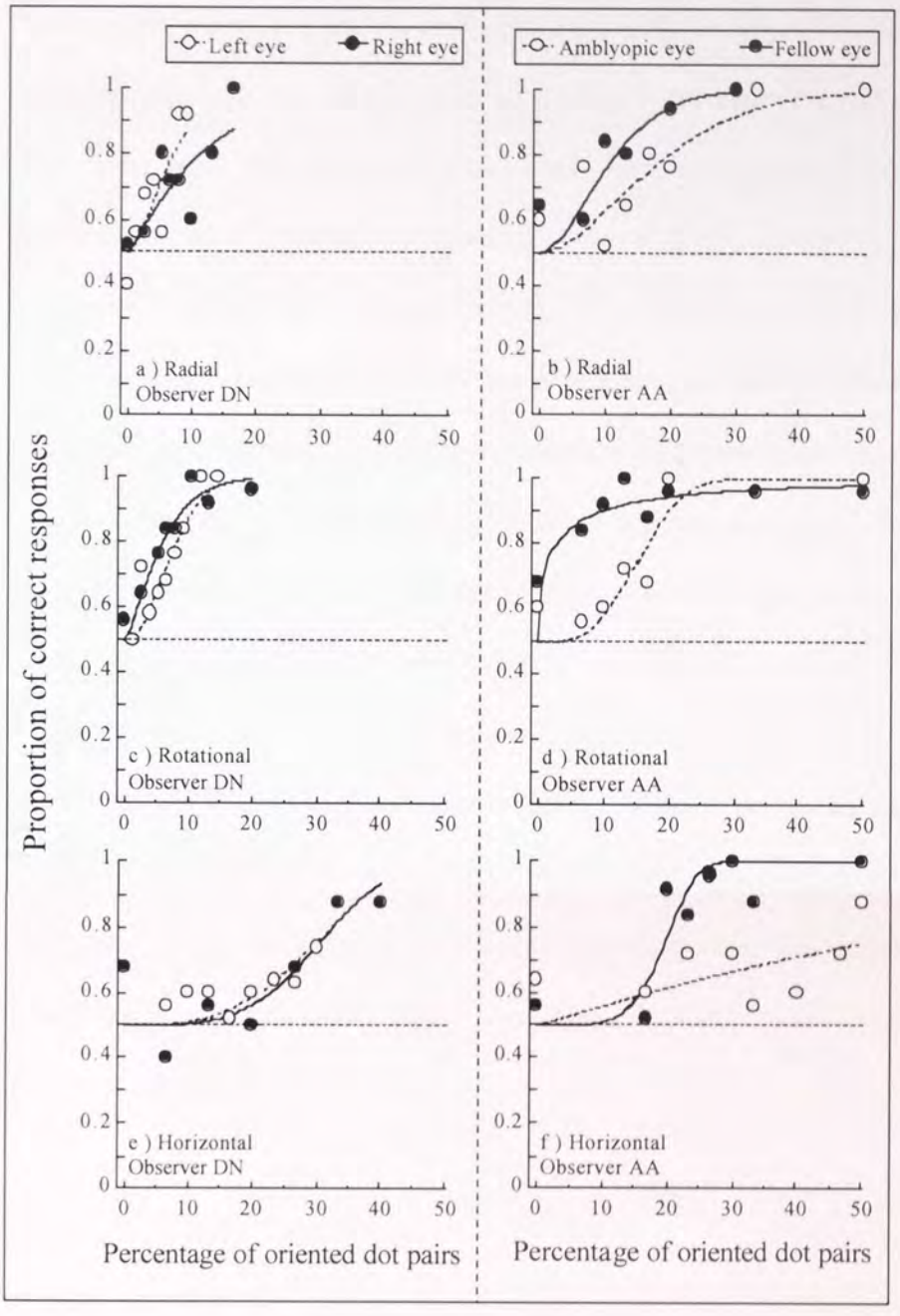

Figure 8.1. Psychometric functions for normally-sighted observer DN (a, c, e) and strabismic observer AA (b, d, f), showing the proportion of correct responses for detecting global structure in radial (a-b), rotational (c-d) and horizontal (e-f) Glass patterns as a function of the percentage of coherently oriented dot pairs in each pattern. Each curve shows the fit of a Weibull function based on 200 trials.

Figure 8.2 shows sagittal and coronal SAM images for the perception of rotational Glass patterns for a) left- and b) right-eye viewing by normally-sighted observer DN, and c) amblyopic- and d) fellow-eye viewing by strabismic observer AA. All images depict statistical estimates of power changes between a pre- and post-stimulus time window of 1 s within the frequency band 15–25 Hz. These conditions were chosen because analyses in chapter 4 showed that power changes were maximal within this time period and frequency range. Power reductions (represented as white-purple colours) were evident in each hemisphere for the amblyopic observer, though biased towards the left hemisphere for fellow-eye viewing and the right hemisphere for amblyopic-eye viewing. The locations of peak voxel activity, delineated by the crosshairs in each image, occurred close to V4 (Hasnain *et al.*, 1998) at the junction of areas BA18 and BA19 in ventral occipital cortex. Bilateral power decreases were also evident for the normally-sighted observer, though the largest decrease occurred in the right hemisphere for both right- and left-eye viewing. Voxels with maximal power change in the ventral occipital region were also at the junction of BA18 and BA19, close to V4 (Hasnain *et al.*, 1998).

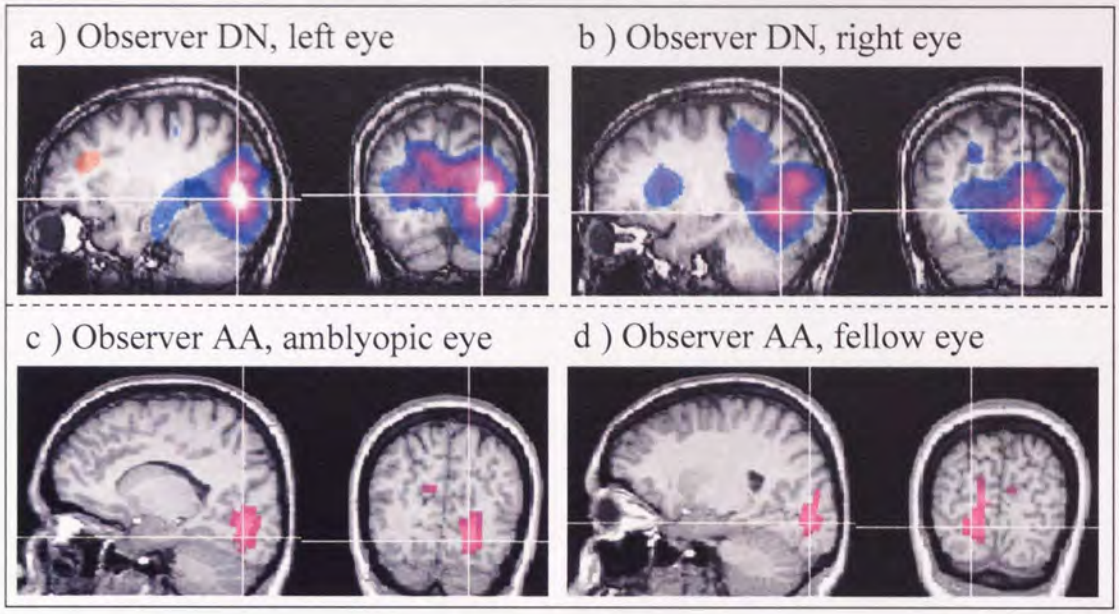

Figure 8.2. Sagittal and coronal SAM images of statistical estimates of power changes between 1 s pre- and 1 s post-onset of rotational Glass patterns within the frequency band 15-25 Hz. Crosshairs indicate the peak voxel in ventral occipital cortex for a) left- (MNI: 28, -75, 6; pseudo t = 6.6) and b) right-eye (MNI: 21,-70, 1; pseudo t = 4.9) viewing for observer DN and c) amblyopic- (MNI: 16, -71, -11; pseudo t = 2.5) and d) fellow- (MNI: -20, -77, -1; pseudo t = 2.5) eye viewing for observer AA. The magnitude of the pseudo t-statistic is indicated by the colour overlay on anatomical MRIs of each observer. White-purple colours indicate a relative decrease, while yellow-orange colours indicate a relative increase during the active phase (1.9 = pseudo t = 6 for DN; 1.9 = pseudo t = 3 for AA).

Figure 8.3 shows time-frequency wavelet plots for activity in response to rotational Glass patterns within BA18/19 for observers AA and DN. Note that with normally-sighted observer DN, the results for right- and left-eye viewing were similar: the principal activity was manifest as a reduction in oscillatory power within the beta frequency band (12 - 30 Hz), beginning 250–300 ms post-stimulus onset. Also common to both eyes was an increase in oscillatory power within the theta frequency band (4–8 Hz), beginning shortly after stimulus onset. For amblyopic observer AA with fellow-eye viewing, the results were similar to those of the control: a reduction in beta activity was

evident from about 300 post-stimulus onset, while an increase in power at low frequencies (< 10 Hz) was evident from 200-800 ms. However, the results obtained for the amblyopic eye were markedly different, there being no evidence of a sustained change (increase or decrease) in oscillatory power within any frequency band.

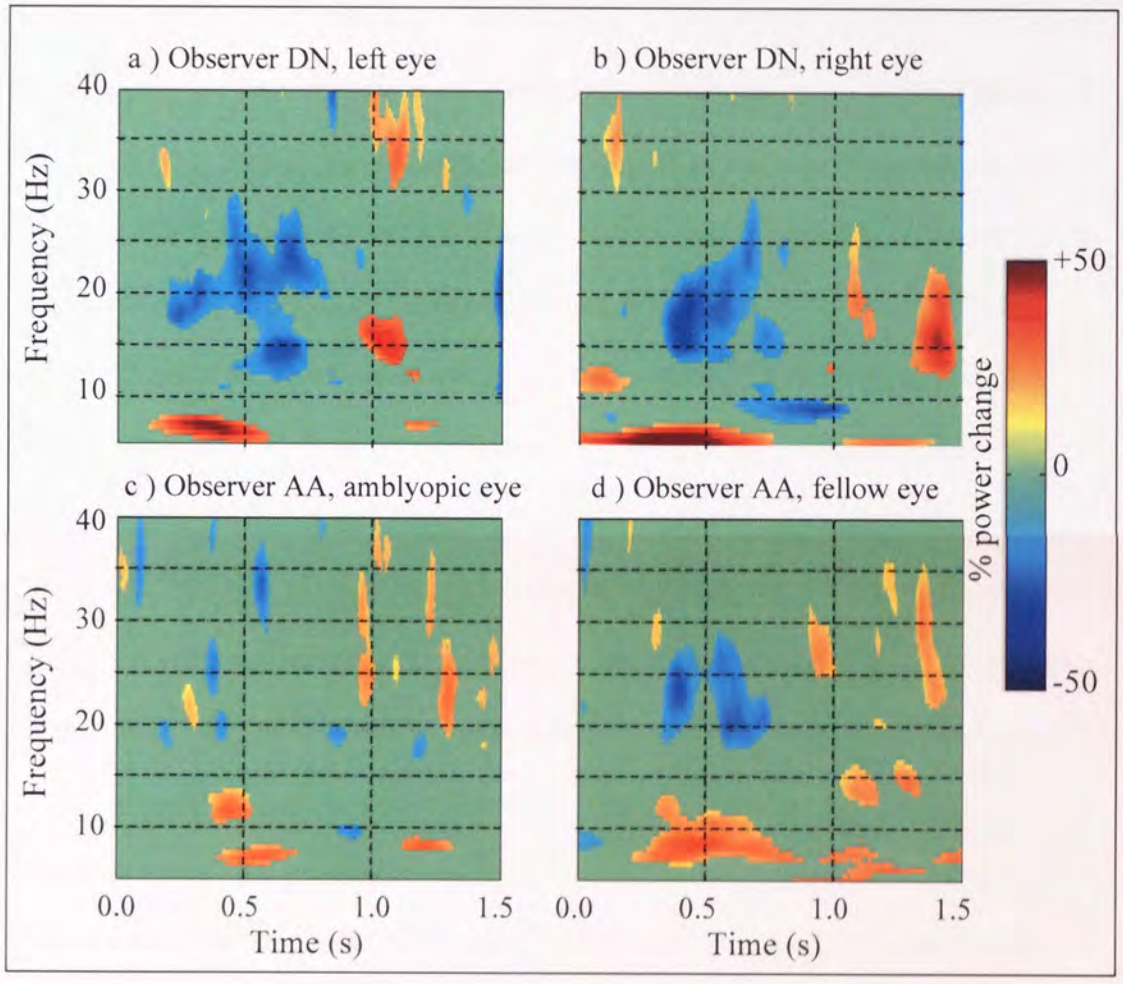

Figure 8.3. Time-frequency wavelet plots for a) left- and b) right-eye viewing for observer DN and c) amblyopic (left)- and d) fellow (right)-eye viewing for observer AA, computed for voxels within extra-striate cortex as delineated by the crosshairs in Figure 8.2. Plots represent frequencies from 5-40 Hz over the time scale zero to 1.5 s and the rotational Glass pattern appeared at time zero. Compared with pre-stimulus activity, significant power reductions and increases are shown as blue and red colours respectively, non-significant ($p > 0.05$) changes in power are green (see "% power change" key.

8.4 Discussion

For both normally-sighted and amblyopic observers, performance for the detection of global structure in horizontal patterns was considerably worse than for either radial or rotational patterns. This pattern-type difference was previously observed with other normally-sighted observers in chapter 4 and has been discussed in section 4.4.

For the amblyopic observer, the sensitivity to radial, rotational and horizontal patterns was poorer when stimuli were viewed with the amblyopic eye than when viewed with the fellow eye (Figure 8.1). Observer AA was able to resolve each dot within a pair and consequently this effect cannot be attributed simply to poorer visual acuity with the amblyopic eye. Additionally, the detection deficit associated with amblyopic-eye viewing was greater for horizontal than for radial or rotational patterns. This is consistent with the findings of Rislove *et al.* (2005) with four other strabismic amblyopes. Detection of rotational global structure by observer AA was near perfect for both eyes at coherences greater than 22 percent and as such the coherence level of 100 percent used in the MEG experiment was sufficient to ensure form perception.

With each eye of both a normally-sighted and an amblyopic observer, the perception of rotational form caused a reduction in oscillatory power in the 15-25 Hz band in ventral occipital cortex (Figure 8.2). The peak of this reduced power was within, or close to, V4 (Hasnain *et al.*, 1998). This is consistent with evidence from recent human studies that suggests area V4 is involved in the processing of global form in Glass patterns (Gallant *et al.*, 2000; Krekelberg, Vatakis, Kourtzi, 2005). Time-frequency analysis of this region of interest revealed prominent reductions in beta band activity for both eyes of the normally-sighted observer but only for the fellow eye of the amblyopic observer.

Analysis of the amblyopic-eye data for AA yielded no evidence of a sustained change in oscillatory power within any frequency band (Figure 8.3). As discussed in section 4.4, it has been argued that reduced power within beta frequency brain rhythms reflects an area of heightened neural activity (Pfurtscheller, 2001; Singh *et al.*, 2002). Therefore, the neural assembly associated with form perception may be dysfunctional in amblyopia. The nature of this dysfunction may relate to a change in the normal temporal pattern of neuronal discharges, affecting a reduced capacity of V4 to engage in the transfer or processing of information associated with the construction of global form from local image features.

9 FMRI: The response to global structure in Glass patterns

9.1 Introduction

Both fMRI and MEG are non-invasive techniques that may be used to investigate human neural function. With a typical study, areas of activation or deactivation associated with presentation of a stimulus are localised. However, ethical considerations with human studies prevent the use of invasive techniques, such as ablation, to confirm the location of such areas in stimulus processing. By using more than one neuroimaging technique, results with each method can be compared and contrasted.

Similar spatial distributions of activity with different imaging techniques increase confidence that the identified neural areas are involved in stimulus processing, while differing spatial distributions may reflect fundamental differences between the techniques. For example, the BOLD signal measured with fMRI is considered indicative of the metabolic demand of neurons (reviewed in Logothetis & Pfeuffer, 2004), but its spatial resolution may be affected by changes of blood flow and oxygenation in remote draining veins (Boxerman *et al.*, 1995). Oscillatory power, as measured using SAM, correlates with the extent of neuronal synchonisation (reviewed in Hillebrand *et al.*, 2005), but deep or radially oriented sources (e.g. crests of gyri) may not produce measurable magnetic fields (Hillebrand & Barnes, 2002). Despite these known differences, Singh *et al.* (2002) have shown that for a variety of cognitive tasks, there is a spatial correspondence between the BOLD response and reduced oscillatory power.

In this chapter, fMRI was used to reveal areas of neural activation following presentation of radial, rotational and horizontal Glass patterns. The Glass patterns had the same stimulus dimensions as those in the MEG experiment of chapter 4, allowing a

direct comparison of the techniques. In particular, the possible involvement of V1 in global form processing was investigated as the BOLD signal is not affected by self cancelling magnetic fields (see section 5.1).

9.2 Methods

9.2.1 Observers

Eight observers (four males and four females, aged 23-38 years) with no history of neurological dysfunction or injury consented to participate in this experiment. All observers were screened with a questionnaire to ensure they did not have any metallic objects on or within their person. Observers had normal or corrected-to-normal vision. All stimuli were viewed monocularly using the dominant eye. The eye not being used was occluded with a dark eye patch. Observers were instructed to maintain fixation.

9.2.2 Stimulus generation and presentation

Stimuli were Glass patterns with a central fixation circle. Dimensions were as in section 4.2.2. The experiment consisted of four runs, each containing 20 epochs of 15 s duration. Within each run, there were five epochs each of radial, rotational and horizontal Glass patterns. The coherence of these Glass patterns was 100 percent. The remaining five epochs contained a zero coherence Glass pattern. The epoch order was pseudo-random. With each epoch, the fixation circle had an 80 and 20 percent chance of being red or grey respectively. To encourage the observer to maintain attention, the observer was asked to count the occurrences of the grey fixation circle and report this number after each run.

9.2.3 Image acquisition

Imaging was performed on a 3-Tesla Siemens Trio Magnetom. The observer lay inside the scanner and stimuli were viewed on a back-projection screen via a single mirror mounted on an 8-channel head coil. Stimulus generation was controlled by a Cambridge Research Systems VSG2/5 card (Cambridge Research Systems, Rochester, Kent, UK) and projected using a Sanyo Multiverse projector. An anatomical image was obtained for each observer either before or after the functional scans. Functional images were acquired transversely, from the anterior to the posterior. Each functional scan was composed of 44 slices covering the entire brain, each 3 mm thick with a 19.2 cm field of view. The scan matrix was 64 x 64 mm, TR was 3 s, TE was 30 ms, voxel size was 3 mm^3 and the flip angle was 90°. Functional scans were motion-corrected online using Siemens' inbuilt program.

Analysis of the fMRI data was performed using SPM99 (Friston *et al.*, 1995). The functional scans were realigned, spatially normalised and then spatially smoothed with a 4 mm Full Width Half Maximum (FWHM) Gaussian kernel. The data were convolved with the haemodynamic response function (HRF) kernel and high-pass temporally filtered at 128 s. Group statistical analyses were performed to compare the neural response to radial, rotational and horizontal patterns with the neural response to zero coherence patterns. A general linear model for random-effects was used and t score maps of increased BOLD amplitude ($p < 0.05$, corrected) are shown displayed on the template brain using SPM99 and mri3dX software. Cortical areas were defined with a combination of the Talairach Daemon database (Lancaster *et al.*, 2000) and the co-ordinates of visual areas mapped by Hasnain *et al.* (1998).

9.3 Results

Figure 9.1 shows areas of increased BOLD amplitude following the presentation of a) radial, b) rotational and c) horizontal Glass patterns. Note that in response to horizontal patterns there were no clusters of activation revealed. However, radial patterns yielded bilateral activity within the middle occipital gyrus, the cuneus, BA19 and V3a. Rotational patterns yielded bilateral activity within the middle occipital gyrus, BA18, V3a and V5.

The areas of activation associated with radial patterns were mainly dorsal to those associated with rotational patterns. This can be observed on coronal (Figure 9.2), axial (Figure 9.3) and sagittal (Figure 9.4) slices. The activation is shown rendered on the brain surface in Figure 9.5. The neural volume activated by both radial and rotational Glass patterns (yellow) was only 0.46 cm^3 whereas the overall volume activated by radial patterns (red) was 1.43 cm^3, and that by rotational patterns (green) was 2.62 cm^3. A voxel of activation to horizontal patterns (blue) can be observed in Figure 9.4 (f) in the limbic lobe. This was one of only three single voxels (0.02 cm^3) activated by horizontal patterns with another in extrastriate cortex and another in the cerebellum.

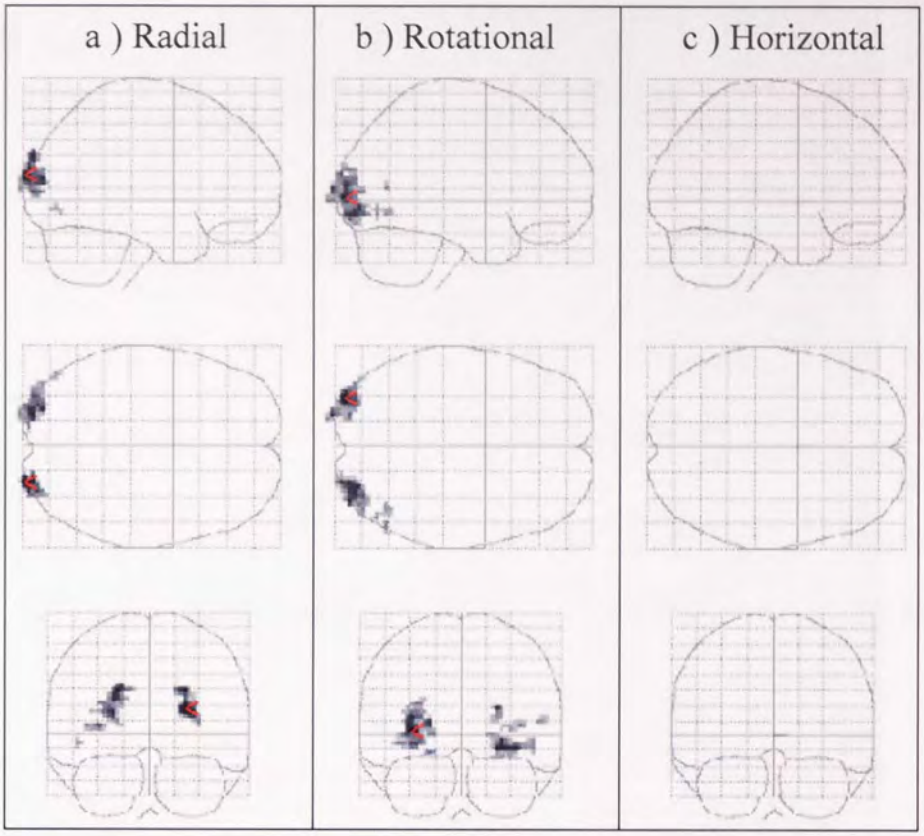

Figure 9.1. Group SPM{t}maps (n = 8) for comparison of BOLD amplitude during presentation of a) radial, b) rotational and c) horizontal Glass patterns (active phase) with that during presentation of random Glass patterns (passive phase). Regions of increased BOLD amplitude in the active phase are shown darkened on an outline of the template brain. Only clusters larger than five voxels and significant at $p < 0.05$ (corrected) are shown. The red arrow points to the voxel with the largest t value, for both radial and rotational patterns this was in the middle occipital gyrus. For horizontal patterns no increases in BOLD amplitude were revealed.

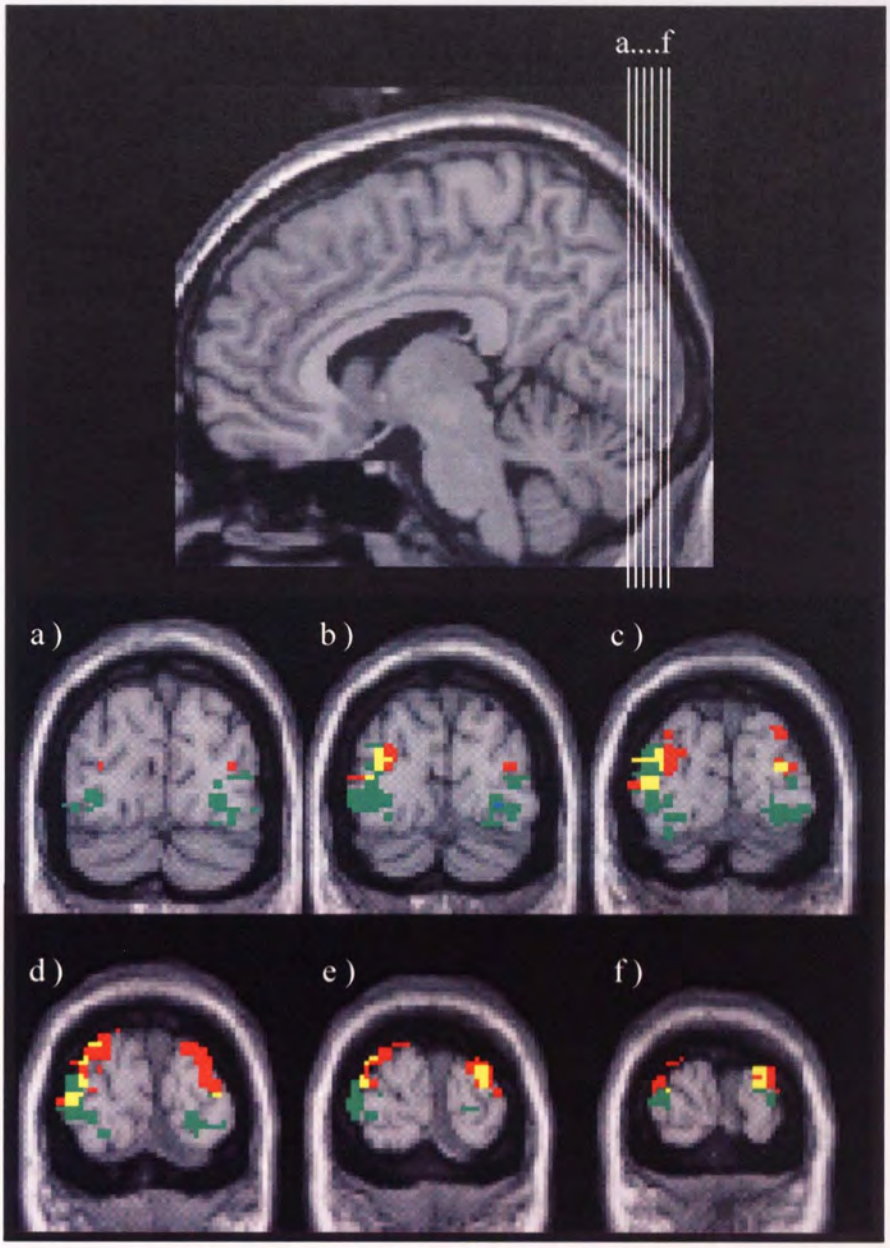

Figure 9.2. Regions of significantly increased BOLD signal ($p < 0.05$, corrected) following radial (red), rotational (green) and both radial and rotational (yellow) Glass patterns are shown on a template brain. Coronal slices at a) -85, b) -88, c) -91, d) -94, e) -97, and f) -100 mm (Talairach space) are shown as illustrated by the white lines on the sagittal slice in the top panel.

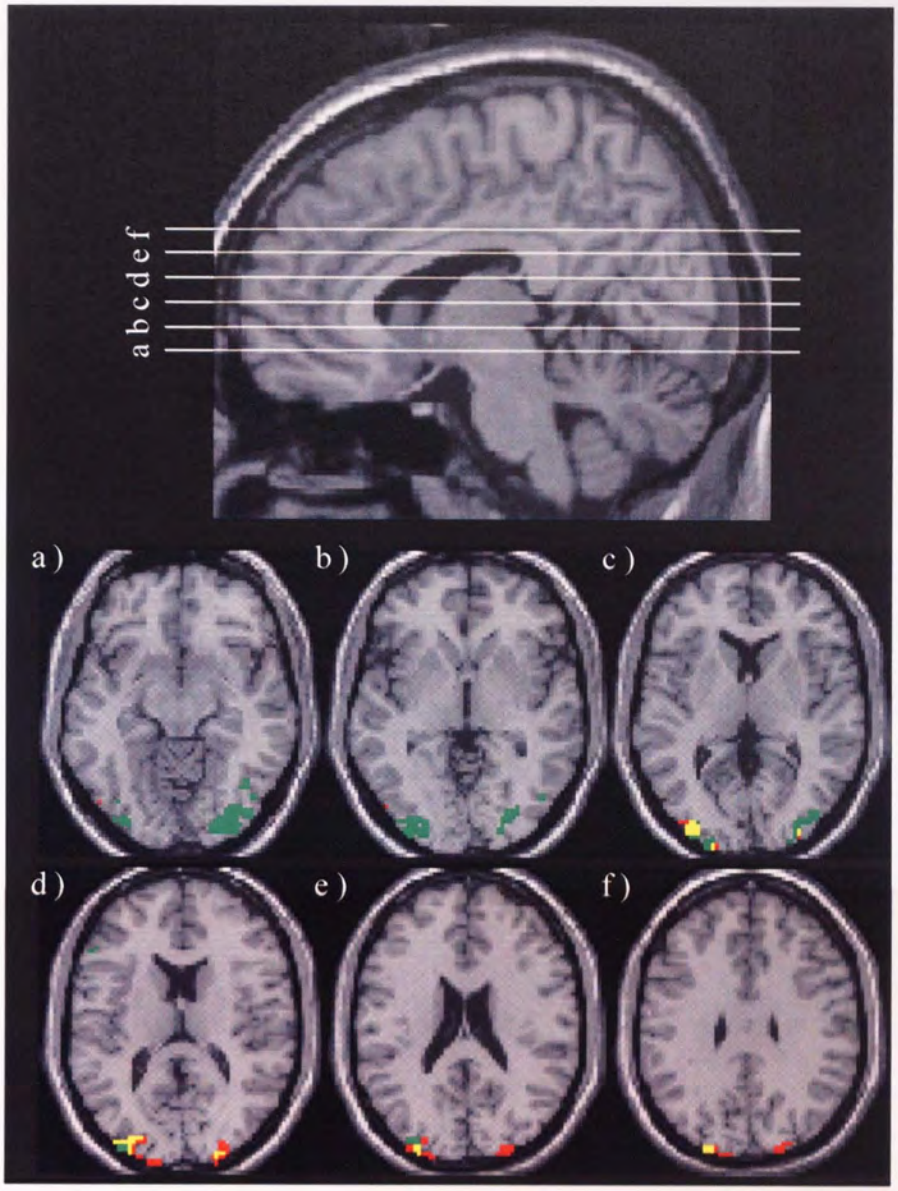

Figure 9.3. As in Figure 9.2 but axial slices at a) -10, b) -2, c) 6, d) 14, e) 22, and f) 30 mm (Talairach space) are shown as illustrated by the white lines on the sagittal slice in the top panel.

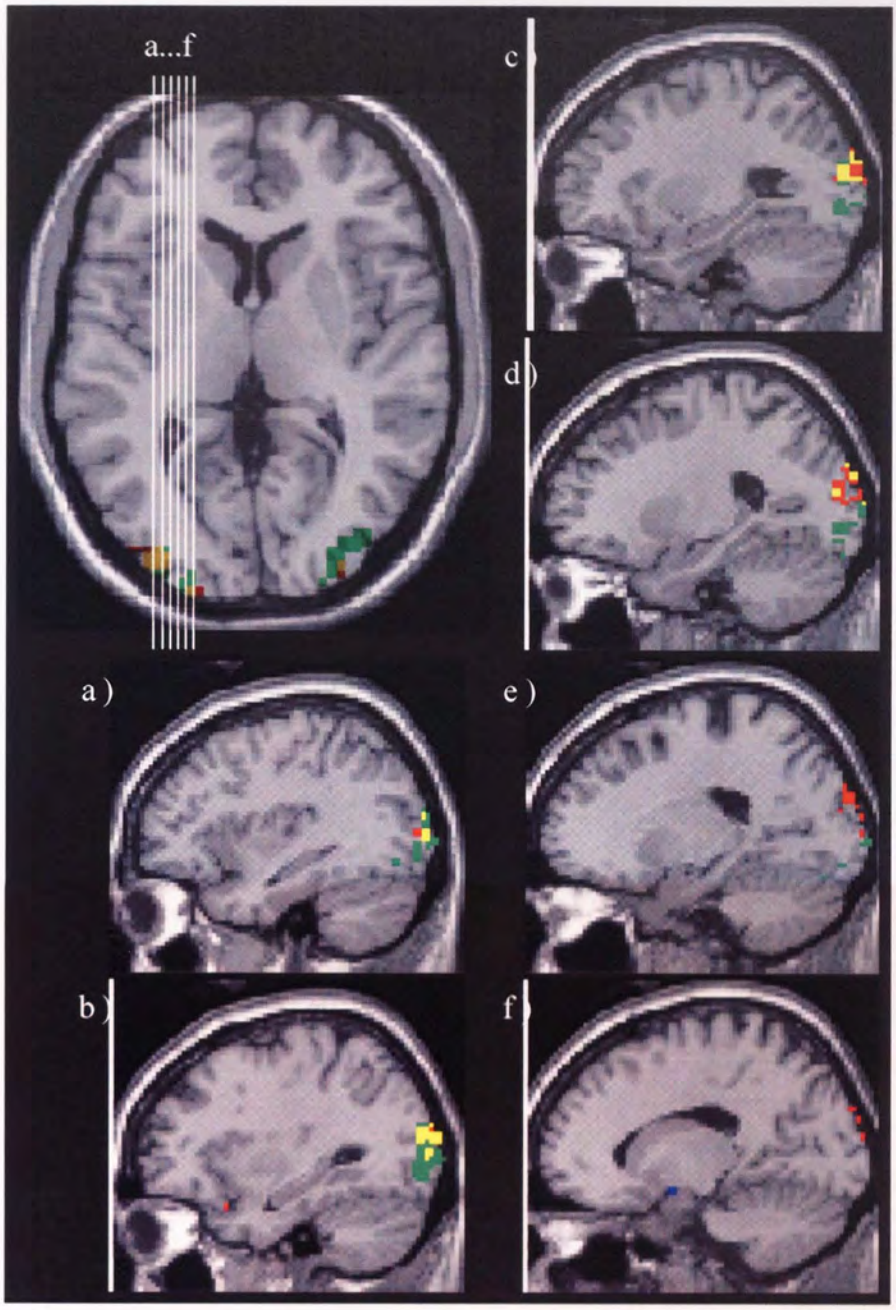

Figure 9.4. As in Figure 9.2 but sagittal slices at a) -35, b) -31, c) -27, d) -23, e) -19, and f) -15 mm (Talairach space) are shown as illustrated by the white lines on the axial slice in the top-left panel.

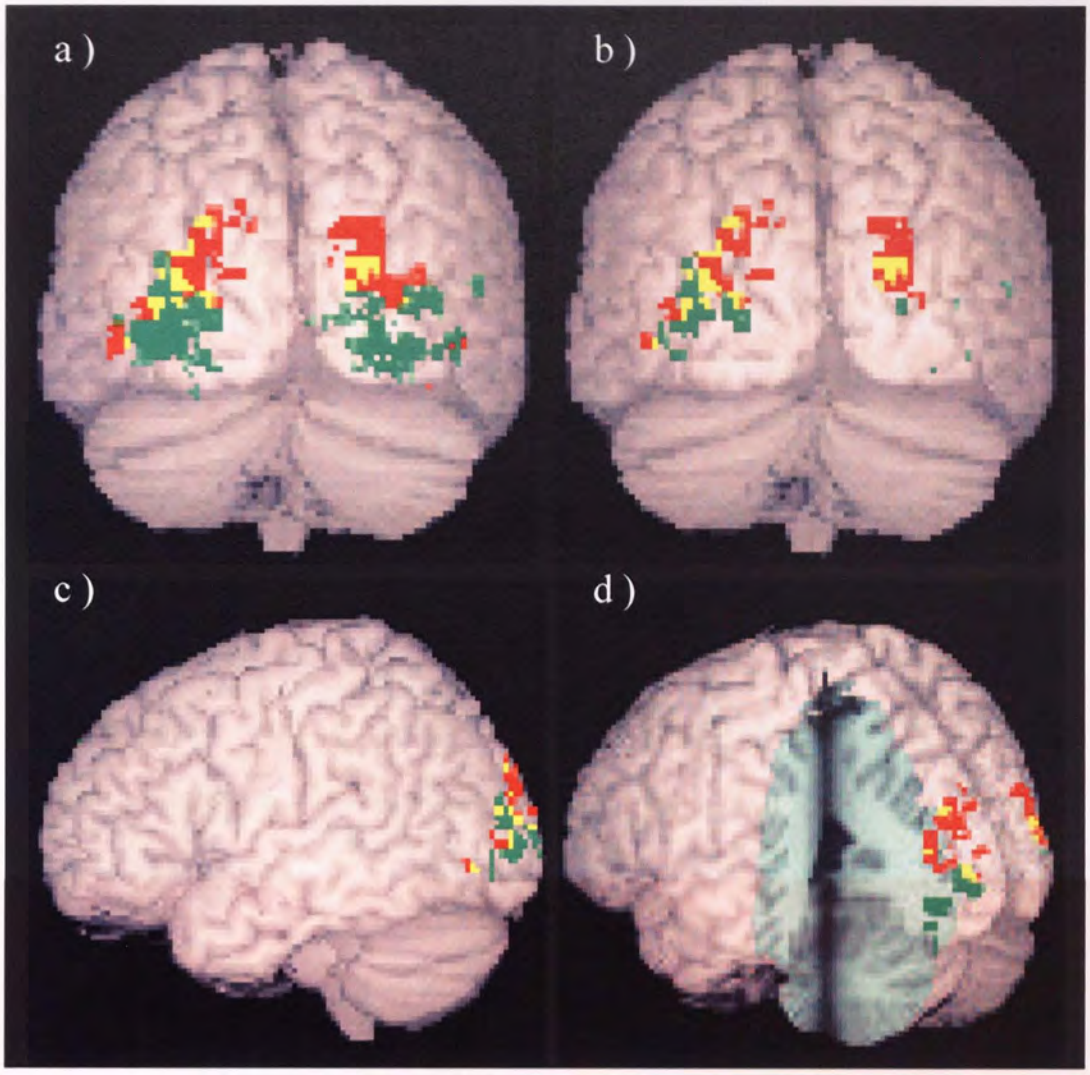

Figure 9.5. Regions of significantly increased BOLD signal ($p < 0.05$, corrected) following radial (red), rotational (green) and both radial and rotational (yellow) Glass patterns are shown rendered on a) the back of the brain with activation pulled 10 mm to the surface; b) the back of the brain with activation pulled 1 mm to the surface; c) the left hemisphere with activation pulled 1 mm to the surface; d) the back of the brain with a cut-away section through the left hemisphere and activation pulled 1 mm to the surface.

9.4 Discussion

The presentation of coherent radial and rotational Glass patterns produced bilateral increases in the BOLD signal in extrastriate cortex. For both pattern types, the areas of

activation covered regions of cortex that had shown reduced oscillatory power with SAM in frequency bands between 5 and 40 Hz (see chapter 4). These results support the belief that the BOLD response may in large part reflect reduced oscillatory power (Singh *et al.*, 2002). However, unlike the results from the MEG experiments, the areas of BOLD response associated with radial and rotational Glass patterns were spatially distinct. Radial patterns elicited more dorsal activation than rotational patterns; the voxel with the largest t value following radial patterns was in V3a whereas that following rotational patterns was close to V5 (see red arrows in Figure 9.1; Hasnain *et al.*, 1998). These spatial differences in the BOLD response may reflect the involvement of dorsal areas in implied- and real-motion processing and ventral areas in global form processing (Krekelberg *et al.*, 2005). Note, however that reduced oscillatory power with MEG was observed in V3a following presentation of stationary Gabor patches with rotational form (see Figure 7.2).

In response to horizontal Glass patterns, no clusters of increased BOLD signal were found. This is in contrast to the findings in chapter 4 where horizontal patterns elicited significant regions of reduced oscillatory power (between 5 and 40 Hz) with group analyses. The absence of a response to horizontal patterns using fMRI may reflect the fact that the data were analysed using a random-effects model which is more conservative than a fixed-effects model. Interestingly, SnPM analyses of the group MEG data found less areas of reduced oscillatory power following radial than following either rotational or horizontal Glass patterns. A possible reason for this difference was spatial variability in the neural response to radial patterns (see section 4.4).

Area V1 did not show a significant BOLD response to coherent Glass patterns. This supports the finding with SnPM that V1 is not a principal neural area for processing global form (chapter 4). It also supports the finding of chapter 5 that this lack of activity with SnPM was not due to self-cancelling magnetic fields.

10 General conclusions

The following general conclusions on global form processing are based on evidence from the behavioural, MEG and fMRI experiments reported in this thesis:

(1) The human visual system is less sensitive to horizontal structure than to either radial or rotational structure; sensitivity to radial and rotational structure is similar (Figure 3.11).

(2) The differences in sensitivity for detecting different types of global structure are reflected in the neuroimaging data for the perception of Glass patterns.

(3) A network of cortical areas is activated by the perception of global form, including dorsal and ventral extrastriate cortex within or close to V3a and V4 respectively.

(4) Areas of increased BOLD response found with fMRI are often, but not always, located in areas of reduced beta band oscillatory power, as measured with MEG. The relationship between these two physiological measures warrants further research.

(5) There was no evidence that the perception of global form initiated feedback from higher cortical areas to the primary visual cortex.

(6) Strabismic amblyopes are less sensitive to global structure, which may be because the neuronal assembly associated with form perception in extrastriate cortex of amblyopes is dysfunctional. The nature of this dysfunction may relate to a change in the normal temporal pattern of neuronal discharges (Figure 8.3).

Determining the temporal thresholds for detection of structure within Glass patterns provided a novel means by which to assess differences in the perception of horizontal, radial and rotational patterns. Regardless of pattern type, the results show that at

coherence levels exceeding approximately 10 % there was a reciprocal relationship between time and coherence, indicative of an efficient integrative process. However, at lower coherences this relationship broke down and integration was less efficient (Figure 3.12). The presence of two different integrative processes in the normal visual system has implications for previously published studies that have examined global structure sensitivity using coherence thresholds (Dakin & Bex, 2002; Kelly *et al.*, 2001; Maloney *et al.*, 1987; Seu & Ferrera, 2001; Wilson & Wilkinson, 1998; Wilson *et al.*, 1997). These studies have been inconclusive as to whether or not the visual system is less sensitive to horizontal structure. The results presented here provide evidence for why this may be so. Namely, by determining the lowest coherence for detection the previous studies may have tapped visual processing at the point where efficiency reduces and the amount of signal needed for detection is more variable. Future studies may benefit from using the temporal threshold technique to examine visual processing at higher coherence levels that best represent overall visual function.

The neuroimaging studies (fMRI and MEG) were in broad agreement with the behavioural studies in demonstrating differences in the neural processing between horizontal patterns and either radial or rotational patterns. FMRI failed to identify any cortical activity in response to the presentation of horizontal Glass patterns, but did identify bilateral clusters of activity (increased BOLD signal) within extrastriate cortex following the presentation of either radial or rotational patterns - the areas of activation in response to radial patterns were dorsal to those in response to rotational patterns (Figure 9.5). This compares with the MEG studies in which bilateral regions of activity (reduced oscillatory power, 5-40 Hz) within extrastriate cortex were evident following the presentation of each pattern type. While the regions of activity identified for radial,

rotational and horizontal Glass patterns using MEG were spatially indistinguishable, further analysis showed that horizontal patterns yielded oscillatory power changes that were weaker and more limited in duration than the power changes yielded by either radial or rotational patterns (Figures 4.11-4.12). The lack of increased BOLD signal and the lesser power changes observed following the presentation of horizontal patterns provides evidence to suggest that the extent of neural activity yielded by such patterns is significantly less that that yielded by either rotational or radial Glass patterns.

The network of extrastriate areas identified as being involved in processing global form included a dorsal focus within or close to V3a, and ventral activation within or close to V4 and V5 (Hasnain *et al.*, 1998). Previous functional imaging studies have charged V3a with motion processing (Braddick *et al.*, 2000; Braddick *et al.*, 2001; Krekelberg *et al.*, 2005; Tootell *et al.*, 1997), but this area was also activated following the presentation of an array of stationary Gabor patches oriented to form a global percept of rotational structure (Figure 7.2). The latter suggests that, in addition to its reported role in motion processing, area V3a may also have a fundamental role to play in global form processing. Area V5 (human MT) has also been implicated in motion processing (reviewed in Born & Bradley, 2005), although the large inter-observer variability in location of V5 and V4 often make it difficult to distinguish between these areas (Hasnain *et al.*, 1998). Based on fMRI studies on neurologically normal observers and behavioural studies on an observer with a lesion in V4, it has been suggested that Glass patterns are processed in V4 (Gallant *et al.*, 2000; Krekelberg *et al.*, 2005). The results presented in this thesis are consistent with this.

Cortical area V1 was not identified as an area of peak activity with MEG (see chapter 4). Due to the cruciform structure of V1, it was possible that magnetic fields produced in this area had self-cancelled (see section 5.1). To examine this possibility, a separate MEG experiment was conducted in which the Glass patterns were viewed within a single visual quadrant (chapter 5). In addition, an fMRI experiment was performed (chapter 9). The results of these experiments provide evidence to suggest that V1 is not an area of peak activity during the perception of global form in Glass patterns. This is consistent with the findings of previous studies of global form processing where the local cues were controlled (Braddick *et al.*, 2000; Ohla *et al.*, 2005; Krekelberg *et al.*, 2005). However, other studies have reported that activity in V1 decreases in response to the perception of global form, concurrent with increases in activity in the LOC (Lerner *et al.*, 2001; Murray *et al.*, 2004). Murray *et al.* interpreted this as evidence of negative feedback from the LOC to V1. To assess the hypothesis of Murray *et al.*, the neural responses to Glass patterns with different degrees of rotational structure were measured relative to neural activity during the presentation of a blank screen. Again, V1 was not identified as an area of peak activity and no systematic coherence-related differences in oscillatory power were found between occipital areas. These results, therefore, do not support the theory of negative feedback to V1 in response to global form.

Strabismic amblyopia is a visual disorder associated with marked uncertainty in positional judgements that cannot be attributed simply to either reduced visual acuity or reduced contrast sensitivity (reviewed in Hess, 2002). Of particular interest to the scope of this thesis was the effect of amblyopia on global form perception. Viewing with the amblyopic eye reduced sensitivity to structure in Glass patterns relative to viewing with the fellow eye (Figure 8.1). This effect was particularly marked for horizontal patterns

compared with radial or rotational patterns, and is consistent with the general findings of Rislove *et al.* (2005). In addition, inter-ocular differences in the neural processing of rotational form were observed using MEG. In response to rotational structure viewed with the fellow eye, reductions in beta band activity were evident within or close to area V4 that were comparable with the activity observed in this area in a normally-sighted observer (Figures 8.2-8.3). However, when rotational structure was viewed with the amblyopic eye the reductions in beta activity within V4 were not observed. This suggests that the neural assembly associated with global form perception may be dysfunctional when driven by the amblyopic eye. The nature of this dysfunction may relate to a change in the normal temporal pattern of neuronal firing and may affect a reduced capacity of V4 to process information about global form. This is consistent with the observation that sensitivity to global form in Glass patterns was reduced in an observer with a discrete lesion in V4 (Gallant *et al.*, 2000). This case study provides evidence that neuronal dysfunction in strabismic amblyopia can extend beyond the primary visual areas although further studies with more amblyopic observers are needed to confirm the generality of this dysfunction.

Over recent years, SAM has become increasingly established as a method for revealing non-phase locked power changes, with the only assumption being that the local field potentials between areas do not interact linearly (reviewed in Hillebrand *et al.*, 2005). SAM studies have shown that: a) it is non-phase locked, rather than phase locked, cortical activity that best correlates with varying stimulus parameters such as temporal frequency (Fawcett, Barnes, Hillebrand, Singh, 2004); b) oscillatory power changes measured with SAM are comparable with changes in local field potentials in primate (Hall *et al.*, 2005); c) neural sources can be resolved across most of the cortex, with

only thin (≈ 2 mm) strips on the crests of gyri not producing measurable magnetic fields (Hillebrand & Barnes, 2002); and d) decreases in beta band oscillatory power occur in the same location as increases in the fMRI BOLD response (Singh *et al.*, 2002). The results of this thesis are in general agreement with the assertion of Singh *et al.* (2002) that an increase in the BOLD response is spatially coincident with a decrease in oscillatory power (principally in the beta band) as measured with SAM (see chapters 4 and 9). However, the results reveal that this simple relationship may not always hold. For example, the perception of horizontal Glass patterns did not elicit any regions of increased BOLD signal, whereas regions of reduced oscillatory power (5-40 Hz) were identified with SAM. In addition, time-frequency analyses revealed that a given voxel could have successive periods of decreased and increased oscillatory power. Thus an increased BOLD response could be spatially coincident with either a decrease or increase in oscillatory power. It is possible that the BOLD response reflects both inhibitory and excitatory synaptic activity as both result in an increased metabolic demand (reviewed in Logothetis & Wandell, 2004).

To perform SAM analyses the time and frequency bands of interest must be defined. In this thesis, several frequency bands between 5 and 40 Hz were analysed. Although it is always possible that activity occurred at other frequencies, this range covered frequencies that have been shown to be involved in other global form processing tasks (Singh *et al.*, 2003). In addition, the maximum pseudo t scores were observed to be greatest with frequency bands in the middle of this range, and there were only small activations at frequencies greater than 30 Hz (Figures 4.5-4.7). A period of reduced power was often followed by a period of increased power in the same frequency band (e.g. Figure 4.11). If a decrease and increase in oscillatory power occurred within the

chosen analysis time window, then only a small pseudo t value would be shown on the SAM image. In such a case, that voxel would not be selected as a region of interest. However, SAM analyses using 500 ms time windows showed that the locations of activation were similar to those observed using 1 s time windows (Figures 4.8-4.10). This increases confidence that principle areas of neural activation were not going undetected. The identification by SAM of activity in neural areas that are consistent with those found in previous global form imaging studies (e.g. Braddick *et al.*, 2000), and the reproducibility of the results when the separation between experiments was as great as ten months (Figures 5.2-5.3), supports the use of SAM as an analysis technique.

References

Achtman RL, Hess RF, Wang YZ. 2003. Sensitivity for global shape detection. *Journal of Vision*, **3**, 616-624.

Algaze A, Leguire LE, Roberts C, Ibinson JW, Lewis JR, Rogers G. 2005. The effects of L-dopa on the functional magnetic resonance imaging response of patients with amblyopia: a pilot study. *Journal of AAPOS*, **9**, 216-223.

Algaze A, Roberts C, Leguire LE, Schmalbrock P, Rogers G. 2002. Functional magnetic resonance imaging as a tool for investigating amblyopia in the human visual cortex: a pilot study. *Journal of AAPOS*, **6**, 300-308.

Altmann CF, Bülthoff HH, Kourtzi Z. 2003. Perceptual organization of local elements into global shapes in the human visual cortex. *Current Biology*, **13**, 342-349.

Amunts K, Malikovic A, Mohlberg H, Schormann T, Zilles K. 2000. Brodmann's areas 17 and 18 brought into stereotaxic space – where and how variable? *Neuroimage*, **11**, 66-84.

Anderson SJ, Hess RF. 1990. Post-receptoral undersampling in normal human peripheral vision. *Vision Research*, **30**, 1507-1515.

Anderson SJ, Holliday IE, Harding GFA. 1999. Assessment of cortical dysfunction in human strabismic amblyopia using magnetoencephalography (MEG). *Vision Research*, **39**, 1723-1738.

Anderson SJ, Swettenham JB. 2006. Neuroimaging in human amblyopia. *Strabismus*, **14**, 21-35.

Andrews TJ, Halpern SD, Purves D. 1997. Correlated size variations in human visual cortex, lateral geniculate nucleus, and optic tract. *The Journal of Neuroscience*, **17**, 2859-2868.

Angelucci A, Levitt JB, Walton EJS, Hupé J-M, Bullier J, Lund JS. 2002. Circuits for local and global signal integration in primary visual cortex. *The Journal of Neuroscience*, **22**, 8633-8646.

Ashburner J, Friston KJ. 1999. Nonlinear spatial normalization using basis functions. *Human Brain Mapping*, **7**, 254-266.

Ashburner J, Friston KJ. 2000. Voxel-based morphometry: the methods. *Neuroimage*, **11**, 805-821.

Ashburner J, Friston KJ. 2001. Why voxel-based morphometry should be used. *Neuroimage*, **14**, 1238-1243.

Attwell D, Iadecola C. 2002. The neural basis of functional brain imaging signals. *Trends in Neuroscience*, **25**, 621-625.

Bair W. 2005. Visual receptive field organization. *Current Opinion in Neurobiology*, **15**, 459-464.

Barnes GR, Hess RF, Dumoulin SO, Achtman RL, Pike GB. 2001. The cortical deficit in humans with strabismic amblyopia. *Journal of Physiology*, **533**, 281-297.

Barnes GR, Hillebrand A, Fawcett IP, Singh KD. 2004. Realistic spatial sampling for MEG beamformer images. *Human Brain Mapping*, **23**, 120-127.

Barrett BT, Pacey IE, Bradley A, Thibos LN, Morrill P. 2003. Nonveridical visual perception in human amblyopia, *Investigative Ophthalmology and Visual Science*, **44**, 1555-1567.

Blakemore C. 1990. Maturation of mechanisms for efficient spatial vision. In: Blakemore C, Eds. *Vision: coding and efficiency*. Cambridge University Press, UK, 254-266.

Born RT, Bradley DC. 2005. Structure and function of visual area MT. *Annual Review of Neuroscience*, **28**, 157-189.

Boxerman JL, Bandettini PA, Kwong KK, Baker JR, Davis TL, Rosen BR, Weisskoff RM. 1995. The intravascular contribution to fMRI signal change – Monte-Carlo modelling and diffusion-weighted studies in-vivo. *Magnetic Resonance in Medicine*, **34**, 4-10.

Boynton GM, Finney EM. 2003. Orientation-specific adaptation in human visual cortex. *Journal of Neuroscience*, **23**, 8781-8787.

Braddick OJ, O'Brien JMD, Wattam-Bell J, Atkinson J, Hartley T, Turner R. 2001. Brain areas sensitive to coherent visual motion. *Perception*, **30**, 61-72.

Braddick OJ, O'Brien JMD, Wattam-Bell J, Atkinson J, Turner R. 2000. Form and motion coherence activate independent, but not dorsal/ventral segregated, networks in the human brain. *Current Biology*, **10**, 731-734.

Brett M, Johnsrude IS, Owen AM. 2002. The problem of functional localization in the human brain. *Nature Reviews Neuroscience*, **3**, 243-249.

Bridge H, Clare S, Jenkinson M, Jezzard P, Parker AJ, Matthews PM. 2005. Independent anatomical and functional measures of the V1/V2 boundary in human visual cortex. *Journal of Vision*, **5**, 93-102.

Burr DC, Santoro L. 2001. Temporal integration of optic flow, measured by contrast and coherence thresholds. *Vision Research*, **41**, 1891-1899.

Callaghan PT. 1991. *Principles of Nuclear Magnetic Resonance Microscopy*. Oxford University Press, USA.

Carandini M, Movshon JA, Ferster D. 1998. Pattern adaptation and cross-orientation interactions in the primary visual cortex. *Neuropharmacology*, **37**, 501-511.

Carlson NR. 1994. Vision. In: Carlson NR, Eds. *Physiology of Behaviour*. Allyn and Bacon, USA, 145-163.

Chan ST, Tang KW, Lam KC, Chan LK, Mendola JD, Kwong KK. 2004. Neuroanatomy of adult strabismus: a voxel based morphometric analysis of magnetic resonance structural scans. *Neuroimage*, **22**, 986-994.

Choi MY, Lee K-M, Hwang J-M, Choi DG, Lee DS, Park KH, Yu YS. 2001. Comparison between anisometropic and strabismic amblyopia using functional magnetic resonance imaging. *British Journal of Ophthalmology*, **85**, 1052-1056.

Choi MY, Lee DS, Hwang J-M, Choi DG, Lee K-M, Park KH, Yu YS. 2002. Characteristics of glucose metabolism in the visual cortex of amblyopes using positron emission tomography and statistical parametric mapping. *Journal of Pediatric Ophthalmology and Strabismus*, **39**, 11-19.

Chua B, Mitchell P. 2004. Consequences of amblyopia on education, occupation, and long term vision loss. *British Journal of Ophthalmology*, **88**, 1119-1121.

Cosmelli D, Olivier D, Lachaux JP, Martinerie J, Garnero L, Renault B, Varela F. 2004. Waves of consciousness: ongoing cortical patterns during binocular rivalry. *Neuroimage*, **23**, 128-140.

Cowan AI, Stricker C. 2004. Functional connectivity in layer IV local excitatory circuits of rat somatosensory cortex. *Journal of Neurophysiology*, **92**, 2137-2150.

Dakin SC, Bex PJ. 2002. Summation of concentric orientation structure: seeing the Glass or the window. *Vision Research*, **42**, 2013-2020.

Daw NW. 1995. *Visual Development*. Plenum Press, USA.

Del Gratta C, Pizzella V, Tecchio F, Romani GL. 2001. Magnetoencephalography - a noninvasive brain imaging method with 1 ms time resolution. *Reports on Progress in Physics*, **64**, 1759-1814.

Demanins R, Wang YZ, Hess RF. 1999. The neural deficit in strabismic amblyopia: sampling considerations. *Vision Research*, **39**, 3575-3585.

Demer JL, Grafton S, Marg E, Mazziotta,JC, Nuwer M. 1997. Positron emission tomographic study of human amblyopia with use of defined visual stimuli. *Journal of AAPOS*, **1**, 158-171.

Demer JL, Von Noorden GK, Volkow ND, Gould KL. 1988. Imaging of cerebral blood flow and metabolism in amblyopia by positron emission tomography. *American Journal of Opthalmology*, **105**, 337-347.

Di Russo F, Martinez A, Sereno MI, Pitzalis S, Hillyard SA. 2001. Cortical sources of the early components of the visual evoked potential. *Human Brain Mapping*, **15**, 95-111.

Duvernoy HM, Delon S, Vannson JL. 1981. Cortical blood-vessels of the human brain. *Brain Research Bulletin*, **7**, 519-579.

Fawcett IP, Barnes GR, Hillebrand A, Singh KD. 2004. The temporal frequency tuning of human visual cortex investigated using synthetic aperture magnetometry. *Neuroimage*, **21**, 1542-1553.

Felleman DJ, Van Essen DC. 1991. Distributed hierarchical processing in the primate cerebral cortex. *Cerebral Cortex*, **1**, 1-47.

Fielder A. 2002. Amblyopia and disability. In: Moseley M, Fielder A. Eds. *Amblyopia: a Multidisciplinary Approach.* Butterworth Heinmann, UK, 105-114.

Frackowiak RSJ, Friston KJ, Frith C, Dolan R, Mazziotta. Eds. *Human Brain Function.* Academic Press, USA.

Friston KJ, Holmes AP, Worsley KJ, Poline JB, Frith CD, Frackowiak RSJ. 1995. Statistical parametric maps in functional imaging: a general linear approach. *Human Brain Mapping*, **2**, 189-210.

Gallant JL, Braun J, Van Essen DC. 1993. Selectivity for polar, hyperbolic, and cartesian gratings in macaque visual cortex. *Science*, **259**, 100-103.

Gallant JL, Connor CE, Rakshit S, Lewis JW, VanEssen DC. 1996. Neural responses to polar, hyperbolic, and Cartesian gratings in area V4 of the macaque monkey. *Journal of Neurophysiology*, **76**, 2718-2739.

Gallant JL, Shoup RE, Mazer JA. 2000. A human extrastriate area functionally homologous to macaque V4. *Neuron*, **27**, 227-235.

Girard P, Hupé JM, Bullier J. 2001. Feedforward and feedback connections between areas V1 and V2 of the monkey have similar rapid conduction velocities. *Journal of Neurophysiology*, **85**, 1328-1331.

Glass L. 1969. Moire effect from random dots. *Nature*, **223**, 578-580.

Glass L, Switkes E. 1976. Pattern-recognition in humans – correlations which cannot be perceived. *Perception*, **5**, 67-72.

Goodyear BG, Nicolle DA, Humphrey GK, Menon RS. 2000. BOLD fMRI response of early visual areas to perceived contrast in human amblyopia. *Journal of Neurophysiology*, **84**, 1907-1913.

Goodyear BG, Nicolle DA, Menon RS. 2002. High resolution fMRI of ocular dominance columns within the visual cortex of human amblyopes. *Strabismus*, **10**, 129-136.

Gottlob I, Stanglerzuschrott E. 1990. Effect of levodopa on contrast sensitivity and scotomas in human amblyopia. *Investigative Ophthalmology & Visual Science*, **31**, 776-780.

Graimann B, Huggins JE, Levine SP, Pfurtscheller G. 2002. Visualization of significant ERD/ERS patterns in multichannel EEG and ECoG data. *Clinical Neurophysiology*, **113**, 43-47.

Grill-Spector K, Kanwisher N. 2005. Visual recognition - As soon as you know it is there, you know what it is. *Psychological Science*, **16**, 152-160.

Grill-Spector K, Kourtzi Z, Kanwisher N. 2001. The lateral occipital complex and its role in object recognition. *Vision Research*, **41**, 1409-1422.

Grill-Spector K, Kushnir T, Edelman S, Itzchak Y, Malach R. 1998. Cue-invariant activation in object-related areas of the human occipital lobe. *Neuron*, **21**, 191-202.

Hadjipapas A, Hillebrand A, Holliday IE, Singh KD, Barnes GR. 2005. Assessing interactions of linear and nonlinear neuronal sources using MEG beamformers: a proof of concept. *Clinical Neurophysiology*, **116**, 1300-1313.

Hall SD, Holliday IE, Hillebrand A, Singh KD, Furlong PL, Hadjipapas A, Barnes GR. 2005. The missing link: analogous human and primate cortical gamma oscillations, *Neuroimage*, **26**, 13-17.

Hämäläinen M, Hari R, Ilmoniemi RJ, Knuutila J, Lounasmaa OV. 1993. Magnetoencephalography - theory, instrumentation, and applications to noninvasive studies of the working human brain. *Reviews of Modern Physics*, **65**, 413-497.

Hasnain MK, Fox PT, Woldorff MG. 1998. Intersubject variability of functional areas in the human visual cortex. *Human Brain Mapping*, **6**, 301-315.

Hasson U, Levy I, Behrmann M, Hendler T, Malach R. 2002. Eccentricity bias as an organizing principle for human high-order object areas. *Neuron*, **34**, 479-490.

Hess RF. 2001. Amblyopia: site unseen. *Clinical and Experimental Optometry*, **84**, 321-336.

Hess RF. 2002. Sensory processing in human amblyopia: snakes and ladders. In: Moseley M, Fielder A. Eds. *Amblyopia: a Multidisciplinary Approach.* Butterworth Heinmann, UK, 19-42.

Hess RF, Anderson SJ. 1993. Motion sensitivity and spatial undersampling in amblyopia. *Vision Research*, **33**, 881-896.

Hess RF, McIlhagga W, Field DJ. 1997. Contour integration in strabismic amblyopia: the sufficiency of an explanation based on positional uncertainty. *Vision Research*, **37**, 3145-3161.

Hess RF, Pointer JS, Simmers A, Bex P. 2003. Border distinctness in amblyopia. *Vision Research*, **43**, 2255-2264.

Hess RF, Wang YZ, Demanins R, Wilkinson F, Wilson HR. 1999. A deficit in strabismic amblyopia for global shape detection. *Vision Research*, **39**, 901-914.

Hillebrand A, Barnes GR. 2002. A quantitative assessment of the sensitivity of whole-head MEG to activity in the adult human cortex. *Neuroimage*, **16**, 638-650.

Hillebrand A, Singh KD, Holliday IE, Furlong PL, Barnes GR. 2005. A new approach to neuroimaging with magnetoencephalography. *Human Brain Mapping*, **25**, 199-211.

Hillis A, Flynn JT, Hawkins BS. 1983. The evolving concept of amblyopia - a challenge to epidemiologists. *American Journal of Epidemiology*, **118**, 192-205.

Horton JC, Stryker MP. 1993. Amblyopia induced by anisometropia without shrinkage of ocular dominance columns in human striate cortex. *Proceedings of The National Academy of Sciences of The United States of America*, **90**, 5494-5498.

Horton JC, Hocking DR. 1996. Pattern of ocular dominance columns in human striate cortex in strabismic amblyopia. *Visual Neuroscience*, **13**, 787-795.

Hubel DH, Wiesel TN. 1968. Receptive fields and functional architecture of monkey striate cortex. *Journal of Physiology*, **195**, 215-243.

Hubel DH, Wiesel TN, Le Vay S. 1977. Plasticity of ocular dominance columns in monkey striate cortex. *Philosophical Transactions of the Royal Society of London Series B-Biological Sciences*, **278**, 377.

Imamura K, Richter H, Fischer H, Lennerstrand G, Franzen O, Rydberg A, Andersson J, Schneider H, Onoe H, Watanabe Y, Langstrom B. 1997. Reduced activity in the extrastriate visual cortex of individuals with strabismic amblyopia. *Neuroscience Letters*, **225**, 173-176.

Kabasakal L, Devranoglu K, Arslan O, Erdil TY, Sonmezoglu K, Uslu I, Tolun H, Isitman AT, Ozker K, Onsel C. 1995. Brain SPECT evaluation of the visual-cortex in amblyopia. *Journal of Nuclear Medicine*, **36**, 1170-1174.

Kanwisher N, Chun MM, McDermott J, Ledden PJ. 1996. Functional imaging of human visual recognition. *Cognitive Brain Research*, **5**, 55-67.

Kelly DM, Bischof WF, Wong-Wylie DR, Spetch ML. 2001. Detection of Glass patterns by pigeons and humans: implications for differences in higher-level processing. *Psychological Science*, **12**, 338-342.

Kiorpes L, Kiper DC, O'Keefe LP, Cavanaugh JR, Movshon JA. 1998. Neuronal correlates of amblyopia in the visual cortex of macaque monkeys with

experimental strabismus and anisometropia. *The Journal of Neuroscience*, **18**, 6411-6424.

Kourtzi Z, Huberle E. 2005. Spatiotemporal characteristics of form analysis in the human visual cortex revealed by rapid event-related fMRI adaptation. *Neuroimage*, **28**, 440-452.

Kourtzi Z, Tolias AS, Altmann CF, Augath M, Logothetis NK. 2003. Integration of local features into global shapes: monkey and human fMRI studies. *Neuron*, **37**, 333-346.

Krekelberg B, Vatakis A, Kourtzi Z. 2005. Implied motion from form in the human visual cortex. *Journal of Neurophysiology*, **94**, 4373-4386.

Kubova Z, Kuba M, Juran J, Blakemore C. 1996. Is the motion system relatively spared in amblyopia? Evidence from cortical evoked responses. *Vision Research*, **36**, 181-190.

Kurki I, Laurinen P, Peromaa T, Saarinen J. 2003. Spatial integration in Glass patterns. *Perception*, **32**, 1211-1220.

Kurki I, Saarinen J. 2004. Shape perception in human vision: specialized detectors for concentric spatial structures? *Neuroscience Letters*, **360**, 100-102.

Lamme VAF, Roelfsema PR. 2000. The distinct modes of vision offered by feedforward and recurrent processing. *Trends in Neuroscience*, **23**, 571-579.

Lancaster JL, Woldorff MG, Parsons LM, Liotti M, Freitas CS, Rainey L, Kochunov PV, Nickerson D, Mikiten SA, Fox PT. 2000. Automated Talairach atlas labels for functional brain mapping. *Human Brain Mapping*, **10**, 120-131.

Lee K-M, Lee S-H, Kim N-Y, Kim C-Y, Sohn J-W, Choi MY, Choi DG, Hwang J-M, Park KH, Lee DS, Yu YS, Chang KH. 2001. Binocularity and spatial frequency dependence of calcarine activation in two types of amblyopia. *Neuroscience Research*, **40**, 147-153.

Leguire LE, Rogers GL, Bremer DL, Walson P, Hadjiconstantinouneff M. 1992. Levodopa and childhood amblyopia. *Journal of Pediatric Ophthalmology & Strabismus*, **29**, 290-298.

Leguire LE, Walson PD, Rogers GLl, Bremer DL, Mcgregor ML. 1995. Levodopa carbidopa treatment for amblyopia in older children. *Journal Of Pediatric Ophthalmology & Strabismus*, **32**, 143-151.

Lerner Y, Hendler T, Ben-Bashat D, Harel M, Malach R. 2001. A hierarchical axis of object processing stages in the human visual cortex. *Cerebral Cortex*, **11**, 287-297.

Lerner Y, Pianka P, Azmon B, Leiba H, Stolovitch C, Loewenstein A, Harel M, Hendler T, Malach R. 2003. Area-specific amblyopic effects in human occipitotemporal object representations. *Neuron*, **40**, 1023-1029.

LeVay S, Wiesel TN, Hubel DH. 1980. The development of ocular dominance columns in normal and visually deprived monkeys. *The Journal of Comparative Neurology*, **191**, 1-51.

Levi DM. 1994. Pathophysiology of binocular vision and amblyopia. *Current Opinion in Ophthalmology*, **5**, 3-10.

Levi DM, Klein SA. 1982a. Differences in vernier discrimination for gratings between strabismic and anisometropic amblyopes. *Investigative Ophthalmology and Visual Science*, **23**, 398-407.

Levi DM, Klein SA. 1982b. Hyperacuity and amblyopia. *Nature*, **298**, 268-270.

Levi DM, Klein SA. 1985. Vernier acuity, crowding and amblyopia. *Vision Research*, **25**, 979-991.

Levi DM, Klein SA. 1986. Sampling in spatial vision. *Nature*, **320**, 360-362.

Levi DM, Klein SA. 1996. Limitations on position coding imposed by undersampling and univariance. *Vision Research*, **36**, 2111-2120.

Levi DM, Klein SA, Sharma V. 1999. Position jitter and undersampling in pattern perception. *Vision Research*, **39**, 445-465.

Levi DM, Klein SA, Wang H. 1994. Amblyopic and peripheral vernier acuity: a test-pedestal approach. *Vision Research*, **34**, 3265-3292.

Levi DM, Klein SA, Wang H. 1994. Discrimination of position and contrast in amblyopic and peripheral vision. *Vision Research*, **34**, 3293-3313.

Levi DM, Saarinen J. 2004. Perception of mirror symmetry in amblyopic vision. *Vision Research*, **44**, 2475-2482.

Levi DM, Waugh SJ, Beard BL. 1994. Spatial scale shifts in amblyopia. *Vision Research*, **34**, 3315-3333.

Levy I, Hasson U, Avidan G, Hendler T, Malach R. 2001. Center-periphery organization of human object areas. *Nature Neuroscience*, **4**, 533-539.

Lewis TL, Ellemberg D, Maurer D, Wilkinson F, Wilson HR, Dirks M, Brent HP. 2002. Sensitivity to global form in Glass patterns after early visual deprivation in humans. *Vision Research*, **42**, 939-948.

Liu GT, Miki A, Francis E, Quinn GE, Modestino EJ, Bonhomme GR, Haselgrove JC. 2004. Eye dominance in visual cortex in amblyopia using functional magnetic resonance imaging. *Journal of AAPOS*, **8**, 184-186.

Logothetis NK, Pfeuffer J. 2004. On the nature of the BOLD fMRI contrast mechanism. *Magnetic Resonance Imaging*, **22**, 1517-1531.

Logothetis NK, Wandell BA. 2004. Interpreting the BOLD signal. *Annual Review of Physiology*, **66**, 735-769.

Malach R, Levy I, Hasson U. 2002. The topography of high-order human object areas. *Trends in Cognitive Sciences*, **6**, 176-184.

Malach R, Reppas JB, Benson RR, Kwong KK, Jiang H, Kennedy WA, Ledden PJ, Brady TJ, Rosen BR, Tootell RBH. 1995. Object-related activity revealed by bunctional Magnetic-Resonance-Imaging in human occipital cortex. *Proceedings of The National Academy of Sciences of The United States of America*, **92**, 8135-8139.

Maloney RK, Mitchison GJ, Barlow HB. 1987. Limit to the detection of Glass patterns in the presence of noise. *Journal of the Optical Society of America, A Optics and Image Science*, **4**, 2336-2341.

Manny RE, Levi DM. 1982. The visually evoked potential in humans with amblyopia: pseudorandom modulation of uniform field and sine-wave gratings. *Experimental Brain Research*, **47**, 15-27.

Mansouri B, Allen HA, Hess RF, Dakin SC, Ehrt O. 2004. Integration of orientation information in amblyopia. *Vision Research*, **44**, 2955-2969.

McKee SP, Levi DM, Movshon JA. 2003. The pattern of visual deficits in amblyopia. *Journal of Vision*, **3**, 380-405.

Mendola JD, Conner IP, Roy A, Chan ST, Schwartz TL, Odom JV, Kwong KK. 2005. Voxel-based analysis of MRI detects abnormal visual cortex in children and adults with amblyopia. *Human Brain Mapping*, **25**, 222-236.

Miki A, Liu GT, Goldsmith ZG, Liu CSJ, Haselgrove JC. 2003. Decreased activation of the lateral geniculate nucleus in a patient with anisometropic amblyopia demonstrated by functional magnetic resonance imaging. *Ophthalmologica*, **217**, 365-369.

Milner AD, Goodale MA. 1997. *The Visual Brain in Action*. Oxford University Press, UK, 22.

Mizoguchi S, Suzuki Y, Kiyosawa M, Mochizuki M, Ishii K. 2005. Differential activation of cerebral blood flow by stimulating amblyopic and fellow eye. *Graefes Archive for Clinical and Experimental Ophthalmology*, **243**, 576-582.

Moradi F, Liu LC, Cheng K, Waggoner RA, Tanaka K, Ioannides AA. 2003. Consistent and precise localization of brain activity in primary visual cortex by MEG and fMRI. *Neuroimage*, **18**, 595-609.

Moseley M. 2002. Amblyopia: treatment and evaluation. In: Moseley M, Fielder A. Eds. *Amblyopia: a Multidisciplinary Approach*. Butterworth Heinmann, UK, 81-104.

Moseley M, Fielder A. 2001. Improvement in amblyopic eye function and contralateral eye disease: evidence of residual plasticity. *The Lancet*, **357**, 902-904.

Movshon JA, Kiorpes L. 1990. The role of experience in visual development. In: Coleman JR. Eds. *Development of Sensory Systems in Mammals*. Wiley Press, UK, 155-202.

Murray SO, Schrater P, Kersten D. 2004. Perceptual grouping and the interactions between visual cortical areas. *Neural Networks*, **17**, 695-705.

Nichols TE, Holmes AP. 2001. Nonparametric permutation tests for functional neuroimaging: a primer with examples. *Human Brain Mapping*, **15**, 1-25.

Ohla K, Busch NA, Markus ADE, Herrmann CS. 2005. Circles are different: the perception of Glass patterns modulates early event-related potentials. *Vision Research*, **45**, 2668-2676.

Olshausen BA, Field DJ. 2005. How close are we to understanding V1? *Neural Computation*, **17**, 1665-1699.

Pfurtscheller, G. 2001. Functional brain imaging based on ERD/ERS. *Vision Research*, **41**, 1257-1260.

Pfurtscheller G, Lopes da Silva FH. 1999. Event-related EEG/MEG synchronisation and desynchronisation: basic principles. *Clinical Neurophysiology*, **110**, 1842-1857.

Pfurtscheller G, Neuper C, Brunner C, Lopes da Silva F. 2005. Beta rebound after diffferent types of motor imagery in man. *Neuroscience Letters*, **378**, 156-159.

Popple AV, Levi DM. 2005. Location coding by the human visual system: multiple topological adaptations in a case of strabismic amblyopia. *Perception*, **34**, 87-107.

Portin K, Vanni S, Virsu V, Hari R. 1999. Stronger occipital cortical activation to lower than upper visual field stimuli – neuromagnetic recordings. *Experimental Brain Research*, **124**, 287-294.

Rislove EM, Hall EC, Kiorpes L. 2005. Global form perception in human amblyopia studied using Glass patterns. *Investigative Ophthalmology and Visual Science*, **46**, 3593 S.

Robinson SE, Vrba J. 1999. Functional neuroimaging by synthetic aperture magnetometry (SAM). In: Yoshimoto T, Kotani M, Kuriki S, Karibe H, Nakasato N. Eds. *Recent Advances in Biomagnetism*. Tohuko University Press, Japan, 302-305.

Roelfsema PR, Konig P, Engel AK, Sireteanu R, Singer W. 1994. Reduced synchronization in the visual cortex of cats with strabismic amblyopia. *European Journal of Neuroscience*, **6**, 1645-1655.

Rogers GL. 2003. Functional magnetic resonance imaging (fMRI) and effects of L-dopa on visual function in normal and amblyopic subjects. *Transactions of the American Ophthalmological Society*, **101**, 401-415.

Ross J. 2004. The perceived direction and speed of global motion in Glass pattern sequences. *Vision Research*, **44**, 441-448.

Ross J, Badcock DR, Hayes A. 2000. Coherent global motion in the absence of coherent velocity signals. *Current Biology*, **10**, 679-682.

Seu L, Ferrera VP. 2001. Detection thresholds for spiral Glass patterns. *Vision Research*, **41**, 3785-3790.

Shan Y, Moster ML, Roemer RA, Siegfried JB. 2000. Abnormal function of the parvocellular visual system in anisometropic amblyopia. *Journal of Pediatric Ophthalmology and Strabismus*, **37**, 73-78.

Sharma V, Levi DM, Coletta NJ. 1999. Sparse-sampling of gratings in the visual cortex of strabismic amblyopes. *Vision Research*, **39**, 3526-3536.

Sharma V, Levi DM, Klein SA. 2000. Undercounting features and missing features: evidence for a high-level deficit in strabismic amblyopia. *Nature*, **3**, 469-501.

Simmers AJ, Bex PJ. 2004. The representation of global spatial structure in amblyopia. *Vision Research*, **44**, 523-533.

Simmers AJ, Ledgeway T, Hess RF, McGraw PV. 2003. Deficits to global motion processing in human amblyopia. *Vision Research*, **43**, 729-738.

Sincich LC, Horton JC. 2005. The circuitry of V1 and V2: integration of color, form and motion. *Annual Review of Neuroscience*, **28**, 303-326.

Singh KD, Barnes GR, Hillebrand A. 2003. Group imaging of task related changes in cortical synchronization using non-parametric permutation testing. *Neuroimage*, **19**, 1589-1601.

Singh KD, Barnes GR, Hillebrand A, Forde EME, Williams AL. 2002. Task-related changes in cortical synchronization are spatially coincident with the hemodynamic response. *Neuroimage*, **6**, 103-114.

Sireteanu R, Tonhausen N, Mickli L, Zanella FF, Singer W. 1998. Cortical site of amblyopic deficit in strabismic and anisometropic subjects. *Investigative Ophthalmology and Visual Science*, **39**, S909.

Stevens K. 1978. Computation of locally parallel structure. *Biological Cybernetics*, **6**, 19-28.

Swettenham JB, Anderson SJ, Holliday IE. 2005. Magnetoencephalographic investigation on the neural basis of global shape analysis. *Journal of Vision*, **4**, 671a.

Talairach J, Tournoux P. 1988. *Co-planar Stereotaxic Atlas of the Human Brain.* Thieme, USA.

Tootell RBH, Hadjikhani NK, Mendola JD, Marrett S, Dale AM. 1998. From retinotopy to recognition: fMRI in human visual cortex. *Trends in Cognitive Sciences*, **2**, 174-183.

Tootell RBH, Mendola JD, Hadjikhani NK, Ledden PJ, Liu AK, Reppas JB, Sereno MI, Dale AM. 1997. Functional analysis of V3a and related areas in human visual cortex. *The Journal of Neuroscience*, **17**, 7060-7078.

Ungerleider LG, Mishkin M. 1982. Two cortical visual systems. In: Ingle DJ, Goodale MA, Mansfield RJW. Eds. *Analysis of Visual Behaviour*. MIT Press, USA.

Von Noorden GK, Crawford ML. 1992. The lateral geniculate nucleus in human strabismic amblyopia. *Investigative Ophthalmology and Visual Science*, **33**, 2729-2732.

Vrba J, Robinson SE. 2001. Signal processing in magnetoencephalography. *Methods*, **25**, 249-271.

Wang YZ, Hess RF. 2005. Contributions of local orientation and position features to shape integration. *Vision Research*, **45**, 1375-1383.

Wang H, Levi DM, Klein SA. 1998. Spatial uncertainty and sampling efficiency in amblyopic position acuity. *Vision Research*, **38**, 1239-1251.

Weibull W. 1951. A statistical distribution function of wide applicability. *Journal of Applied Mechanics*, **18**, 292-297.

Wilkinson F, James TW, Wilson HR, Gati JS, Menon RS, Goodale MA. 2000. An fMRI study of the selective activation of human extrastriate form vision areas by radial and concentric gratings. *Current Biology*, **10**, 1455-1458.

Wilson HR. 1991. Model of peripheral and amblyopic hyperacuity. *Vision Research*, **31**, 967-982.

Wilson HR, Wilkinson F. 1998. Detection of global structure in Glass patterns: implications for form vision. *Vision Research*, **38**, 2933-2947.

Wilson HR, Wilkinson F, Asaad W. 1997. Concentric orientation summation in human form vision. *Vision Research*, **37**, 2325-2330.

Yang C-I, Yang M-L, Huang J-C, Wan Y-L, Tsai RJ-F, Wai Y-Y, Liu H-L. 2003. Functional MRI of amblyopia before and after levodopa. *Neuroscience Letters*, **339**, 49-52.

Zheng D, Lamantia AS, Purves D. 1991. Specialized vascularization of the primate visual cortex. *Journal of Neuroscience*, **11**, 2622-2629.